Inaugural - Dissertation

zur Erlangung der Doktorwürde der
Naturwissenschaftlich-Mathematischen Gesamtfakultät der
Ruprecht-Karls-Universität
Heidelberg

Development and Implementation of Theoretical Methods for the Description of Electronically Core-Excited States

Vorgelegt von
Jan Wenzel, Master of Science Chemie
aus Hanau

Development and Implementation of Theoretical Methods for the Description of Electronically Core-Excited States

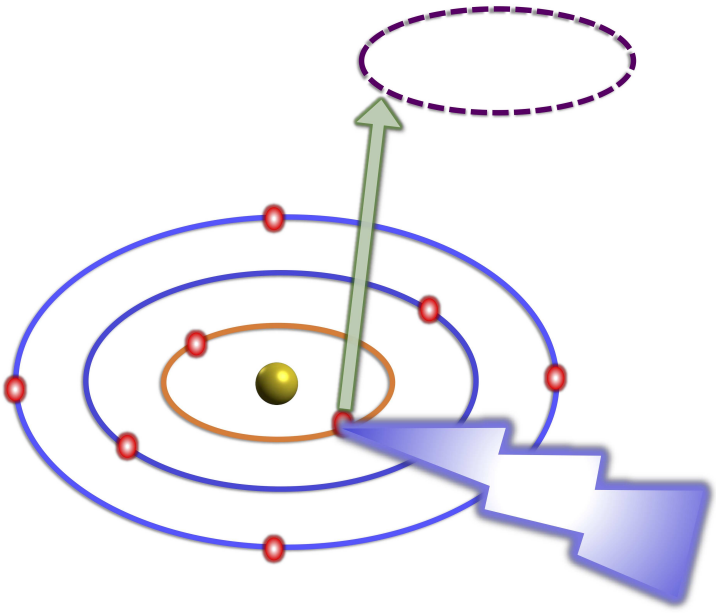

Referees:

Prof. Dr. Andreas Dreuw
PD Dr. Markus Pernpointner

Oral examination: March 23, 2016

Meiner Familie

Preface

Abstract

Nowadays, X-ray absorption spectroscopy (XAS) techniques are important tools to investigate the electronic structure of molecules. Mostly, these methods are applied in the field of organic electronics to study unoccupied molecular levels, which provide information about charge generation and transport properties. With the help of modern synchrotron soft beam sources, molecules can absorb high-energy X-ray photons, thereby promoting an electron from the core level, e.g. K-shell 1s orbitals, to the unoccupied molecular level. As a result, meta-stable bound core-excited states are generated. Since core orbitals are energetically well-separated from the remaining occupied and virtual orbital space, they are strongly contracted and the corresponding core-excited states are very localized. As a consequence, the generated core-hole interaction induces a rearrangement of the valence electrons, because the effective shielding of the nucleus is reduced. This effect leads to a lowering of the core-excitation energy of the final state. This rearrangement of the electrons can be understood as an orbital relaxation effect.

To fully understand and interpret experimental spectra, an accurate knowledge about core-excitation energies, transition moments, the character of the core-excited states as well as their corresponding properties is necessary. Such information can be obtained with quantum chemical (QC) methods. They help to analyze and interpret experimental spectra, thereby providing a deep insight into the nature of core-excited states. Generally, a plethora of methods is available to calculate excited states and simulate absorption spectra. The larger the system, the more expensive are the computations. Hence, certain levels of approximation have to be introduced to lower the computational cost. This leads to a loss of reliability and accuracy of the results. The time-dependent density functional theory (TD-DFT), for example, currently is the prevalently used excited-state method for the calculation of large molecules up to 300 atoms. However, TD-DFT has several disadvantages like the self-interaction error (SIE), which leads to wrong descriptions of certain kinds of excited states, e.g. charge-transfer states or core-excited states. The excitation energies of these types of states are strongly underestimated, but if these issues are kept in mind, TD-DFT is a useful tool, providing proper spectral features.

The algebraic diagrammatic construction scheme (ADC) is a prominent QC method for the calculation of excited states, which is known to provide accurate valence-excited states of small- and medium-sized molecules in an adequate computational time. The ADC approach is based on a Green's function formalism in combination with partitioning the Hamiltonian using perturbation theory. Due to its size-consistency and Hermitian ADC secular matrix structure, the level of approximation can be improved systematically and properties can be computed straightforwardly. It is possible to calculate one-particle state properties in combination with the intermediate state representation (ISR) approach, e.g. static dipole moments and state densities, which altogether provide enhanced information about absorption spectra. A further advantage of ADC is the indirect inclusion of orbital relaxation effects via couplings to higher-excited configurations, which are important to describe core-excited states properly. However, the calculation of core excitations is tedious using the unmodified ADC approach, because, in order to solve the ADC eigenvalue problem, numerical iterative eigenvalue solvers are employed usually only providing the energetically lowest eigenstates. Core-excited states, however, are located in the high-energy X-ray region of the optical spectrum and in order to calculate them directly, one has to compute all energetically underlying valence excitations as well. This is computationally very expensive and not feasible for medium-sized systems. The direct calculation of the core excitations is prevented by couplings between the valence and core-excited states. A solution to this issue is the application of the core-valence separation (CVS) approximation

to the ADC approach, which results in the CVS-ADC method. This approximation is based on the fact that core orbitals are energetically well-separated from the remaining orbital spaces and as a consequence, the couplings between core- and valence-excited states are small and can be neglected. In other words, the CVS approximation decouples the core and valence excitation spaces from each other and allows for a direct computation of core-excited states. In former work, it was proven that a very good agreement with experiments can be obtained at the extended second order level CVS-ADC(2)-x.

My PhD project mainly consists of two important parts. One was to enhance and develop variants of the CVS-ADC method and implement all approaches efficiently in the `adcman` program, which is part of the `Q-chem` program package. Secondly, I benchmarked these implementations and simulated X-ray absorption spectra of small- and medium-sized molecules from different fields. In this thesis, I present my implementations, as well as the results and applications obtained with the CVS-ADC methods and give a general introduction into quantum chemical methods. At first, I implemented the CVS-ADC approach up to the extended second in an efficient way. The program is able to deal with systems up to 500 basis functions in an adequate computational time, which allows for accurate calculations of medium-sized closed-shell molecules, e.g. acenaphthenequinone (ANQ). Afterwards, the CVS-ADC implementation was extended for the first time to deal with open-shell systems, i.e. ions and radicals, which implies a treatment of unrestricted wave functions and spin-orbitals. The resulting method is denoted as CVS-UADC(2)-x. For the first time, I applied the CVS approximation to the the third order ADC scheme, derived the working equations, and implemented the CVS-ADC(3) method in `adcman`. As the last step, I applied the CVS formalism for the first time to the ISR approach to enable calculations of core-excited state properties and densities. This provides the basis for subsequent evaluations of transition- and density matrices, which give access to exciton sizes, e.g. hole sizes or distances between hole and electron densities. All implementations are presented and discussed in the scope of my thesis.

To benchmark all restricted and unrestricted CVS-ADC/CVS-ISR methods up to third order in perturbation theory, I chose a set of small molecules, e.g. carbon monoxide (CO). The calculated values of core-excitation energies, transition moments and static dipole moments are compared with experimental data or other approaches, thereby estimating complete basis set (CBS) limits. Furthermore, a comprehensive study of different basis sets is performed. As it turns out, the CVS-ADC(2)-x method provides the best agreement with experiments, while CVS-ADC(3) overestimates the core excitation energies. In combination with the CBS limit of the aug-cc-series, a mean error of -0.23%$\pm$0.12% for core-excitation energies can be identified at the CVS-ADC(2)-x level for carbon, nitrogen and oxygen K-edge excitations, whereas CVS-ADC(3) exhibits errors of 0.61%$\pm$0.32%. This is due to fortuitous error compensation of basis set truncation, electron correlation, orbital relaxation and neglect of relativistic effects at the CVS-ADC(2)-x level. I show that this error compensation is broken at the third order level, because the ratio between terms describing relaxation and polarization effects is shifted in a way that the excitation energy increases. However, transition moments and spectral features, as well as static dipole moments, are excellently described with both CVS-ADC(2)-x and CVS-ADC(3). Overall, considering the detailed investigation of the basis set influence on the results, I conclude that the use of restricted or unrestricted CVS-ADC(2)-x in combination with a diffuse triple-ζ basis set in its Cartesian version can be seen as a black-box method for the calculation of core-excited states of organic molecules. Especially the 6-311++G** basis set provides an excellent ratio of accuracy to computational time.

Another important topic is the description of orbital relaxation effects. In the scope of this thesis, I show, how these effects are included indirectly within the CVS-ADC

approaches. For this purpose, two different descriptors are used, i.e. electron promotion numbers and the amount of doubly excited amplitudes. Furthermore, with the help of detachment/attachment (D/A) densities, which can be constructed via the CVS-ISR approach, relaxation effects can be visualized. For this purpose, the (D/A) densities are compared with hole/electron (h/e) densities based on the transition density matrix.

With this knowledge, the X-ray absorption spectra of medium-sized molecules and radicals from the fields of organic electronics and biology are investigated and analyzed. On the basis of these studies, the restricted and unrestricted versions of CVS-ADC(2)-x in combination with the 6-311++G** basis set exhibit mean errors of core-excitation energies around 0.1%, compared to experimental values. Additionally, core-excited state characters are analyzed with the help of state densities obtained via the CVS-ISR approach or the transition density matrix.

To demonstrate that the CVS-ADC(2)-x approach can be employed as a benchmark black-box method, TD-DFT results are compared directly with the ones at the CVS-ADC(2)-x level. As expected, TD-DFT underestimates core-excitation energies up to 4% due to the SIE, which is about 10 eV in the case of carbon 1s excitations.

Since the CVS approximation leads to both a simplification of the ADC working equations, as well as a restriction of the excitation space to correspond only to core excitations, the computational cost is reduced compared to the general ADC approach. To demonstrate the computational savings as a function of the size of the core space, several systems are investigated. CVS-ADC(3) calculations take about 8 – 10 times longer than CVS-ADC(2)-x calculations and since the results are generally more accurate with the latter method, the use of CVS-ADC(3) is not justified. Compared to general ADC(2)-x, the speed-up at the CVS-ADC(2)-x level is about a factor of 4.0, but this factor strongly depends on the size of the system and the size of the core space.

Next, I present applications from the field of organic electronics. The remarkable agreement with experimental data at the CVS-ADC(2)-x level justifies the prediction of yet non-recorded experimental X-ray absorption spectra. Therefore, I chose the anthracene cation, which can be seen as a model system of pentacene and its derivatives, which are commonly used as hole conductors (p-type). X-ray absorption spectra of the pentacene cation could provide deeper insight into its charge carrier properties, but measurements of experimental spectra of ionized species are usually very challenging. With the help of CVS-UADC(2)-x calculations, I show that the anthracene cation exhibits additional peaks due to the half-filled single-occupied molecular orbital. They are located approximately 3.5 eV – 1.5 eV below the first peak of neutral anthracene, which may help to distinguish a cation from the neutral species. Furthermore, the cationic spectrum exhibits peak broadening, compared to the two first peaks of neutral anthracene. Other applications concentrate on the trends of core-excited state properties along important potential energy surfaces (PES) of ANQ, phenol and bithiophene. Therefore, static dipole moments, energies, and exciton sizes are analyzed as a function of the C–O distances of ANQ and phenol, as well as the torsion around the central dihedral angle of bithiophene.

Finally, another aspect of the CVS-ISR method is the accessibility of transition moments between two states, which can be used to calculate oscillator strengths for core-excited state absorption (CESA) spectra. To the best of my knowledge, no experimental data of CESA processes between two core-excited states have been recorded yet. However, such spectroscopic data could exhibit new insights and the calculation of CESA transition moments using the CVS-ADC/CVS-ISR approach is straightforward. Hence, first results of CESA processes were calculated and are presented in this thesis. In the case of ANQ, particularly bright transitions can be identified from the lowest oxygen 1s excited-state to higher ones.

Zusammenfassung

Röntgenabsorptionsspektroskopie (XAS) ist heutzutage eine wichtige Methode, um die elektronische Struktur von Molekülen zu untersuchen. Diese Technik wird vor allem auf dem Gebiet der organischen Elektronik zur Untersuchung der unbesetzten Energieniveaus eingesetzt, wodurch Informationen über Ladungserzeugungs- und Ladungstransporteigenschaften erhalten werden. Mit Hilfe moderner Synchrotron-Strahlungsquellen können Moleküle hoch-energetische Röntgenphotonen absorbieren, wodurch Elektronen aus kernnahen Orbitalen in Valenzorbitale angeregt werden. Dies führt zu einem elektronisch kernangeregten Zustand, der meta-stabil ist und damit als quasi-gebunden bezeichnet wird. Da Kernorbitale energetisch von dem übrigen besetzten und virtuellen Orbitalraum getrennt sind, werden sie stark kontrahiert und die entsprechenden kernangeregten Zustände sind räumlich lokalisiert. Die erzeugte Wechselwirkung zwischen dem Kernloch und der Valenzschale induziert eine Umlagerung der Valenzelektronen, da die effektive Abschirmung des Kerns reduziert wird. Diese Umlagerung der Elektronen wird als Orbitalrelaxationseffekt bezeichnet und führt zu einer Absenkung der Anregungsenergie des kernangeregten Endzustandes.

Um experimentelle Spektren vollständig verstehen und interpretieren zu können, ist ein genaues Wissen über Anregungsenergien, Übergangsmomente und den Charakter der kernangeregten Zustände, sowie ihre entsprechenden Eigenschaften, erforderlich. Solche Informationen können mit quantenchemischen (QC) Methoden erhalten werden. Diese helfen bei der Auswertung und Interpretation experimenteller Spektren, wodurch ein tiefer Einblick in die Natur der kernangeregten Zustände erreicht werden kann. Heutzutage stehen im Allgemeinen eine Vielzahl von Methoden zur Berechnung angeregter Zustände zur Verfügung. Je größer das System, desto mehr Rechenzeit wird benötigt. Aus diesem Grund muss man zur Verringerung des Rechenaufwandes bestimmte Näherungen einführen, wodurch sich jedoch die Zuverlässigkeit und Genauigkeit der Ergebnisse verringert. Zum Beispiel ist die zeitabhängige Dichtefunktionaltheorie (TD-DFT) derzeit das am häufigsten verwendete Verfahren zur Berechnung angeregter Zustände von großen Molekülen bis zu 300 Atomen. Jedoch hat TD-DFT einige Nachteile, wie den Selbstwechselwirkungsfehler (SIE), wodurch bestimmte Arten von angeregten Zuständen falsch beschrieben werden. Beispielsweise werden durch den SIE die Anregungsenergien von Ladungstransferzuständen oder kernangeregten Zuständen stark unterschätzt. Wenn man allerdings diese Probleme beachtet, kann TD-DFT zur Berechnung spektraler Eigenschaften von Molekülen eingesetzt werden.

Das algebraisch-diagrammatische Konstruktionsschema (ADC) ist eine bekannte Methode zur Berechnung angeregter Zustände von kleinen und mittelgroßen Molekülen. Dabei wird bei angemessener Rechenzeit eine hohe Genauigkeit für valenzangeregte Zustände erreicht. ADC basiert auf einem Formalismus der Greenschen Funktion in Kombination mit einer störungstheoretischen Partitionierung des Hamilton-Operators. Neben Eigenschaften wie Größen-Konsistenz hat die ADC Säkularmatrix eine hermitische Struktur, wodurch die Methode systematisch verbessert werden kann und sich Zustandseigenschaften verhältnismäßig einfach berechnen lassen. In Kombination mit der *intermediate state representation (ISR)* lassen sich Ein-Teilchen-Zustandseigenschaften, wie zum Beispiel Dipolmomente und Zustandsdichten, berechnen, wodurch erweiterte Informationen über Absorptionsspektren zur Verfügung stehen. Ein weiterer Vorteil von ADC ist die indirekte Erfassung von Orbitalrelaxationseffekten über Kopplungen zu höher angeregten Konfigurationen, was zur korrekten Beschreibung von kernangeregten Zuständen wichtig ist. Allerdings ist die Berechnung der Kernanregungen mit dem unmodifizierten ADC Ansatz schwierig, da numerisch iterative Algorithmen eingesetzt werden, um das ADC Eigenwert-

problem zu lösen. Dadurch erhält man in der Regel immer die energetisch niedrigsten Eigenzustände. Kernangeregte Zustände liegen jedoch im hoch-energetischen Röntgenbereich des optischen Spektrums und um diese direkt zu berechnen, müsste man ebenfalls alle energetisch niedrigeren valenzangeregten Zustände mitberechnen. Dies ist rechnerisch sehr aufwendig und für mittelgroße Systeme nicht möglich. Die direkte Berechnung der Kernanregungen wird durch Kopplungen zwischen valenzangeregten und kernangeregten Zuständen verhindert. Eine Lösung für dieses Problem ist die *core-valence sepparation (CVS)* Näherung, die mit dem ADC-Ansatz kombiniert werden kann. Die resultierende Methode wird CVS-ADC genannt. Diese Näherung basiert auf der Tatsache, dass die kernnahen Orbitale energetisch von den übrigen Orbitalräumen getrennten sind. Als Folge sind die Kopplungen zwischen Kern- und Valenzzuständen klein und können deswegen vernachlässigt werden. Das heißt also, dass die CVS Näherung zu einer Entkopplung der Kern- und Valenzanregungsräume führt und so eine direkte Berechnung der kernangeregten Zustände ermöglicht. In früheren Arbeiten konnte nachgewiesen werden, dass eine sehr gute Übereinstimmung mit experimentellen Daten erreicht werden kann, wenn man die erweiterte zweite Ordnungs-Näherung CVS-ADC(2)-x verwendet.

Mein Promotionsprojekt besteht hauptsächlich aus zwei wichtigen Teilen. Zum einen habe ich die CVS-ADC Methode weiterentwickelt und alle Ansätze effizient im `adcman` Programm implementiert, das Teil des `Q-chem` Programmpaketes ist. Zweitens habe ich diese Implementierungen getestet, bewertet und angewendet. Dabei sind Röntgenabsorptionsspektren von kleinen und mittelgroßen Molekülen aus verschiedenen Bereichen simuliert worden. In dieser Arbeit stelle ich meine Implementierung sowie die Ergebnisse und Anwendungen mit den CVS-ADC Verfahren vor und gebe eine allgemeine Einführung in quantenchemische Methoden. Zuerst habe ich die CVS-ADC Methode bis zur erweiterten zweiten Ordnung auf effiziente Weise implementiert. Das Programm ist in der Lage, Systeme mit bis zu 500 Basisfunktionen in angemessener Rechenzeit zu behandeln, wodurch eine genaue Berechnung von mittelgroßen geschlossenschaligen Molekülen, wie zum Beispiel Bithiophen und Acenaphthenchinon (ANQ), möglich ist. Im nächsten Schritt wurde die CVS-ADC Methode zum ersten Mal für offenschalige Systeme, d.h. Ionen und Radikale, erweitert. Dazu musste die Behandlung von unbeschränkten Wellenfunktionen und Spin-Orbitalen ermöglicht werden. Die resultierende Methode wird als CVS-UADC(2)-x bezeichnet. Zum ersten Mal habe ich anschließend die CVS Näherung auf das ADC(3) Schema angewendet. Dabei wurden die Arbeitsgleichungen hergeleitet und die CVS-ADC(3) Methode in `adcman` implementiert. Zum Abschluss habe ich den CVS Formalismus zum ersten Mal auf den ISR Ansatz angewendet, um die Berechnungen von kernangeregten Zustandseigenschaften und Zustandsdichten zu ermöglichen. Dies stellt die Grundlage für nachfolgende Analysen von Übergangs- und Dichtematrizen dar. Diese geben Zugang zu Exzitongrößen, wie zum Beispiel Lochgrößen oder Abstände zwischen Loch- und Elektronendichten. Im Rahmen meiner Arbeit werden alle Implementierungen präsentiert und diskutiert.

Um alle eingeschränkten und uneingeschränkten CVS-ADC/CVS-ISR Methoden bis zur dritten Ordnung Störungstheorie zu bewerten, habe ich eine Reihe von kleinen Molekülen, wie zum Beispiel Kohlenmonoxid (CO), ausgewählt und die berechneten Werte der Kernanregungsenergien, Übergangsmomente und Dipolmomenten mit experimentellen Daten oder anderen Methoden verglichen. Zusätzlich wird dabei das vollständige Basissatz (CBS) Limit abgeschätzt. Weiterhin wird eine umfassende Studie über den Einsatz verschiedener Basissätze durchgeführt. Es stellt sich heraus, dass die CVS-ADC(2)-x Methode die beste Übereinstimmung mit Experimenten bietet, während CVS-ADC(3) die Kernanregungsenergien überschätzt. Für Kohlenstoff, Stickstoff und Sauerstoff 1s Anregungen beträgt der mittlere Fehler für Kernanregungsenergien -0.23%±0.12% auf dem CVS-ADC(2)-x

Niveau, während CVS-ADC(3) im Gegensatz einen Fehler von 0.61%±0.32% aufweist. Der Grund dafür ist eine zufällige Fehlerkompensation auf dem CVS-ADC(2)-x Niveau basierend auf der Nutzung eines unvollständigen Basissatzes, Elektronenkorrelation, Orbitalrelaxation und Vernachlässigung relativistischer Effekte. Dabei zeige ich, dass diese Fehlerkompensation bei CVS-ADC(3) gebrochen wird, weil das Verhältnis zwischen Termen, die Relaxations- und Polarisationseffekte beschreiben, in einer ungünstigen Weise verschoben wird. Allerdings werden Übergangsmomente und spektralen Eigenschaften sowie Dipolmomente sowohl mit CVS-ADC(2)-x als auch CVS-ADC(3) ausgezeichnet beschrieben. Unter Berücksichtigung der detaillierten Untersuchung des Basissatzeinflusses kann man schließen, dass die Benutzung der eingeschränkten und uneingeschränkten Varianten der CVS-ADC(2)-x Näherung in Kombination mit einem diffusen kartesischen triple-ζ Basissatz als *Black-Box* Methode für die Berechnung kernangeregter Zustände von organischen Molekülen angesehen werden kann. Vor allem der 6-311++G** Basissatz bietet ein hervorragendes Verhältnis von Genauigkeit und Rechenzeit.

Ein weiteres wichtiges Thema ist die Beschreibung der Orbitalrelaxationseffekte. Im Rahmen dieser Arbeit zeige ich, wie diese Effekte indirekt in den CVS-ADC Ansätzen berücksichtigt werden. Dafür werden zwei verschiedene Deskriptoren verwendet, diese sind die Elektronenpromotionszahl und die Menge an doppelt angeregten Amplituden. Darüber hinaus werden mit Hilfe von *Detachment/Attachment (D/A)* Dichten, die über den CVS-ISR Ansatz verfügbar sind, Relaxationseffekte visualisiert. Zu diesem Zweck werden die (D/A) Dichten mit Loch/Elektronen (h/e) Dichten verglichen, die aus der Übergangsdichtematrix berechnet werden.

Mit diesem Wissen können nun Röntgenabsorptionsspektren von mittelgroßen Molekülen und Radikalen aus den Bereichen der organischen Elektronik und Biologie untersucht und analysiert werden. Auf der Grundlage dieser Studien zeigt sich, dass die eingeschränkten und uneingeschränkten Versionen von CVS-ADC(2)-x in Kombination mit dem 6-311++G** Basissatz einen mittleren Fehler für Kernanregungsenergien von etwa 0.1% im Vergleich zu experimentellen Werten aufweisen. Außerdem werden mit Hilfe von Zustandsdichten, die u.a. mit der CVS-ISR Methode berechnet werden können, die Charaktere der kernangeregten Zustände analysiert.

Um zu demonstrieren, dass der CVS-ADC(2)-x Ansatz als *Benchmark Black-Box-Verfahren* eingesetzt werden kann, werden die Ergebnisse zudem direkt mit TD-DFT Rechnungen verglichen. Auf Grund des SIE unterschätzt TD-DFT die Kernanregungsenergien um bis zu 4%, was in etwa 10 eV im Falle einer Kohlenstoff 1s Anregung ist.

Da die CVS Näherung zu einer Vereinfachung der ADC Gleichungen führt und zudem der Anregungsraum auf Kernanregungen eingeschränkt wird, reduziert sich der Rechenaufwand im Vergleich zu der allgemeinen ADC Methode. Um diese Einsparungen in Abhängigkeit von der Größe des Kernraumes zu demonstrieren, werden verschiedene Systeme untersucht, wodurch die Rechenzeiten der CVS-ADC Methode quantifiziert wird. Eine CVS-ADC(3) Rechnung dauert in etwa 8 bis 10 mal länger als eine CVS-ADC(2)-x Rechnung und da die Ergebnisse in der Regel auf dem CVS-ADC(2)-x Niveau genauer sind, ist die Nutzung von CVS-ADC(3) nicht gerechtfertigt. Im Vergleich zur allgemeinen ADC(2)-x Methode, verringert sich der Rechenaufwand durch die CVS Näherung um den Faktor 4.0, wobei dieser Wert stark von der Größe des Systems und der Größe des Kernraumes abhängt.

In einem nächsten Schritt präsentiere ich Anwendungen aus dem Bereich der organischen Elektronik. Aufgrund der bemerkenswerten Übereinstimmung mit experimentellen Daten auf dem CVS-ADC(2)-x Niveau, ist es gerechtfertigt, noch nicht experimentell gemessene Röntgenabsorptionsspektren mit dieser Methode vorherzusagen. Deshalb habe ich das Anthracen-Kation ausgewählt, welches als Modellsystem von Pentacen und seinen

Derivaten benutzt werden kann, die gemeinhin als Lochleiter (p-Typ) verwendet werden. Röntgenabsorptionsspektren des Pentacen Kations könnten tiefere Einblicke in die Ladungsträgereigenschaften liefern, aber experimentelle Messungen von ionisierten Molekülen sind in der Regel sehr schwierig. Mit der Hilfe von CVS-UADC(2)-x Rechnungen zeige ich, dass das Anthracen-Kation aufgrund der halbgefüllten einfach besetzten Orbitale zusätzliche Signale etwa 3.5 eV – 1.5 eV unter dem ersten Signal des neutralen Anthracens aufweist. Weiterhin hat das kationische Spektrum Signalverbreiterungen im Vergleich zu den beiden ersten Signalen der neutralen Anthracen Spezies. Andere Anwendungen konzentrieren sich auf die Entwicklung von kernangeregten Zustandseigenschaften entlang wichtiger Potentialflächen (PES) von ANQ, Phenol und Bithiophen. Dabei werden Dipolmomente, Energien und Exziton Größen als Funktion der C–O Abstände von ANQ und Phenol, sowie die Drehung um den mittleren Diederwinkel von Bithiophen analysiert.

Abschließend werden Übergangsmomente zwischen zwei Zuständen diskutiert, die über die CVS-ISR zugänglich sind. Diese können verwendet werden, um Oszillatorstärken für kernangeregte Zustandsabsorptionen (CESA) zu berechnen. Soweit mir bekannt ist, gibt es noch keine experimentellen Daten von CESA Prozessen von einem kernangeregten Zustand zu einem anderen. Allerdings könnten solche spektroskopischen Daten neue Erkenntnisse hervorbringen. Da die Berechnung der CESA Übergangsmomente unter Verwendung des CVS-ADC/CVS-ISR Ansatzes relativ einfach möglich ist, werden erste Ergebnisse von berechneten CESA Prozessen in dieser Arbeit vorgestellt. Dazu wurde eine Reihe von repräsentativen Molekülen ausgewählt. Im Falle von ANQ, können beispielsweise besonders helle Übergänge von dem energetisch niedrigsten Sauerstoff 1s angeregten Zustand zu höher Zuständen identifiziert werden.

Contents

Chapter 1

Introduction

Photochemistry is a special branch of chemistry, which deals with the interaction of atoms or molecules with electromagnetic radiation. Nowadays, the investigation of photochemical processes is of great practical importance in many different fields. For example, a detailed knowledge about light-absorbing molecules that are applied in organic electronics helps to improve and develop organic solar cells or organic light-emitting diodes.[1–4] In the field of medical biology, photo-initiated DNA damages are investigated to understand cancer formations and to improve radiation cancer therapies.[5–8]

Without any external radiation, a molecule is usually in its electronic ground state (S_0). When the system absorbs light, i.e. a photon, the molecule is promoted to an optically allowed excited state, thereby transferring an electron from an occupied molecular orbital (MO) to a virtual MO level. The corresponding excitation energy (ω) depends on the energy of the absorbed photon. Such excitation processes are usually ultra-fast, so-called vertical Franck-Condon excitations that involve vibration levels according to the structure of the potential energy surface (PES) of the corresponding excited state.[9] Generally, an electronically excited state has a certain lifetime which depends on environmental influences and the molecular system itself. There are a plethora of subsequent decay processes after vertical excitations, e.g. fluorescence, internal conversion, intersystem crossings, charge and energy transfers and many more. Eventually, the molecule essentially relaxes back to the ground state level. Depending on the decay mechanism, either its initial structure or a photoproduct, which differs chemically or structurally, is obtained. Besides excitations into virtual MOs, which results in a bound-excited state, an electron can also be excited into the continuum, thereby ionizing the molecule.

A special kind of electronic photo-excitation is the promotion of core electrons into the virtual MO level, which results in a core-excited state.[10] Core electrons are usually occupying the energetically lowest molecular orbitals, i.e 1s orbitals in the case of light elements like carbon. Regarding heavier atoms, e.g. sulfur, 2s or 2p electrons belong to the core space too. Since core electrons are strongly bound to the atomic nucleus, due to Coulombic attraction, a large amount of energy is necessary to excite them. Hence, a molecule needs to absorb X-ray photons to excite core electrons, while valence-excited states are generated via absorption of ultraviolet (UV) or visible (VIS) light. If the energy of the X-ray photon is larger than the ionization threshold of the respective core orbital, a core-ionized state can be generated. This results in an released electron with a large kinetic energy.[10] Figure 1.1 illustrates the different kinds of significant photo-absorption processes in a simplified scheme.

Optically allowed core-exited states can be studied experimentally by means of X-ray

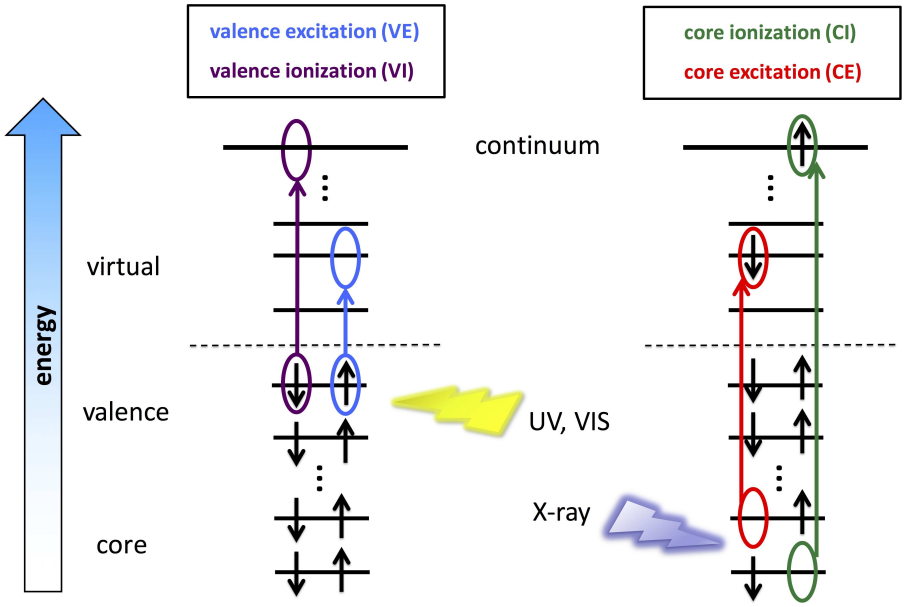

Figure 1.1: Schematic overview of different types of significant photo-absorption processes. The energies are not true to scale. Valence excitations are blue and valence ionizations are purple. Excitations from the core level are red, while core ionizations are green.

absorption spectroscopy (XAS) techniques.[11] Over the last years, modern synchrotron soft beam sources have been developed.[12,13] They provide tunable and intense X-ray beams, which are suited to measure organic compounds. Since core orbitals are energetically well-separated from the remaining occupied and virtual orbital space, excitations of core electrons generate a typical sharp rise in the absorption spectrum, i.e. when the energy of the incoming X-ray photon is equal to the binding energy of the respective core orbital. Those edges correspond to the level (electron shell with quantum numbers K, L, ...), where the vacancy is generated.[10] Hence, K-edge spectroscopy probes 1s core excitations, while L-edge corresponds to 2s or 2p core electron promotions. These edges are element specific, because the strength of the Coulombic attraction depends on the charge of the nucleus. For example, typical K-edges of carbon atoms are around 285 eV, while nitrogen 1s core excitations are around 400 eV.[14] In Figure 1.2, an arbitrary K-edge X-ray absorption spectrum is illustrated schematically. The K-edge can generally be divided into three different regions.[10] Firstly, there is the pre-edge, which is dominated by excitations of core electrons from 1s to π^*, d-orbitals. Sharp signals in this region exist for transition metals where d-orbitals are partially occupied and thus correspond to the lowest half- or unoccupied orbitals. These signals usually have a low intensity.[15] Secondly, there is the rising-edge which contains core excitations dominated by 1s to π^*, p transitions. These signals are usually strong and lead to a characteristic spectrum. Both rising and pre-edge regions correspond to core excitations and are experimentally probed with X-ray absorption near edge structure (XANES) spectroscopy or near edge X-ray absorption fine structure (NEXAFS) spectroscopy. Both techniques correspond to the measurement of absorption cross-sections of condensed matter, thin films or liquids, while gas-phase experiments are often just called XAS.[16,17] The third region, of the XAS spectrum corresponds to the signals above the ionization threshold of the core orbitals, i.e. core electron promotions to

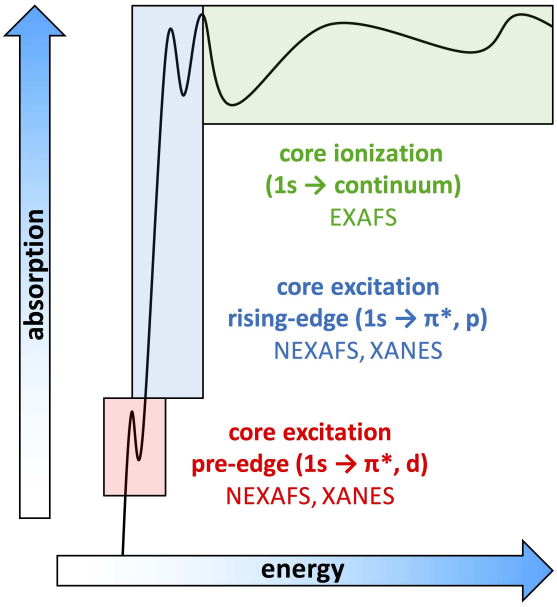

Figure 1.2: Schematic illustration of an arbitrary K-edge X-ray absorption spectrum. The different regions of the K-edge are marked and the corresponding spectroscopic method is denoted.

the continuum. This region is probed with the extended X-Ray absorption fine structure (EXAFS) spectroscopy technique.[10]

Core-excited states are meta-stable or quasi-bound states which have a short lifetime. Due to the strong Coulomb attraction, core orbitals are contracted and the corresponding core-excited states are very localized. Typical decay mechanisms after core excitations are resonant Auger (RA)[18–21] decay, dissociation[22,23] of the molecule or emission[24] of a photon. The RA decay can be divided into intramolecular or intermolecular mechanisms. The most important intramolecular mechanisms are spectator RA (sRA) decay, participator RA (pRA) decay and the so-called "shake up or down" RA (mRA) decay. In the sRA decay, the core-excited electron remains as a "spectator" in the virtual level, while the core hole is refilled by an electron from the valence occupied level via relaxation. The released energy of this process is then used to promote another electron from the valence level to the continuum, which produces a highly excited valence-ionized state. In the pRA mechanism, the initially core-excited electron participates directly in the decay via relaxing back to the occupied level, thereby releasing energy which is used to detach a valence electron and thus ionize the system. The mRA decay describes situations where the core-excited electron hops to a higher or lower virtual level during the decay mechanism. An important intermolecular decay mechanism is the interatomic Coulombic decay (ICD) process, which was first formulated in 1997 by *Cederbaum et al.*[25] Generally, an electronically excited molecule, placed in a molecular environment, can transfer its excess energy to a neighboring molecule which subsequently emits an electron.[26–29] Such ICD processes can originate from core-excited states through a sRA cascade mechanism.[7,8] Electrons, that are released through ICD after core-excitation, are highly energy and site selective due to their local character. This leads to possible applications in radiation biology, where the localized

emitted electron may allow for a more targeted cancer radiotherapy.

The most important applications of XAS correspond to the analysis of the electronic structure of molecules.[11,13,30,31] As mentioned above, due to the strongly bound and contracted 1s orbital, K-edge core-excited states are element specific and strongly localized, thus they serve as chemical fingerprints.[11] NEXAFS and XANES spectroscopies are applied in surface science, medical biological research and organic electronics.[12,13,32,33] For example, information about the band structure of electrical conducting molecules can be obtained with NEXAFS spectroscopy.[17,34–36] In recent studies, the orientation between adsorbed molecules on gold surfaces has been investigated with XAS techniques, which helped to understand biomolecular surface interactions.[37,38] Another example from the field of biology, is the analysis of tautomers of the deoxyribonucleic acid (DNA) bases cytosine and uracil.[33] The population of tautomers was determined via analyzing the signal structures of their NEXAFS spectra. Furthermore, there are techniques in the field of time-resolved and *in situ* X-ray spectroscopy which help to explain chemical reaction mechanisms with radicals as intermediate species or that provide information about inorganic coordination compounds.[30,31,39] Examples from this field are the investigation of the electronic structure of nitronyl nitroxide radical derivatives or the radical formation of titanium oxide dimers.[40,41] Generally, radical or open-shell systems are difficult to measure experimentally. Nevertheless, X-ray absorption (XA) spectra of the allyl radical could be obtained and helped to identify key radical intermediate species in reaction mechanisms.[42]

To fully understand and interpret experimental spectra, it is necessary to obtain an accurate knowledge of excitation energies, transition moments, the character of the excited states, as well as their corresponding properties. Such information can be obtained by quantum chemical (QC) methods, which help to analyze and interpret experimental spectra, thereby providing a deep insight into the nature of excited states. Furthermore, accurate theoretical methods are able to predict excited states of molecular species and simulate their absorption spectra. Nowadays, a plethora of QC methods is available to describe excited states, but very accurate black-box methods are usually limited to small systems up to fifteen atoms.[43] However, a quantitative agreement with experiments can be achieved with these methods. For the calculations of larger systems, additional approximations have to be introduced in order to reduce the computational effort. Consequently, investigating large systems requires a proper knowledge about the limitations of the method of choice as well as the comparison with benchmark calculations. Additional problems arise when core-excited states are investigated. Usually, the iterative numerical diagonalization algorithms, which are employed to solve the QC eigenvalue problems, yield the lowest eigenvalues. Since core-excited states are in the high energy X-ray region of the excitation spectrum, all underlying valence-excited states must be calculated as well, which is computationally expensive and is not possible for accurate methods or large systems. There are approaches to tackle this problem, e.g. the core-valence separation (CVS)[44,45] approximation, which is based on the fact that core orbitals are energetically well-separated from the other occupied or virtual orbital spaces and, as a consequence, couplings between core- and valence-excited states can be neglected. In other words, the CVS approximation decouples the space of core excitations from the space of valence excitations which allows for a direct computation of core-excited states. Since core electrons are strongly bound, the generated core-hole interaction induces a rearrangement of the valence electrons, because the effective shielding of the nucleus is reduced.[46–50] This effect leads to a lowering of the core-excitation energy of the final state compared to valence excitations where usually no rearrangement of the valence electrons occurs. The electron rearrangement can be understood as an orbital relaxation effect and accurate quantum chemical methods for the calculation of core-excited states require consideration of this process.

Over the last years, several QC approaches have been developed to simulate XAS spectra, for example, the coupled cluster (CC)[51–54] family, like equation-of motion coupled cluster (EOM-CC)[55–59], the symmetry adapted cluster configuration interaction (SAC-CI)[60–65] or the approximate coupled cluster scheme of second order (CC2)[66,67]. All of these CC methods are known to provide accurate results compared to experiments, but they are limited to medium-sized systems with about 60 atoms. Large systems are usually treated with time-dependent density functional theory (TD-DFT)[68–73] in reasonable computational time, exploiting the CVS approximation. Experimental X-ray absorption spectra are often well-reproduced at the TD-DFT level, but the self-interaction error (SIE) in combination with the small energetic gap between occupied and unoccupied electronic levels leads to a large underestimation of core-excitation energies.[74,75] To correct this error, there are, for example, correction schemes based on the resonant-convergent first-order polarization propagator.[71,72] Without a correction scheme, an additional energy-shift is necessary to agree with experiments.

Another prominent QC method to study the photochemistry of small and medium-sized molecules is the algebraic diagrammatic construction scheme (ADC) of the polarization propagator.[76–79] Due to its size-consistency and Hermitian structure, the ADC scheme is known to be an accurate and reliable approach for the calculation of excited states and their properties. Generally, the approach is based on a Green's function formalism in combination with the typical Møller-Plesset (MP)[80] partitioning of the Hamiltonian. Restricted ADC for closed-shell molecules provides an overall accuracy of the strict second order version ADC(2)-s of 0.22 eV±0.5 eV, while at the third order level ADC(3) an average error of 0.12 eV±0.28 eV for singlet valence-excited states for standard organic molecules is obtained.[81] Its unrestricted variant (UADC) for valence-excited states exhibits an averaged mean deviation in excitation energies of 0.3 eV – 0.4 eV.[82] A big advantage of ADC is the indirect inclusion of orbital relaxation effects via couplings to doubly- or higher-excited configurations, which are included in second or higher order in perturbation theory. Furthermore, the ADC method in combination with the intermediate state representation (ISR)[78,83] approach provides an elegant way to calculate one-particle excited-state properties, e.g. static dipole moments and excited-state densities, which provide enhanced information about a system of interest. Since excited-state vectors mostly consist of a mixture of different MO transitions, a proper characterization of an electronically excited state can be difficult. Thus it is an advantage to look at state densities rather than considering MOs.[84] Furthermore, the total ADC state density contains information about orbital relaxation effects that can be visualized by plotting electron detachment/attachment (D/A) densities[85] or which can be quantified by calculating the electron promotion numbers.[84,86–88] However, the calculation of core-excited states with ADC methods is generally challenging, because the solution of the ADC eigenvalue problem is achieved via an iterative diagonalization procedure designed to yield the energetically lowest states of the excitation spectrum. As mentioned above, a solution to this problem is the CVS approximation, which results in the CVS-ADC approach. It could be shown in former publications that the extended second order approach CVS-ADC(2)-x achieves excellent results for core-excited states.[89–91] However, efficient implementations in modern quantum chemistry programs were not available and the programs used in the quoted literature were limited to less than 200 basis functions.[92]

In the scope of my dissertation, I enhanced the CVS-ADC approach and efficiently implemented the methods into a development version of the `adcman`[93] program, which is part of the `Q-Chem`[94] program package. At first, I implemented the restricted CVS-ADC scheme up to the extended second order for closed shell systems allowing efficient calculations of systems with 500 basis functions in a reasonable computational time. Next,

this implementation was expanded for open-shell molecules by introducing the unrestricted variant CVS-UADC(2)-x for the first time. Both restricted and unrestricted versions provide very accurate results compared to experiments, thus the question arose, whether a higher-order CVS-ADC(3) approach improves the description of core-excited states. Therefore, I derived the CVS-ADC(3) approach by applying the CVS approximation for the first time to the ADC(3) working equations and I also implemented this approach in the `adcman` program. Finally, to enable calculations of core-excited state properties and densities, I applied the CVS formalism for the first time to the ISR approach and the resulting CVS-ISR method was implemented in `adcman` too. In combination with the wave function analysis package `libwfa`[84,86–88], a deeper evaluation of transition- and density matrices can be performed, which provide access to exciton sizes, e.g. hole sizes or distances between hole and electron densities.

In this thesis, I would like to present the CVS-ADC/CVS-ISR methods and the results that I obtained with my implementations. Quantum chemical methods and theoretical aspects for the calculation of ground and (core-)excited states are introduced in chapter 2. The focus is on the (CVS-)ADC method but basic concepts of quantum chemistry and electronic structure theory are also briefly explained as well as alternative approaches. Next, the implementation of the CVS-ADC/CVS-ISR methods in the `adcman/Q-Chem` environment is presented in chapter 3. Here, the general interface, implemented features and the modified working equations are discussed. In the following chapters 4 – 10, calculations and results using the CVS-ADC/CVS-ISR methods are discussed in detail. In chapter 4 I present benchmark calculations of the CVS-ADC methods up to the third order using a set of small organic molecules. The calculated results are compared with experimental data or in the case of the CVS-ISR approach with values obtained at the SAC-CI level of theory. Alongside, the complete basis set limit is estimated and a detailed study of basis set influences is performed. Next in chapter 5, the contribution of orbital relaxation effects on core-excitation energies is discussed by means of CVS-ADC calculations up to the third order. Here, the CVS-ISR approach is used to calculate detachment/attachment densities, which provide a possibility to visualize relaxation effects. After benchmarking the CVS-ADC methods, I present in chapter 6 calculated XA spectra of chosen medium-sized molecules from the fields of organic electronics and biology to demonstrate the capability of the CVS-ADC(2)-x approach to successfully simulate XA spectra of chemically relevant systems. Furthermore, the first XA spectra of radicals ever calculated with the CVS-UADC method are presented too. Afterwards in chapter 7, the core-excitation energies at the CVS-ADC(2)-x level presented in chapter 6 are compared with TD-DFT and CVS-ADC(2)-s results to demonstrate the self-interaction error (SIE) problem inherent in pure TD-DFT and to clarify the accuracy at the CVS-ADC(2)-x level. Chapter 8 contains an analysis of computational timings of my implementation of the CVS-ADC methods up to the third order. The focus is on the correlation of the computational time and the size of the core orbital space. In chapter 9, I present some applications of CVS-ADC calculations in the field of organic electronics. The first study is about pentacene and its derivatives, which are often used in organic field-effect transistors (OFET) as hole conductors (p-type). A deeper insight into the charge carrier properties of pentacene systems could be provided by XA spectra of their cations, which are, however, very challenging to measure experimentally. Therefore, I predict the XA spectrum of the anthracene cation, which was chosen as a model system for pentacene. The second investigation presented in chapter 9 is about trends of core-excited state properties along potential energy surfaces (PES) of chosen molecules. In the following chapter, another aspect of the CVS-ISR method is presented, i.e. the accessibility of transition moments between two states. These transition moments are used to calculate oscillator strengths

for core-excited state absorption (CESA) spectra. Finally, chapter 11 provides concluding remarks and an outlook on future projects. There, the results and calculations presented in this thesis are summarized.

At this point, I would like to mention that most of the parts of this dissertation have already been published by me as author (five publications) or co-author (three publications) in peer-reviewed journals.[84,93–99] These publications are listed below.

- **Physical properties, exciton analysis and visualization of core-excited states: an intermediate state representation approach**
  Jan Wenzel and Andreas Dreuw
  submitted for publication in Journal of Chemical Theory and Computation, (2016)

- **Statistical Analysis of Electronic Excitation Processes: Quantification of Location, Compactness, and Excitonic Correlation Effects**
  Felix Plasser, Benjamin Thomitzni, Stefanie A. Bäppler, Jan Wenzel, Dirk R. Rehn, Michael Wormit, and Andreas Dreuw
  Journal of Computational Chemistry, 36 (2015), pages 1609-1620

- **Analysis and comparison of CVS-ADC approaches up to third order for the calculation of core-excited states**
  Jan Wenzel, Andre Holzer, Michael Wormit, and Andreas Dreuw
  Journal of Chemical Physics, 142 (2015), pages 214104

- **Advances in molecular quantum chemistry contained in the Q-Chem 4 program package**
  Yihan Shao, Zhengting Gan, Evgeny Epifanovsky, Andrew T. B. Gilbert, Michael Wormit, Joerg Kussmann, Adrian W. Lange, Andrew Behn, Jia Deng, Xintian Feng, Debashree Ghosh, Matthew Goldey, Paul R. Horn, Leif D. Jacobson, Ilya Kaliman, Rustam Z. Khaliullin, Tomasz Ku, Arie Landau, Jie Liu, Emil I. Proynov, Young Min Rhee, Ryan M. Richard, Mary A. Rohrdanz, Ryan P. Steele, Eric J. Sundstrom, H. Lee Woodcock III, Paul M. Zimmerman, Dmitry Zuev, Ben Albrecht, Ethan Alguire, Brian Austin, Gregory J. O. Beran, Yves A. Bernard, Eric Berquist, Kai Brandhorst, Ksenia B. Bravaya, Shawn T. Brown, David Casanova, Chung-Min Chang, Yunquing Chen, Siu Hung Chien, Kristina D. Closser, Deborah L. Crittenden, Michael Diedenhofen, Robert A. DiStasio Jr., Hainam Do, Anthony D. Dutoi, Richard G. Edgar, Shervin Fatehi, Laszlo Fusti-Molnar, An Ghysels, Anna Golubeva-Zadorozhnaya, Joseph Gomes, Magnus W. D Hanson-Heine, Philipp H. P. Harbach, Andreas W. Hauser, Edward G. Hohenstein, Zachary C. Holden, Thomas-C. Jagau, Hyunjun Ji, Ben Kaduk, Kirill Khistyaev, Jaehoon Kim, Jihan Kim, Rollin A. King, Phil Klunzinger, Dmytro Kosenkov, Tim Kowalczyk, Caroline M. Krauter, Ka Un Lao, Adle Laurent, Keith V. Lawler, Sergey V. Levchenko, Ching Yeh Lin, Fenglai Liu, Ester Livshits, Rohini C. Lochan, Arne Luenser, Prashant Manohar, Samuel F. Manzer, Shan-Ping Mao, Narbe Mardirossian, Aleksandr V. Marenich, Simon A. Maurer, Nicholas J. Mayhall, Eric Neuscamman, C. Melania Oana, Roberto Olivares-Amaya, Darragh P. O'Neill, John A. Parkhill, Trilisa M. Perrine, Roberto Peverati, Alexander Prociuk, Dirk R. Rehn, Edina Rosta, Nicholas J. Russ, Shaama M. Sharada, Sandeep Sharma, David W. Small, Alexander Sodt, Tamar Stein, David Stck, Yu-Chuan Su, Alex J. W. Thom, Takashi Tsuchimochi, Vitalii Vanovschi, Leslie Vogt, Oleg Vydrov, Tao Wang, Mark A Watson, Jan Wenzel, Alec White, Christopher F. Williams, Jun Yang, Sina Yeganeh, Shane R. Yost, Zhi-Qiang You, Igor Ying Zhang, Xing Zhang, Yan Zhao, Bernard R. Brooks, Garnet K. L. Chan, Daniel M. Chipman, Christopher J. Cramer, William A. Goddard III,

Mark S. Gordon, Warren J. Hehre, Andreas Klamt, Henry F. Schaefer III, Michael W. Schmidt, C. David Sherrill, Donald G. Truhlar, Arieh Warshel, Xin Xu, Aln Aspuru-Guzik, Roi Baer, Alexis T. Bell, Nicholas A. Besley, Jeng-Da Chai, Andreas Dreuw, Barry D. Dunietz, Thomas R. Furlani, Steven R. Gwaltney, Chao-Ping Hsu, Yousung Jung, Jing Kong, Daniel S. Lambrecht, WanZhen Liang, Christian Ochsenfeld, Vitaly A. Rassolov, Lyudmila V. Slipchenko, Joseph E. Subotnik, Troy Van Voorhis, John M. Herbert, Anna I. Krylov, Peter M. W. Gill, and Martin Head-Gordon
Molecular Physics, 113 (2015), pages 184-215

- **Calculating X-ray absorption spectra of open-shell molecules with the unrestricted algebraic-diagrammatic construction scheme for the polarization propagator**
  Jan Wenzel, Michael Wormit, and Andreas Dreuw
  Journal of Chemical Theory and Computation, 10 (2014), pages 4583-4598

- **Calculating core-level excitations and x-ray absorption spectra of medium-sized closed-shell molecules with the algebraic-diagrammatic construction scheme for the polarization propagator**
  Jan Wenzel, Michael Wormit, and Andreas Dreuw
  Journal of Computational Chemistry, 35 (2014), pages 1900-1915

- **Investigating excited electronic states using the algebraic diagrammatic construction (ADC) approach of the polarisation propagator**
  Michael Wormit, Dirk R. Rehn, Philipp H. P. Harbach, Jan Wenzel, Caroline M. Krauter, Evgeny Epifanovsky, and Andreas Dreuw
  Molecular Physics, 112 (2014), pages 774-784

- **Charge and energy transfer in a bithiophene perylenediimide based donor-acceptor-donor system for use in organic photovoltaics**
  Jan Wenzel, Andreas Dreuw, and Irene Burghardt
  Physical Chemistry Chemical Physics, 15 (2013), pages 11704-11716

Chapter 2

Theoretical Methods

In this chapter, I introduce the basic concepts of quantum chemistry and discuss the theoretical methods that are used in the chapters 4 – 10 to study X-ray absorption processes. The focus is on the algebraic-diagrammatic construction (ADC) scheme for the polarization propagator[76–79] (chapter 2.5), which is the quantum chemical excited state method that I have enhanced via implementing and deriving certain core-valence separated variants (CVS-ADC) for the calculation of core-excited states. The ADC method is discussed in detail, thereby presenting the derivation via the intermediate state representation (ISR)[78,83] and introducing the core-valence separation approximation (CVS)[44,45,100]. Since ADC is based on elemental concepts, e.g. the Hartree-Fock (HF) method[101], I introduce these approaches at first.

Therefore, I start with the explanation of elementary approaches of quantum chemistry in chapter 2.1 followed by an introduction to general methods for the description of the electronic ground state in chapter 2.2. There, I concentrate on the HF method as well as the many-body perturbation theory (MBPT)[101], because these approaches are important to understand the ADC method. Furthermore, alternative prominent methods, which are applied in the scope of this thesis, i.e. the density functional theory (DFT)[102], the configuration interaction (CI)[101] and the coupled-cluster (CC)[103] family are introduced briefly to provide a broader picture of quantum chemical approaches. In chapter 2.3, I give a general overview to excited state methods, followed by discussions of approaches to calculate core excitations in 2.4. The focus is on the configuration interaction singles (CIS)[104] method, the time-dependent variant of the density functional theory (TD-DFT)[68–70] and approaches to calculate excited states with CC methods. This chapter is concluded, as mentioned above, with the detailed introduction of the ADC scheme (chapter 2.5). Note that semi-empirical approaches[105] as well as multireference (MR)[106] methods, which are based on using of more than one Slater determinant, e.g. the complete active space self-consistent field (CASSCF)[107] approach, are not discussed in the scope of this thesis. For comprehensive reviews of all mentioned methods and concepts, please refer to the cited literature.

If not otherwise stated, p, q, r, and s correspond to general orbitals, while i, j, k, and l denote occupied orbitals. Unoccupied or virtual orbitals refer to a, b, c and d, while ϵ is generally used to denote orbital energies. All equations are written in atomic units, thus the elementary charge (e), the electron mass (m_e) and the speed of light (c) are set to one using the Planck constant ($\hbar$).

2.1 Basic Concepts of Quantum Chemistry

Let me start this chapter with an introduction to fundamental concepts of quantum and computational chemistry. I would like to mention the textbooks *"Modern Quantum Chemistry"*, written by *Szabo and Ostlund* as well as *"Molecular Electronic-Structure Theory" by Helgaker et al.*, where all topics and information, which are given in this chapter, are discussed in more detail.[101,108]

2.1.1 Schrödinger Equation

The time-dependent Schrödinger equation is the quantum mechanical equation of motion, thus it describes the evolution of the wave function $\Psi(x,t)$ with the time t as

$$i\hbar\frac{\partial}{\partial t}\Psi(x,t) = \hat{H}\Psi(x,t), \tag{2.1}$$

where x are the degrees of freedom in space and $\hat{H}$ is the Hamilton operator (Hamiltonian), which describes the energy of the system and is given in the non-relativistic case as

$$\hat{H}(x,t) = -\frac{\hbar^2}{2m}\frac{d^2}{dx^2} + V(x,t). \tag{2.2}$$

Here, m is the reduced mass and $V(x,t)$ is the potential energy of the respective particle. However, to describe most of the chemically relevant problems, the formalism can be simplified, because in closed systems like an isolated molecule, the total energy is preserved, thus the Hamiltonian is time-independent:

$$\hat{H} = -\frac{\hbar^2}{2m}\frac{d^2}{dx^2} + V(x). \tag{2.3}$$

In such cases, the wave function $\Psi(x,t)$ can be separated into time-dependent and space-dependent parts

$$\Psi(x,t) = \Psi(x)\Psi(t) \quad \text{with} \quad \Psi(t) = e^{-\frac{iEt}{\hbar}}, \tag{2.4}$$

where the energy E is assumed to be constant. After inserting equation 2.4 in equation 2.1, the Schrödinger equation can be formulated as

$$E\Psi(x)\Psi(t) = \hat{H}\Psi(x)\Psi(t) \tag{2.5}$$

and since $\Psi(t)$ is constant, the prominent time-independent Schrödinger equation (TISE) is given as

$$\hat{H}\Psi(x) = E\Psi(x). \tag{2.6}$$

Hence, the TISE does not describe the equation of motion of a quantum mechanical system, but the so-called stationary state of a molecular system. Depending on the degrees of freedom, the wave function is given as $\Psi(x_1, x_2, ..., x_n)$ and the TISE represents an ordinary differential equation. Since the Hamiltonian $\hat{H}$ comprises all interactions that describe the total energy E of the system, the TISE is also a multidimensional eigenvalue problem and if the wave function is an eigenfunction of the Hamiltonian, the total energy of the stationary state can be obtained.

2.1.2 Born-Oppenheimer Approximation

Formally, the TISE is exact for a closed system. However, analytic solutions for systems with more than one electron cannot be calculated, because the Hamiltonian contains many-body interactions. To explain this problem, let me consider a molecule with n electrons $a, b, ...$ and N atomic nuclei $A, B, ...$. These particles then have $x = \{x_a, x_b, ..., x_n\}$ and $X = \{X_A, X_B, ..., X_N\}$ positions in space, respectively, and the TISE transforms to

$$\hat{H}(x, X)\Psi(x, X) = E\Psi(x, X). \tag{2.7}$$

The full Hamilton operator in atomic units is given as

$$\begin{aligned}\hat{H} = & -\sum_{a=1}^{n}\frac{1}{2}\nabla_a^2 - \sum_{a=1}^{n}\sum_{A=1}^{N}\frac{Z_A}{|x_a - X_A|} + \sum_{a=1}^{n}\sum_{b>a}^{n}\frac{1}{|x_a - x_b|} \\ & + \sum_{A=1}^{N}\sum_{B>A}^{N}\frac{Z_A Z_B}{|X_A - X_B|} - \frac{1}{2}\sum_{I=1}^{N}\frac{\nabla_I^2}{M_I},\end{aligned} \tag{2.8}$$

where Z is the charge and M is the mass of the nuclei, while $\nabla = \frac{\partial}{\partial x, X}$ is the differential operator for the electrons and nuclei, respectively. The five contributions to the Hamiltonian can be summarized to

$$\hat{H} = \hat{T}_{el} + \hat{V}_{el-nuc} + \hat{V}_{el-el} + \hat{V}_{nuc-nuc} + \hat{T}_{nuc} \tag{2.9}$$

according to the order of the terms in equation 2.8. T describes the kinetic energy, while V denotes the potential energy of the electrons and nuclei, respectively. Now it is obvious, why the TISE cannot be solved analytically if more than one electron or nucleus is involved, because all of the three potential energy terms depend on many-body interactions. Hence, it is necessary to introduce approximations for the potential energy terms, otherwise it is impossible to calculate the total energy of a stationary state. The most important approach in this context is the Born-Oppenheimer approximation (BO). At first, according to equation 2.9, the Hamiltonian can be split into two parts $\hat{H} = \hat{H}_{el} + \hat{H}_{nuc}$, where $\hat{H}_{nuc}$ contains all parts, which only depend on the nuclei as

$$\hat{H}_{nuc} = \hat{T}_{nuc} + \hat{V}_{nuc} \tag{2.10}$$

and $\hat{H}_{el}$ contains all remaining contributions of the electrons as well as the interaction between the electrons and the nuclei $\hat{V}_{el-nuc}$. Since the kinetic energy of the nuclei $\hat{T}_{nuc}$ is given as

$$\hat{T}_{nuc} = -\frac{1}{2}\sum_{I=1}^{N}\frac{\nabla_I^2}{M_I}, \tag{2.11}$$

it depends on the factor M_I^{-1}, which is about 1850^{-1} in atomic units. This means that the nuclei move about 2000 times slower than the electrons. Therefore, it is an appropriate assumption to keep the position of the nuclei frozen and treat the movement of the electrons around the fixed nuclei. As a consequence, the total wave function of the system can also be divided into two parts

$$\Psi(x, X) = \Psi_{el}(x, \bar{X})\Psi_{nuc}(X) = \Psi_n(\bar{X}), \tag{2.12}$$

where $\bar{X}$ indicates that the electronic wave function Ψ_{el} only depends parametrically on the spatial positions of the fixed nuclei. Hence, the electrons are instantaneously adapted

to any change of the nuclear geometry. Since the positions of the nuclei are fixed, $\hat{H}_{nuc}$ is transformed to a constant energy contribution and the Hamiltonian can be written as

$$\begin{aligned}\hat{H}_E &= \hat{T}_{el} + \hat{V}_{el-nuc}(x, \bar{X}) + \hat{V}_{el-el}(x) + \hat{H}_{nuc}(X) \\ &= -\sum_{a=1}^{n} \frac{1}{2}\nabla_a^2 - \sum_{a=1}^{n}\sum_{A=1}^{N} \frac{Z_A}{|x_a - \bar{X}_A|} + \sum_{a=1}^{n}\sum_{b>a}^{n} \frac{1}{|x_a - x_b|} + \hat{H}_{nuc}(X),\end{aligned} \tag{2.13}$$

which defines the electronic Hamiltonian that contains the fixed positions of the nuclei as a parameter $\bar{X}$. Since $\hat{H}_E$ now depends on $\bar{X}$, the corresponding eigenvalues $E_n(\bar{X})$ and eigenfunctions depend on the fixed nuclei, too. Furthermore, the force on the atoms is given as

$$F = -\frac{dE}{d\bar{X}}, \tag{2.14}$$

thus the atoms move in a mean potential of the electrons, which establishes the picture of potential energy surfaces (PES). Eventually, the TISE can be formulated for the electronic Hamiltonian as

$$\hat{H}_E \Psi_n(\bar{X}) = E_n(\bar{X})\Psi_n(\bar{X}), \tag{2.15}$$

where n indicates the n^{th} excited state with $n = 0$ being the electronic ground state. The BO is now defined as follows: If the energy difference $\Delta E(\bar{X}) = E_1(\bar{X}) - E_0(\bar{X})$ between two potentials is large, then the interaction between two states $\Psi_0(\bar{X})$ and $\Psi_1(\bar{X})$ is small and as a consequence, the motion of the nuclei can be treated separately within the potentials $E_1(\bar{X})$ and $E_0(\bar{X})$, respectively.

These concepts are important for quantum chemical calculations. Due to the BO, only the $\hat{V}_{el-el}$ term remains as a real many-body problem and most of the research in the field of electronic structure theory concentrates on finding efficient approximations to describe this electron-electron interaction potential. A few of them are introduced in the following chapters, e.g the HF method, where it is assumed that the electrons move in the mean field induced by all others. Since all concepts and methods that are discussed in this thesis are based on the electronic time-independent Schrödinger equation in the Born-Oppenheimer picture, I neglect the explicit mention of this fact from now on and equation 2.15 is simply defined as

$$\hat{H}\Psi_n = E_n\Psi_n. \tag{2.16}$$

2.1.3 The Electronic Wave Function

With the knowledge about the electronic TISE in the BO picture, the electronic Hamiltonian is defined. However, the representation of the electronic wave function Ψ_n is not yet clarified. Therefore, I introduce the concept of Slater determinants as a consequence of the Pauli exclusion principle and the representation of the wave function in terms of basis sets in the following chapter.

Slater Determinants

So far, the electronic Hamiltonian only depends on the spatial coordinates of the electrons. However, in quantum mechanics, an electron has another important property, its spin state. The corresponding spin functions are denoted as $\alpha(s)$ and $\beta(s)$, which describe the up and down spin state, respectively. s is used to define the spin coordinate. These spin functions are orthonormal, thus $\langle\alpha(s)|\beta(s)\rangle = 0$ and $\langle\alpha(s)|\alpha(s)\rangle = 1$, which is also valid if α and β are interchanged. Hence, the electronic wave function Ψ_n depends on the spatial

coordinates x and the spin coordinates s, which are both merged to the general parameter r with $r = \{x, s\}$. Considering a wave function of a system with N electrons, the famous Pauli exclusion or antisymmetry principle states that

"a many-electron wave function must be antisymmetric with respect to the interchange of the coordinate r of any two electrons,

$$\Psi_n(r_1, r_2, ..., r_i, r_j, ..., r_N) = -\Psi_n(r_1, r_2, ..., r_j, r_i, ..., r_N)". ^{101} \tag{2.17}$$

This principle is based on the fact that the Hamilton operator does not contain any information about the electronic spin and it is not sufficient to just include the spin within the description of the wave function. A common description of the wave function, which fulfills the antisymmetry principle, is the so-called Slater Determinant. Therefore, the electronic wave function is written as a Hartree product

$$\Psi_n^{HP} = \psi_i(r_1)\psi_j(r_2)...\psi_k(r_N), \tag{2.18}$$

where

$$\psi(r) = \begin{cases} \chi(x)\alpha(s) \\ \chi(x)\beta(s) \end{cases} \tag{2.19}$$

are single-electron orbitals with separated spin (α and β) and spatial (χ) parts. The Slater determinant for an N-electron system is then given as

$$\Psi_n(r_1, r_2, ..., r_i, r_j, ..., r_N) = |\Psi_n^{HP}| = \frac{1}{\sqrt{N!}} \begin{vmatrix} \psi_i(r_1) & \psi_j(r_1) & ... & \psi_k(r_1) \\ \psi_i(r_2) & \psi_j(r_2) & ... & \psi_k(r_2) \\ \vdots & \vdots & \ddots & \vdots \\ \psi_i(r_N) & \psi_j(r_N) & ... & \psi_k(r_N) \end{vmatrix}, \tag{2.20}$$

where $\frac{1}{\sqrt{N!}}$ is a normalization factor. If the coordinates of two electrons are interchanged, the corresponding rows of the Slater determinant have to be interchanged as well, which leads to a change of the sign. For example, the Slater determinant of a simple two-electron system is given as

$$\Psi_n(r_1, r_2) = \frac{1}{\sqrt{2}}(\psi_1(r_1)\psi_2(r_2) - \psi_2(r_1)\psi_1(r_2)). \tag{2.21}$$

Hence, the Slater determinant is an appropriate construct to describe electronic wave functions.

Gaussian Basis Sets

As the next step, explicit descriptions of the single-electron functions $\psi(r)$ have to be constructed to establish an analytic expression of the electronic wave function. In the case of polyatomic systems, i.e. molecules, the single-electron orbitals are expanded in a set of atomic basis functions $\phi_\mu(r)$ with

$$\psi_n(r) = \sum_\mu C_{\mu n}\phi_\mu(r). \tag{2.22}$$

This ansatz is called linear-combination of atomic orbitals (LCAO) and via optimization of the coefficients $C_{\mu n}$ a set of n so-called molecular orbitals (MO) is obtained. The

optimization of the coefficients is explained in chapter 2.2.1. Here, I want to discuss the nature of the atomic orbitals $\phi(r)$, which constitute a basis set for every kind of atom.

Let me consider a simple one-electron system, i.e. the hydrogen atom. Since there are only two particles (one electron and one nucleus), this two-body problem can be solved analytically. The full Hamiltonian transforms to

$$\hat{H}_H = \frac{1}{2}\nabla_x^2 - \frac{1}{|x-X|} = \hat{T}_{el}(x) + \hat{V}_{el-nuc}(x,X), \tag{2.23}$$

which describes the motion of the electron in the field of the nucleus at the position X. After solving the eigenvalue problem of the TISE employing $\hat{H}_H$, the resulting eigenfunctions correspond to so-called Slater-type orbitals (STO):

$$\phi_{nlm}^{\mathrm{STO}}(d,\Lambda,\Theta) = R_n(d,\zeta)Y_{lm}(\Lambda,\Theta), \tag{2.24}$$

where $d = |x-X|$ is the distance between the nucleus and the electron, $R_n(d,\zeta)$ determines the radial part and $Y_{lm}(\Lambda,\Theta)$ the angular part, which is based on spherical harmonics. The indices n, l and m correspond to the principle quantum numbers. The radial part of a Slater orbital is formulated as

$$R_n(d,\zeta) = \frac{(2\zeta)^{\frac{3}{2}}}{\sqrt{(2n)!}}(2\zeta d)^{n-1}e^{-\zeta d}, \tag{2.25}$$

where ζ describes the compactness of the orbital. Eventually, the STOs establish a good basis for the hydrogen atom. However, there are numerical problems that complicate the employment of STOs for many-body systems, because solving typical types of integrals inherent in quantum chemical approaches is computationally expensive using STOs.

An alternative description of atomic basis functions is provided via Gaussian-type functions (GTO), which can be used to approximate the STOs. The GTOs can be integrated much more easily and computationally faster than Slater functions, thus they are usually employed in modern quantum chemical calculations. Generally, a GTO exhibits the same separation of radial and angular contributions (see equation 2.24), but the radial part differs compared to STOs:

$$R_{nl}(d,\alpha)^{\mathrm{GTO}} = \sqrt[4]{\frac{2(2\alpha)^3}{\pi}}\sqrt{\frac{2^{2n-l-2}}{(4n-2l-3)!!}}\left(\sqrt{2\alpha}d\right)^{2n-l-2}e^{-\alpha d^2}. \tag{2.26}$$

Besides the quantum number n it depends also on the complex spherical harmonics with the degree l and instead of ζ, the orbital exponent α is employed. By introducing GTOs with variable exponents and real spherical harmonics in a Cartesian space, the final GTOs can be written as

$$\phi_{lm\alpha}^{\mathrm{GTO}}(d,x,y,z) = N_{lm\alpha}^{\mathrm{GTO}}S_{lm}(x,y,z)e^{-\alpha d^2}, \tag{2.27}$$

which does not depend on n any longer. $N_{lm\alpha}^{\mathrm{GTO}}$ is the constant normalization factor and $S_{lm}(x,y,z)$ describes the real spherical harmonics in Cartesian coordinates. To resemble Slater functions, linear combinations of the GTOs are fitted according to

$$\phi^{\text{STO-kG}} = \sum_{i=1}^{k} C_i\phi^{\mathrm{GTO}}(\alpha_i), \tag{2.28}$$

where k is the number of GTOs that are used to approximate one STO. Eventually, the atomic Slater functions can be approximated by linear combinations of Gaussian-type

functions, which can be further employed to establish an atomic basis set to describe the single-electron wave functions (orbitals) via the LCAO ansatz (equation 2.22).

Nowadays, a plethora of systematically constructed basis sets are available. Since an individual Gaussian function poorly describes the electronic wave function near the nucleus, the GTOs are usually contracted. This leads to several levels of basis set contraction schemes. Furthermore, basis sets are generated at a specific ζ-level, that correspond to the exponent in STOs. Different ζ-levels can be established using multiple basis functions corresponding to each atomic orbital that improves the description of the basis. The higher the ζ-level, the more accurate the basis set. 6-311G[109,110], for example, is a triple-ζ basis set, which is characterized by the following contraction scheme:

- There are 6 Gaussian functions employed to describe each core atomic orbital basis function.
- The three numbers in 311G indicate that the valence orbitals are at the triple-ζ level and thus composed of three basis functions, respectively.
- Each of the numbers in 311 indicates the number of linear combinations of Gaussian functions used to describe the different zeta basis functions, respectively.

The 6-311G basis set belongs to the family of Pople's split-valence basis sets.[109,111–114] Besides the contraction and ζ-levels, the split-valence basis sets can be further improved via adding polarization (*) or diffuse functions (+). For polarization effects, usually, one has to extend the basis of an atom with functions of the next higher unoccupied orbital level. For example, p-functions are added to the hydrogen atom and d-orbitals are added to the first row atoms Li – F. This allows for the adaption to a uniform electric field, since the resulting hybrid orbitals provide a larger flexibility for the charge distribution. Diffuse functions are very flat basis functions, which describe orbitals that are higher in energy. Their linear combinations lead to MOs that are often spatially delocalized over and beyond the molecular system. These additional basis functions are important when considering larger molecules, as well as ions or higher-lying excited states like core excitations, which are the topic of my thesis. Therefore, I would like to mention the 6-311++G** basis set, which I have employed in most of the calculations that are presented in the application chapters. Besides the triple-ζ level, this basis set contains a set of polarization and diffuse functions for all atoms including hydrogen, which is indicated via the second * and +. In chapter 4, the benefits of employing the 6-311++G** basis set are explained.

Other typical basis sets that are often used in quantum chemical calculations are correlation-consistent polarized valence basis sets (cc-pVX)[115], where the diffuse functions are called augmented (aug)[116] and doubly augmented (d-aug)[116,117] with the cardinal number X ranging from double-ζ (DZ) to sextuple-ζ (6Z). Furthermore, the Ahlrichs series with basis sets of the type def2-TZVP are also commonly used.[118,119]

Note that the expansion in a basis set approximates the single-electron wave functions, because a complete basis must contain an infinite number of basis functions. In real calculations, the employed basis sets are finite according to equation 2.22. However, it is possible to estimate the complete basis set (CBS) limit via extrapolating the ground state energies using a few calculations with increasing basis set sizes. For ground state correlation energies, the correlated consistent basis set series converge systematically towards a CBS limit, which can be extrapolated using

$$E_X = E_{\mathrm{CBS}} + Ae^{-(X-1)} + Be^{-(X-1)^2}, \tag{2.29}$$

where E_{CBS} is the resulting estimated energy of the CBS limit, X is the cardinal number of the basis set (for example 2 for DZ) and E_X is the calculated energy using the basis

set with the cardinal number X.[120,121] This provides the possibility to avoid basis set truncation errors.

At last, I comment on the difference between Cartesian 6D/10F and pure 5D/7F basis functions. Generally, one can decompose Cartesian functions into pure spherical functions, which leads to a reduction in the number of basis functions, because the Cartesian functions form the space of a reducible representation of the rotation group. Using pure functions therefore leads to computational savings. However, the Cartesian version of diffuse functions can afford a better description of energetically higher-lying states, since they further extend the basis set and provide additional diffuse functions. This topic is discussed numerically in chapter 4.2.2.

2.1.4 Second Quantization

Before I discuss the concept of second quantization, the Dirac notation for vectors, matrices and two-electron integrals is introduced, which is used from now on. Table 2.1 summarizes the common short-hand notions.

Table 2.1: Summary of the Dirac notations for one- and two-electron integrals over one-particle wave functions, orbitals as well as for state vectors and operators.

State vectors and operators
$\|a\rangle = \sum_i a_i \|\alpha_i\rangle \quad \rightarrow \quad (\alpha_1, \alpha_2, ...)^T$
$\hat{A} = \sum_{ij} A_{ij} \|\alpha_i\rangle\langle\alpha_j\|$
$\langle a\|a\rangle = \sum_i a_i^\star a_i = \sum_i \|a_i\|^2$
One- and two-electron integrals
$\langle p\|\hat{o}\|q\rangle = \langle\psi_p\|\hat{o}\|\psi_q\rangle = \int dr_1 \psi_p^\star(r_1) o(x_1) \psi_q(r_1)$
$\langle pq\|rs\rangle = \langle\psi_p\psi_q\|\psi_r\psi_s\rangle = \int dr_1 dr_2 \frac{\psi_p^\star(r_1)\psi_q^\star(r_2)\psi_r(r_1)\psi_s(r_2)}{\|x_1 - x_2\|}$
$\langle pq\|\|rs\rangle = \langle pq\|rs\rangle - \langle pq\|sr\rangle$

Generally, observables in quantum chemistry are represented as operators, while wave functions are used to define a state. In second quantization, states are also described in terms of operators. Therefore, one has to introduce an abstract linear vector space, i.e. the Fock space. Considering the Slater determinant (equation 2.20), each determinant in the Fock space is given in a notion of many-particle states as vectors of occupation numbers n_i as

$$|\mathbf{n}\rangle = |n_1, n_2, ..., n_M\rangle \quad \text{with} \quad n_i = \begin{cases} 0 & \text{if } \psi_i \text{ is } \underline{\text{not}} \text{ occupied} \\ 1 & \text{if } \psi_i \text{ is occupied} \end{cases} . \tag{2.30}$$

Within the Fock space, the completeness relations

$$\langle \mathbf{n}|\mathbf{m}\rangle = \prod_{p=1}^{M} \delta_{n_i, m_i} = \delta_{\mathbf{nm}} \quad \text{and} \quad \sum_n |\mathbf{n}\rangle\langle\mathbf{n}| = 1 \tag{2.31}$$

of a scalar product of two states **n** and **m** are given. M is the size of the one-particle basis and in the case of the identity expression, the sum over n runs over all possible values of the vector **n**. A state that contains no electrons is defined as the true vacuum state $|\text{vac}\rangle = |0_1, 0_2, ..., 0_M\rangle$.

To change the occupation number of a many-particle state, the concept of particle creation $\hat{c}_p^\dagger$ and annihilation $\hat{c}_p$ operators is employed, with p and q being general orbitals. The creation operator is defined by the relation

$$\hat{c}_p^\dagger|n_1, ..., n_p, ...\rangle = (1 - n_p)(-1)^{\sum_{q<p} n_q}|n_1, ..., n_p + 1, ...\rangle. \tag{2.32}$$

In other words, the creation operator only creates a particle in ψ_p if ψ_p is not occupied. Otherwise, if the orbital is already occupied, applying $\hat{c}_p^\dagger$ would lead to zero. Strings of creation operator can be used, for example, to construct many-particle states starting from $|\text{vac}\rangle$ as

$$\hat{c}_1^\dagger \hat{c}_2^\dagger ... \hat{c}_{M-1}^\dagger|\text{vac}\rangle = |1_1, 1_2, ..., 1_{M-1}, 0_M\rangle. \tag{2.33}$$

The Hermitian adjoint counterpart to the creation operator is the so-called annihilation operator, which removes a particle in the respective orbital and thereby reduces the occupation number by one:

$$\hat{c}_p|n_1, ..., n_p, ...\rangle = n_p(-1)^{\sum_{q<p} n_q}|n_1, ..., n_p - 1, ...\rangle. \tag{2.34}$$

If ψ_p is not occupied, the annihilation operation yields zero. Both creation and annihilation operators can be combined to operator strings like the one-particle excitation operator $\hat{C}_i^a = \hat{c}_a^\dagger \hat{c}_i$. Such excitation operators can be used to describe electron excitation processes, where an electron is removed from an occupied orbital i and promoted to an unoccupied level a. Another special string is the number-conserving operator $\hat{N}_p = \hat{c}_p^\dagger \hat{c}_p$, which conserves the number of particles when applied to a state. An important characteristic of operator strings of creation and annihilation operators are the anti-commutation relations, which show the influence of the order of the operators on the resulting state:

$$\left\{\hat{c}_p^\dagger, \hat{c}_q^\dagger\right\} = 0 \quad \left\{\hat{c}_p^\dagger, \hat{c}_q\right\} = \delta_{pq} \quad \left\{\hat{c}_p, \hat{c}_q\right\} = 0 \quad \text{with} \left\{\hat{Y}, \hat{Z}\right\} = \hat{Y}\hat{Z} + \hat{Z}\hat{Y}. \tag{2.35}$$

A big advantage of the second quantization picture is the possibility to represent any arbitrary physical operator $\hat{O}$ in terms of creation and annihilation operators. Let me consider an arbitrary single-particle operator in an N-particle system, which is given as

$$\hat{O} = \sum_{i=1}^{N} \hat{o}(i) = \sum_{pq} \langle\psi_p|\hat{o}|\psi_q\rangle \sum_{i=1}^{N} |\psi_p(r_i\rangle\langle\psi_q(r_i)|. \tag{2.36}$$

In second quantization, the latter part of equation 2.36 is completely described via a simple operator string $\hat{C}_q^p$. Any one-particle operator can thus be expressed as

$$\hat{O} = \sum_{pq} O_{pq}\hat{C}_{pq} = \sum_{pq} \langle\psi_p|\hat{o}|\psi_q\rangle \hat{c}_p^\dagger \hat{c}_q. \tag{2.37}$$

In the same way, a two-particle operator $\hat{G}$ can be expressed as

$$\hat{G} = \sum_{pqrs} G_{pqrs}\hat{c}_p^\dagger \hat{c}_q^\dagger \hat{c}_s \hat{c}_r. \tag{2.38}$$

Finally, I conclude this chapter with the definition of the molecular electronic Hamilton operator in second quantization. According to equation 2.13, the electronic Hamiltonian

can be separated in different parts. Since the positions of the nuclei are fixed within the BO, the kinetic energy $\hat{T}_{el}$ and the electron-nuclear interaction $\hat{V}_{el-nuc}$ are single particle operators, while the remaining electron-electron interaction $\hat{V}_{el-el}$ is a two-particle operator. The electronic Hamiltonian in second quantization is then simply given as:

$$\hat{H} = \sum_{pq} h_{pq} \hat{c}_p^\dagger \hat{c}_q + \frac{1}{2} \sum_{pqrs} V_{pqrs} \hat{c}_p^\dagger \hat{c}_q^\dagger \hat{c}_s \hat{c}_r + \hat{H}_{nuc} \tag{2.39}$$

with

$$\begin{aligned} h_{pq} &= \langle \psi_p | -\frac{1}{2}\nabla^2 - \sum_A \frac{Z_A}{x_A} | \psi_q \rangle \\ V_{pqrs} &= \langle \psi_p \psi_q | \frac{1}{x_{12}} | \psi_r \psi_s \rangle, \end{aligned} \tag{2.40}$$

where x_A is the electron-nuclear separation, while x_{12} refers to the electron-electron distance. $\hat{H}$ in second quantization is independent of the number of electrons and thus can be used for any system, but it depends on the chosen one-particle basis.

2.2 Electronic Structure of the Ground State

In this chapter I give a brief introduction to quantum chemical approaches for the description of the electronic ground state. As shown in chapter 2.1, the electronic time-independent Schrödinger equation (equation 2.16) cannot be solved exactly, because the electronic Hamiltonian contains electron-electron interactions, which prevent analytic solutions. One of the main challenges in quantum chemistry is to find adequate approximations for this many-body problem, which preferably should be as accurate as possible and in addition computationally cheap. The most important standard model is the Hartree-Fock (HF) approximation, which is a practical method on its own and further provides a convenient starting point for other enhanced and more accurate methods, i.e. the so-called post-HF methods. One of these advanced approaches is the Møller-Plesset (MP) perturbation theory, which is based on Rayleigh-Schrödinger many-body perturbation theory and important in the context of the ADC approach (see chapter 2.5). Furthermore, I introduce the coupled-cluster (CC) and configuration interaction (CI) theories, which are also commonly applied post-HF approaches. Besides methods based on the HF model, a different ansatz to approximate the electron-electron interactions is provided via the density functional theory (DFT), which is briefly presented in this chapter, too. Again, I would like to mention the textbooks *"Modern Quantum Chemistry"* and *"Molecular Electronic-Structure Theory"*, in which more detailed information about the standard models in this chapter can be found.[101,108]

2.2.1 Hartree-Fock Approximation

The HF approximation is based on the variational principle for the electronic ground state. It states that the expectation value of the Hamiltonian is an upper bound to the exact ground state energy, if a normalized wave function $|\Psi\rangle$ is employed that satisfies boundary conditions to vanish at infinity. In other words, if $\langle\Psi|\Psi\rangle = 1$, the energy of an approximate wave function is always too high:

$$\langle\Psi|\hat{H}|\Psi\rangle \geq E_0. \tag{2.41}$$

Hence, the lower the ground state energy E_0, the higher the accuracy of the wave function. Computationally, one has to employ a parameterized trial wave function Ψ_T and vary these parameters as long as the expectation value of equation 2.41 converges against a minimum, where $\Psi_T \to \Psi_0^{\text{exact}}$. Considering the construction of wave functions in terms of basis sets (see chapter 2.1.3), this minimum represents the exact ground state energy within the employed basis set.

At first, an expression of the expectation value of the electronic Hamiltonian with Slater-Determinants has to be derived. As mentioned before (see equations 2.39 and 2.40), the electronic Hamiltonian can be divided into a single-particle and a two-particle part as well as the remaining constant nuclear contributions. The expectation values of both the single- and the two-particle part can be evaluated using the Slater-Condon rules[101] and, without going into detail, the final results are given as

$$\begin{aligned}\langle\Psi_n|\sum_{pq} h_{pq}\hat{c}_p^\dagger\hat{c}_q|\Psi_n\rangle &= \sum_{pq} h_{pq}\langle\Psi_n|\hat{c}_p^\dagger\hat{c}_q|\Psi_n\rangle = \sum_i h_{ii}\langle\Psi_n|\hat{c}_i^\dagger\hat{c}_i|\Psi_n\rangle \\ &= \sum_i \langle i|h_{ii}|i\rangle\end{aligned} \tag{2.42}$$

$$\begin{aligned}\langle\Psi_n|\frac{1}{2}\sum_{pqrs}V_{pqrs}\hat{c}_p^\dagger\hat{c}_q^\dagger\hat{c}_s\hat{c}_r|\Psi_n\rangle &= \frac{1}{2}\sum_{pqrs}V_{pqrs}\langle\Psi_n|\hat{c}_p^\dagger\hat{c}_q^\dagger\hat{c}_s\hat{c}_r|\Psi_n\rangle \\ &= \frac{1}{2}\sum_{pq}V_{pqpq}\langle\Psi_n|\hat{c}_p^\dagger\hat{c}_q^\dagger\hat{c}_q\hat{c}_p|\Psi_n\rangle = \frac{1}{2}\sum_{ij}\langle ij||ij\rangle,\end{aligned} \tag{2.43}$$

where i and j correspond to occupied spin orbitals. Hence, the one-electron energy of a Slater determinant corresponds to the sum of all occupied orbitals, while the two-electron energy can be interpreted as the Coulomb-exchange energy. The latter accounts for the electrostatic interactions between the electrons, considering the Pauli principle. Eventually, the energy of a Slater determinant is given as

$$E_0(\Psi_n) = \sum_i\langle i|h_{ii}|i\rangle + \frac{1}{2}\sum_{ij}\langle ij||ij\rangle + \hat{H}_{nuc}. \tag{2.44}$$

However, one has to find an appropriate Slater determinant for the electronic ground state, which can be optimized variationally. In the HF approach, the variational minimization is performed under the orthonormal constraint $\langle\psi_i|\psi_j\rangle = \delta_{ij}$, which results in the famous HF equation for single-electron orbitals

$$\hat{f}_i|\psi(r_i)\rangle = \epsilon_i|\psi(r_i)\rangle. \tag{2.45}$$

ϵ_i are the Lagrange multipliers, which represent the orbital energies, and $\hat{f}_i$ is the Fock-operator

$$\hat{f} = \sum_{pq}f_{pq}\hat{c}_p^\dagger\hat{c}_q + \hat{H}_{nuc} = \hat{h} + \hat{V}^{HF} + \hat{H}_{nuc}. \tag{2.46}$$

f_{pq} corresponds to the elements of the Fock-matrix and $\hat{h}$ resembles the one-particle operator in the electronic Hamiltonian. The two-particle operator $\hat{V}_{pqrs}$, which contains the electron-electron interactions, is replaced by an effective one-electron Fock potential

$$\hat{V}^{HF} = \sum_{pq}V_{pq}\hat{c}_p^\dagger\hat{c}_q = \sum_{pqi}(v_{pqii} - v_{piiq}), \tag{2.47}$$

where $v_{pqrs} = \langle pq|\frac{1}{x_{12}}|rs\rangle$. The index i runs over all occupied single-electron orbitals, while p and q correspond to the complete set of orbitals. The first contribution to the Fock potential, i.e v_{pqii}, can be thus interpreted as a classical Coulomb interaction, which describes the repulsion between one electron and all others. The second term v_{piiq} arises from the antisymmetry principle and corresponds to the exchange between the electrons. Classically, in first quantization, the Fock operator is given as:

$$\hat{f}_i = -\frac{1}{2}\nabla_i^2 - \sum_{A=1}\frac{Z_A}{x_A} + \sum_j(\hat{J}_j(i) - \hat{K}_j(i)), \tag{2.48}$$

where the Coulomb and exchange operators acting on a single-electron function are defined as:

$$\begin{aligned}\hat{J}_j(1)\psi_i(1) &= \left(\int dr_2\frac{\psi_j^\star(2)\psi_j(2)}{x_{12}}\right)\psi_i(1) \\ \hat{K}_j(1)\psi_i(1) &= \left(\int dr_2\frac{\psi_j^\star(2)\psi_i(2)}{x_{12}}\right)\psi_j(1).\end{aligned} \tag{2.49}$$

After introducing a basis via the LCAO ansatz (equation 2.22), the HF eigenvalue problem (equation 2.45) is transformed to

$$\hat{f}_i\sum_\mu C_{\mu i}\phi_\mu = \epsilon_i\sum_\mu C_{\mu i}\phi_{\mu i}. \tag{2.50}$$

When multiplying $\phi^{\star}_{\lambda i}$ from the right and integrating, equation 2.50 is transformed into a matrix representation

$$\sum_{\mu} \mathbf{F}_{\mu\lambda}\mathbf{C}_{\mu i} = \epsilon_i \sum_{\mu} \mathbf{S}_{\mu\lambda}\mathbf{C}_{\mu i}, \tag{2.51}$$

which is called the Roothaan equations with $\mathbf{F}_{\mu\lambda} = \langle\mu|f|\lambda\rangle$ representing the Fock matrix and $\mathbf{S}_{\mu\lambda} = \langle\mu|\lambda\rangle$ describing the overlap matrix between the atomic orbitals ϕ_μ and ϕ_λ. If the basis functions are orthonormal to each other, then $\mathbf{S}_{\mu\lambda} = 1$ and the remaining Roothaan equations are given in short form as

$$\mathbf{FC} = \epsilon_i \mathbf{C}, \tag{2.52}$$

which can be solved by diagonalization of the Fock matrix. Then, the resulting eigenvectors correspond to the canonical orbitals and the eigenvalues refer to the orbital energies, respectively:

$$\mathrm{diag}(F_{\mu\lambda}) = \delta_{\mu\lambda}\epsilon_\mu. \tag{2.53}$$

This set of orthonormal canonical orbitals can be used to form a Slater-determinant, which is called the HF ground state wave function Ψ_0^{HF} and, according to the variational principle, it is a very good approximation of a wave function. Since the Fock matrix is defined in terms of its own eigenvectors, the diagonalization has to be performed iteratively. For this purpose, the self-consistent field (SCF)[101] method is usually employed. The final HF ground state energy E_{HF} is then given with respect to the Hamiltonian as

$$E_{HF} = \langle\Psi_0^{HF}|\hat{H}|\Psi_0^{HF}\rangle = \sum_i \langle i|h_{ii}|i\rangle + \frac{1}{2}\sum_{ij}\langle ij||ij\rangle + \hat{H}_{nuc}, \tag{2.54}$$

where the antisymmetrized two-electron integral $\langle ij||ij\rangle = \langle ij|ij\rangle - \langle ij|ji\rangle$ describes the Coulomb-exchange interactions.

Eventually, the HF equations can be interpreted to describe the motion of every electron in the mean electric field off all others. The Coulomb integral corresponds to the mean repulsion and the exchange integral determines the mean exchange of one electron with all others, respectively. As a consequence, the direct interaction between the electrons as well as dynamic effects in terms of electron motions are neglected within the HF approximation. The difference between the exact ground state energy E_0 and E_{HF} is defined as the so-called correlation energy

$$E_c = E_0 - E_{HF}, \tag{2.55}$$

which is a usually small (<5%), but chemically important energy change, since e.g., barriers between an initial state and a transition state are of the same magnitude. Hence, the error in total energies due the lack of correlation can be important for the description of molecular systems. To improve the description of the ground state energy, post-HF methods were developed, which include approximations of the correlation energy.

2.2.2 Configuration Interaction

The configuration interaction (CI) approach is the first post-HF method, which I want to introduce. CI can be employed to calculate the electronic ground state as well as excited states and features an improved description of the total energy by correcting the correlation error of HF. The derivation is conceptionally simple, but the practical application is limited to small systems due to high computational cost.

Let me assume a system with N-electrons. So far within the HF theory, one Slater determinant (SD) is constructed with respect to N-single-particle basis functions, which

completely describes the N-electron Hamiltonian. This SD accounts for the electronic ground state and all corresponding energies and properties are based on this representation. The basic idea of the CI scheme is to describe the N-electron Hamiltonian using a basis of N-excited Slater determinants (N-eSD) with respect to N-single-particle basis functions, including the ground state SD as a zeroth excited SD. The CI wave function $|\Phi_0\rangle$ is then generated as a linear combination of these N-eSD using N-particle excitation operators $\hat{C}_N$, which are applied to the ground state reference wave-function $|\Psi_0\rangle$:

$$\begin{aligned} |\Phi_0\rangle &= \sum_{\omega=0}^{N} k_\omega \hat{C}_N |\Psi_0\rangle = \sum_{\omega=0}^{N} k_\omega |\Psi_\omega\rangle \\ &= |\Psi_0\rangle + k_I \sum_{ai} \hat{C}_i^a |\Psi_0\rangle + k_J \sum_{abij} \hat{C}_{ij}^{ab} |\Psi_0\rangle + k_K \sum_{abcijk} \hat{C}_{ijk}^{abc} |\Psi_0\rangle + ... \\ &= |\Psi_0\rangle + k_I |\Psi^S\rangle + k_J |\Psi^D\rangle + k_K |\Psi^T\rangle + ... \end{aligned} \tag{2.56}$$

with

$$\hat{C}_N = \left\{ \mathbb{1};\ \hat{c}_a^\dagger \hat{c}_i;\ \hat{c}_a^\dagger \hat{c}_b^\dagger \hat{c}_i \hat{c}_j, a<b, i<j;\ \hat{c}_a^\dagger \hat{c}_b^\dagger \hat{c}_c^\dagger \hat{c}_i \hat{c}_j \hat{c}_k, a<b<c, i<j<k;\ ... \right\}, \tag{2.57}$$

where a, b, c, ... correspond to virtual unoccupied orbitals and i, j, k, ... denote the occupied orbitals. The ground state reference wave function refers to the HF solution after solving Roothaan's equation (equation 2.51). The resulting N-tuply excited determinants are named after the type of excitation as singles (S), doubles (D), triples (T), and so on. The coefficients k_ω are optimized with respect to the variational principle and the expectation value of the CI energy as

$$0 = \frac{\partial}{\partial k_\omega} \frac{\langle \Phi_0 | \hat{H} | \Phi_0 \rangle}{\langle \Phi_0 | \Phi_0 \rangle}. \tag{2.58}$$

The CI wave function and its corresponding energy are then exact within a given atomic basis set. Using this N-eSD basis, a matrix representation of the Hamiltonian can be established with the CI matrix elements

$$H_{IJ} = \langle \Psi^I | \hat{H} | \Psi^J \rangle, \tag{2.59}$$

where I and J correspond to N-tuply excited configurations. The diagonalization of the complete CI matrix results in the exact eigenvalues (energies, E_0^{CI}) and corresponding eigenstates of the Hamiltonian within a given atomic basis set. If the full set of N-eSD is employed, the scheme is called Full-CI. However, it is obvious that the Full-CI matrix can be very large, since it grows exponentially with the number of electrons. Hence, this method usually can be applied for systems with a maximum of only 10 electrons, because for larger systems the computational cost becomes too large. A solution to this limitation is provided via truncation of the excitation space by using only a subset of determinants. For example, the CISD approximation only contains the singly and doubly excited determinants, which is already sufficient to improve the HF result. Note that only the Full-CI and CI singles (CIS) approaches are size consistent due to the linear variational parametrization (see equation 2.56). The latter has a special importance, since it only describes singly excited states and provides no improvement of the ground state due to Brillouin's theorem.[101] The CIS method is thus discussed in more detail in chapter 2.3.1.

2.2.3 Many-Body Perturbation Theory

Many-body perturbation theory (MBPT) is a powerful concept to systematically derive approximations for any kinds of quantum chemical problems that correspond to many-particle

operators. Here, I want to focus on approaches that provide perturbative descriptions of the electronic Hamilton operator. Therefore, I will introduce the Rayleigh-Schrödinger perturbation theory (RSPT), which provides a strict way to approximate the correlation energy of uncorrelated reference states. A special case of RSPT is the Møller-Plesset (MP) theory, in which the reference state corresponds to the HF ground state.[80]

Rayleigh-Schrödinger Perturbation Theory

The basis idea of RSPT is to partition the electronic Hamiltonian into two parts $\hat{H}_0$ and $\hat{U}$:

$$\hat{H} = \hat{H}_0 + \hat{U}. \tag{2.60}$$

The first part corresponds to a zero-order Hamiltonian, whose exact solutions are known, and the second part determines a small unspecified perturbation to the $\hat{H}_0$ system. The solution of the corresponding eigenvalue problem of $\hat{H}_0$, i.e.

$$\hat{H}_0|0^{(0)}\rangle = E_0^{(0)}|0^{(0)}\rangle, \tag{2.61}$$

results in a set of zero-order orthonormal eigenvectors $|0^{(0)}\rangle$ and the energy eigenvalues $E_0^{(0)}$, which can be used to expand the wave-function and energy in orders of the perturbation (i) as

$$\begin{aligned} |\Psi_0\rangle &= \sum_{i=0}^{\infty} |0^{(i)}\rangle \\ E_0 &= \sum_{i=0}^{\infty} E_0^{(i)}. \end{aligned} \tag{2.62}$$

These expansions establish the solutions of the exact Hamiltonian as

$$\begin{aligned} \hat{H}|\Psi_0\rangle &= E_0|\Psi_0\rangle \\ (\hat{H}_0 + \hat{U}) \sum_{i=0}^{\infty} |0^{(i)}\rangle &= \sum_{i=0}^{\infty} E_0^{(i)} \sum_{i=0}^{\infty} |0^{(i)}\rangle. \end{aligned} \tag{2.63}$$

Since it is practically impossible to expand the energy and wave function expressions to an infinity order, one has to introduce a certain truncation n. Equation 2.63 is then reformulated recursively to equation 2.64 to account for the underlying corrections with orders $i < n$ that are needed to correct the n^{th}-order expression. In other words, higher corrections to the wave function are generated from those of lower orders:

$$(\hat{H}_0 - E_0^{(0)})|0^{(n)}\rangle = -\hat{U}|0^{(n-1)}\rangle + \sum_{i=0}^{n} E_0^{(i)}|0^{(n-i)}\rangle. \tag{2.64}$$

Since it is assumed that the the zeroth-order wave functions are orthonormalized, the following relations for $i > 0$ simplify the subsequent discussion:

$$\begin{aligned} \langle 0^{(0)}|0^{(i)}\rangle &= 0 \\ \langle 0^{(0)}|\Psi_0\rangle &= \sum_{i=0}^{\infty} \langle 0^{(0)}|0^{(i)}\rangle = \langle 0^{(0)}|0^{(0)}\rangle = 1. \end{aligned} \tag{2.65}$$

The perturbative corrections for the energy are then given by multiplying equation 2.63 from the left using the zeroth-order wave function $0^{(0)}$:

$$E_0^{(n)}) = \begin{cases} \langle 0^{(0)}|\hat{H}_0|0^{(0)}\rangle, & n = 0 \\ \langle 0^{(0)}|\hat{U}|0^{(n-1)}\rangle, & n > 0 \end{cases} \tag{2.66}$$

To obtain the n$^{\text{th}}$-order expression of the wave function, equation 2.64 is multiplied from the left using $(\hat{H}_0 - E_0^{(0)})^{-1}$, resulting in

$$|0^{(n)}\rangle = -\frac{\hat{U}|0^{(n-1)}\rangle - \sum_{i=0}^{n} E_0^{(i)}|0^{(n-i)}\rangle}{\hat{H}_0 - E_0^{(0)}}. \tag{2.67}$$

With the introduction of the projection operator $\hat{P} = 1 - |0^{(0)}\rangle\langle 0^{(0)}|$, this equation can be transformed in a more convenient form

$$|0^{(n)}\rangle = -\frac{\hat{P}\left(\hat{U}|0^{(n-1)}\rangle - \sum_{i=0}^{n-1} E_0^{(i)}|0^{(n-i)}\rangle\right)}{\hat{P}(\hat{H}_0 - E_0^{(0)})}. \tag{2.68}$$

This provides an intuitive description of the n$^{\text{th}}$-order wave function, which is constructed in terms of all lower order corrections with $i < n$.

Møller-Plesset Perturbation Theory

So far, the RSPT was introduced for a general reference state and the small perturbation is unspecified yet. Since the HF equation can be solved exactly within a given basis set, it is straightforward to employ the HF solution as a zeroth-order reference and to describe the missing correlation energy perturbatively. This idea is implemented within Møller-Plesset (MP) perturbation theory, where the Fock-operator $\hat{f}$ (see equations 2.46 and 2.48) is employed as the unperturbed $\hat{H}_0$ operator and the perturbation operator $\hat{U}$ is defined as the difference between the full Hamiltonian and the Fock-operator:

$$\hat{H} = \hat{H}_0 + \hat{U} = \hat{f} + (\hat{H} - \hat{f}). \tag{2.69}$$

Considering that the Fock-operator is already diagonal, its canonical form is then given as

$$\hat{f} = \sum_p \epsilon_p \hat{c}_p^\dagger \hat{c}_p, \tag{2.70}$$

describing the sum over all orbital energies. Accordingly, the perturbation can be written as

$$\hat{U} = \hat{H} - \hat{f} = \hat{V}_{pqrs} - \hat{V}^{HF} = \frac{1}{2}\sum_{pqrs}\langle pq|rs\rangle c_p^\dagger c_q^\dagger c_s c_r - \sum_{pq}\sum_i \langle pi||qi\rangle c_p^\dagger c_q, \tag{2.71}$$

where the non-diagonal Fock-operator is assumed (see equations 2.46 ff). Using Ψ_0^{HF} as the zeroth-order wave function $|0^{(0)}\rangle$ and according to equation 2.66, the zeroth-order MP (MP0) and first order MP (MP1) energy corrections can be simply written down as

$$E_0^{(0)} = \langle 0^{(0)}|\hat{H}_0|0^{(0)}\rangle = \langle 0^{(0)}|\hat{f}|0^{(0)}\rangle = \sum_i^n \epsilon_i \tag{2.72}$$

and

$$\begin{aligned} E_0^{(1)} &= \langle 0^{(0)}|\hat{U}|0^{(0)}\rangle = \langle 0^{(0)}|\hat{H} - \hat{f}|0^{(0)}\rangle = \langle 0^{(0)}|\hat{H}|0^{(0)}\rangle - \langle 0^{(0)}|\hat{f}|0^{(0)}\rangle \\ &= -\frac{1}{2}\sum_{ij}\langle ij||ij\rangle. \end{aligned} \tag{2.73}$$

Hence, the MP0 energy is just the sum of the occupied HF orbital energies, while the MP1 energy correction accounts for the difference of the expectation value of the Hamiltonian and the Fock-operator. Eventually, the total sum of the MP0 and MP1 energy corrections resembles the HF energy and provides no correction to the missing correlation energy:

$$E_0^{\mathrm{MP1}} = E_0^{(0)} + E_0^{(1)} + \hat{H}_{nuc} = E_0^{HF}. \tag{2.74}$$

Obviously, real descriptions of the correlation energy are provided firstly at second order. To evaluate the second order MP (MP2) energy $E_0^{(2)} = \langle 0^{(0)}|\hat{U}|0^{(1)}\rangle$, an explicit expression of the first-order wave function is required. According to equation 2.68, the first order wave function is given as

$$\begin{aligned} |0^{(1)}\rangle = & -\frac{\hat{P}\left(\hat{U}|0^{(0)}\rangle - \sum_{i=0}^{0} E_0^{(0)}|0^{(0)}\rangle\right)}{\hat{P}(\hat{H}_0 - E_0^{(0)})} \\ = & -\frac{\hat{P}\hat{U}|0^{(0)}\rangle}{\hat{P}(\hat{f} - E_0^{(0)})} \end{aligned} \tag{2.75}$$

To reformulate this expression into a practical form, certain definitions have to be clarified. At first, an unspecified N-tuply excited determinant based on the HF ground state reference is defined as

$$|\Psi^N\rangle = \hat{C}_N|0^{(0)}\rangle, \tag{2.76}$$

using the CI excitation operator in equation 2.57. For example, the doubly excited configuration is

$$|\Psi^D\rangle = \hat{C}_{ij}^{ab}|0^{(0)}\rangle = \hat{c}_a^\dagger \hat{c}_b^\dagger \hat{c}_i \hat{c}_j |0^{(0)}\rangle, \quad a < b, i < j \tag{2.77}$$

and all excited determinants and the corresponding HF ground state constitute an orthonormal set of states $\langle \Psi^N|\Psi^M\rangle = \delta_{NM}$. Furthermore, the zeroth-order excited determinants are eigenfunctions of $\hat{f}$:

$$\hat{f}|\Psi^N\rangle = E_N^{(0)}|\Psi^N\rangle = (E_0^{(0)} + \epsilon_N)|\Psi^N\rangle, \tag{2.78}$$

where ϵ_N denotes the orbital energy differences of occupied and virtual orbitals of the respective excited determinant. Exemplary, in the case of doubly excited configurations, $\epsilon_D = \epsilon_a + \epsilon_b - \epsilon_i - \epsilon_j$. The expectation value of the perturbation operator with respect to an excited determinant and the ground state is given as

$$\langle \Psi^N|\hat{U}|0^{(0)}\rangle = \langle \Psi^N|\hat{H}|0^{(0)}\rangle. \tag{2.79}$$

At last, note that Brillouin's theorem[101] is valid, thus the singly-excited determinant does not couple to the HF ground state:

$$\langle \Psi^S|\hat{H}|0^{(0)}\rangle = \langle 0^{(0)}|\hat{H}|\Psi^S\rangle = 0 \tag{2.80}$$

Furthermore, due to the Slater-Condon rules, only doubly excited configurations can interact with the HF ground state, because the Hamiltonian is a two-electron operator and thus couplings between determinants that differ by more than two levels of excitation are zero.

Using the definition of $\hat{P}$, equation 2.75 is multiplied with the resolution of the identity $|\Psi^N\rangle\langle\Psi^N|$ and is thus transformed to

$$|0^{(1)}\rangle = -\sum_{N>0} \frac{|\Psi^N\rangle\langle\Psi^N|\hat{U}|0^{(0)}\rangle}{E_N^{(0)} - E_0^{(0)}}. \tag{2.81}$$

Considering Brillouins theorem and the Slater-Condon rules, Ψ^N can only correspond to doubly excited configurations. Using the definitions above, the first order wave function can be written as

$$|0^{(1)}\rangle = -\sum_D \frac{|\Psi^D\rangle\langle\Psi^D|\hat{H}|0^{(0)}\rangle}{\epsilon_D}. \tag{2.82}$$

The final MP1 wave function is obtained by inserting the explicit Hamilton operator resulting in

$$|0^{(1)}\rangle = -\sum_{\substack{i<j \\ a<b}} \frac{\langle ab||ij\rangle}{\epsilon_a + \epsilon_b - \epsilon_i - \epsilon_j}|\Psi^D\rangle = -\sum_{\substack{i<j \\ a<b}} t_{abij}|\Psi^D\rangle, \tag{2.83}$$

which defines the MP2 t-amplitudes t_{abij}. The second order MP2 energy correction is then given as

$$\begin{aligned} E_0^{(2)} = \langle 0^{(0)}|\hat{U}|0^{(1)}\rangle &= -\sum_{\substack{i<j \\ a<b}} \frac{|\langle ab||ij\rangle|^2}{\epsilon_a + \epsilon_b - \epsilon_i - \epsilon_j} = -\frac{1}{4}\sum_{abij} \frac{|\langle ab||ij\rangle|^2}{\epsilon_a + \epsilon_b - \epsilon_i - \epsilon_j} \\ &= -\frac{1}{4}\sum_{abij} t_{abij}\langle ab||ij\rangle \end{aligned} \tag{2.84}$$

and finally, the total MP2 energy can be written as

$$E_0^{\mathrm{MP2}} = E_0^{HF} + E_0^{(2)} + \hat{H}_{nuc}. \tag{2.85}$$

The third order energy correction can be derived via the same procedure, the final result is given as:

$$\begin{aligned} E_0^{(3)} = \langle 0^{(0)}|\hat{U}|0^{(2)}\rangle = &\frac{1}{8}\sum_{abijkl}\langle ij||kl\rangle t_{abij}t_{abkl} + \frac{1}{8}\sum_{abcdij} t_{cdij}t_{abij}\langle ab||cd\rangle \\ &- \sum_{abcijk} t_{abij}t_{acik}\langle kb||jc\rangle. \end{aligned} \tag{2.86}$$

The MP theory, in particular MP2, has been established in quantum chemical applications as a powerful method to describe the electronic ground state and its properties very accurately. Note that all MP schemes are not variational, because MP just provides a correction to the HF energy in a certain order of perturbation theory. Hence, the total energy in a certain MP order is not an upper bound of the exact ground state energy. However, the MP schemes are size-consistent at any order and due to efficient implementations in modern quantum chemical programs, they are frequently employed. Besides the derivation shown in this chapter, the general MBPT theory can also be derived diagrammatically using Feynman and Goldstone diagrams.[101] Via this picturesque ansatz, it is easier to derive explicit expressions for higher order approximations as well as for more complicated problems than the electronic Hamilton operator. Concerning the ADC method, the MBPT and MP theories are important, since they provide the basis to construct explicit and truncated expressions of the polarization propagator, which is shown in chapter 2.5.

2.2.4 Coupled-Cluster Approach

Next, the discussion of post-HF ground state methods is concluded with an introduction of the coupled-cluster (CC) approach. As mentioned in chapter 2.2.2, the truncation of the CI space leads to a loss of size-consistency compared to the Full-CI approach. Within

the CC theory, this issue is corrected by constructing the wave function as a product of excitation processes, so called coupled-clusters as

$$\begin{aligned} |\Phi_0^{CC}\rangle &= \prod_{ai}(1 + t_\omega \hat{c}_a^\dagger \hat{c}_i) \prod_{abij}(1 + \hat{c}_a^\dagger \hat{c}_b^\dagger \hat{c}_i \hat{c}_j \{a < b, i < j\})...|\Psi_0\rangle \\ &= \prod_{\omega}(1 + t_\omega \hat{C}_\omega)|\Psi_0\rangle, \end{aligned} \tag{2.87}$$

where t_ω defines the CC amplitudes. Similar to the CI coefficient k_ω, t_ω accounts for the probability of the excitation process, respectively. The combined sum of the cluster amplitudes and N-particle excitation operators $\hat{C}_\omega$ is called cluster operator

$$\hat{T} = \sum_{\omega}^{M} t_\omega \hat{C}_\omega = \hat{T}_S + \hat{T}_D + ... + \hat{T}_M \tag{2.88}$$

and can be ordered depending on the excitation classes. M corresponds to the number of maximum possible excitations with respect to the amount of electrons N. In Full-CC, N is equal to M, while M defines the truncation if $M < N$. For example, within the CCSD approximation, only $\hat{T}_S$ and $\hat{T}_D$ are employed. Hence, the CI and CC wave functions are in principle equal, but differ in their parametrization. Applied to the ground state reference wave function, i.e. usually the HF ground state, each operator according to equation 2.87 creates a superposition of the original ground state reference and a correction term, which corresponds to excitations from the reference state:

$$(1 + \hat{T}_\omega)|\Psi_0\rangle = |\Psi_0\rangle + t_\omega \Psi_\omega. \tag{2.89}$$

The CC product ansatz (equation 2.87) is not well-suited for algebraic manipulations. Since $(\hat{C}_\omega)^2 = 0$ and due to the anti-commutator rules (see equation 2.35), it is therefore convenient to expand the cluster operators T_ω in an exponential form

$$1 + \hat{T}_\omega = 1 + \hat{T}_\omega + \frac{1}{2!}\hat{T}_\omega^2 + \frac{1}{3!}\hat{T}_\omega^3 + ... = e^{\hat{T}_\omega}, \tag{2.90}$$

which transforms the CC wave function to

$$|\Phi_0^{CC}\rangle = \prod_{\omega}(1 + t_\omega \hat{C}_\omega)|\Psi_0\rangle = e^{\hat{T}}|\Psi_0\rangle. \tag{2.91}$$

In contrast to CI and HF, the CC wave function is not optimized variationally, because this would result in an intractable set of nonlinear equations. To solve the CC Schrödinger equation

$$\hat{H}e^{\hat{T}}|\Psi_0\rangle = E_{CC}e^{\hat{T}}|\Psi_0\rangle, \tag{2.92}$$

a set of configurations $\langle\mu| = \langle\Psi_0|\hat{C}_\omega^\dagger$ of the reference ground state and those determinants that enter the CC state with connected amplitudes is defined, which are projected against equation 2.92. As a result, the CC eigenvalue problem is transformed into the projected CC equations

$$\langle\mu|\hat{H}e^{\hat{T}}|\Psi_0\rangle = E_0^{CC}\langle\mu|e^{\hat{T}}|\Psi_0\rangle \tag{2.93}$$

and the final CC energy is then given as

$$E_0^{CC} = \langle\Psi_0|e^{-\hat{T}}\hat{H}e^{\hat{T}}|\Psi_0\rangle. \tag{2.94}$$

Due to its size-consistency, CC approaches are commonly employed in quantum chemical calculations. However, the computational demand is still large, which restricts

the application of strict truncated CCX (with $X > S$) methods to small and medium-sized molecules. A disadvantage of the CC approach is that the CC eigenvalue problem is non-Hermitian and as a consequence, the left-hand and right-hand eigenvectors differ from each other and to obtain properties other than the energy, one has to solve the CC eigenvalue twice. Besides the full-CC and the corresponding truncated approaches, there are extended approximate schemes like the approximate coupled cluster scheme of second order (CC2)[66] or the the symmetry adapted cluster (SAC)[60–65] methods. Both approaches are known to provide accurate results and thereby require less computational effort than the corresponding truncated CC techniques. Another prominent representative from the CC family is the "gold standard" CCSD(T) method, where the triply excited configurations are treated perturbatively.[58,122]

2.2.5 Density Functional Theory

I conclude this chapter with a brief discussion of an alternative ansatz of solving the electronic TISE, i.e. the density functional theory (DFT).[102,123,124] Since the electron correlation is considered in an empirical way within the Kohn-Sham DFT approach, the method is able to provide a good description of the electronic ground state. It is based on the fact that the electron density ρ completely and exactly determines all ground state properties of an N-electron system. Based on the electronic Hamiltonian (2.13), the Hohenberg-Kohn theorems provide proofs of the existence of an energy functional $E[\rho]$ for the electronic ground state that consists of the total kinetic energy $T[\rho]$ and the total Coulomb interaction $V[\rho]$ of the electrons:

$$E[\rho] = T[\rho] + V[\rho]. \tag{2.95}$$

This energy functional neglects the total external nuclear potential v_{ex}, which contains all nuclear interactions of the electronic Hamiltonian in the BO picture. Using the variational principle, it could be further proven that

$$E[\rho_T] + \int v_{ex}\rho_T \geq E[\rho] + \int v_{ex}\rho = E_0, \tag{2.96}$$

where $\rho_T \neq \rho$ is an external test potential according to the variational principle. Although the existence of $T[\rho]$ and $V[\rho]$ was proven, their explicit expressions cannot be defined. However, *Kohn and Sham* found possible approximations for the kinetic energy and Coulomb potential functionals. Expressed as a single Slater determinant with a basis of non-interacting electrons in N orthonormal orbitals, the density can be written as

$$\rho = \sum_N |\psi_N|^2, \tag{2.97}$$

the total kinetic energy can be approximated to

$$T[\rho] \approx T_0 = -\frac{1}{2}\sum_N \int \psi_N \nabla^2 \psi_N, \tag{2.98}$$

and the Coulomb potential can be described as a simple Coulomb self-energy potential with

$$V[\rho] \approx J[\rho] = \frac{1}{2}\int\int \frac{\rho(1)\rho(2)}{x_{12}} d1d2. \tag{2.99}$$

Similar to the correlation energy problem in the HF picture, the errors due to the approximations above are defined as the difference of the exact and approximated energy functionals with

$$E_{xc}[\rho] = T[\rho] + V[\rho] - T_0[\rho] - J[\rho]. \tag{2.100}$$

The introduced error $E_{xc}[\rho]$ is called exchange-correlation functional and the total Kohn-Sham energy functional is finally given as

$$E^{KS}[\rho] = T_0[\rho] + \int v_{ex}\rho + J[\rho] + E_{xc}[\rho]. \tag{2.101}$$

Next, $E^{KS}[\rho]$ has to be minimized using the variational principle with respect to single-particle orbitals, which yields the Kohn-Sham equation

$$\left(-\frac{1}{2}\nabla^2 + v_{KS}\right)\psi_i = \epsilon_i\psi_i, \tag{2.102}$$

where ψ_i are called Kohn-Sham orbitals and ϵ_i are their corresponding energies. The term v_{KS} contains all many-particle interaction potentials, inclusive of the unknown exchange-correlation (xc) potential v_{xc}:

$$v_{KS}(x_a) = v_{el} + v_{ex} + v_{xc} = -\sum_A \frac{Z_A}{x_A} + \int dx_b \frac{\rho(x_b)}{x_{ab}} + v_{xc}(x_a[\rho]). \tag{2.103}$$

Note that formally, the Kohn-Sham equation is exact within the BO approximation. However, an exact expression for v_{xc} has not been found yet, thus the exact electron density cannot be calculated. Nowadays, a plethora of approximations for v_{xc} are available, which are generally obtained via empirical fittings. Within the Coulomb potential (equation 2.99), the spurious interaction of an electron with itself is not corrected as it is in HF theory, where the exchange is exactly and explicitly canceled via K_j (see equation 2.49). Some xc functionals are able to correct this self-interaction error (SIE), but not exactly as in HF. Practically, the prominent group of hybrid xc functionals, e.g. B3LYP, developed by *Becke*, enjoy widespread applications in quantum chemistry.[125–127] They are constructed using a mixture of HF and density based exchange contributions leading to adequate results, because the SIE is partially compensated. Pure xc functionals, like LDA[128] or BLYP[129], are also commonly employed, depending on the kind of application. Note that xc functionals are not variational with respect to the Hamiltonian due to their empirical construction, thus the DFT ground state energy can be lower than the exact one. Eventually, the practical use of DFT is based on the quality of the employed xc functionals and strongly depends on the kind of the investigated systems and problems of interest.

2.3 Calculation of Electronically Excited States

In the following chapter, I give an overview of single reference methods for the description of electronically excited states. For further reading, I would like to mention the reviews published by *Dreuw et al.*[43,130] Nowadays, a plethora of methods for calculating electronic excitations are available. Since most of these methods provide access to excitation energies, oscillator strengths and other advanced properties like static excited states dipole moments, they are employed to simulate photo-initiated processes, e.g. absorption spectra. According to their ground state references, one can classify the excited state methods into wave function based post-HF and electron-density based approaches. The computational time is growing exponentially with the size of the investigated system. The correlation between computational accuracy of common available excited state methods depending on the system size that can be computationally handled is illustrated in Figure 2.1.

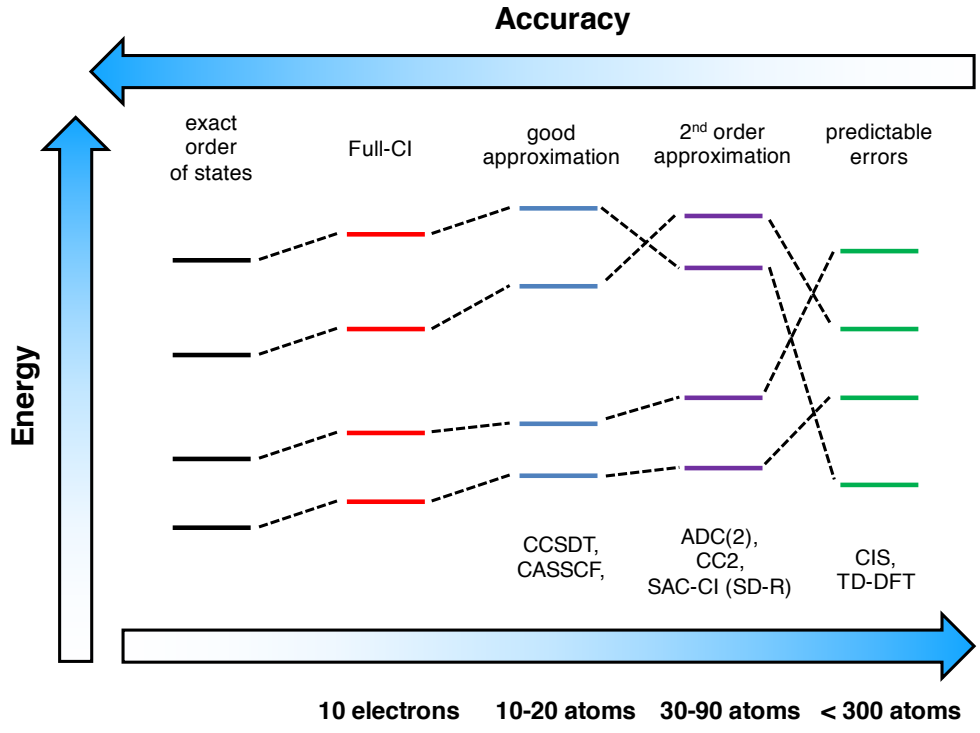

Figure 2.1: Schematic sketch of the computational accuracy at different levels of theory depending on the size of molecular systems that can be computationally handled. The horizontal solid lines represent excited state energies, while the dotted lines indicate energy shifts due to different levels of theories.

Compared to the exact order of states, the result at the Full-CI level is correct, but the energy might be shifted constantly due to basis set truncations. However, one can only calculate systems with about 10 electrons in an acceptable computational time as mentioned in chapter 2.2.2. Other wave-function based methods like multireference (MR) or multiconfigurational (MC) approaches demonstrate a good approximation compared to Full-CI, but the relative energy difference between the states might be shifted and

the calculations are computationally limited to 10 – 20 atoms. Within the CC family, there are approaches based on the equation-of-motion (EOM)[55,58,131] formalism or linear response[132,133] theory. Both approaches for excited states within the CC family depend on the level of truncation, similar to the ground state schemes. At the EOM-CCSDT level, a very high accuracy can be achieved for systems that can be well-described by a single reference ground state. A significantly reduced computational time compared to higher order EOM-CC methods can be reached with second order approximations like ADC(2) and CC2, because these approaches include correlation effects, but due to the second order truncations, the order of states might be incorrect compared to the Full-CI approach. However, ADC(2) as well as CC2 can only be employed for medium-sized systems up to 90 atoms, because the computational effort is still demanding. SAC-CI at the SD-R level[60–65] is also a second order approach, where only single and double excitations are considered. Note that, in general, the calculated energies of wave-function based post-HF approaches strongly depend on the basis set due to the underlying variational principle. The energies converge to a basis set limit, thus large basis sets are required to calculate adequate energies. Since the size of the basis set scales with the computational cost, accurate wave-function based calculations are usually computationally expensive.

For large molecules up to 300 atoms, the computationally cheapest possibilities are the time dependent Hartree-Fock (TDHF)[134] and CIS approaches. Both methods usually overestimate the excitation energies, because they do not include correlation effects directly. Alternatively, one can employ the time dependent density functional theory (TD-DFT), which is computationally at the same level as the CIS approach. Similar to the ground state equivalent, the results depend much on the choice of the exchange-correlation (xc) functionals that are based on empirical fitting. Limitations of pure TD-DFT approaches are the description of charge transfer states, Rydberg states, extended π-systems and doubly excited states.[135–137] However, the results at the TD-DFT level can be very accurate, if the limitations are considered and the employed xc functional is validated against wave-function based benchmark calculations and experimental data.

In the following sections, I introduce the CIS, TD-DFT and CC approaches for excited states methods briefly. The ADC method is introduced in detail in the subsequent chapter 2.5.

2.3.1 Configuration Interaction Singles

In chapter 2.2.2 I introduced the CI approach. The first and simplest truncation of Full-CI is the CIS approximation, where only singly excited configurations are considered. Due to Brillouin's theorem (see equation 2.80), the CIS scheme does not improve the HF ground state, because the couplings between the singly-excited determinant and the HF ground state are zero. As a consequence, the CIS approach is size-consistent and only yields excited-state energies and their corresponding properties. Due to equation 2.59, the full CIS matrix can be formulated as

$$\mathbf{M}^{\mathrm{CIS}} = \langle \Psi^S | \hat{H} | \Psi^S \rangle \tag{2.104}$$

with the matrix elements

$$M^{\mathrm{CIS}}_{ia,jb} = \langle \Psi^a_i | \hat{H} | \Psi^b_j \rangle. \tag{2.105}$$

The Hamiltonian can be shifted by the HF ground state energy, which results in

$$M^{\mathrm{CIS}}_{ia,jb} = \langle \Psi^a_i | \hat{H} - E_0^{HF} | \Psi^b_j \rangle = (\epsilon_a - \epsilon_i)\delta_{ab}\delta_{ij} - \langle aj||bi\rangle \tag{2.106}$$

and the corresponding eigenvalue problem

$$\mathbf{M}^{\mathrm{CIS}}\mathbf{X} = \omega \mathbf{X}, \tag{2.107}$$

with $\mathbf{X}$ being the matrix of the CIS expansion coefficients, has to be solved via diagonalization of the CIS matrix $\mathbf{M}^{\mathrm{CIS}}$ to obtain the excitation energies ω:

$$(\mathbf{M}^{\mathrm{CIS}} - \omega)\mathbf{X} = 0. \tag{2.108}$$

Since the excited states of interest are in the majority of cases the energetically lowest in the spectrum, the diagonalization of the full CIS matrix, which can be computationally expensive depending on the size of the system, is avoided via employing diagonalization schemes like the Davidson algorithm[138], typically yielding the X lowest eigenvalues and eigenvectors.

The CIS scheme is indeed a practical method, but one cannot expect a quantitative accuracy compared to experimental data. Excitation energies of valence excited states are usually overestimated by about 0.5 - 2 eV, because the dominating orbital energy difference term provides an unbalanced description for N-electron systems due to the one electron attachment and ionization picture.[43] Since there are no couplings to the ground state, correlation effects are also not included in the CIS scheme. Therefore, higher order extensions or configurations are needed to correct the excitation energies provided at the CIS level.

2.3.2 Time-Dependent Density Functional Theory

Nowadays, TD-DFT is the most important quantum chemical excited state approach for large systems up to 300 atoms. Besides excitation energies, linear response (LR) Kohn-Sham TD-DFT provides also access to properties like oscillator strengths, excited state geometries and dipole moments. There are many review articles in the literature that discuss the theoretical foundations of TD-DFT as well as the accuracy, advantages and limitations of certain xc functionals. Here, I would like to mention the reviews of *Dreuw/Head-Gordon*[43] and *Casida/Huix-Rotllant*[139] as well as the overview published by *Laurent and Jacquemin*[140]. In the scope of this thesis I give a brief summary of the TD-DFT scheme and its limitations.

The formal foundation of TD-DFT are the Runge-Gross theorems, which can be seen as the time-dependent analogues to the Hohenberg-Kohn theorem.[68–70] They state and prove that a one-to-one mapping between the time-dependent density and an external potential up to a time-dependent constant exist. Furthermore, a so-called action potential was defined for the time-depended density, where the exact density is described as a stationary point. Due to these basic proofs provided by the Runge-Gross theorem, a Kohn-Sham ansatz of non-interacting particles was introduced with the time-dependent electron density

$$\rho(x,t) = \sum_{i}^{N} |\psi_i(x,t)|^2, \tag{2.109}$$

where x indicates the spatial coordinates and t refers to the time. Similar to the time-independent equivalent (see equation 2.102), the time-dependent one-particle Schrödinger equation with respect to the basis of single-electron orbitals ψ_i is given as

$$i\frac{\partial}{\partial t}\psi_i(x,t) = \left(-\frac{1}{2}\nabla_i^2 + v_{KS}(x,t)\right)\psi_i(x,t), \tag{2.110}$$

with the interaction potential

$$v_{KS}(x,t) = v_{el}(x,t) + v_{ex}(x,t) + v_{xc}(x,t), \tag{2.111}$$

where the unknown xc functional is defined as

$$v_{xc}(x,t) = \frac{\delta A_{xc}[\rho](x,t)}{\delta\rho(x,t)}. \tag{2.112}$$

$A_{xc}[\rho](x,t)$ describes the xc part of the action integral. Formally, the time-dependent Kohn-Sham equation is exact and if the correct xc action integral was known, the resulting density of the non-interacting system would be identical to the density of the interacting system. However, the xc action functional is unknown and has to be fitted empirically, similar to its time-independent equivalent v_{xc}.

To obtain excitation energies and oscillator strengths for the simulation of absorption spectra, which is the major application of TD-DFT, the linear response (LR) approach is employed as an ad hoc extension of DFT.[139,141] The LR TD-DFT scheme is based on the linear time-dependent response of the time-independent ground state electron density to a time-dependent external electric field, treating the poles of the dynamic polarizability analytically. The final working equations are similar to the random phase approximation (RPA).[68] I omit the detailed derivation of the LR TD-DFT scheme, but I present the final non-Hermitian eigenvalue TD-DFT equation, which is given as

$$\begin{pmatrix} \mathbf{A} & \mathbf{B} \\ \mathbf{B}^\star & \mathbf{A}^\star \end{pmatrix} \begin{pmatrix} \mathbf{X} \\ \mathbf{Y} \end{pmatrix} = \omega \begin{pmatrix} 1 & 0 \\ 0 & -1 \end{pmatrix} \begin{pmatrix} \mathbf{X} \\ \mathbf{Y} \end{pmatrix}. \tag{2.113}$$

$\mathbf{X}$ and $\mathbf{Y}$ represent the TD-DFT amplitudes that contain the spectral information, while ω is the excitation energy. The matrix elements of $\mathbf{A}$ and $\mathbf{B}$ are defined as

$$\begin{aligned} A_{ia,jb} &= \delta_{ij}\delta_{ab}(\epsilon_a - \epsilon_i) + \int\int d1d2\ \psi_i^\star(1)\psi_a(1)\frac{1}{x_{12}}\psi_b^\star(2)\psi_j(2) \\ &\quad + \int\int d1d2\ \psi_i^\star(1)\psi_a(1)f_{xc}\psi_b^\star(2)\psi_j(2) \\ B_{ia,jb} &= \int\int d1d2\ \psi_i^\star(1)\psi_a(1)\frac{1}{x_{12}}\psi_j^\star(2)\psi_b(2) \\ &\quad + \int\int d1d2\ \psi_i^\star(1)\psi_a(1)f_{xc}\psi_j^\star(2)\psi_b(2), \end{aligned} \tag{2.114}$$

where f_{xc} denotes to the so-called xc kernel, which contains the second functional derivative of the xc energy (E_{xc}) to describe the response of the xc potential:

$$f_{xc} = \frac{\delta^2 E_{xc}}{\delta\rho(1)\delta\rho(2)}. \tag{2.115}$$

The LR ansatz and the resulting RPA TD-DFT eigenvalue problem allow for simple implementations in modern quantum chemical programs and the same xc functionals as in ground state DFT can be employed. A further approximation to the RPA TD-DFT scheme is provided via the Tamm-Dancoff approximation (TDA)[142], where the $\mathbf{B}$ matrix is set to zero. Since correlation is already included in the ground state, TD-DFT with TDA is usually a very good approximation to RPA TD-DFT.[43]

For locally valence-excited states, which often dominate the absorption spectra, TD-DFT is well-known to provide accurate results, if an appropriate benchmarked xc functional is employed.[43] Due to its simple construction, the computational cost is low and the method can be thus applied for large systems. However, TD-DFT is afflicted by the self-interaction error as normal Kohn-Sham DFT. As a consequence, pure TD-DFT without additional correction schemes fail to describe charge transfer and Rydberg states as

well as extended π-systems and doubly excited states.[135–137] The main reason for the wrong description of Rydberg states and extended π-systems is that typically employed xc functionals often show the wrong asymptotic behavior for electron-nuclei distances. Charge transfer state energies are calculated much too low, which is known as the electron-transfer self-interaction error. Hence, TD-DFT is not a black-box method, but considering its limitations, it can be successfully employed for many photochemical problems.

2.3.3 Excited States via the Coupled-Cluster Approach

Next, I would like to introduce excited state approaches within the coupled cluster family. The most important approaches are based on the equation-of-motion (EOM)[55,58,103,131] and linear-response (LR)[132,133] theories.

The EOM ansatz is based on a simultaneous consideration of two time-independent Schrödinger equations

$$\begin{aligned} \hat{H}\Psi_0^{CC} &= E_0^{CC}\Psi_0^{CC} \\ \hat{H}\Psi_n &= E_n\Psi_n, \end{aligned} \tag{2.116}$$

where the first one corresponds to the CC ground state reference and the other one to an n$^{\text{th}}$ excited state Ψ_n, which are given as:

$$\begin{aligned} \Psi_0^{CC} &= e^{\hat{T}}\Psi_0^{HF} \\ \Psi_n &= \hat{C}_n\Psi_0^{CC}. \end{aligned} \tag{2.117}$$

Here, the typical excitation operator $\hat{C}$ (see chapters 2.2.2 and 2.2.4) is employed to construct the excited state wave function. Since the ground state reference excitation operator $\hat{T}$ is constructed using $\hat{C}$ (see chapter 2.2.4), their commutator is zero:

$$\left[\hat{C},\hat{T}\right] = 0. \tag{2.118}$$

Considering the projected CC equation, the transformed Hamiltonian is written as

$$\begin{aligned} \hat{H}_{CC} &= e^{-\hat{T}}\hat{H}e^{\hat{T}} \\ &= \hat{H} + \left[\hat{H},\hat{T}\right] + \frac{1}{2}\left[\left[\hat{H},\hat{T}\right]\hat{T}\right] + \frac{1}{3!}\left[\left[\left[\hat{H},\hat{T}\right]\hat{T}\right]\hat{T}\right] \\ &\quad + \frac{1}{4!}\left[\left[\left[\left[\hat{H},\hat{T}\right]\hat{T}\right]\hat{T}\right]\hat{T}\right], \end{aligned} \tag{2.119}$$

where the Baker-Campbell-Hausdorff terminating expansion for any $\hat{T}$ is used.[108] To construct the EOM equation, the difference of both Schrödinger equations has to be built and using the commutator rule (equation 2.118) and the transformed CC Hamiltonian (2.119), the final EOM equations are than given as

$$\begin{aligned} \left[\hat{H},\hat{C}_n\right]\Psi_0^{CC} &= \omega_n\hat{C}_n\Psi_0^{CC} \\ \left[\hat{H}_{CC},\hat{C}_n\right]\Psi_0^{HF} &= \omega_n\hat{C}_n\Psi_0^{HF}. \end{aligned} \tag{2.120}$$

Here, the excitation energy of an n$^{\text{th}}$ excited state is defined as $\omega_n = E^n - E_0^{CC}$ and the eigenvalue problem in matrix form can be written as

$$\mathbf{H}_{CC}\mathbf{C} = \mathbf{C}\omega. \tag{2.121}$$

To obtain the excitation energies, it is sufficient to solve equation 2.121, which results in the right-hand eigenvectors $\mathbf{C}$. Therefore, it is reasonable to define $\mathbf{C} = \mathbf{R}$. Properties, e.g. oscillator strengths, require the solution of the left-hand eigenvalue problem

$$\mathbf{L}\mathbf{H}_{CC} = \mathbf{L}\omega \tag{2.122}$$

due to the non-Hermitian CC Hamiltonian. Hence, the CC eigenvalue problem has to be solved twice to obtain all spectral information. An advantage of the EOM-CC approach is its size-consistency, which is independent of the order of truncation. Furthermore, excited states and their properties are generally well-described due to the accurate CC ground state reference.[58] However, the applications are limited by computational power, thus only EOM-CCSD and EOM-CCSD(T) can be employed for chemically relevant systems and problems.

In contrast to EOM, the linear response ansatz for CC is based on the time-dependent Schrödinger equation and provides broader application, since it can be employed to the approximated CC2 model. In principle, the excitation energies are obtained via the same procedure as in EOM-CC, but the derivation differs. In LR-CC, the excitation energies are derived via taking the poles of the CC response function.[143] Here, the right-hand and left-hand eigenvalue CC equations are written as

$$\mathbf{A}\mathbf{R}_n = \omega_n \mathbf{R}_n \quad \text{and} \quad \mathbf{L}_n\mathbf{A} = \omega_n \mathbf{L}_n, \tag{2.123}$$

where $\mathbf{A}$ denotes the Jacobian matrix with

$$A_{\mu\nu} = \frac{\partial \left(\langle \mu | e^{-\hat{T}} \hat{H} e^{\hat{T}} | \Psi_0^{HF} \rangle \right)}{\partial t_\nu} = \langle \mu | e^{-\hat{T}} \left[\hat{H}, \hat{C}_\nu \right] e^{\hat{T}} | \Psi_0^{HF} \rangle. \tag{2.124}$$

Both CC approaches for excited-states provide reliable results and are commonly applied in quantum chemical calculations.[58,144]

Besides the LR and EOM approaches, there is a third prominent route to access excited states via the CC scheme, i.e. the symmetry adapted cluster configuration interaction (SAC-CI)[60–65] method. This approach is theoretically equivalent to the EOM and LR approaches, but the coding algorithm differs. In principle, a CC like ground state wave function based on symmetry-adapted clusters (SAC) is defined as

$$\begin{aligned} |\Psi_0^{\mathrm{SAC}}\rangle &= e^{\sum_n t_n \hat{S}_n} |\Psi_0^{HF}\rangle \\ &= \left(1 + \sum_n t_n \hat{S}_n + \frac{1}{2} \sum_{n,m} t_n t_m \hat{S}_n \hat{S}_m + ... \right) |\Psi_0^{HF}\rangle, \end{aligned} \tag{2.125}$$

where t_n is the cluster coefficient and $\hat{S}_n$ corresponds to symmetry-adapted excitation operators that contain linked terms of totally symmetric single ($\hat{S}_i^a$) and double excitation ($\hat{S}_i^a \hat{S}_j^b$) operators, which have the form

$$\hat{S}_i^a = \frac{1}{\sqrt{2}} \left(\hat{c}_{\alpha a}^\dagger \hat{c}_{\alpha i} + \hat{c}_{\beta a}^\dagger \hat{c}_{\beta i} \right). \tag{2.126}$$

Unlinked cluster operators, e.g. $\hat{S}_n \hat{S}_m$, can be included, which results in different kinds of approximation levels. To obtain excited states, the SAC wave function is used as a reference, which results in the CI like ansatz

$$|\Psi_n\rangle = \sum_k d_k R_k |\Psi_0^{\mathrm{SAC}}\rangle, \tag{2.127}$$

where d_k is a coefficient and R_k denotes symmetry-adapted excitation operators like $\hat{S}_n$. A commonly employed variant is the SAC-CI SD-R method, where only single and double excitation operators are included in R_k.[145]

2.4 Approaches for the Calculation of Core-Excited States

Next, I discuss popular methods to calculate core-excited states. Since XAS did not received a lot of attention in the past, quantum chemical methods for a proper description of core-excited states were limited. Nowadays, due to modern synchrotron soft-beam sources, the research and the applications of XAS are strongly increasing and thus quantum chemical methods are important to help characterizing these states. The calculation of core-excited states with standard quantum chemical approaches is tedious, because they are located in the high-energy X-ray spectrum and typical algorithms that are employed to solve the respective quantum chemical eigenvalue problem usually yield the energetically lowest solutions. Furthermore, core excitations are accompanied by strong orbital relaxation effects, which have to be described properly to achieve quantitative agreement with experiments. The aim of this thesis is to show that for the ADC scheme, the core-valence separation (CVS) approximation is a successful solution for this problem. In the following sections, I give a brief overview to approaches to simulate XAS spectra with other methods than ADC, which is introduced in detail in the following chapter 2.5. Here, the focus is on the static exchange method, CC approaches and DFT methods. For information on other prominent approaches for the calculation of core-excited states like the GW approximation to the Bethe-Salpeter equation[146], the second-order perturbative corrected CIS scheme (CIS(D))[74,147] or multi-configuration self-consistent-field (MCSCF)[106] approaches, I refer to the literature.[73]

To distinguish between core and the remaining occupied orbitals, capital letters I, J, K, ... denote core orbitals, while lower cases i, j, k, ... refer to the remaining occupied orbitals, if not otherwise stated.

2.4.1 Static Exchange Method

The first method I introduce is the static exchange (STEX) method.[73,148,149] STEX is based on HF theory and contains single excitations, in which the particle and the hole are independent. Due to its construction, the virtual HF orbitals often do not provide a good description of an excited state, while besides correlation effects, the occupied orbitals describe the ground state adequately.[101] A possibility to improve this description is provided within the STEX theory, where the virtual HF orbitals of an (N-1)-electron system are used to describe the core-exited state orbitals of the N-electron system. Therefore, a restricted open-shell HF (ROHF)[150] calculation is performed using a determinant in which an electron is removed from the core-orbital space. This solution provides the occupied orbitals of the (N-1)-electron system. Next, an electron is placed to the virtual level of the ROHF solution, which results in the STEX eigenvalue problem:

$$\hat{F}_I^{\mathrm{STEX}} \psi_{Ia} = \epsilon_{Ia} \psi_{Ia}. \tag{2.128}$$

Here, ψ_{Ia} is the excited orbital with the corresponding orbital energy ϵ_{Ia} in the (N-1) approximation. The STEX-Fock operator is given as

$$\hat{F}_I^{\mathrm{STEX}} = \hat{h} + \sum_{I,j}^{\text{all occ.}} (\hat{J}_j - \hat{K}_j) + \hat{J}_I + \hat{K}_I \tag{2.129}$$

and based on the (N-1) ROHF solution with separated core and valence occupied parts. Since the eigenvectors of the STEX-Fock operator are non-orthogonal to the occupied

orbitals of the (N-1)-system, one has to project them out. After the projection procedure, the STEX eigenvalue problem can be solved, which results in a good approximation of the core-excited state orbitals. The final core excitation energy is then given as

$$\omega_{Ia} = \mathrm{IP}_I + \epsilon_{Ia}, \tag{2.130}$$

where IP_I is the ionization potential of the core electron I, which is given as the difference between the neutral N-electron and the (N-1)-electron systems.

Although the ansatz is simple, the technical application can be difficult, because the core-hole ROHF-SCF solution for the (N-1)-electron system often does not converge on the desired state or does not converge at all due to electrons that refill the core hole. However, there are possible solutions of this problem, e.g. the maximum overlap method.[151] Although the STEX method includes orbital relaxation, quantitative results compared to experiment cannot be achieved, since only singly excited configurations are considered. Usually, one has to shift the core excitation energies about 10 eV to correspond to experimental values.[73] This is comparable to CVS-ADC(1) (see chapter 4), i.e CVS-CIS, where in contrast to the STEX approach no convergence problems are to be expected.

2.4.2 Coupled-Cluster Approaches for Core Excitations

In the field of CC, some approaches for the calculation of core-excited states are available. In a recent publication of *Coriani and Koch*, the CVS approximation was applied to LR-CC for the very first time.[54] Generally, the CVS approximation is based on decoupling of core excitations from the valence-excited states, which is justified due to the large energetic separation and contraction of core orbitals compared to the remaining ones.[44,45] The CVS approximation is explained in detail in chapter 2.5.6 in the scope of the ADC method. Other available LR-CC approaches are based on asymmetric Lanczos algorithms that are employed to solve complex LR-CC equations using a complex polarization propagator formalism.[52,53,152–154] Furthermore, another recent study by *Peng et al.* was published, where the EOM-CC ansatz is combined with a special non-Hermitian energy-specific eigensolver employed to calculate core-excited states directly.[59] In this chapter, I summarize these recent and older approaches without going into detail.

The CVS-LR-CC Method

Within the CC-LR theory, the CVS approximation can be simply implemented to compute the core excitations directly.[54] Therefore, a projector $\hat{P}_I$ is introduced, which removes all vector elements that do not correspond to a set of defined core orbitals. Applying such a projector to a trial vector $\mathbf{B}$, which contains singly and and doubly excited configurations, leads to

$$0 = \begin{cases} \hat{P}_I B_{ja} & \text{if } i \neq j \\ \hat{P}_I B_{jkab} & \text{if } j \neq I \text{ or } k \neq I \end{cases}. \tag{2.131}$$

If a Davidson solver is applied, the CC-LR eigenvalue problem (see equation 2.123) is transformed to the projected eigenvalue problem

$$\hat{P}_I(\mathbf{A}\hat{P}_I\mathbf{R}_n) = \omega_n \hat{P}_I \mathbf{R}_n, \tag{2.132}$$

which has to be solved for the left-hand and right-hand eigenvectors. The first test results obtained with the CVS-LR-CC method show only derivations of a few hundredths of eV from the full LR-CC approach.[54] However, the results have not been compared with experimental data so far.

Core Excitations with the SAC-CI Method

The SAC-CI method can be easily employed to calculate core excitations similar as the CVS-LR-CC approach. For this, the symmetry-adapted excitation operators are restricted to correspond to at least one core orbital or a set of core orbitals, which is called core-window approach.[155] Hence, only the relevant core excitations are included in the active space and can be computed directly using typical solvers.

Complex Polarization Propagator CC

A totally different ansatz for the description of core-excited states is provided via the complex polarization propagator (CPP) method.[52,53] In principle, the CPP approach for calculating core-excited states can be combined with any electronic structure theory for excited states, but it has been successfully implemented for CC methods and TD-DFT so far.[67] The CPP approach is based on the linear response function[156] R for two generic operators $\hat{X}$ and $\hat{Y}$, which contain damping terms that correspond to the finite lifetimes of the respective excited state and to line broadening in the absorption spectra:

$$R_{\hat{X}\hat{Y}}(\omega) = -\sum_n \left(\frac{\langle \Psi_0 | \hat{X} | \Psi_n \rangle \langle \Psi_n | \hat{Y} | \Psi_0 \rangle}{\omega_n - (\omega + \eta i)} + \frac{\langle \Psi_0 | \hat{Y} | \Psi_n \rangle \langle \Psi_n | \hat{X} | \Psi_0 \rangle}{\omega_n + (\omega + \eta i)} \right). \tag{2.133}$$

This damped LR function depends on the frequency ω of an external field and on the transition frequency ω_n of the n^{th} excited state. The damping factor η has certain physical origins, e.g. emission broadening, and is usually obtained empirically. Generally, introducing this complex frequency $(\omega + \eta i)$ results in complex response equations, which are in the case of CC given as

$$(\mathbf{A} - (\omega + \eta i)\,\mathbb{1})\,\mathbf{t}^{\hat{Y}}\,(\omega + \eta i) = -\zeta^{\hat{Y}}. \tag{2.134}$$

$\mathbf{A}$ is the coupled-cluster Jacobian matrix as introduced in chapter 2.3.3, while $\mathbf{t}$ denotes the cluster response amplitudes and ζ is the first order CC building block as

$$\zeta_n^{\hat{Y}} = \langle \Psi_n | e^{-T} \hat{Y} e^{T} | \Psi_0^{HF} \rangle. \tag{2.135}$$

For isotropic properties, e.g. energies, where $\hat{X} = \hat{Y}$, the solution of the complex damped response function can be obtained using an asymmetric Lanczos chain solver.[52,53] For the computation of excited states of the full spectrum, the electric-dipole approximation is used, where the cross-section for linear absorption processes is given as

$$\sigma(\omega) = \frac{4\pi\omega}{c} \mathrm{Im}[\bar{\alpha}(\omega)]. \tag{2.136}$$

Here, $\mathrm{Im}[\bar{\alpha}(\omega)]$ denotes the imaginary part of the averaged isotropic electric-dipole polarizability and c is the speed of light. The asymmetric Lanczos method provides an elegant way to obtain core-excited states directly. The total spectrum for all ω is constructed iteratively using one common approximation of the Jacobian matrix in a reduced space. The number of iterations is defined as the Lanczos chain-length. The larger the chain-length the higher the accuracy. Hence, the relevant response functions for calculating the absorption converges via increasing the chain-length, thus it is possible to converge the eigenvectors in a specific wave range of the spectrum, if the chain-length has a sufficient size. Since it is possible to identify transitions with a large dominant absorption cross-section, the spectral core excitations can be identified among others.

The CPP-CC approach has been proven to provide accurate core-excitation energies and spectral features. A disadvantage of this method is that a prior knowledge of the system is necessary. Furthermore, there are convergence problems and one has to converge the bright intense states thereby loosing information about the dark states in the same region.[52,53]

Energy-Specific EOM-CC

The energy-specific EOM-CC (ES-EOM-CC) approach is based on a non-Hermitian eigensolver, which is able to obtain the core-excited states directly without introducing further approximations like the CVS to the EOM-CC scheme.[59] Hence, the method also includes couplings to valence-excited states, which have to be neglected within CVS approaches. The ES-EOM-CC follows a two-step strategy, with different loops of ES eigensolver procedures. As the first step, a set of trial vectors has to be generated, which correspond to the high-energy core-excited states of interest. For this purpose, the CIS method is employed and the results are refined using the low scaling partitioned EOM-MBPT2 (P-EOM-MBPT2)[157] approach, which is a special second order MBPT approximation of the EOM-CCSD approach. The P-EOM-MBPT2 vectors are obtained using the ES eigensolver procedure, which works as follows. Starting with a set of full orbital space left-hand $\mathbf{L}_T$ and right-hand $\mathbf{R}_T$ trial vectors, which are based on the initial guess of core-excited states, i.e. CIS or P-EOM-MBPT2 solutions, respectively, the EOM Hamiltonian $\mathbf{H}_{CC}$ is projected onto a subspace spanned by the trial vectors as

$$\mathbf{h} = \mathbf{L}_T \hat{H}_{CC} \mathbf{R}_T. \tag{2.137}$$

Note that the left-hand and right-hand vectors are related to each other through the biorthonormality condition

$$\langle \Psi_0 | \hat{L}_a \hat{R}_b | \Psi_0 \rangle = \delta_{ab}, \tag{2.138}$$

where Ψ_0 is the reference wave function. The reduced Hamiltonian $\mathbf{h}$ is then diagonalized, which results in sets of new left-hand $\mathbf{l}$ and right-hand $\mathbf{r}$ eigenvectors as well as the corresponding excitation energies ω. The eigenpairs in the reduced subspace are then screened and only those above the desired energy threshold are kept. At the last step, the eigenpairs of interest are transformed back from the reduced space to the full orbital space with

$$\tilde{\mathbf{R}} = \mathbf{R}_T \mathbf{r} \quad \text{and} \quad \tilde{\mathbf{L}} = \mathbf{L}_T \mathbf{l}, \tag{2.139}$$

which provides new sets of eigenvectors. The procedure is repeated until the desired convergence criteria are reached. To ensure proper convergence, the typical procedures of Davidson algorithms[138], e.g. adding residual norms and extending subspaces, are employed. Via this ES eigensolver procedure, the P-EOM-MBPT2 solutions are obtained using the CIS solution as a guess, while the P-EOM-MBPT2 solutions are then used as trial vectors for other EOM-CC methods like EOM-CCSD.

First test results at the ES-EOM-CCSD level provide accurate results compared to experiment. Computationally, the implementation is capable to calculate three core-excited states of the dibenzothiophene molecule employing the 6-311++G* basis set at this level of theory.[59]

2.4.3 (TD-)DFT Techniques for Core Excitations

Since DFT based approaches are commonly employed for calculations of large systems, a plethora of approaches for core excitations are available. In the scope of my thesis, I

do not introduce all of them, but I would like to concentrate on a few chosen methods. For a broader review, I refer to the article of *Besley* and *Asmuruf*, as well as to the chapter *"Nonlinear Spectroscopy of Core and Valence Excitations Using Short X-ray Pulses: Simulation Challenges"* by *Zhang et al.*, which has been published in the book *"Topics in Current Chemistry 368"* edited by *Ferré et al.*[73,75]

The Delta-DFT method

A similar theoretical concept as the one of the STEX method (see chapter 2.4.1) can be transferred to the DFT approach, resulting in the Δ-DFT or rather ΔKohn-Sham method.[75,158–160] Within this approach, the core excitation energy is given as the difference between the neutral and singly core-excited species. Therefore, the orbitals have to be variationally optimized for the different states, respectively, using the SCF procedure. To avoid convergence problems of the core-excited SCF solution, the maximum overlap method can be employed in the same way as in STEX. The largest advantage of this approach is the direct inclusion of relaxation effects, since the orbitals are optimized for the core-excited state. This provides a good agreement with experimental data.[75] However, convergence can be very difficult and the method is only usable for systems where the old and new sets of orbitals differ significantly. Furthermore, only one state of interest is the target in a single ΔKohn-Sham calculation.

TD-DFT approaches

Let me turn to a discussion of TD-DFT approaches for the calculation of core-excited states. The simplest way to obtain the core excitations directly is to apply the CVS approximation by restricting the single excitation space to the relevant excitations from core orbitals.[161] This method is called restricted excitation window (REW) TD-DFT, which provides errors of only 0.01 eV compared to the respective full space calculation.[75] Generally, core-excited states calculated with TD-DFT often reproduce experimental spectra qualitatively well. However, the self-interaction error (SIE) inherent in the TD-DFT formalism leads to a strong underestimation of core-excited states.[74,75,162] Since 1s core orbitals have a large energy compared to higher occupied valence orbitals, the SIE is particularly large regarding core excitations. Similar to charge-transfer states, the integrals of the TD-DFT matrix (see equation 2.114) are almost zero, because the overlap between contracted 1s core orbitals and the virtual orbitals is small.[73] Hence, the excitation energy is dominated by the orbital energy difference $\delta_{IJ}\delta_{ab}(\epsilon_a - \epsilon_I)$. Since virtual Kohn-Sham orbitals are obtained for an N+1-electron system, Koopman's theorem[101] is not valid and the gap between occupied and unoccupied orbitals is very small, which results in the large underestimation of the core excitation energy.[43] This can be proven using diagnostics like the overlap between electron donating and accepting orbitals, which results in values close to zero, indicating a small overlap.[75] As a consequence, absolute core excitation energies obtained at the TD-DFT level usually have to be corrected by an additional energy shift of several eV to agree with experimental data. This error increases for heavier atoms, because the energy and compactness of the core orbitals increase due to stronger Coulomb attraction of the nucleus.[163] Furthermore, studying XA spectra requires an xc functional evaluation for every molecular system of interest due to the empirical characters of the xc functionals.[43]

During the last 10 years, various approaches have been developed to overcome the SIE problem. A possible correction scheme is based on nonlinear response theory using the first-order hyperpolarizability which results in a CPP ansatz similar to the CPP-CC approach (see chapter 2.4.2).[71,164,165] This approach considers relaxation effects and besides a single-determinant, multi-determinant reference states can be included, too. The

CPP-TD-DFT approach provides good agreement with experiment, but the excitation energies are still underestimated and an additional blue shift is often necessary.[67,165,166] A possible SIE correction for core orbitals is described by *Tu et al.*[72] The idea is based on the simple SIE correction[167] by *Perdew* and *Zunger*:

$$\Delta E = -\sum_i \left(J[\rho_i] + E_{xc}[\rho_i]\right). \tag{2.140}$$

Here, the sum runs over all occupied spin orbitals i. The derivative of this expression results in a SIE correction potential, which is exact for single electron systems. To correct core orbitals of many-electron molecules, the correction functional is fitted using experimental data of core ionization potentials, which results in

$$\Delta E_{core} = \int V_i(x)\rho_i(x)d\tau, \tag{2.141}$$

where V_i is the empirically fitted SIE correction potential. In combination with the CPP-TD-DFT approach, the SIE correction provides a successful way to calculate almost correct absolute core excitation energies at the TD-DFT level.[72]

However, the quality of the results obtained with both REW and CPP approaches depend on the used xc functional. Besides correction schemes, there are plenty of specially constructed xc functionals for the calculation of core-excited states with the TD-DFT method. Hybrid functionals[102] with a high percentage of HF exchange are a possibility to improve core-excitation energies.[75] The TD-DFT matrix elements for core excitations using hybrid functionals are given as

$$\begin{aligned}
A_{Ia,Jb} = \delta_{IJ}\delta_{ab}(\epsilon_a - \epsilon_I) &+ \int\int d1d2\ \psi_I^\star(1)\psi_a(1)\frac{1}{x_{12}}\psi_b^\star(2)\psi_J(2) \\
&+ c_{HF}\int\int d1d2\ \psi_I^\star(1)\psi_J(1)\frac{1}{x_{12}}\psi_b^\star(2)\psi_a(2) \\
&+ (1-c_{HF})\int\int d1d2\ \psi_I^\star(1)\psi_a(1)f_{xc}\psi_b^\star(2)\psi_J(2) \\
B_{Ia,Jb} = \int\int d1d2\ &\psi_I^\star(1)\psi_a(1)\frac{1}{x_{12}}\psi_j^\star(2)\psi_b(2) \\
&+ c_{HF}\int\int d1d2\ \psi_I^\star(1)\psi_b(1)\frac{1}{x_{12}}\psi_J^\star(2)\psi_a(2) \\
&+ (1-c_{HF})\int\int d1d2\ \psi_I^\star(1)\psi_a(1)f_{xc}\psi_J^\star(2)\psi_b(2),
\end{aligned} \tag{2.142}$$

where the HF scaling factor is c_{HF}. The terms marked in red are integrals, which are almost zero in the case of core-excited states, since the overlap is small. Hence the **B**-matrix is still almost zero using hybrid-functionals, but the integral that corresponds to pure HF Coulomb exchange, which is marked in blue, is non-zero. This leads to a generation of hole and electron interactions that correct the excitation energy of a core-excited state. This correction depends on the HF exchange scaling factor. However, this correction is usually not sufficient to achieve quantitative agreement with experiments, but there are a few examples, where the HF exchange correction works.[162] Other possibilities to compensate the SIE are long-ranged corrected functionals (LRC), which were originally designed to correct the description of charge-transfer states.[43,168] These functionals are also hybrid functionals, but they do not have a constant percentage of HF exchange. The Coulombic repulsion operator of LRC functionals is split into a long-range and a short-range part as

$$\frac{1}{x_{12}} = \frac{1-\vartheta(\mu x_{12})}{x_{12}} + \frac{\vartheta(\mu x_{12})}{x_{12}}, \tag{2.143}$$

where the HF exchange is included with respect to an error function $\vartheta(\mu x_{12})$, which depends on the factor μ that controls the separation of the long- and short-range interactions. The first term describes the short-range part, while the second one corresponds to long-range interactions. Popular representative LRC-functionals, e.g. CAM-B3LYP[169], were employed to calculate XAS spectra.[67,170,171] However, such LRC-functionals work well for valence-excited charge-transfer states, but for core-excited states the improvement is small.[75] The reason for this is that a large amount of HF exchange is usually used for the long-range part, while the short-range part is dominated by pure DFT contributions, which provides a large improvement for spatially separated charge-transfer processes. Core orbitals, in contrast, are very contracted and localized. Hence, processes involving core orbitals are mostly dominated by short-range contributions. A solution for this problem is provided via LCgau-core-BOP functionals.[172,173] Here, HF exchange is introduced for the short-range part, i.e. small x_{12}, using a Gaussian correction term G that transforms equation 2.143 to

$$\frac{1}{x_{12}} = \frac{1-\vartheta(\mu x_{12})}{x_{12}} + G + \frac{\vartheta(\mu x_{12})}{x_{12}} - G \quad \text{with} \quad G = k\frac{2\mu}{\sqrt{\pi}} e^{-\frac{\mu^2 x_{12}^2}{a}}, \tag{2.144}$$

where k and a are additional parameters to introduce HF exchange for the short-range interactions. Using such LCgau-core-BOP functionals provide core-excitation energies of light elements with errors less than 1 eV compared to experimental data.[173] This error can be further reduced using schemes introduced by *Besley et al.*, where the Coulomb repulsion operator is partitioned as

$$\frac{1}{x_{12}} = X^{\mathrm{HF}} - X^{\mathrm{DFT}} \tag{2.145}$$

with

$$\begin{aligned} X^{\mathrm{HF}} &= c_S \frac{1-\vartheta(\mu_S x_{12})}{x_{12}} + c_L \frac{\vartheta(\mu_L x_{12})}{x_{12}} \\ X^{\mathrm{DFT}} &= c_S \frac{1-\vartheta(\mu_S x_{12})}{x_{12}} + c_L \frac{\vartheta(\mu_L x_{12})}{x_{12}} - \frac{1}{x_{12}}, \end{aligned} \tag{2.146}$$

where c_S and c_L are parameters that regulate the HF exchange in the short- and long-range parts, respectively.[174] In this scheme, X^{HF} is treated with HF exchange and X^{DFT} with pure DFT exchange.

At last, I would like to mention the CV-B3LYP[175] and CVR-B3LYP[176] functionals developed by *Nakai et al.*, which are not based on partitioning the Coulomb repulsion operator in real space into short- and long-range parts. In principle, the occupied Kohn-Sham orbital space is split into a core and remaining valence space, thus the interaction potentials are partitioned into core-core, core-valence and valence-valence terms. Via introducing hybrid parameters, every interaction term is treated with a different HF exchange. Again, these functionals provide errors in the sub-1 eV region.

2.5 Algebraic-Diagrammatic Construction Scheme for the Polarization Propagator

In this chapter, I introduce the algebraic-diagrammatic construction (ADC) scheme for the polarization propagator in detail. ADC is a quantum chemical excited state method based on perturbation theory.[76–79] Due to its size-consistency and Hermitian structure, the ADC scheme is well-known to be an accurate and reliable approach for the calculation of excited states and their properties. Historically, the ADC scheme was introduced via the Green's function theory using the typical Møller-Plesset partitioning of the Hamiltonian. However, a more elegant way to derive the ADC approach exists via the intermediate state representation (ISR), which provides also access to excited state properties and open-shell variants of the ADC matrix.[78,82,83] Both ways of derivation are summarized in this chapter with a focus on the ISR approach, while the original way via the Green's function theory is briefly outlined. Besides the calculation of valence-excited states, the ADC scheme can be employed to describe core-excited states. Therefore, the core-valence separation (CVS) approximation has to be applied to the ADC working equations, resulting in the CVS-ADC approach.[44,45,100] This approximation is explained in detail, followed with a summary about the final (CVS-)ADC working equations. An overview of techniques to analysis excited state densities that help to interpret the nature of electronically excited states is given afterwards and the chapter is concluded with a discussion about the inclusion of relaxation effects within the CVS-ADC method.

2.5.1 Original Derivation via Green's Function Theory

Generally, Green's function theory was developed to solve inhomogeneous differential equations $f(\mathbf{r})$ by replacing the original inhomogeneity $I(\mathbf{r}')$ by the Dirac delta distribution $\delta(\mathbf{r}-\mathbf{r}')$.[76,79] Any such inhomogeneous differential equation can be expressed as

$$f(\mathbf{r}) = \int d\mathbf{r}' G(\mathbf{r}-\mathbf{r}') I(\mathbf{r}'). \tag{2.147}$$

Although it is straightforward to define a unique Green's function for the time-dependent single-particle Schrödinger equation, it is impossible to construct this for many-body systems. However, one can build so-called Green's function propagators, which are designed to yield solutions for certain kinds of problems that are inherent in many-body systems. For the calculation of excited states, a two-particle propagator can be employed. However, the simpler polarization propagator is a better choice, because the relevant information that describes the excitation spectrum of a molecule is fully included. This propagator is applied to the time-dependent ground state reference wave functions of many-body systems and thereby initiates time-dependent density fluctuations. In its spectral representation the polarization propagator $\Pi_{pq,rs}(\omega)$ is given as

$$\begin{aligned}\Pi_{pq,rs}(\omega) &= \sum_{n\neq 0}\left(\frac{\langle\Psi_0|\hat{c}_p^\dagger\hat{c}_q|\Psi_n\rangle\langle\Psi_n|\hat{c}_r^\dagger\hat{c}_s|\Psi_0\rangle}{\omega-(E_n-E_0)+\eta i} - \frac{\langle\Psi_0|\hat{c}_r^\dagger\hat{c}_s|\Psi_n\rangle\langle\Psi_n|\hat{c}_p^\dagger\hat{c}_q|\Psi_0\rangle}{\omega+(E_n-E_0)-\eta i}\right) \\ &= \Pi^+(\omega)+\Pi^-(\omega),\end{aligned} \tag{2.148}$$

where, as usual, Ψ_0 and Ψ_n denote the ground and n^{th} excited state wave functions with their corresponding energies E, respectively. Note that the complex term ηi, which originates from the Fourier transformation of the polarization propagator from its time-depended to its spectral form, can be neglected, because the limit $\eta \to 0$ is taken. Since the

right-hand and left-hand terms ($\Pi^+(\omega)$ and $\Pi^-(\omega)$) contain the same information, only one part has to considered to obtain the vertical excitation energies $\omega_n = E^n - E^0$, which are the poles of the polarization propagator. Besides the excitation energies, the polarization propagator provides also access to the spectral amplitudes using the expectation value $\langle\Psi_0|\hat{c}_p^\dagger\hat{c}_q|\Psi_m\rangle$ in the nominator of equation 2.148 to define the transition moment T_m of an m^{th} excited state of an arbitrary single particle operator $\hat{O}$ via

$$T_m = \langle\Psi_0|\hat{O}|\Psi_m\rangle = \sum_{pq} O_{pq}\langle\Psi_0|\hat{c}_p^\dagger\hat{c}_q|\Psi_m\rangle. \tag{2.149}$$

In the case of many-body systems, e.g. chemical molecules, the polarization operator is expressed in the eigenstates with respect to the molecular Hamiltonian. This representation is called the diagonal form of the polarization propagator, because the eigenstates of a molecular system diagonalize the Hamiltonian. For simplification, the diagonal form can be written as

$$\Pi^+(\omega) = \sum_{n\neq 0} \frac{\langle\Psi_0|\hat{c}_p^\dagger\hat{c}_q|\Psi_n\rangle\langle\Psi_n|\hat{c}_r^\dagger\hat{c}_s|\Psi_0\rangle}{\omega - (E_n - E_0)} = \mathbf{x}_{pq}^\dagger \left(\mathbb{1}\omega - \mathbf{\Omega}\right)^{-1} \mathbf{x}_{rs}, \tag{2.150}$$

where $\mathbf{\Omega}$ denotes the diagonal matrix of ω_n and $\mathbf{x}$ contain the information about the spectral amplitudes.

So far, the description of the excited states is formally exact. However, neither the exact ground state nor the excited state wave functions are known. Hence, approximations have to be applied to the polarization propagator formalism. In the ADC approximation, the existence of a non-diagonal matrix representation of equation 2.150 is postulated based on Feynman-Goldstone diagrammatic perturbation series:

$$\Pi^+(\omega) = \mathbf{F}^\dagger \left(\mathbb{1}\omega - \mathbf{M}\right)^{-1} \mathbf{F}. \tag{2.151}$$

The matrix $\mathbf{M}$ is the non-diagonal representation of an so-called effective Hamiltonian and further denoted as the ADC secular matrix. Accordingly, $\mathbf{F}$ is the effective transition moment matrix. Both matrices are expanded via the usual Møller-Plesset partitioning of the Hamiltonian that results in

$$\mathbf{M} = \mathbf{M}^{(0)} + \mathbf{M}^{(1)} + \mathbf{M}^{(2)} + \ldots \tag{2.152}$$

$$\mathbf{F} = \mathbf{F}^{(0)} + \mathbf{F}^{(1)} + \mathbf{F}^{(2)} + \ldots. \tag{2.153}$$

Hence, the ADC approach is just a reformulation of the polarization propagator in terms of a perturbation series. Explicit terms of the ADC secular matrix and the transition amplitudes can thus be derived by analyzing the perturbation scheme of $\Pi^+(\omega)$ in a specific overall order n. Depending on n, the partitioning leads to a truncation of the configuration space of singly, doubly, ... excited configurations, which are further called excitation classes. Furthermore, n accounts for a consistent description in perturbation theory of every term in every block corresponding to the excitation classes resulting in an ADC(n) approximation scheme.

Finally, the polarization propagator can now be described analytically. Since the vertical excitation energies are the poles of $\Pi^+(\omega)$, the ADC secular matrix has to be diagonalized to obtain them, resulting in the Hermitian eigenvalue problem

$$\mathbf{MY} = \mathbf{Y\Omega}, \tag{2.154}$$

where $\mathbf{Y}$ is the matrix of ADC eigenvectors $\mathbf{y}$. The transition moments between the ground state and an excited state m are then straightforwardly given as

$$T_m = \mathbf{y}_m^\dagger \mathbf{F}. \tag{2.155}$$

Besides the polarization propagator, the ADC scheme is also available for other propagators, e.g. the hole propagator that provides access to ionization energies. Since this thesis only deals with electron excitation processes, the underlying principle of the ADC method in this work corresponds generally to the polarization operator.

2.5.2 Intermediate State Representation

The intermediate state representation (ISR) is an alternative approach to derive the ADC matrix and transition amplitudes in a more elegant way. The ISR offers an intuitive scheme in second quantization by applying excitation operators based on creation and annihilation operators to the ground state. This ansatz is similar to CI, but the Hamiltonian is represented in a basis of intermediate states (IS) instead of a basis of HF determinants. These IS can be interpreted as correlated excited determinants. Besides the derivation of the ADC matrix elements and transition moments, the ISR provides access to excited-state properties based on one-particle operators like the dipole operator. Furthermore, it is possible to derive open-shell ADC schemes based on an unrestricted MP reference via the ISR, which is not possible using the original pathway, because the open-shell polarization operator is unknown. In this chapter, I introduce the derivation of the ADC scheme via the ISR approach, starting with the derivation of the correlated excited-states, followed by the explicit construction of the IS basis and concluding with the ISR for a general one-particle operator.

The ISR for Correlated Excited States

In the ISR approach, the exact excited states $|\Psi_n\rangle$ are expanded in terms of a complete set of intermediate states $|\tilde{\Psi}_J\rangle$ according to

$$|\Psi_n\rangle = \sum_J X_{nJ} |\tilde{\Psi}_J\rangle. \tag{2.156}$$

The set of intermediate states is constructed in such a way that it establishes a matrix representation of the Hamiltonian shifted by the exact ground state energy E_0

$$M_{IJ} = \langle \tilde{\Psi}_I | \hat{H} - E_0 | \tilde{\Psi}_J \rangle, \tag{2.157}$$

leading to the corresponding Hermitian eigenvalue problem

$$\mathbf{MX} = \mathbf{X\Omega}, \qquad \mathbf{X}^\dagger \mathbf{X} = \mathbf{1}. \tag{2.158}$$

$\mathbf{\Omega}$ denotes the diagonal matrix of eigenvalues ω_n and $\mathbf{X}$ is the matrix of eigenvectors. Consequently, the diagonalization of the ISR secular matrix $\mathbf{M}$ easily yields the exact excitation energies ω_n within the given basis set.

$$\omega_n = E_n - E_0 \tag{2.159}$$

Analogously, one can derive the transition moments T_n of the general form

$$T_n = \langle \Psi_n | \hat{D} | \Psi_0 \rangle \tag{2.160}$$

using the one-particle operator

$$\hat{D} = \sum_{r,s} d_{rs} \hat{c}_r^\dagger \hat{c}_s, \tag{2.161}$$

where d_{rs} describes the one-particle matrix elements associated with $\hat{D}$. Within the ISR formalism, the transition moments F_J and the corresponding transition amplitudes $f_{J,rs}$ with respect to $\hat{D}$ can be constructed straightforwardly as

$$F_J = \langle \tilde{\Psi}_J | \hat{D} | \Psi_0 \rangle = \sum_{r,s} f_{J,rs} d_{rs} = \sum_{r,s} \langle \tilde{\Psi}_J | \hat{c}_r^\dagger \hat{c}_s | \Psi_0 \rangle d_{rs}. \tag{2.162}$$

In combination with the eigenvector X_{nJ} in the intermediate state basis, the final transition moment of an excited state n is

$$T_n = \sum_J X_{nJ} F_J. \tag{2.163}$$

Construction of the IS basis

Next, the configuration of the IS basis is discussed. A complete set of correlated excited states $|\Psi_J\rangle$ can be created by applying an excitation operator $\hat{C}_J$ based on creation and annihilation operators to the exact ground state wave function Ψ_0:

$$\{\hat{C}_J\} = \{\hat{c}_a^\dagger \hat{c}_i; \;\; \hat{c}_a^\dagger \hat{c}_b^\dagger \hat{c}_i \hat{c}_j; \;\; ...\} \text{ with } a < b, i < j; \;\; ... \tag{2.164}$$

$$\{\hat{C}_I^\dagger\} = \{\hat{c}_i^\dagger \hat{c}_a; \;\; \hat{c}_i^\dagger \hat{c}_j^\dagger \hat{c}_a \hat{c}_b; \;\; ...\} \text{ with } a < b, i < j; \;\; ... \tag{2.165}$$

$$|\Psi_J^0\rangle = \hat{C}_J |\Psi_0\rangle = \hat{c}_a^\dagger \hat{c}_i |\Psi_0\rangle; \;\; \hat{c}_a^\dagger \hat{c}_b^\dagger \hat{c}_i \hat{c}_j |\Psi_0\rangle \;\; ... \tag{2.166}$$

In the case of open-shell systems, the excitation operator acquires spin indices:

$$\{\hat{C}_J\}_u = \{\hat{c}_{a\sigma}^\dagger \hat{c}_{k\sigma}; \;\; \hat{c}_{a\sigma}^\dagger \hat{c}_{b\tau}^\dagger \hat{c}_{k\sigma} \hat{c}_{l\tau}; \;\; ...\} \text{ with } a\sigma < b\tau, k\sigma < l\tau \;\; ... \tag{2.167}$$

Generally, the excitation operators establish different excitation classes $\mu = 1, 2, ..$, where the first class is called particle-hole (p-h), the second two-particle-two-hole (2p-2h) and so on. Equation 2.157 can only be established if the IS are constructed to be orthonormal and orthogonal with respect to the ground state and all successive excitation classes μ. The ground state is defined as a zeroth excitation class. However, the correlated excited states are not necessarily orthogonal, thus they have to be orthogonalized using the Gram-Schmidt orthogonalization procedure. At first, the precursor states $|\Psi_J^\#\rangle$ are generated as:

$$|\Psi_J^\#\rangle = \hat{C}_J |\Psi_0\rangle - |\Psi_0\rangle \langle \Psi_0 | \hat{C}_J | \Psi_0 \rangle. \tag{2.168}$$

Subsequently, the final IS $|\tilde{\Psi}_J\rangle$ are obtained via a symmetrical orthonormalization procedure of the precursor states:

$$|\tilde{\Psi}_J\rangle = \sum_I |\Psi_I^\#\rangle \left(S^{-\frac{1}{2}} \right)_{I,J}. \tag{2.169}$$

$S_{I,J}$ denotes the overlap between two precursor states I and J, which is given as:

$$\begin{aligned} S_{I,J} = \langle \Psi_I^\# | \Psi_J^\# \rangle &= \left(\langle \Psi_0 | \hat{C}_I^\dagger - \langle \Psi_0 | \hat{C}_I^\dagger | \Psi_0 \rangle \langle \Psi_0 | \right) \left(\hat{C}_J | \Psi_0 \rangle - |\Psi_0\rangle \langle \Psi_0 | \hat{C}_J | \Psi_0 \rangle \right) \\ &= \langle \Psi_0 | \hat{C}_I^\dagger \hat{C}_J | \Psi_0 \rangle - 2 \langle \Psi_0 | \hat{C}_I^\dagger | \Psi_0 \rangle \langle \Psi_0 | \hat{C}_J | \Psi_0 \rangle \\ &\quad + \langle \Psi_0 | \hat{C}_I^\dagger | \Psi_0 \rangle \langle \Psi_0 | \Psi_0 \rangle \langle \Psi_0 | \hat{C}_J | \Psi_0 \rangle \\ &= \langle \Psi_0 | \hat{C}_I^\dagger \hat{C}_J | \Psi_0 \rangle - \langle \Psi_0 | \hat{C}_I^\dagger | \Psi_0 \rangle \langle \Psi_0 | \hat{C}_J | \Psi_0 \rangle. \end{aligned} \tag{2.170}$$

Finally, a set of orthogonal orthonormalized intermediate states are constructed, which can be used to establish a matrix of the shifted Hamiltonian by inserting equation 2.169 in equation 2.157 that results in the ISR secular matrix

$$M_{IJ} = \sum_{K,L} \left(S^{-\frac{1}{2}}\right)_{I,K} \left(\langle \Psi_K^{\#} | \hat{H} - E_0 | \Psi_L^{\#} \rangle\right) \left(S^{-\frac{1}{2}}\right)_{L,J}. \tag{2.171}$$

The middle term, i.e. the shifted Hamilton matrix, is analogous to equation 2.170 given as:

$$\begin{aligned} \langle \Psi_I^{\#} | \hat{H} - E_0 | \Psi_J^{\#} \rangle = & \langle \Psi_0 | \hat{C}_I^{\dagger} \left(\hat{H} - E_0\right) \hat{C}_J | \Psi_0 \rangle \\ & - \langle \Psi_0 | \hat{C}_I^{\dagger} \left(\hat{H} - E_0\right) | \Psi_0 \rangle \langle \Psi_0 | \hat{C}_J | \Psi_0 \rangle \\ & - \langle \Psi_0 | \hat{C}_I^{\dagger} | \Psi_0 \rangle \langle \Psi_0 | \left(\hat{H} - E_0\right) \hat{C}_J | \Psi_0 \rangle \\ & + \langle \Psi_0 | \hat{C}_I^{\dagger} | \Psi_0 \rangle \langle \Psi_0 | \left(\hat{H} - E_0\right) | \Psi_0 \rangle \langle \Psi_0 | \hat{C}_J | \Psi_0 \rangle. \end{aligned} \tag{2.172}$$

The ISR for a General One-Particle Operator

Besides the derivation of correlated excited states and transition moments, the ISR approach provides also an elegant way to obtain physical properties of an excited state vector. Analogously to equations 2.160 and 2.161, one can define a general one-particle operator $\hat{D}$, e.g. dipole moment, and its corresponding property D_n of the n$^{\text{th}}$ excited state as

$$D_n = \langle \Psi_n | \hat{D} | \Psi_n \rangle \qquad \text{with} \qquad \hat{D} = \sum_{r,s} d_{rs} \hat{c}_r^{\dagger} \hat{c}_s. \tag{2.173}$$

Expression (2.173) can be reformulated to

$$\langle \Psi_n | \hat{D} | \Psi_m \rangle = \langle \Psi_n | \sum_{r,s} d_{rs} \hat{c}_r^{\dagger} \hat{c}_s | \Psi_m \rangle = \sum_{r,s} d_{rs} \langle \Psi_n | \hat{c}_r^{\dagger} \hat{c}_s | \Psi_m \rangle = \sum_{r,s} d_{rs} \rho_{rs}, \tag{2.174}$$

thus it is straightforward to calculate excited state densities ρ_{rs} if the expectation value of D_n is known. In cases where $n = m$, ρ_{rs} describes the one-particle density of a state, while the transition density between two states ρ^{nm} is provided if $n \neq m$.

In the ISR picture, the excited state property with respect to $\hat{D}$ is

$$D_n = \langle \vec{X}_n^{\dagger} | \tilde{\mathbf{D}} | \vec{X}_n \rangle, \tag{2.175}$$

where $\vec{X}_n$ is the n$^{\text{th}}$ eigenvector of the correlated excited state matrix and $\tilde{\mathbf{D}}$ is the representation of $\hat{D}$ in the ISR basis according to

$$\tilde{D}_{IJ} = \langle \tilde{\Psi}_I | \hat{D} | \tilde{\Psi}_J \rangle. \tag{2.176}$$

Similar to the expansion of the Hamiltonian shifted by the ground state energy (see equation 2.157), the representation of $\hat{D}$ in the ISR basis can be shifted by the ground state property D_0, which is given as

$$D_0 = \langle \Psi_0 | \hat{D} | \Psi_0 \rangle. \tag{2.177}$$

$\tilde{D}_{IJ}$ can thus be formulated as

$$\tilde{D}_{IJ} = \langle \tilde{\Psi}_I | \hat{D} - D_0 | \tilde{\Psi}_J \rangle = D_0 \delta_{IJ} + D_{IJ}. \tag{2.178}$$

Hence, it is possible to extract equations for the one-particle (transition) density matrices from the above ISR expressions for the calculation of excited state densities or one-particle properties. Furthermore, transition moments between two excited states n and m can be obtained to investigate excited state absorption phenomena using the ISR ansatz

$$T_{nm} = \langle \Psi_n | \hat{D} | \Psi_m \rangle = \langle \vec{X}_n^\dagger | \tilde{\mathbf{D}} | \vec{X}_m \rangle. \tag{2.179}$$

2.5.3 Perturbation Expansions and the Structure of the ADC Matrix

So far, I have introduced the ISR generally, which provides an elegant way to derive correlated excited states and their properties. However, the ISR secular matrix (equation 2.171) as well as the equations for the transition moments (equation 2.163) and state properties (equation 2.176) cannot be solved yet, because there are two significant problems. At first, neither the exact ground state wave function nor the exact ground state energy is known and secondly, the whole configuration space cannot be treated in an appropriate computational time. These problems can be solved by expanding the matrix $\mathbf{M}$, the transition amplitude matrix $\mathbf{F}$ and the general one-particle property matrix $\tilde{\mathbf{D}}$ using perturbation theory and the typical Møller-Plesset partitioning, which establishes the ADC approach:

$$\begin{aligned} \mathbf{M} &= \mathbf{M}^{(0)} + \mathbf{M}^{(1)} + \mathbf{M}^{(2)} + \ ... \\ \mathbf{F} &= \mathbf{F}^{(0)} + \mathbf{F}^{(1)} + \mathbf{F}^{(2)} + \ ... \\ \tilde{\mathbf{D}} &= \tilde{\mathbf{D}}^{(0)} + \tilde{\mathbf{D}}^{(1)} + \tilde{\mathbf{D}}^{(2)} + \ ... \end{aligned} \tag{2.180}$$

Expanding equation 2.171 leads to

$$M_{IJ}^{(k+l+m)} \lambda^{(k+l+m)} = \sum_{K,L} \left(S_{I,K}^{-\frac{1}{2}} \right)^{(k)} \lambda^k \left(\langle \Psi_K^\# | \hat{H} - E_0 | \Psi_L^\# \rangle \right)^{(l)} \lambda^l \left(S_{L,J}^{-\frac{1}{2}} \right)^{(m)} \lambda^m, \tag{2.181}$$

where the auxiliary index $\lambda = 1$ is employed to collect the expressions with the same order of perturbation theory k, l and m. Using this perturbation ansatz, $\mathbf{M}$ is now called ADC secular matrix and solving the ADC eigenvalue problem provides excitation energies and ADC eigenvectors that can be used to calculate transition moments and one particle properties.

For a given truncation n, the highest m-fold excitation classes (mp-mh) needed to construct the ADC matrix elements are

$$m = \frac{1}{2} n + 1, \qquad \text{n even} \tag{2.182}$$

and

$$m = \frac{1}{2}(n-1) + 1, \qquad \text{n odd.} \tag{2.183}$$

Hence, the ADC(2) and ADC(3) matrices consist of four different blocks: p-h,p-h; p-h,2p-2h; 2p-2h,p-h; 2p-2h,2p-2h. These blocks are treated in a different order of perturbation theory. The ADC(2) method is in principle available in two variants: in the strict version ADC(2)-s the matrix elements of the 2p-2h,2p-2h block are expanded only in zeroth order, while in the extended variant ADC(2)-x they are obtained in first order of perturbation theory. When beginning from an MP2 ground state, ADC(2)-s is thus derived rigorously, while ADC(2)-x is an ad hoc extension of the strict scheme. Since the description of the doubly excited amplitudes is improved due to the first order treatment of the 2p-2h,2p-2h

block, the coupling between the singles and doubles is also influenced, which commonly results in a lowering of the excitation energy.[79] However, the computational time of an ADC(2)-x calculation is increased compared to ADC(2)-s, because the 2p-2h,2p-2h block is non-diagonal in ADC(2)-x, while the doubles block in ADC(2)-s only consists of orbital energy differences. The computational effort is thus increased from the order of (M^5) to (M^6) with M being the number of basis functions. In contrast to ADC(2)-x, the third order scheme is again derived rigorously. Every block in ADC(3) is treated one order in perturbation theory higher than in ADC(2)-s, thus the 2p-2h,2p-2h blocks of ADC(3) and ADC(2)-x are equal and the computational effort of both ADC(2)-x and ADC(3) is O(N^6). The complete ADC(n) matrix for $n = 2, 3$ is illustrated in Figure 2.2.

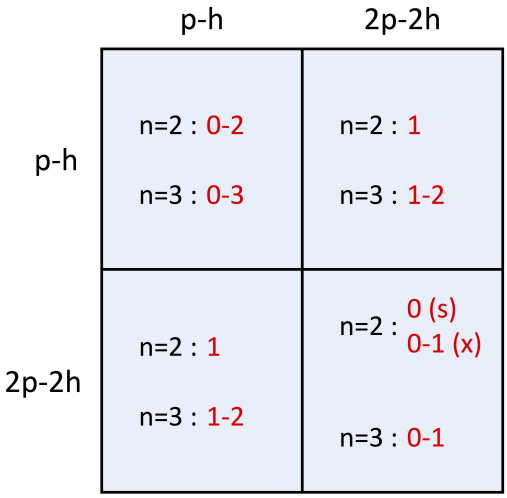

Figure 2.2: Schematic block structure of the ADC matrix $\mathbf{M}^{(n)}$ in second and third order of perturbation theory. In every block, the n^{th}-order ADC matrix is given in black, while the order in perturbation theory of the contributing terms are given in red.

Due to its construction, the ADC scheme exhibits three important inherent characteristics: at first, the ADC matrix as well as the transition amplitudes and excited state properties are size-consistent independently of the overall truncation order. Hence, the ADC scheme can be improved systematically going to higher orders. Secondly, the ADC secular matrix is Hermitian, which allows for the computation of transition moments and excited state-properties without solving a twofold eigenvalue problem, where the right and left eigenvectors of a non-Hermitian secular matrix, like the CC matrix, have to be computed separately from each other to obtain the properties. Therefore, the calculation of excited state properties and transition moments is straightforward using the ADC method, because the eigenvalue problem has to be solved only once and additional time demanding calculations are not required. Thirdly, the ADC scheme provides a compact configuration space with respect to the consistent perturbation theoretical description of the singly excited states and the truncation order n. As indicated in equations 2.182 and 2.183, the number of the m-tuply excited configurations, which are necessary to construct the ADC matrix for a truncation n, is smaller or equal to n (exception: zeroth order). Since n corresponds to the n^{th} order of perturbation theory of the singly excited configurations, the ADC approach is much compacter than for example the CI method, where n is equal to m in all cases. Triply excited configurations first appear in ADC(4),

thus ADC(3) contains only doubly excited configurations.

Besides the beneficial characteristics, the ADC scheme is well known to provide accurate and reliable results. For singlet valence-excited states, the accuracy of the excitation energies is 0.22±0.38 eV at the ADC(2)-s level, -0.70±0.37 eV at the ADC(2)-x level, and ADC(3) exhibits the largest accuracy with 0.12±0.28 eV.[81] This indicates that ADC(3) offers a well-balanced description of valence-excited state energies due to its strict derivation in third order of perturbation theory.

Since the ISR approach provides the possibility of constructing a correlated open-shell excited state via employing the unrestricted excitation operator (see equation 2.167), the derivation of an unrestricted ADC variant (UADC) is straightforward. According to the restricted approach, the unrestricted Møller-Plesset (UMP) ground state is employed as reference ground state. UADC is sensitive to spin contamination, which is typical for single-reference excited state methods, and thus the $\langle \hat{S}^2 \rangle$ value of the ground state reference has to be checked carefully. However, it could be demonstrated that $\langle \hat{S}^2 \rangle$ values below 1.25 for doublet radicals are still appropriate for UADC(2) calculations and the accuracy of UADC(2)-s is with 0.25±0.20 eV at the same level as its restricted equivalent.[82]

Finally, the expansions of the spectral amplitude matrix and the excited-state property matrix are briefly summarized. According to the ADC secular matrix, the sub-blocks of $\tilde{\mathbf{D}}$ at the second order level are expanded as

$$\begin{aligned} \tilde{\mathbf{D}}_{11} &= \tilde{\mathbf{D}}_{11}^{(0)} + \tilde{\mathbf{D}}_{11}^{(1)} + \tilde{\mathbf{D}}_{11}^{(2)} \\ \tilde{\mathbf{D}}_{12} &= \tilde{\mathbf{D}}_{12}^{(0)} + \tilde{\mathbf{D}}_{12}^{(1)} \\ \tilde{\mathbf{D}}_{22} &= \tilde{\mathbf{D}}_{22}^{(0)}. \end{aligned} \tag{2.184}$$

The p-h block of the transition amplitude matrix $\mathbf{F}$ is expanded in zeroth, first and second order, while the 2p-2h block is only expanded in first order in perturbation theory. Note that at the ADC(3) level, no algebraic expressions for the spectral amplitudes and for the ISR of a general one-particle operator are available yet. To overcome this problem, the ADC(3) excitation vectors can be contracted with the second order expressions of the spectral amplitudes or properties, respectively. In the case of the transition amplitudes, the accuracy of this approximation for valence-excited states was validated.[81] For consistency, the method for calculating oscillator strengths and excited state properties at the third order ADC level is denoted as ADC(3,2).

2.5.4 Wick's Theorem and Normal-Ordered Operators

After introducing the derivation of the ADC scheme via the ISR approach, the explicit matrix elements have to be derived. To construct the ADC matrix elements explicitly, one has to find a formalism to solve the application of the excitation operators to the ground state wave function. Wick's Theorem is an elegant approach to evaluate these matrix elements in second quantization by contracting arbitrary products of creation and annihilation operators.[177] To introduce Wick's Theorem, first normal-ordered operators have to be defined.

Normal-Ordered Operators

Normal-ordered operators are a useful tool for analyzing diagrammatic, algebraic and coupled-cluster equations in second quantization.[178] A normal-ordered product of creation and annihilation operators is one in which all creation operators lie to the left-hand side of all annihilation operators. With the help of the anti-commutation relations (see

equation 2.35), any product of creation and annihilation operators may be expressed in normal-ordered form. A normal-ordered product yields zero when applied to the true vacuum state, if the string contains any annihilation operators.

However, the excitation operators used in the ISR are not applied to the true vacuum, but to the reference ground state wave function. Hence, zero is only obtained when the annihilation operators corresponding to states unoccupied in the ground state or creation operators corresponding to states occupied in the ground state are applied to the reference. Therefore, normal-ordering of a string of annihilation and creation operators means that all annihilation operators corresponding to a virtual orbital $\hat{c}_a, \hat{c}_b, ...$ and all creation operators corresponding to an occupied orbital $\hat{c}_i^\dagger, \hat{c}_j^\dagger, ...$ lie to the right-hand side of (i.e. are applied before) all creation operators corresponding to a virtual orbital $\hat{c}_a^\dagger, \hat{c}_b^\dagger, ...$ and annihilation operators corresponding to an occupied orbital $\hat{c}_i, \hat{c}_j, ...$ within an operator string.

The following example demonstrates how an arbitrary string of operators is rearranged to its normal-ordered form by exploiting the anti-commutation relations:

$$\begin{aligned} &\text{String of creation/annihilation operators:} \quad c_i^\dagger c_a^\dagger c_b c_j \\ &\text{Rewritten in normal ordered form:} \qquad \{c_i^\dagger c_a^\dagger c_b c_j\} = -c_a^\dagger c_j c_i^\dagger c_b. \end{aligned} \tag{2.185}$$

The curly brackets $\{\}$ denote the normal-ordering. As a consequence, the expectation value of the HF ground state vanishes by applying normal ordered operators:

$$\langle \Psi^{(0)} | \{\hat{A}^\dagger \hat{B}, ...\} | \Psi^{(0)} \rangle = 0. \tag{2.186}$$

Wick's Theorem

Wick's theorem is named after Gian-Carlo Wick, who developed an elegant way to transform arbitrary products of annihilation and creation operators to sums of pairwise operator products.[177,178]

At first, the general contraction $\bullet$ of two operators is defined as

$$\hat{A}^\bullet \hat{B}^\bullet = \hat{A}\hat{B} - \{\hat{A}\hat{B}\}. \tag{2.187}$$

Wick's theorem states that a string of operators can be expressed as a sum of all of its possible normal ordered contractions:

$$\begin{aligned} \hat{A}\hat{B}\hat{C}\hat{D}\hat{E}\hat{F}... = &\{\hat{A}\hat{B}\hat{C}\hat{D}\hat{E}\hat{F}...\} \\ &+ \sum_{\substack{\text{single} \\ \text{contraction}}} \{\hat{A}^\bullet \hat{B}^\bullet \hat{C}\hat{D}\hat{E}\hat{F}...\} \\ &+ \sum_{\substack{\text{double} \\ \text{contraction}}} \{\hat{A}^\bullet \hat{B}^\bullet \hat{C}^{\bullet\bullet} \hat{D}^{\bullet\bullet} \hat{E}\hat{F}...\} \\ &+ \ ... \\ &+ \sum_{\substack{\text{full} \\ \text{contraction}}} \{\hat{A}^\bullet \hat{B}^\bullet \hat{C}^{\bullet\bullet} \hat{D}^{\bullet\bullet} \hat{E}^{\bullet\bullet\bullet} \hat{F}^{\bullet\bullet\bullet}...\}. \end{aligned} \tag{2.188}$$

Besides the fully contracted term, every other part of equation 2.187 contains uncontracted operators. Considering equation 2.186, only the fully contracted part exhibits a non zero contribution to the expectation value of the HF ground state. As a consequence, the

expectation value of the HF ground state with respect to an operator string of creation and annihilation operators is given as

$$\langle\Psi^{(0)}|\hat{A}\hat{B}\hat{C}\hat{D}\hat{E}\hat{F}...|\Psi^{(0)}\rangle = \sum_{\substack{\text{full}\\ \text{contraction}}} \langle\Psi^{(0)}|\{\hat{A}^{\bullet}\hat{B}^{\bullet}\hat{C}^{\bullet\bullet}\hat{D}^{\bullet\bullet}\hat{E}^{\bullet\bullet\bullet}\hat{F}^{\bullet\bullet\bullet}...\}|\Psi^{(0)}\rangle. \tag{2.189}$$

Hence, all operators in the string have to be eliminated via contractions to provide a non-zero result.

The contractions of all possible pairs of annihilation and creation operators can be obtained using the anti-commutator relations and equation 2.188:

1. Contractions of two annihilation operators ($\hat{c}_a^{\bullet}\hat{c}_i^{\bullet}$) or creation operators $\left(\hat{c}_a^{\dagger\bullet}\hat{c}_i^{\dagger\bullet}\right)$ are zero, because they anti-commute.

2. The contraction of an already normal-order string yields zero: $\hat{c}_i^{\dagger\bullet}\hat{c}_a^{\bullet} = \hat{c}_i^{\dagger}\hat{c}_a - \{\hat{c}_i^{\dagger}\hat{c}_a\} = 0$.

3. If the string is not normal-ordered, the order must be reversed: $\hat{c}_i^{\dagger\bullet}\hat{c}_q^{\bullet} = \hat{c}_i^{\dagger}\hat{c}_q - \{\hat{c}_i^{\dagger}\hat{c}_q\} = \hat{c}_i^{\dagger}\hat{c}_q + \hat{c}_q\hat{c}_i^{\dagger}$. Since the anti-commutator is zero unless $i = q$, the contraction yields $\hat{c}_i^{\dagger\bullet}\hat{c}_j^{\bullet} = \delta_{ij}$ and with the same reason $\hat{c}_a^{\bullet}\hat{c}_b^{\dagger\bullet} = \delta_{ab}$.

Hence, there are only two contractions $\hat{c}_i^{\dagger\bullet}\hat{c}_j^{\bullet} = \delta_{ij}$ and $\hat{c}_a^{\bullet}\hat{c}_b^{\dagger\bullet} = \delta_{ab}$ that give non-zero contributions. All possible pairwise contractions of creation and annihilation operators are summarized in Table 2.2.

Table 2.2: Summary of all possible pairwise contractions of creation and annihilation operators due to the anti-commutator relations. The $\bullet$ symbol is omitted in this Table.

$\hat{c}_p\hat{c}_q$	$\hat{c}_p^{\dagger}\hat{c}_q$	$\hat{c}_p\hat{c}_q^{\dagger}$	$\hat{c}_p^{\dagger}\hat{c}_q^{\dagger}$
$\hat{c}_i\hat{c}_j = 0$	$\mathbf{\hat{c}_i^{\dagger}\hat{c}_j = \delta_{ij}}$	$\hat{c}_i\hat{c}_j^{\dagger} = 0$	$\hat{c}_i^{\dagger}\hat{c}_j^{\dagger} = 0$
$\hat{c}_i\hat{c}_a = 0$	$\hat{c}_i^{\dagger}\hat{c}_a = 0$	$\hat{c}_i\hat{c}_a^{\dagger} = 0$	$\hat{c}_i^{\dagger}\hat{c}_a^{\dagger} = 0$
$\hat{c}_a\hat{c}_i = 0$	$\hat{c}_a^{\dagger}\hat{c}_i = 0$	$\hat{c}_a\hat{c}_i^{\dagger} = 0$	$\hat{c}_a^{\dagger}\hat{c}_i^{\dagger} = 0$
$\hat{c}_a\hat{c}_b = 0$	$\hat{c}_a^{\dagger}\hat{c}_b = 0$	$\mathbf{\hat{c}_a\hat{c}_b^{\dagger} = \delta_{ab}}$	$\hat{c}_a^{\dagger}\hat{c}_b^{\dagger} = 0$

2.5.5 Explicit Derivation of the ADC Matrix Elements

With the knowledge about Wick's Theorem it is now possible to solve the ADC secular matrix (equation 2.181) and explicitly derive the ADC matrix elements and working equations. In the following discussion, I explain this procedure generally using selected examples by analyzing the different contributions to M_{IJ}, i.e. the overlap matrix and the shifted Hamilton matrix up to first order in perturbation theory. Since the ground state reference wave function is expanded as a perturbation series based on MP, certain expressions of MP2, which were derived in Chapter 2.2.3, are needed for the construction of the ADC matrix equations. These terms are summarized in Table 2.3.

Construction of the Overlap Matrix S

At first, the equations for the overlap matrix **S** are derived. Using the definition in equation 2.170 and applying the perturbation expansions, the overlap between two states I and J is

Table 2.3: Summary of the MP2 ground state terms, which are used in this chapter to derive the ADC matrix expressions. Their origin is explained in chapter 2.2.3.

$$\hat{H} = \hat{f} + \hat{U} = \hat{H}^{(0)} + \hat{H}^{(1)}$$

$$\hat{H}^{(0)} = \sum_p \epsilon_p c_p^\dagger c_p$$

$$\hat{H}^{(1)} = \hat{H} - \hat{f} = -\sum_{pq}\sum_k \langle pk||qk\rangle c_p^\dagger c_q + \tfrac{1}{2}\sum_{pqrs}\langle pq|rs\rangle c_p^\dagger c_q^\dagger c_s c_r$$

$$|\Psi_0^{(0)}\rangle = |\Psi_0^{\mathrm{HF}}\rangle$$

$$E_0^{(0)} = \langle\Psi_0^{(0)}|\hat{H}^{(0)}|\Psi_0^{(0)}\rangle = \sum_i \epsilon_i$$

$$E_0^{(1)} = \langle\Psi_0^{(0)}|\hat{H}^{(1)}|\Psi_0^{(0)}\rangle = -\tfrac{1}{2}\sum_{ij}\langle ij||ij\rangle$$

defined as

$$\begin{aligned} S_{I,J} =& \sum_n \lambda^{(n)} S_{I,J}^{(n)} = \sum_{k,l} \lambda^{(k+l)} \langle\Psi_0^{(k)}|\hat{C}_I^\dagger \hat{C}_J|\Psi_0^{(l)}\rangle \\ &- \sum_{k,l,m,n} \lambda^{(k+l+m+n)} \langle\Psi_0^{(k)}|\hat{C}_I^\dagger|\Psi_0^{(l)}\rangle\langle\Psi_0^{(m)}|\hat{C}_J|\Psi_0^{(n)}\rangle. \end{aligned} \tag{2.190}$$

Accordingly, the ground state wave function is described with a perturbation ansatz:

$$|\Psi_0\rangle = \sum_{n=1}^{\infty} |\Psi_0^{(n)}\rangle. \tag{2.191}$$

The $S_{I,J}$ result in zeroth order is then given as

$$\begin{aligned} S_{I,J}^{(0)} &= \langle\Psi_0^{(0)}|\hat{C}_I^\dagger \hat{C}_J|\Psi_0^{(0)}\rangle - \langle\Psi_0^{(0)}|\hat{C}_I^\dagger|\Psi_0^{(0)}\rangle\langle\Psi_0^{(0)}|\hat{C}_J|\Psi_0^{(0)}\rangle \\ &= \langle\Psi_0^{(0)}|\hat{C}_I^\dagger \hat{C}_J|\Psi_0^{(0)}\rangle \\ &= \delta_{IJ}. \end{aligned} \tag{2.192}$$

Here, the second term vanishes, because $\hat{C}_I^\dagger$ is normal-ordered and the first term is only non zero if $I = J$. The same result can be obtained using Wick's theorem as shown in equation 2.193 as an example for the p-h,p-h block:

$$\begin{aligned} S_{ai,bj}^{(0)} &= \langle\Psi_0^{(0)}|c_i^\dagger c_a c_b^\dagger c_j|\Psi_0^{(0)}\rangle - \langle\Psi_0^{(0)}|\{c_i^\dagger c_a\}|\Psi_0^{(0)}\rangle\langle\Psi_0^{(0)}|c_b^\dagger c_j|\Psi_0^{(0)}\rangle \\ &= \langle\Psi_0^{(0)}|c_i^\dagger c_a c_b^\dagger c_j|\Psi_0^{(0)}\rangle \\ &= \langle\Psi_0^{(0)}|\{c_i^{\dagger\bullet\bullet} c_a^\bullet c_b^{\dagger\bullet} c_j^{\bullet\bullet}\}|\Psi_0^{(0)}\rangle \\ &= \langle\Psi_0^{(0)}|\delta_{ab}\delta_{ij}|\Psi_0^{(0)}\rangle = \delta_{ab}\delta_{ij}\langle\Psi_0^{(0)}|\Psi_0^{(0)}\rangle \\ &= \delta_{ab}\delta_{ij}. \end{aligned} \tag{2.193}$$

To derive the expression for the first order overlap matrix, the relation

$$\langle\Psi_0^{(0)}|\{\hat{C}_I^\dagger\}|\Psi_0^{(n)}\rangle = \langle\Psi_0^{(n)}|\{\hat{C}_I^\dagger\}|\Psi_0^{(0)}\rangle = 0 \tag{2.194}$$

is needed. This expression is zero, because the normal-ordered operator acting on $\Psi_0^{(0)}$ yields zero. With the help of equation 2.194 and equation 2.192, the first order expression of $S_{I,J}$ can be formulated as

$$\begin{aligned} S_{I,J}^{(1)} &= \langle \Psi_0^{(1)} | \hat{C}_I^\dagger \hat{C}_J | \Psi_0^{(0)} \rangle + \langle \Psi_0^{(0)} | \hat{C}_I^\dagger \hat{C}_J | \Psi_0^{(1)} \rangle \\ &\quad - \langle \Psi_0^{(1)} | \hat{C}_I^\dagger | \Psi_0^{(0)} \rangle \langle \Psi_0^{(0)} | \hat{C}_J | \Psi_0^{(0)} \rangle - \langle \Psi_0^{(0)} | \hat{C}_I^\dagger | \Psi_0^{(1)} \rangle \langle \Psi_0^{(0)} | \hat{C}_J | \Psi_0^{(0)} \rangle \\ &\quad - \langle \Psi_0^{(0)} | \hat{C}_I^\dagger | \Psi_0^{(0)} \rangle \langle \Psi_0^{(1)} | \hat{C}_J | \Psi_0^{(0)} \rangle - \langle \Psi_0^{(0)} | \hat{C}_I^\dagger | \Psi_0^{(0)} \rangle \langle \Psi_0^{(0)} | \hat{C}_J | \Psi_0^{(1)} \rangle \\ &= \langle \Psi_0^{(1)} | \hat{C}_I^\dagger \hat{C}_J | \Psi_0^{(0)} \rangle + \langle \Psi_0^{(0)} | \hat{C}_I^\dagger \hat{C}_J | \Psi_0^{(1)} \rangle \\ &= \langle \Psi_0^{(1)} | \delta_{IJ} | \Psi_0^{(0)} \rangle + \langle \Psi_0^{(0)} | \delta_{IJ} | \Psi_0^{(1)} \rangle \\ &= 0. \end{aligned} \tag{2.195}$$

Via the same procedure, the second order term of $S_{I,J}$ can be derived. The final result is given as

$$S_{I,J}^{(2)} = \langle \Psi_0^{(1)} | \hat{C}_I^\dagger \hat{C}_J | \Psi_0^{(1)} \rangle. \tag{2.196}$$

Note that $S_{I,J}^{(2)}$ is only valid for the single excitations, i.e. the p-h,p-h block contributions. Since the first order contribution vanishes, the elements of the overlap matrix can be written as

$$S_{I,J} = \delta_{IJ} + S_{I,J}^{(2)} + O(3), \tag{2.197}$$

where $O(3)$ contains all third and higher order contributions.

As the next step, $\mathbf{S}$ has to be transformed to $\mathbf{S}^{-\frac{1}{2}}$. This can be achieved via developing $\mathbf{S}^{-\frac{1}{2}}$ as a Taylor series. In principle $\mathbf{S}$ has the form

$$\mathbf{S}(\mathbf{x}) = \mathbb{1} + \mathbf{x} \qquad \text{with} \quad \mathbf{x} = \mathbf{S}^{(2)} + \mathbf{O}(3). \tag{2.198}$$

The Taylor series is then given as

$$\begin{aligned} \mathbf{S}^{-\frac{1}{2}}(\mathbf{x}) &= \mathbf{S}^{-\frac{1}{2}}(0) + \left(\mathbf{S}^{-\frac{1}{2}}(0)\right)' (\mathbf{x} - 0) + \ ... \\ &= \mathbb{1} - \frac{1}{2}\mathbf{x} \\ &= \mathbb{1} - \frac{1}{2}\left(\mathbf{S}^{(2)} + \mathbf{O}(3)\right) \end{aligned} \tag{2.199}$$

and finally, $S_{I,J}^{-\frac{1}{2}}$ is formulated as

$$S_{I,J}^{-\frac{1}{2}} = \delta_{IJ} - \frac{1}{2}\left(S_{I,J}^{(2)} + O(3)\right). \tag{2.200}$$

Expansion of the Hamilton Matrix

After deriving the terms for the overlap matrix $\mathbf{S}$, the matrix representation of the shifted Hamiltonian is investigated. With the knowledge about normal-ordered operators acting on the HF ground state reference wave function (see equations 2.186 and 2.194), the matrix of the shifted Hamiltonian (equation 2.172) is simplified to

$$\langle \Psi_I^\# | \hat{H} - E_0 | \Psi_J^\# \rangle = \langle \Psi_0 | \hat{C}_I^\dagger \left(\hat{H} - E_0\right) \hat{C}_J | \Psi_0 \rangle. \tag{2.201}$$

After expanding the expression using perturbation theory, the shifted Hamilton matrices up to second order are given as

$$\begin{aligned}
\left(\langle\Psi_I^{\#}|\hat{H}-E_0|\Psi_J^{\#}\rangle\right)^{(0)} &= \langle\Psi_0^{(0)}|\hat{C}_I^{\dagger}\hat{H}^{(0)}\hat{C}_J|\Psi_0^{(0)}\rangle - \langle\Psi_0^{(0)}|\hat{C}_I^{\dagger}E_0^{(0)}\hat{C}_J|\Psi_0^{(0)}\rangle \\
\left(\langle\Psi_I^{\#}|\hat{H}-E_0|\Psi_J^{\#}\rangle\right)^{(1)} &= \langle\Psi_0^{(0)}|\hat{C}_I^{\dagger}\hat{H}^{(1)}\hat{C}_J|\Psi_0^{(0)}\rangle - \langle\Psi_0^{(0)}|\hat{C}_I^{\dagger}E_0^{(1)}\hat{C}_J|\Psi_0^{(0)}\rangle \\
\left(\langle\Psi_I^{\#}|\hat{H}-E_0|\Psi_J^{\#}\rangle\right)^{(2)} &= \langle\Psi_0^{(1)}|\hat{C}_I^{\dagger}\hat{H}^{(1)}\hat{C}_J|\Psi_0^{(0)}\rangle + \langle\Psi_0^{(0)}|\hat{C}_I^{\dagger}\hat{H}^{(1)}\hat{C}_J|\Psi_0^{(1)}\rangle \\
&\quad + \langle\Psi_0^{(1)}|\hat{C}_I^{\dagger}\hat{H}^{(0)}\hat{C}_J|\Psi_0^{(1)}\rangle - \langle\Psi_0^{(0)}|\hat{C}_I^{\dagger}E_0^{(2)}\hat{C}_J|\Psi_0^{(0)}\rangle \\
&\quad - \langle\Psi_0^{(1)}|\hat{C}_I^{\dagger}E_0^{(0)}\hat{C}_J|\Psi_0^{(1)}\rangle.
\end{aligned} \tag{2.202}$$

Example: Detailed Derivation of the ADC(1) Matrix

Now, all prerequisites to derive the final ADC matrix equations are fulfilled. As an example, the zeroth and first order terms of the p-h,p-h block, which correspond to ADC(1) matrix, are evaluated.

1. Zeroth order p-h,p-h block:

Let me start with the evaluation of the zeroth order Hamilton matrix. Including the explicit expressions of the excitation operators leads to

$$\begin{aligned}
\langle\Psi_0^{(0)}|\hat{C}_I^{\dagger}\hat{H}^{(0)}\hat{C}_J|\Psi_0^{(0)}\rangle &= \langle\Psi_0^{(0)}|c_i^{\dagger}c_a\hat{H}^{(0)}c_b^{\dagger}c_j|\Psi_0^{(0)}\rangle \\
&= \sum_p \epsilon_p\langle\Psi_0^{(0)}|c_i^{\dagger}c_a c_p^{\dagger}c_p c_b^{\dagger}c_j|\Psi_0^{(0)}\rangle.
\end{aligned} \tag{2.203}$$

Next, the string of operators $c_i^{\dagger}c_a c_p^{\dagger}c_p c_b^{\dagger}c_j$ has to be evaluated exploiting Wick's theorem:

$$\begin{aligned}
c_i^{\dagger}c_a c_p^{\dagger}c_p c_b^{\dagger}c_j &= \sum_{\substack{\text{full}\\ \text{contraction}}} \{c_i^{\dagger}c_a c_p^{\dagger}c_p c_b^{\dagger}c_j\} \\
&= \{c_i^{\dagger\bullet}c_a^{\bullet\bullet}c_p^{\dagger\bullet\bullet}c_p^{\bullet\bullet}c_b^{\dagger\bullet\bullet}c_j^{\bullet}\} + \{c_i^{\dagger\bullet}c_a^{\bullet\bullet}c_p^{\dagger\bullet\bullet}c_p^{\bullet\bullet}c_b^{\dagger\bullet\bullet}c_j^{\bullet}\} \\
&\quad - \{c_i^{\dagger\bullet}c_a^{\bullet\bullet}c_p^{\dagger\bullet\bullet}c_p^{\bullet}c_b^{\dagger\bullet\bullet}c_j^{\bullet\bullet}\} \\
&= \delta_{ij}\delta_{ab}\delta_{pp} + \delta_{ij}\delta_{ap}\delta_{pb} - \delta_{ip}\delta_{ab}\delta_{pj} \\
&= A + B + C.
\end{aligned} \tag{2.204}$$

Due to the definition of normal-ordered operators, p in part A must correspond to the occupied orbital space to be nonzero. The terms B and C are only nonzero if p corresponds to the occupied orbital space (C) and to the virtual orbital space (B), respectively. Since $E_0^{(0)} = \sum_i \epsilon_i$, this results in

$$\begin{aligned}
\sum_p \epsilon_p\langle\Psi_0^{(0)}|c_i^{\dagger}c_a c_p^{\dagger}c_p c_b^{\dagger}c_j|\Psi_0^{(0)}\rangle &= \sum_p \epsilon_p\langle\Psi_0^{(0)}|A+B+C|\Psi_0^{(0)}\rangle \\
&= \left(\sum_{p_i}\epsilon_{p_i}\delta_{ij}\delta_{ab}\right) + \epsilon_a\delta_{ij}\delta_{ab} - \epsilon_i\delta_{ij}\delta_{ab} \\
&= \delta_{ij}\delta_{ab}\left(E_0^{(0)} + \epsilon_a - \epsilon_i\right).
\end{aligned} \tag{2.205}$$

Analogously, the expectation value of the zeroth order energy can be formulated as

$$\langle\Psi_0^{(0)}|\hat{C}_I^\dagger E_0^{(0)}\hat{C}_J|\Psi_0^{(0)}\rangle = \langle\Psi_0^{(0)}|c_i^\dagger c_a E^{(0)} c_b^\dagger c_j|\Psi_0^{(0)}\rangle = \delta_{ij}\delta_{ab}E_0^{(0)}. \tag{2.206}$$

Finally, the whole matrix element for the zeroth order p-h,p-h block is given as

$$\begin{aligned} M_{ai,bj}^{(0)} &= \sum_{ckdl}\left(S_{ai,ck}^{-\frac{1}{2}}\right)^{(0)}\left(\langle\Psi_{ck}^{\#}|\hat{H}-E_0|\Psi_{dl}^{\#}\rangle\right)^{(0)}\left(S_{dl,bj}^{-\frac{1}{2}}\right)^{(0)} \\ &= \sum_{ckdl}\delta_{ac}\delta_{ik}\left(\langle\Psi_0^{(0)}|c_i^\dagger c_a\hat{H}^{(0)}c_b^\dagger c_j|\Psi_0^{(0)}\rangle - \langle\Psi_0^{(0)}|c_i^\dagger c_a E_0^{(0)}c_b^\dagger c_j|\Psi_0^{(0)}\rangle\right)\delta_{bd}\delta_{jl} \\ &= \delta_{ij}\delta_{ab}\left(E_0^{(0)}+\epsilon_a-\epsilon_i\right) - \delta_{ij}\delta_{ab}E_0^{(0)} \\ &= \delta_{ij}\delta_{ab}\left(\epsilon_a-\epsilon_i\right). \end{aligned} \tag{2.207}$$

2. First order p-h,p-h block:

The evaluation of the first order terms of the p-h,p-h block is more complicated. Starting with the first order Hamilton matrix

$$\begin{aligned} \langle\Psi_0^{(0)}|\hat{C}_I^\dagger\hat{H}^{(1)}\hat{C}_J|\Psi_0^{(0)}\rangle &= \langle\Psi_0^{(0)}|c_i^\dagger c_a\hat{H}^{(1)}c_b^\dagger c_j|\Psi_0^{(0)}\rangle \\ &= m_A^{(1)} + m_B^{(1)} \\ &= -\sum_{pq}\sum_k\langle pk||qk\rangle\langle\Psi_0^{(0)}|c_i^\dagger c_a c_p^\dagger c_q c_b^\dagger c_j|\Psi_0^{(0)}\rangle \\ &\quad + \frac{1}{2}\sum_{pqrs}\langle pq|rs\rangle\langle\Psi_0^{(0)}|c_i^\dagger c_a c_p^\dagger c_q^\dagger c_r c_s c_b^\dagger c_j|\Psi_0^{(0)}\rangle, \end{aligned} \tag{2.208}$$

it is clearer to divide this expression into two parts, i.e. $m_A^{(1)}$ and $m_B^{(1)}$. The full contraction of the operator string of $m_A^{(1)}$ is given as

$$\begin{aligned} c_i^\dagger c_a c_p^\dagger c_q c_b^\dagger c_j &= \sum_{\substack{\text{full}\\ \text{contraction}}}\{c_i^\dagger c_a c_p^\dagger c_q c_b^\dagger c_j\} \\ &= \{c_i^{\dagger\bullet}c_a^{\bullet\bullet}c_p^{\dagger\bullet\bullet\bullet}c_q^{\bullet\bullet\bullet}c_b^{\dagger\bullet\bullet}c_j^{\bullet}\} + \{c_i^{\dagger\bullet}c_a^{\bullet\bullet}c_p^{\dagger\bullet\bullet}c_q^{\bullet\bullet\bullet}c_b^{\dagger\bullet\bullet\bullet}c_j^{\bullet}\} \\ &\quad - \{c_i^{\dagger\bullet}c_a^{\bullet\bullet}c_p^{\dagger\bullet\bullet\bullet}c_q^{\bullet}c_b^{\dagger\bullet\bullet}c_j^{\bullet\bullet\bullet}\} \\ &= \delta_{ij}\delta_{ab}\delta_{pq} + \delta_{ij}\delta_{ap}\delta_{qb} - \delta_{iq}\delta_{ab}\delta_{pj} \\ &= A + B + C. \end{aligned} \tag{2.209}$$

Again, the terms A and C exhibit only a nonzero contribution if p and q belong to the occupied orbital space and in B, p and q must correspond to the virtual orbital space. Furthermore, p must be equal to q in term A. Considering these conditions, $m_A^{(1)}$ is finally

given as

$$\begin{aligned} m_A^{(1)} &= -\sum_{pq}\sum_{k}\langle pk||qk\rangle\langle\Psi_0^{(0)}|c_i^\dagger c_a c_p^\dagger c_q c_b^\dagger c_j|\Psi_0^{(0)}\rangle \\ &= -\sum_{pq}\sum_{k}\langle pk||qk\rangle\langle\Psi_0^{(0)}|A+B+C|\Psi_0^{(0)}\rangle \\ &= -\sum_{ik}\langle ik||ik\rangle\delta_{ij}\delta_{ab} - \sum_{abk}\langle ak||bk\rangle\delta_{ij} + \sum_{ijk}\langle jk||ik\rangle\delta_{ab} \\ &= 2E_0^{(1)}\delta_{ab}\delta_{ij} - \sum_{abk}\langle ak||bk\rangle\delta_{ij} + \sum_{ijk}\langle jk||ik\rangle\delta_{ab}. \end{aligned} \tag{2.210}$$

The full contraction of the operator string of $m_B^{(1)}$ results in 14 terms. Here, only the final delta terms are listed below:

$$c_i^\dagger c_a c_p^\dagger c_q^\dagger c_r c_s c_b^\dagger c_j = \sum_{\substack{\text{full}\\ \text{contraction}}} \{c_i^\dagger c_a c_p^\dagger c_q^\dagger c_r c_s c_b^\dagger c_j\} = A+B+C+D \tag{2.211}$$

$$A = \delta_{is}\delta_{aq}\delta_{pj}\delta_{rb} - \delta_{is}\delta_{ap}\delta_{qj}\delta_{rb} + \delta_{ir}\delta_{ap}\delta_{qj}\delta_{sb} - \delta_{ir}\delta_{aq}\delta_{pj}\delta_{sb} \tag{2.212}$$

$$B = \delta_{is}\delta_{ab}\delta_{pj}\delta_{qr} - \delta_{is}\delta_{ab}\delta_{pr}\delta_{qj} + \delta_{ir}\delta_{ab}\delta_{ps}\delta_{qj} - \delta_{ir}\delta_{ab}\delta_{pj}\delta_{qs} \tag{2.213}$$

$$C = \delta_{ij}\delta_{ap}\delta_{qs}\delta_{rb} - \delta_{ij}\delta_{ap}\delta_{qr}\delta_{sb} - \delta_{ij}\delta_{aq}\delta_{ps}\delta_{rb} + \delta_{ij}\delta_{aq}\delta_{pr}\delta_{sb} \tag{2.214}$$

$$D = \delta_{ij}\delta_{ab}\delta_{pr}\delta_{qs} - \delta_{ij}\delta_{ab}\delta_{ps}\delta_{qr}. \tag{2.215}$$

Similar to the other examples above, every delta term and the normal-ordered operators define a certain condition for p, q, r and s. For simplification, $m_B^{(1)}$ is split into four parts:

$$\begin{aligned} m_B^{(1)} &= \frac{1}{2}\sum_{pqrs}\langle pq|rs\rangle\langle\Psi_0^{(0)}|A+B+C+D|\Psi_0^{(0)}\rangle \\ &= m_{B(A)}^{(1)} + m_{B(B)}^{(1)} + m_{B(C)}^{(1)} + m_{B(D)}^{(1)}. \end{aligned} \tag{2.216}$$

The $m_{B(X)}^{(1)}$ terms can be evaluated using the definition of an antisymmetrized two-electron integral $\langle pq||rs\rangle = \langle pq|rs\rangle - \langle pq|sr\rangle$ and exploiting the relations

$$\langle pq||rs\rangle = \langle rs||pq\rangle^\star \tag{2.217}$$

and

$$\langle pq|rs\rangle = \langle qp||sr\rangle. \tag{2.218}$$

Since the orbitals are real, the expressions of $m_{B(X)}^{(1)}$ can be summarized to

$$\begin{aligned} m_{B(A)}^{(1)} &= \frac{1}{2}\sum_{abij}\left(\langle ja|bi\rangle - \langle aj|bi\rangle + \langle aj|ib\rangle - \langle ja|ib\rangle\right) \\ &= \frac{1}{2}\sum_{abij}\left(\langle ja||bi\rangle + \langle aj||ib\rangle\right) = -\sum_{abij}\langle aj||bi\rangle \end{aligned} \tag{2.219}$$

$$\begin{aligned} m_{B(B)}^{(1)} &= \frac{1}{2}\sum_{ijk}\delta_{ab}\left(\langle jk|ki\rangle - \langle kj|ki\rangle + \langle kj|ik\rangle - \langle jk|ik\rangle\right) \\ &= \frac{1}{2}\sum_{ijk}\left(\langle jk||ki\rangle + \langle kj||ik\rangle\right)\delta_{ab} = -\sum_{ijk}\langle jk||ik\rangle\delta_{ab} \end{aligned} \tag{2.220}$$

$$\begin{aligned} m^{(1)}_{B(C)} &= \frac{1}{2}\sum_{abk}\delta_{ij}\left(\langle ak|bk\rangle - \langle ak|kb\rangle - \langle ka|bk\rangle + \langle ka|kb\rangle\right) \\ &= \frac{1}{2}\sum_{abk}\left(\langle ak||bk\rangle + \langle ka||kb\rangle\right)\delta_{ij} = \sum_{abk}\langle ak||bk\rangle\delta_{ij} \end{aligned} \tag{2.221}$$

$$\begin{aligned} m^{(1)}_{B(D)} &= \frac{1}{2}\sum_{kl}\delta_{ab}\delta_{ij}\left(\langle kl|kl\rangle - \langle kl|lk\rangle\right) \\ &= \frac{1}{2}\sum_{kl}\langle kl||kl\rangle\delta_{ab}\delta_{ij} = -E^{(1)}_0\delta_{ab}\delta_{ij}. \end{aligned} \tag{2.222}$$

Summing up all $m^{(1)}_{B(X)}$ terms yields

$$\begin{aligned} \langle\Psi^{(0)}_0|c^\dagger_i c_a \hat{H}^{(1)} c^\dagger_b c_j|\Psi^{(0)}_0\rangle &= m^{(1)}_A + m^{(1)}_B \\ &= 2E^{(1)}_0\delta_{ab}\delta_{ij} - \sum_{abk}\langle ak||bk\rangle\delta_{ij} + \sum_{ijk}\langle jk||ik\rangle\delta_{ab} \\ &\quad - \sum_{abij}\langle aj||bi\rangle - \sum_{ijk}\langle jk||ik\rangle\delta_{ab} + \sum_{abk}\langle ak||bk\rangle\delta_{ij} \\ &\quad - E^{(1)}_0\delta_{ab}\delta_{ij} \\ &= E^{(1)}_0\delta_{ab}\delta_{ij} - \sum_{abij}\langle aj||bi\rangle. \end{aligned} \tag{2.223}$$

Finally, the ultimate matrix element for the first order p-h,p-h block is

$$\begin{aligned} M^{(1)}_{ai,bj} &= \sum_{ckdl}\left(S^{-\frac{1}{2}}_{ai,ck}\right)^{(0)}\left(\langle\Psi^{\#}_{ck}|\hat{H} - E_0|\Psi^{\#}_{dl}\rangle\right)^{(1)}\left(S^{-\frac{1}{2}}_{dl,bj}\right)^{(0)} \\ &= \sum_{ckdl}\delta_{ac}\delta_{ik}\left(\langle\Psi^{(0)}_0|c^\dagger_i c_a\hat{H}^{(1)}c^\dagger_b c_j|\Psi^{(0)}_0\rangle - \langle\Psi^{(0)}_0|c^\dagger_i c_a E^{(1)}_0 c^\dagger_b c_j|\Psi^{(0)}_0\rangle\right)\delta_{bd}\delta_{jl} \\ &= \delta_{ij}\delta_{ab}E^{(1)}_0 - \langle aj||bi\rangle - \delta_{ij}\delta_{ab}E^{(1)}_0 \\ &= -\langle aj||bi\rangle. \end{aligned} \tag{2.224}$$

3. Summary:

Summarizing the final ADC(0) and ADC(1) matrix elements yields

$$M^{(ADC(0))}_{ai,bj} = \delta_{ij}\delta_{ab}\left(\epsilon_a - \epsilon_i\right) \tag{2.225}$$

$$M^{(ADC(1))}_{ai,bj} = \delta_{ij}\delta_{ab}\left(\epsilon_a - \epsilon_i\right) - \langle aj||bi\rangle. \tag{2.226}$$

Hence, ADC(0) just provides the orbital energy difference, while ADC(1) contains an antisymmetrized two-electron integral, which is identical to the CIS expression. Obviously, double excitations are first treated at the ADC(2) level. The matrix elements at the ADC(2) and ADC(3) levels can be evaluated according to the procedures that were explained exemplarily for the ADC(1) matrix. In the same manner, the final equations of the transition moments and ISR properties can be derived, too. The final results of the ADC working equations up to third order in perturbation theory as well as the respective spectral amplitude and ISR property equations are given in chapter 2.5.7.

2.5.6 Exploiting the Core-Valence Separation Approximation to Calculate Core-Excited States

So far, the general ADC scheme has been derived and introduced. To obtain the vertical excitation energies, the ADC eigenvalue problem (equation 2.158) has to be solved via diagonalization of the ADC secular matrix (equation 2.181). Regarding ADC(2)-x and ADC(3), where only two excitation classes are included, the size of the ADC matrix increases with $(OV)^6$, where O and V are the numbers of occupied and virtual orbitals, respectively. Considering the demand of being as exact as possible and thus using preferably large basis sets, it is computationally too expensive and inefficient to build and diagonalize the whole ADC secular matrix for systems larger than 10 electrons. However, the focus of interest often lies on the energetically lowest excited states of the spectrum, i.e. the valence excited states in the UV region. Therefore, typical iterative diagonalization algorithms like the Davidson method[138] are usually employed to solve such large eigenvalue problems. These schemes are designed to yield the lowest eigenvalues of interest without computing the whole matrix.

As mentioned before, core-excited electronic states are located in the high-energy X-ray region of the electronic spectrum, thus calculations of XAS spectra with the ADC method are challenging. A solution to this dilemma would be the direct diagonalization of the core-excited state space, but the couplings between the core-excited and underlying valence-excited states prevent this ansatz (see Figure 2.3). However, these couplings

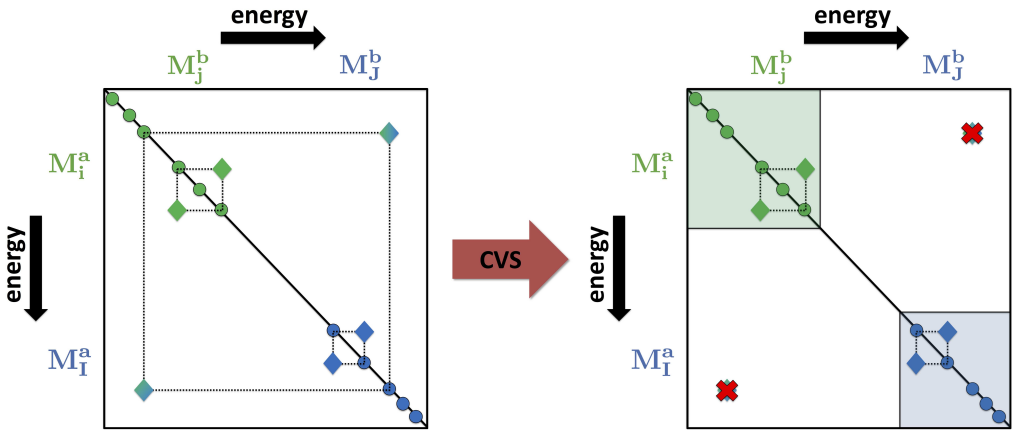

Figure 2.3: Schematic illustration of the CVS approximation acting on the p-h,p-h block of the ADC matrix. Valence (M_i^a and M_j^b, green) and core (M_I^a and M_J^b, blue) excited configurations are ordered by energy and the rhombi represent couplings between the excited configurations. Due to the CVS approximation the couplings between the core-excitation and valence-excitation spaces, which prevent the direct diagonalization of the core-excited space, are neglected. Hence, the spaces are decoupled from each other and the core-excited states can be computed directly.

are very small, because there is an important characteristic of core orbitals: they are strongly localized in space and thus tightly contracted due to the Coulomb attraction of the nucleus. As a consequence, the probability of the propagation of an induced hole from a core orbital ψ_I to another ψ_J is almost zero. In the case of degenerate core orbitals, e.g. due to point group symmetry, the situation is described by linear combinations of these core orbitals resulting in a basis of strongly localized orbitals. Furthermore, the core

orbitals are energetically well separated from the valence orbitals, leading to a large energy difference between the core- and valence-excited states, too. Based on these matters of fact, the core-valence separation approximation (CVS) was developed in the early 1980s.[44,45] Within this approximation, it is assumed that the full electronic Hamiltonian can be split into a core $\hat{H}_c$ and valence $\hat{H}_v$ part as

$$\hat{H}_{cv} = \hat{H}_c + \hat{H}_v + \hat{S}_{cv}, \tag{2.227}$$

where $\hat{S}_{cv}$ is the spin-interaction term, which is not discussed in this context. To construct the core-valence separated Hamiltonian $\hat{H}_{cv}$, one has to omit certain terms in the full Hamiltonian that contain a different number of core creation $\hat{c}_c^\dagger$ and core annihilation operators $\hat{c}_c$. $\hat{H}_c$ and valence $\hat{H}_v$ are then given as

$$\hat{H}_c = \epsilon_c \hat{c}_c^\dagger \hat{c}_c + \langle cc|cc\rangle \hat{c}_c^\dagger \hat{c}_c^\dagger \hat{c}_c \hat{c}_c - \sum_k \langle ck||ck\rangle \hat{c}_c^\dagger \hat{c}_c \tag{2.228}$$

and

$$\hat{H}_v = \sum_p \epsilon_p \hat{c}_p^\dagger \hat{c}_p + \frac{1}{2} \sum_{pqrs} \langle pq|rs\rangle \hat{c}_p^\dagger \hat{c}_q^\dagger \hat{c}_r \hat{c}_s - \sum_{pq} \left(\sum_k \langle pk||qk\rangle \hat{c}_p^\dagger \hat{c}_q \right). \tag{2.229}$$

Therefore, $\hat{H}_c$ only contains interactions of the cores, while the valence term $\hat{H}_v$ includes all other interactions, where p, q, r and s are valence occupied or virtual orbitals without considering core orbitals, which are denoted as c.

Considering the CVS approximation, the following types of Coulomb integrals that describe the interaction between core and valence orbitals practically vanish and can thus be neglected:

$$\begin{aligned} \langle Ip|qr\rangle = \langle pI|qr\rangle = \langle pq|Ir\rangle = \langle pq|rI\rangle = 0 \\ \langle IJ|pq\rangle = \langle pq|IJ\rangle = 0 \\ \langle IJ|Kp\rangle = \langle IJ|pK\rangle = \langle Ip|JK\rangle = \langle pI|JK\rangle = 0, \end{aligned} \tag{2.230}$$

where capital letters I, J, K refer to core orbitals and small letters p, q, r to valence occupied or virtual orbitals.[100]

In combination with the ADC scheme, the resulting CVS-ADC approach provides an intuitive way to calculate core-excited states. As shown in Figure 2.3, the CVS approximation leads to a complete decoupling of the core excitations from the valence excitation space by discarding the couplings between them. In the p-h configurations, the index of the occupied orbital has to be restricted to a core orbital. In the case of the coupling and 2p-2h configurations, one of the occupied indices has to correspond to a core orbital, while the other is restricted to the remaining valence occupied space. Hence, only matrix elements corresponding to $M_{Ia,Kc}$ (p-h,p-h block), $M_{Ijab,Kc}$ (2p-2h,p-h block), $M_{Ia,Klcd}$ (p-h,2p-2h block) and $M_{Ijab,Klcd}$ (2p-2h,2p-2h block) need to be considered, where I, J and K correspond to core orbitals, while j and l describe occupied valence orbitals and a, b, c, and d represent virtual orbitals. In Figure 2.4, this strict separation of singly core-excited states from the singly excited, doubly excited and doubly core-excited states is illustrated. Eventually, the size of the ADC matrix as well as the matrix equations are strongly reduced, which leads to computational savings compared to the general ADC approach. The diagonalization of the CVS-ADC(n) matrix $\mathbf{M}^{\mathrm{CVS}}$ provides direct access to core-excited states and due to the structure of $\mathbf{M}^{\mathrm{CVS}}$, iterative diagonalization schemes can be employed straightforwardly, because the energetically lowest eigenvalues of $\mathbf{M}^{\mathrm{CVS}}$ correspond to the spectroscopic core-excited states of interest, respectively. The explicit

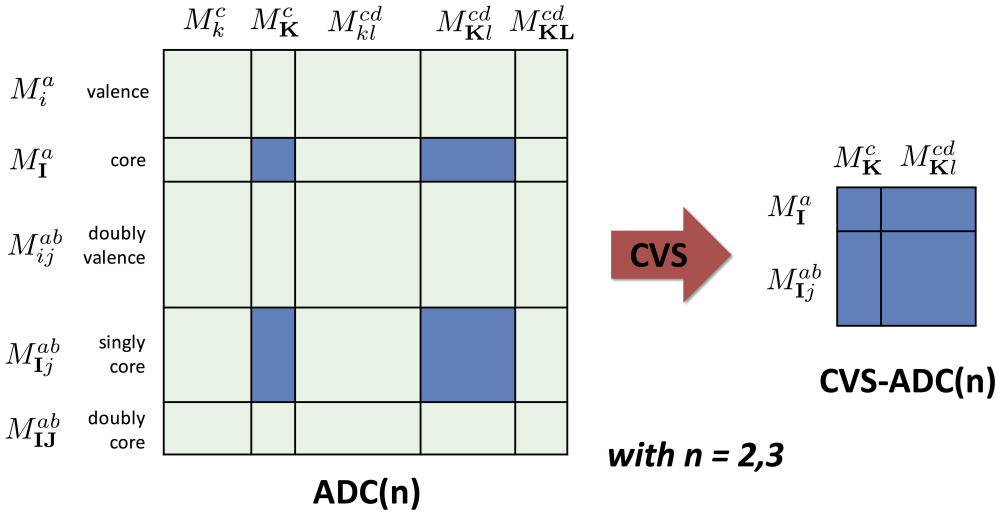

Figure 2.4: Scheme of the block structure of the whole second and third order ADC matrix, where the occupied orbital space is separated into the core (capital letters I, J, ...) and valence occupied (small letters i, j, ...) part. The singly core-excited states of both excitation classes are decoupled from the rest of the ADC(n) matrix after applying the CVS approximation. Therefore, the ADC(n) matrix is reduced, because one index of the occupied orbital space has to correspond to a core orbital.

CVS-ADC working equations accompanied by a detailed discussion about the application of the CVS approximation to the original ADC equations is given in chapter 2.5.7.

Finally, note that relativistic effects are neither included in the strict CVS-ADC approach nor in the ADC scheme in general. However, XAS of light elements are not significantly influenced by relativistic effects. The contribution to the spectrum is a positive shift of the absolute energy, which depends almost constantly on the weight of the investigated atom, thus it is common to neglect these influences. For the following K-shell excitations, these energy shifts due to relativistic effects can be estimated to be about: 0.1 eV for carbon, 0.2 eV for nitrogen, 0.4 eV for oxygen and 8.0 eV for sulfur.[100,179]

2.5.7 The ADC and CVS-ADC Equations

In this chapter, the complete final ADC and CVS-ADC equations are presented and I show explicitly how the CVS approximation acts on the ADC working equations. The matrix elements are given up to third order in perturbation theory, while the equations for the spectral amplitudes and the ISR properties are only available in second order. Note that the CVS approximation was already applied to the ADC(2) secular matrix and corresponding spectral amplitudes by *Schirmer et al.*[100] For the very first time, I applied the CVS approximation to the ADC(3) scheme and the ISR for a general one-particle operator. The CVS-ADC(3) equations are already published in *Journal of Chemical Physics, 142 (2015), 214104*, while the equations of the CVS-ISR approach have been submitted for publication in *Journal of Chemical Theory and Computation, (2016).*[98,99]

For clearness, the following notations that are used to describe the equations are repeated: I, J ,K, ... label core orbitals and i, j, k, ... refer to valence occupied ones.

Furthermore, virtual unoccupied orbitals are denoted as a, b, c, ..., while p, q, r and s describe general orbitals. For simplification, the short-hand notations

$$t_{pqrs} = \frac{\langle pq \| rs \rangle}{\epsilon_r + \epsilon_s - \epsilon_p - \epsilon_q} = -t^{\star}_{rspq} \tag{2.231}$$

and

$$t^{\star}_{pqrs} = \frac{\langle rs \| pq \rangle}{\epsilon_r + \epsilon_s - \epsilon_p - \epsilon_q} \tag{2.232}$$

are used, where ϵ denotes the HF orbital energies and $\langle pq \| rs \rangle = \langle pq | rs \rangle - \langle pq | sr \rangle$ describes the antisymmetrized two-electron integrals. The equations are grouped in blocks of the configuration space of particles (p) and holes (h).

Applying the CVS Approximation to the Original ADC Working Equations

At first, the original ADC and ISR expressions up to third order without the CVS approximation, which are taken from the literature[76–78], are listed below. Furthermore, the influence of the CVS approximation is discussed and visually indicated by marking the types of integrals and matrix elements that are neglected in the CVS approximation (see equation 2.230) in red.

1. ADC Secular Matrix:

Let me start with the explicit expressions of the ADC secular matrix up to third order in perturbation theory. The CVS approximation is applied with respect to the restriction of the index i and j to correspond to core orbitals regarding the p-h,p-h block, while within the equations for the couplings and doubles blocks, the indices i and k refer to core orbitals. As shown in detail in chapter 2.5.5, the zeroth and first order terms of the **p-h,p-h block** are given as:

$$M^{(0)}_{ia,jb} = (\epsilon_a - \epsilon_i)\, \delta_{ab} \delta_{ij} \tag{2.233}$$

$$M^{(1)}_{ia,jb} = -\langle aj \| bi \rangle. \tag{2.234}$$

These terms are fully preserved within the CVS approximation. The second order term of the singles block can be written in three parts as

$$M^{(2)}_{ia,jb} = M^{(2)\,A}_{ia,jb} + M^{(2)\,B}_{ia,jb} + M^{(2)\,C}_{ia,jb}, \tag{2.235}$$

with

$$M^{(2)\,A}_{ia,jb} = \frac{1}{4}\delta_{ij} \sum_{ckl} \left(\frac{\langle ac||kl\rangle\langle kl||bc\rangle}{\epsilon_a + \epsilon_c - \epsilon_k - \epsilon_l} + \frac{\langle ac||kl\rangle\langle kl||bc\rangle}{\epsilon_b + \epsilon_c - \epsilon_k - \epsilon_l} \right) \tag{2.236}$$

$$M^{(2)\,B}_{ia,jb} = \frac{1}{4}\delta_{ab} \sum_{cdk} \left(\frac{\langle cd||ik\rangle\langle jk||cd\rangle}{\epsilon_c + \epsilon_d - \epsilon_i - \epsilon_k} + \frac{\langle cd||ik\rangle\langle jk||cd\rangle}{\epsilon_c + \epsilon_d - \epsilon_j - \epsilon_k} \right) \tag{2.237}$$

$$M^{(2)\,C}_{ia,jb} = -\frac{1}{2} \sum_{ck} \left(\frac{\langle ac||ik\rangle\langle jk||bc\rangle}{\epsilon_a + \epsilon_c - \epsilon_i - \epsilon_k} + \frac{\langle ac||ik\rangle\langle jk||bc\rangle}{\epsilon_b + \epsilon_c - \epsilon_j - \epsilon_k} \right), \tag{2.238}$$

where only the first term $M^{(2)\,A}_{ia,jb}$ is preserved after the CVS approximation is applied, because the B and C terms contain two-electron integrals of the types defined in equation

2.230. Going to the third order contributions of the p-h,p-h block, the complexity of the expressions increases. There are 29 contributing terms that originate from 23 Feynman diagrams of the polarization propagator:

$$M^{(3)}_{ia,jb} = \sum_{x=1}^{29} M^{(3,x)}_{ia,jb}. \tag{2.239}$$

I will discuss them via references to the original diagrams, which were evaluated by *Schirmer and Trofimov*, because some of the terms have a distinct physical meaning.[77] Diagrams (1)-(6) are related to the special ADC quantities of the one particle Green's function according to

$$\tilde{M}^{(3)}_{ia,jb} = -\delta_{ab} C^{(3)-}_{ij} + \delta_{ij} C^{(3)+}_{ab}, \tag{2.240}$$

where $C^{(3)+}_{ab}$ and $C^{(3)-}_{ij}$ describe the effective interaction for the (N-1)- and (N+1)-electron case, respectively.[180] These six diagrams lead to twelve terms, which are given as

$$\begin{aligned} M^{(3,1)}_{ia,jb} = &-\frac{1}{8}\delta_{ab} \sum_{cdklm} t^{\star}_{klcd} \langle im\|cd\rangle \langle jm\|kl\rangle \\ &\times \left(\frac{1}{\epsilon_c + \epsilon_d - \epsilon_i - \epsilon_m} - \frac{1}{\epsilon_c + \epsilon_d - \epsilon_j - \epsilon_m} \right) + \text{h.c.} \end{aligned} \tag{2.241}$$

$$M^{(3,2)}_{ia,jb} = -\frac{1}{8}\delta_{ab} \sum_{cdfgk} \langle cd\|fg\rangle \left(\frac{t^{\star}_{ikfg} \langle jk\|cd\rangle}{\epsilon_c + \epsilon_d - \epsilon_i - \epsilon_k} + \frac{t_{jkcd} \langle fg\|ki\rangle}{\epsilon_g + \epsilon_f - \epsilon_j - \epsilon_k} \right) \tag{2.242}$$

$$\begin{aligned} M^{(3,3)}_{ia,jb} = &-\frac{1}{2}\delta_{ab} \sum_{cdfkl} t^{\star}_{klcd} \langle jl\|cf\rangle \langle kf\|id\rangle \\ &\times \left(\frac{1}{\epsilon_d + \epsilon_f - \epsilon_j - \epsilon_l} + \frac{1}{\epsilon_d + \epsilon_f - \epsilon_i - \epsilon_l} \right) + \text{h.c.} \end{aligned} \tag{2.243}$$

$$M^{(3,4)}_{ia,jb} = -\frac{1}{2}\delta_{ab} \sum_{cdfkl} \langle cl\|fk\rangle \left(\frac{t^{\star}_{ildf} \langle jk\|cd\rangle}{\epsilon_c + \epsilon_d - \epsilon_i - \epsilon_k} + \frac{t_{jkcd} \langle fd\|il\rangle}{\epsilon_d + \epsilon_f - \epsilon_j - \epsilon_l} \right) \tag{2.244}$$

$$\begin{aligned} M^{(3,5)}_{ia,jb} = &-\frac{1}{8}\delta_{ij} \sum_{cdekl} t^{\star}_{klcd} \langle kl\|be\rangle \langle ae\|cd\rangle \\ &\times \left(\frac{1}{\epsilon_b + \epsilon_e - \epsilon_k - \epsilon_l} + \frac{1}{\epsilon_a + \epsilon_e - \epsilon_k - \epsilon_l} \right) + \text{h.c.} \end{aligned} \tag{2.245}$$

$$M^{(3,6)}_{ia,jb} = -\frac{1}{8}\delta_{ij} \sum_{cklmn} \langle nm\|kl\rangle \left(\frac{t^{\star}_{nmac} \langle kl\|bc\rangle}{\epsilon_a + \epsilon_c - \epsilon_k - \epsilon_l} + \frac{t_{klbc} \langle ac\|nm\rangle}{\epsilon_b + \epsilon_c - \epsilon_m - \epsilon_n} \right) \tag{2.246}$$

$$\begin{aligned} M^{(3,7)}_{ia,jb} = &-\frac{1}{2}\delta_{ij} \sum_{cdklm} t^{\star}_{klcd} \langle km\|bd\rangle \langle al\|mc\rangle \\ &\times \left(\frac{1}{\epsilon_a + \epsilon_d - \epsilon_k - \epsilon_m} + \frac{1}{\epsilon_b + \epsilon_d - \epsilon_k - \epsilon_m} \right) + \text{h.c.} \end{aligned} \tag{2.247}$$

$$M^{(3,8)}_{ia,jb} = -\frac{1}{2}\delta_{ij} \sum_{cdklm} \langle mc\|kd\rangle \left(\frac{t^{\star}_{lmad} \langle kl\|bc\rangle}{\epsilon_a + \epsilon_c - \epsilon_k - \epsilon_l} + \frac{t_{klbc} \langle ad\|lm\rangle}{\epsilon_b + \epsilon_d - \epsilon_l - \epsilon_m} \right) \tag{2.248}$$

$$M^{(3,9)}_{ia,jb} = -\frac{1}{2}\sum_{cdklm} t_{klcd} t^{\star}_{lmcd} \left(\delta_{ab}\langle jm\|ik\rangle - \delta_{ij}\langle ma\|kb\rangle\right) \tag{2.249}$$

$$M^{(3,10)}_{ia,jb} = -\frac{1}{2}\sum_{cdekl} t_{klcd} t^{\star}_{klde} \left(\delta_{ij}\langle ac\|be\rangle - \delta_{ab}\langle jc\|ie\rangle\right) \tag{2.250}$$

$$M^{(3,11)}_{ia,jb} = \frac{1}{2}\sum_{cdekl} \frac{t_{klcd}\langle cd\|le\rangle \left(\delta_{ab}\langle je\|ki\rangle + \delta_{ij}\langle ae\|bk\rangle\right)}{\epsilon_e - \epsilon_k} + \text{h.c.} \tag{2.251}$$

$$M^{(3,12)}_{ia,jb} = \frac{1}{2}\sum_{cdklm} \frac{t_{klcd}\langle md\|kl\rangle \left(\delta_{ab}\langle jc\|im\rangle - \delta_{ij}\langle ac\|bm\rangle\right)}{\epsilon_c - \epsilon_m} + \text{h.c.} \tag{2.252}$$

After applying the CVS approximation, these twelve terms are reduced to eight, because some of the terms that arise from the $\delta_{ab}C^{(3)-}_{ij}$ part contain two-electron integrals that are neglected within the CVS approximation. A further special case are the terms with $x = 9, 10, 11, 12$. These expressions fully remain after applying the CVS approximation. In these cases, the relation $C^{(3)}_{pq} = \Sigma^{(3)}_{pq}$ with $\Sigma^{(3)}_{pq}$ describing the static self-energy is valid.

The remaining third order expressions of the singles block according to the diagrams (7) - (23) are given as follows:

$$M^{(3,13)}_{ia,jb} = \frac{1}{2}\sum_{cdkl} \frac{t^{\star}_{klcd}\langle al\|ci\rangle\langle kj\|bd\rangle}{\epsilon_a + \epsilon_d - \epsilon_i - \epsilon_k} + \text{h.c.} \tag{2.253}$$

$$M^{(3,14)}_{ia,jb} = -\frac{1}{2}\sum_{cdkl}\langle lc\|kd\rangle \left(\frac{t^{\star}_{liad}\langle lj\|bc\rangle}{\epsilon_a + \epsilon_c - \epsilon_k - \epsilon_i} + \frac{t_{kjcb}\langle ad\|li\rangle}{\epsilon_b + \epsilon_d - \epsilon_j - \epsilon_l}\right) \tag{2.254}$$

$$M^{(3,15)}_{ia,jb} = -\frac{1}{4}\sum_{cdkl} t_{klcd} t^{\star}_{klac}\langle dj\|bi\rangle + \text{h.c.} \tag{2.255}$$

$$M^{(3,16)}_{ia,jb} = \frac{1}{2}\sum_{cdkl} \frac{t^{\star}_{klcd}\langle la\|cd\rangle\langle kj\|bi\rangle}{\epsilon_a - \epsilon_k} + \text{h.c.} \tag{2.256}$$

$$M^{(3,17)}_{ia,jb} = \frac{1}{2}\sum_{cklm} \frac{t^{\star}_{lmac}\langle lm\|kc\rangle\langle kj\|bi\rangle}{\epsilon_a - \epsilon_k} + \text{h.c.} \tag{2.257}$$

$$M^{(3,18)}_{ia,jb} = -\frac{1}{4}\sum_{cdkl} t_{klcd} t^{\star}_{licd}\langle aj\|bk\rangle + \text{h.c.} \tag{2.258}$$

$$M^{(3,19)}_{ia,jb} = \frac{1}{2}\sum_{cdkl} \frac{t^{\star}_{klcd}\langle kl\|di\rangle\langle ja\|cb\rangle}{\epsilon_c - \epsilon_i} + \text{h.c.} \tag{2.259}$$

$$M^{(3,20)}_{ia,jb} = \frac{1}{2}\sum_{cdfk} \frac{t^{\star}_{kidf}\langle ck\|df\rangle\langle aj\|cb\rangle}{\epsilon_c - \epsilon_i} + \text{h.c.} \tag{2.260}$$

$$\begin{aligned} M^{(3,21)}_{ia,jb} = &-\frac{1}{2}\sum_{cdkl} t^{\star}_{klad}\langle kj\|bc\rangle\langle cl\|di\rangle \\ &\times \left(\frac{1}{\epsilon_b + \epsilon_c - \epsilon_j - \epsilon_k} + \frac{1}{\epsilon_a + \epsilon_c - \epsilon_i - \epsilon_k}\right) + \text{h.c.} \end{aligned} \tag{2.261}$$

$$\begin{aligned} M^{(3,22)}_{ia,jb} = &-\frac{1}{2}\sum_{cdkl} t^{\star}_{licd}\langle kj\|bc\rangle\langle la\|dk\rangle \\ &\times \left(\frac{1}{\epsilon_b + \epsilon_c - \epsilon_j - \epsilon_k} + \frac{1}{\epsilon_a + \epsilon_c - \epsilon_i - \epsilon_k}\right) + \text{h.c.} \end{aligned} \tag{2.262}$$

$$M^{(3,23)}_{ia,jb} = \frac{1}{4}\sum_{cdfk} t^{\star}_{kicd}\langle jk\|bf\rangle\langle af\|cd\rangle \times \left(\frac{1}{\epsilon_b+\epsilon_f-\epsilon_j-\epsilon_k}+\frac{1}{\epsilon_a+\epsilon_f-\epsilon_i-\epsilon_k}\right) + \text{h.c.} \tag{2.263}$$

$$M^{(3,24)}_{ia,jb} = \frac{1}{4}\sum_{cklm} t^{\star}_{klac}\langle jm\|cb\rangle\langle kl\|im\rangle \times \left(\frac{1}{\epsilon_b+\epsilon_c-\epsilon_j-\epsilon_m}+\frac{1}{\epsilon_a+\epsilon_c-\epsilon_i-\epsilon_m}\right) + \text{h.c.} \tag{2.264}$$

$$M^{(3,25)}_{ia,jb} = -\frac{1}{2}\sum_{cdkl} t_{kldb}t^{\star}_{klac}\langle dj\|ci\rangle \tag{2.265}$$

$$M^{(3,26)}_{ia,jb} = -\frac{1}{2}\sum_{cdkl} t_{jlcd}t^{\star}_{kicd}\langle ak\|bl\rangle \tag{2.266}$$

$$M^{(3,27)}_{ia,jb} = -\sum_{cklm} t^{\star}_{klac}t_{lmbc}\langle kj\|im\rangle \tag{2.267}$$

$$M^{(3,28)}_{ia,jb} = -\sum_{cdfk} t^{\star}_{ikcd}t_{kjdf}\langle af\|bc\rangle \tag{2.268}$$

$$M^{(3,29)}_{ia,jb} = -\sum_{cdkl} t^{\star}_{klac}t_{ljcd}\langle dk\|bi\rangle + \text{h.c.} \tag{2.269}$$

If the CVS approximation acts on these equations, only the five equations based on diagrams (8), (9), (16) and (18) are fully preserved, while the ones that arise from the rest are neglected completely. Eventually, the third order equations of the singles block are reduced from 29 to 13 after applying the CVS approximation, where the dominant part of the remaining equations arise from contributions that are also included in the (N+1-) and (N-1)-electron cases.

Next, the **coupling blocks** are discussed. Theses equations are known to be related to orbital relaxation and polarization effects.[49,76] The explanation concerning the impact of the vanishing terms on the orbital relaxation effects are given in detail in the following chapter 2.5.9. Note that the ADC secular matrix is Hermitian and since the orbitals are real, only the $M_{ia,klcd}$ elements are shown. The ones of the 2p-2h,p-h block are just complex conjugated, thus the equations of both coupling blocks are identical with respect to their indices.

$$M^{(1)}_{ia,klcd} = \langle kl||id\rangle\delta_{ac} - \langle kl||ic\rangle\delta_{ad} - \langle al||cd\rangle\delta_{ik} + \langle ak||cd\rangle\delta_{il} \tag{2.270}$$

The last part of the first order contribution to the coupling blocks is neglected due to the type of the integral. The second order terms can be written in six parts as

$$M^{(2)}_{ia,klcd} = \sum_{x=1}^{6} M^{(2,x)}_{ia,klcd} \tag{2.271}$$

with

$$M^{(2,1)}_{ia,klcd} = -\delta_{ac}\sum_{bj} t_{kjdb}\langle lb\|ji\rangle + \delta_{ad}\sum_{bj} t_{kjcb}\langle lb\|ji\rangle + \delta_{ac}\sum_{bj} t_{ljdb}\langle kb\|ji\rangle - \delta_{ad}\sum_{bj} t_{ljcb}\langle kb\|ji\rangle \tag{2.272}$$

$$M^{(2,2)}_{ia,klcd} = -\frac{1}{2}\delta_{ac}\sum_{be} t_{klbe}\langle be\|id\rangle + \frac{1}{2}\delta_{ad}\sum_{be} t_{klbe}\langle be\|ic\rangle \tag{2.273}$$

$$\begin{aligned} M^{(2,3)}_{ia,klcd} = {} & \delta_{ik}\sum_{bj}\left(-t_{ljdb}\langle ab\|jc\rangle + t_{ljcb}\langle ab\|jd\rangle\right) \\ & + \delta_{il}\sum_{bj}\left(t_{kjdb}\langle ab\|jc\rangle - t_{kjcb}\langle ab\|jd\rangle\right) \end{aligned} \tag{2.274}$$

$$M^{(2,4)}_{ia,klcd} = -\frac{1}{2}\delta_{ik}\sum_{jm} t_{jmcd}\langle la\|jm\rangle + \frac{1}{2}\delta_{il}\sum_{jm} t_{jmcd}\langle ka\|jm\rangle \tag{2.275}$$

$$M^{(2,5)}_{ia,klcd} = -\sum_{b} t_{klcb}\langle ab\|di\rangle + \sum_{b} t_{kldb}\langle ab\|ci\rangle \tag{2.276}$$

$$M^{(2,6)}_{ia,klcd} = -\sum_{j} t_{ljcd}\langle ak\|ji\rangle + \sum_{j} t_{kjcd}\langle al\|ji\rangle. \tag{2.277}$$

After the CVS approximation is applied, the six second order terms are reduced to four. However, the remaining expressions are not completely preserved, because repeating terms, in which for example p and q are interchanged, lead to two-electron integrals that vanish within the CVS approximation.

At last, the equations of the 2p-2h,2p-2h block are given in zeroth and first order as

$$M^{(0)}_{ijab,klcd} = \left(\epsilon_a + \epsilon_b - \epsilon_i - \epsilon_j\right)\delta_{ac}\delta_{bd}\delta_{ik}\delta_{jl} \tag{2.278}$$

$$\begin{aligned} M^{(1)}_{ijab,klcd} = {} & \langle ab||cd\rangle\delta_{ik}\delta_{jl} + \langle kl||ij\rangle\delta_{ac}\delta_{bd} \\ & - \left(\langle ak||ci\rangle\delta_{bd}\delta_{jl} + \langle al||cj\rangle\delta_{bd}\delta_{ik} + \langle bk||di\rangle\delta_{ac}\delta_{jl} + \langle bl||dj\rangle\delta_{ac}\delta_{ik}\right) \\ & + \left(\langle al||ci\rangle\delta_{jk}\delta_{bd} + \langle ak||cj\rangle\delta_{il}\delta_{bd} + \langle bl||di\rangle\delta_{jk}\delta_{ac} + \langle bk||dj\rangle\delta_{il}\delta_{ac}\right) \\ & + \left(\langle ak||di\rangle\delta_{bc}\delta_{jl} + \langle al||dj\rangle\delta_{bc}\delta_{ik} + \langle bk||ci\rangle\delta_{ad}\delta_{jl} + \langle bl||cj\rangle\delta_{ad}\delta_{ik}\right) \\ & - \left(\langle al||di\rangle\delta_{jk}\delta_{bc} + \langle ak||dj\rangle\delta_{il}\delta_{bc} + \langle bl||ci\rangle\delta_{jk}\delta_{ad} + \langle bk||cj\rangle\delta_{il}\delta_{ad}\right). \end{aligned} \tag{2.279}$$

The zeroth order term just consists of the orbital energy differences that are fully preserved within the CVS approximation with respect to the restriction of the indices, while the first order contribution is reduced from 18 to 10 terms according to the two-electron integrals that are practically zero.

2. ADC Spectral Amplitudes:

Next, I discuss the spectral amplitudes that provide access to oscillator strengths. D_{pq} refers to the matrix representation of an arbitrary one-particle operator. The CVS approximation is applied with respect to the restriction of the index i to correspond to a core orbital. The zeroth order element is simply given as

$$F^{(0)}_{ia} = D_{ai}. \tag{2.280}$$

$F^{(0)}_{ia}$ is fully preserved after applying the CVS approximation, while the first order term

$$F^{(1)}_{ia} = \sum_{bj}\frac{\langle ab||ji\rangle}{\epsilon_a + \epsilon_b - \epsilon_j - \epsilon_i} D_{jb} \tag{2.281}$$

completely vanishes. According to the diagrammatic origin, there are 13 second order terms of the p-h excitations. However, only three terms, i.e. $F^{(2)A}_{ia}$, $F^{(2,1)}_{ia}$ and $F^{(2,2)}_{ia}$, are

preserved after applying the CVS approximation due to certain two-electron integrals that are neglected:

$$F_{ia}^{(2)A} = -\frac{1}{4}\sum_{bjck}\frac{\langle ab||jk\rangle\langle jk||cb\rangle}{(\epsilon_a+\epsilon_b-\epsilon_j-\epsilon_k)(\epsilon_c+\epsilon_b-\epsilon_j-\epsilon_k)}D_{ci} \tag{2.282}$$

$$F_{ia}^{(2)B} = -\frac{1}{4}\sum_{bjck}\frac{\langle bc||ij\rangle\langle kj||bc\rangle}{(\epsilon_b+\epsilon_c-\epsilon_i-\epsilon_j)(\epsilon_b+\epsilon_c-\epsilon_k-\epsilon_j)}D_{ak} \tag{2.283}$$

$$F_{ia}^{(2)C} = \frac{1}{2}\sum_{bjck}\frac{\langle ab||ij\rangle\langle kj||cb\rangle}{(\epsilon_a+\epsilon_b-\epsilon_i-\epsilon_j)(\epsilon_c+\epsilon_b-\epsilon_k-\epsilon_j)}D_{ck} \tag{2.284}$$

$$F_{ia}^{(2,1)} = -\frac{1}{2}\sum_{bjck}\frac{\langle bc||jk\rangle\langle ja||bc\rangle}{(\epsilon_b+\epsilon_c-\epsilon_j-\epsilon_k)(\epsilon_a-\epsilon_k)}D_{ki} \tag{2.285}$$

$$F_{ia}^{(2,2)} = \frac{1}{2}\sum_{bjkl}\frac{\langle ba||jk\rangle\langle jk||bl\rangle}{(\epsilon_a+\epsilon_b-\epsilon_j-\epsilon_k)(\epsilon_a-\epsilon_l)}D_{li} \tag{2.286}$$

$$F_{ia}^{(2,3)} = -\frac{1}{2}\sum_{bjck}\frac{\langle bc||jk\rangle\langle jk||ic\rangle}{(\epsilon_b+\epsilon_c-\epsilon_j-\epsilon_k)(\epsilon_b-\epsilon_i)}D_{ab} \tag{2.287}$$

$$F_{ia}^{(2,4)} = \frac{1}{2}\sum_{bcjd}\frac{\langle bc||ij\rangle\langle dj||bc\rangle}{(\epsilon_b+\epsilon_c-\epsilon_i-\epsilon_j)(\epsilon_d-\epsilon_i)}D_{ad} \tag{2.288}$$

$$F_{ia}^{(2,5)} = \sum_{bjck}\frac{\langle bc||kj\rangle\langle aj||bi\rangle}{(\epsilon_b+\epsilon_c-\epsilon_k-\epsilon_j)(\epsilon_a+\epsilon_c-\epsilon_i-\epsilon_k)}D_{kc} \tag{2.289}$$

$$F_{ia}^{(2,6)} = \sum_{bjck}\frac{\langle ab||ji\rangle\langle jc||kb\rangle}{(\epsilon_a+\epsilon_b-\epsilon_j-\epsilon_i)(\epsilon_a+\epsilon_c-\epsilon_i-\epsilon_k)}D_{kc} \tag{2.290}$$

$$F_{ia}^{(2,7)} = -\sum_{bjck}\frac{\langle cb||ji\rangle\langle aj||kc\rangle}{(\epsilon_c+\epsilon_b-\epsilon_j-\epsilon_i)(\epsilon_a+\epsilon_b-\epsilon_i-\epsilon_k)}D_{kb} \tag{2.291}$$

$$F_{ia}^{(2,8)} = -\sum_{bjck}\frac{\langle ac||kj\rangle\langle jb||ci\rangle}{(\epsilon_a+\epsilon_c-\epsilon_k-\epsilon_j)(\epsilon_a+\epsilon_b-\epsilon_i-\epsilon_k)}D_{kb} \tag{2.292}$$

$$F_{ia}^{(2,9)} = -\frac{1}{2}\sum_{bjcd}\frac{\langle cd||ji\rangle\langle ab||cd\rangle}{(\epsilon_c+\epsilon_d-\epsilon_j-\epsilon_i)(\epsilon_a+\epsilon_b-\epsilon_i-\epsilon_j)}D_{jb} \tag{2.293}$$

$$F_{ia}^{(2,10)} = -\frac{1}{2}\sum_{bjkl}\frac{\langle ab||kl\rangle\langle kl||ji\rangle}{(\epsilon_a+\epsilon_b-\epsilon_k-\epsilon_l)(\epsilon_a+\epsilon_b-\epsilon_i-\epsilon_j)}D_{jb}. \tag{2.294}$$

The matrix element of the double excitations can be written as

$$\begin{aligned} F_{ijab}^{(1)} = &\sum_k\frac{\langle ab||ki\rangle}{\epsilon_a+\epsilon_b-\epsilon_k-\epsilon_i}D_{kj} - \sum_k\frac{\langle ab||kj\rangle}{\epsilon_a+\epsilon_b-\epsilon_k-\epsilon_j}D_{ki} \\ &+\sum_c\frac{\langle cb||ij\rangle}{\epsilon_c+\epsilon_b-\epsilon_i-\epsilon_j}D_{ac} - \sum_c\frac{\langle ca||ij\rangle}{\epsilon_c+\epsilon_a-\epsilon_i-\epsilon_j}D_{bc} \end{aligned}, \tag{2.295}$$

thus only the second term is preserved after applying the CVS approximation. Eventually, all terms that contain the matrix representation D_{cp} of an arbitrary one-particle operator are preserved, where c corresponds to a core orbital and p refers to a virtual or valence occupied orbital.

3. ISR for a General One-Particle Operator:

At last, the matrix equations of the ISR of a general one-particle operator are discussed. In the case of the p-h,p-h block, the indices i and j correspond to core orbitals if the CVS approximation is applied, while the indices i and k refer to core orbitals in the case of the couplings and doubles blocks. Note that all first order contributions are zero:

$$D^{(1)}_{ia,jb} = 0 \qquad D^{(1)}_{ia,klcd} = 0 \qquad D^{(1)}_{ijab,kc} = 0 \qquad D^{(1)}_{ijab,klcd} = 0 \tag{2.296}$$

Let me start with the equations for the **p-h,p-h block**. The zeroth order term is given as

$$D^{(0)}_{ia,jb} = \delta_{ij} d_{ab} - \delta_{ab} d_{ji}, \tag{2.297}$$

which is fully preserved within the CVS approximation. There are seven second order contributions to the singles block according to

$$D^{(2)}_{ia,jb} = \sum_{x=1}^{7} D^{(2,x)}_{ia,jb}, \tag{2.298}$$

with

$$D^{(2,1)}_{ia,jb} = -\delta_{ij} \sum_{k} (\rho_{kb} d_{ak} + \rho_{ak} d_{kb}) - \delta_{ab} \sum_{c} (\rho_{jc} d_{ci} + \rho_{ci} d_{jc}) \tag{2.299}$$

$$D^{(2,2)}_{ia,jb} = -\frac{1}{4} \delta_{ij} \sum_{cdkl} (t_{klcd} t^{\star}_{klad} d_{cb} + t^{\star}_{klcd} t_{klbd} d_{ac}) \tag{2.300}$$

$$D^{(2,3)}_{ia,jb} = -\delta_{ij} \left(\frac{1}{2} \sum_{cdkl} t_{klbc} t^{\star}_{klad} d_{cd} - \sum_{dklm} t_{klbd} t^{\star}_{mlad} d_{mk} \right) \tag{2.301}$$

$$D^{(2,4)}_{ia,jb} = \frac{1}{4} \delta_{ab} \sum_{cdkl} (t_{klcd} t^{\star}_{ilcd} d_{jk} + t^{\star}_{klcd} t_{jlcd} d_{ik}) \tag{2.302}$$

$$D^{(2,5)}_{ia,jb} = -\delta_{ab} \left(\sum_{cdek} t_{jkce} t^{\star}_{ikde} d_{ce} + \frac{1}{2} \sum_{celk} t_{jkce} t^{\star}_{ilce} d_{lk} \right) \tag{2.303}$$

$$\begin{aligned} D^{(2,6)}_{ia,jb} = {} & \frac{1}{2} \left(\sum_{cdl} t_{jlcd} t^{\star}_{ilad} d_{cb} - \sum_{dkl} t_{klbd} t^{\star}_{ilad} d_{jl} \right) \\ & + \frac{1}{2} \left(\sum_{cdl} t^{\star}_{ilcd} t_{jlbd} d_{ca} - \sum_{dkl} t^{\star}_{klad} t_{jlbd} d_{il} \right) \end{aligned} \tag{2.304}$$

$$D^{(2,7)}_{ia,jb} = -\sum_{dkl} t_{jlbd} t^{\star}_{ikad} d_{kl} + \sum_{cdl} t_{jlbc} t^{\star}_{ilad} d_{cd}, \tag{2.305}$$

where ρ_{pq} describes the second order corrections to the one-particle ground state density matrix. The first term contains ground state density matrices of the type ρ_{cv}, which are zero within the CVS approximation, where c corresponds to core orbitals and v to virtual orbitals. Since all terms with $x > 3$ contain two-electron integrals of the types described in equation 2.230, they vanish within the CVS approximation. The **coupling blocks** (only $D^{(0)}_{ia,klcd}$ is shown due to the real Hermitian matrix) in zeroth order are given as

$$D^{(0)}_{ia,klcd} = -\delta_{ac}\delta_{ik} d_{ld} + \delta_{ac}\delta_{il} d_{kd} + \delta_{ad}\delta_{ik} d_{lc} - \delta_{ad}\delta_{il} d_{kc}. \tag{2.306}$$

The zeroth-order contributions of the coupling blocks are reduced from four terms to only two by applying the CVS approximation. The terms that vanish contain δ_{co} expressions, where c describes the core space and o the valence occupied space. These terms are always 0, because contents belonging to these different spaces cannot be equal. The following eight second-order contributions to the coupling blocks are reduced to three after applying the CVS approximation, because they contain the types of two-electron integrals that are neglected as well as delta terms of the type δ_{co}:

$$\begin{aligned} D^{(2)}_{ia,klcd} = {} & \delta_{ac}\delta_{ik}\sum_{bj} t_{ljdb}d_{bj} - \delta_{ac}\delta_{il}\sum_{bj} t_{kjdb}d_{bj} - \delta_{ad}\delta_{ik}\sum_{bj} t_{ljcb}d_{bj} \\ & + \delta_{ad}\delta_{il}\sum_{bj} t_{kjcb}d_{bj} - \delta_{ac}\sum_{b} t_{klbd}d_{bi} + \delta_{ad}\sum_{b} t_{klbc}d_{bi} \\ & - \delta_{ik}\sum_{j} t_{jlcd}d_{aj} + \delta_{il}\sum_{j} t_{jkcd}d_{aj}. \end{aligned} \tag{2.307}$$

The same applies for the zeroth-order contributions to the **2p-2h,2p-2h block**. Here, eight terms are reduced to six by applying the CVS approximation.

$$\begin{aligned} D^{(0)}_{ijab,klcd} = {} & \delta_{ik}\delta_{jl}\left(\delta_{bd}d_{ac} - \delta_{bc}d_{ad} - \delta_{ad}d_{bc} + \delta_{ac}d_{bd}\right) \\ & - \delta_{ac}\delta_{bd}\left(\delta_{jl}d_{ki} - \delta_{jk}d_{li} - \delta_{il}d_{kj} + \delta_{ik}d_{lj}\right). \end{aligned} \tag{2.308}$$

Summary of the Final CVS-ADC Equations

Finally, the CVS-ADC secular matrix working equations up to third order in perturbation theory are listed below, followed by the CVS-ADC spectral amplitudes and CVS-ISR equations up to second order.

1. CVS-ADC Secular Matrix:

The **p-h,p-h block** expanded up to third order is given as:

$$M^{(0)}_{Ia,Jb} = \left(\epsilon_a - \epsilon_I\right)\delta_{ab}\delta_{IJ} \tag{2.309}$$

$$M^{(1)}_{Ia,Jb} = -\langle aJ\|bI\rangle \tag{2.310}$$

$$M^{(2)}_{Ia,Jb} = \frac{1}{4}\delta_{IJ}\sum_{klc}\left(t^{\star}_{klac}\langle kl\|bc\rangle + \langle ac\|kl\rangle t_{klbc}\right) \tag{2.311}$$

In the case of the third order terms after applying the CVS approximation, there are 13 contributing terms to the CVS-ADC(3) scheme that are ordered according to the diagrammatic origin of the original ADC(3) equations:

$$M^{(3)}_{Ia,Jb} = \sum_{x=1}^{13} M^{(3,x)}_{Ia,Jb} \tag{2.312}$$

with

$$\begin{aligned} M^{(3,1)}_{Ia,Jb} = {} & -\frac{1}{8}\delta_{IJ}\sum_{cdekl} t^{\star}_{klcd}\langle kl\|be\rangle\langle ae\|cd\rangle \\ & \times\left(\frac{1}{\epsilon_b + \epsilon_e - \epsilon_k - \epsilon_l} + \frac{1}{\epsilon_a + \epsilon_e - \epsilon_k - \epsilon_l}\right) + \text{h.c.} \end{aligned} \tag{2.313}$$

$$M^{(3,2)}_{Ia,Jb} = -\frac{1}{8}\delta_{IJ} \sum_{cklmn} \langle nm\|kl\rangle \left(\frac{t^\star_{nmac}\langle kl\|bc\rangle}{\epsilon_a+\epsilon_c-\epsilon_k-\epsilon_l} + \frac{t_{klbc}\langle ac\|nm\rangle}{\epsilon_b+\epsilon_c-\epsilon_m-\epsilon_n} \right) \tag{2.314}$$

$$\begin{aligned} M^{(3,3)}_{Ia,Jb} = &-\frac{1}{2}\delta_{IJ} \sum_{cdklm} t^\star_{klcd}\langle km\|bd\rangle\langle al\|mc\rangle \\ &\times \left(\frac{1}{\epsilon_a+\epsilon_d-\epsilon_k-\epsilon_m} + \frac{1}{\epsilon_b+\epsilon_d-\epsilon_k-\epsilon_m} \right) + \text{h.c.} \end{aligned} \tag{2.315}$$

$$M^{(3,4)}_{Ia,Jb} = -\frac{1}{2}\delta_{IJ} \sum_{cdklm} \langle mc\|kd\rangle \left(\frac{t^\star_{lmad}\langle kl\|bc\rangle}{\epsilon_a+\epsilon_c-\epsilon_k-\epsilon_l} + \frac{t_{klbc}\langle ad\|lm\rangle}{\epsilon_b+\epsilon_d-\epsilon_l-\epsilon_m} \right) \tag{2.316}$$

$$M^{(3,5)}_{Ia,Jb} = -\frac{1}{2} \sum_{cdklm} t_{klcd}t^\star_{lmcd} \left(\delta_{ab}\langle Jm\|Ik\rangle - \delta_{IJ}\langle ma\|kb\rangle\right) \tag{2.317}$$

$$M^{(3,6)}_{Ia,Jb} = -\frac{1}{2} \sum_{cdekl} t_{klcd}t^\star_{klde} \left(\delta_{IJ}\langle ac\|be\rangle - \delta_{ab}\langle Jc\|Ie\rangle\right) \tag{2.318}$$

$$M^{(3,7)}_{Ia,Jb} = -\frac{1}{2} \sum_{cdekl} \frac{t_{klcd}\langle cd\|le\rangle \left(\delta_{ab}\langle Je\|kI\rangle + \delta_{IJ}\langle ae\|bk\rangle\right)}{\epsilon_e-\epsilon_k} + \text{h.c.} \tag{2.319}$$

$$M^{(3,8)}_{Ia,Jb} = \frac{1}{2} \sum_{cdklm} \frac{t_{klcd}\langle md\|kl\rangle \left(\delta_{ab}\langle Jc\|Im\rangle - \delta_{IJ}\langle ac\|bm\rangle\right)}{\epsilon_c-\epsilon_m} + \text{h.c.} \tag{2.320}$$

$$M^{(3,9)}_{Ia,Jb} = -\frac{1}{4} \sum_{cdkl} t_{klcd}t^\star_{klac}\langle dJ\|bI\rangle + \text{h.c.} \tag{2.321}$$

$$M^{(3,10)}_{Ia,Jb} = \frac{1}{2} \sum_{cdkl} \frac{t^\star_{klcd}\langle la\|cd\rangle\langle kJ\|bI\rangle}{\epsilon_a-\epsilon_k} + \text{h.c.} \tag{2.322}$$

$$M^{(3,11)}_{Ia,Jb} = \frac{1}{2} \sum_{cklm} \frac{t^\star_{lmac}\langle lm\|kc\rangle\langle kJ\|bI\rangle}{\epsilon_a-\epsilon_k} + \text{h.c.} \tag{2.323}$$

$$M^{(3,12)}_{Ia,Jb} = -\frac{1}{2} \sum_{cdkl} t_{kldb}t^\star_{klac}\langle dJ\|cI\rangle \tag{2.324}$$

$$M^{(3,13)}_{Ia,Jb} = -\sum_{cklm} t^\star_{klac}t_{lmbc}\langle kJ\|Im\rangle. \tag{2.325}$$

Next, the matrix elements of the **p-h,2p-2h block** are presented. Note that only the matrix elements $M_{Ia,Klcd}$ of the p-h,2p-2h block are shown due to the Hermitian ADC secular matrix.

$$M^{(1)}_{Ia,Klcd} = \langle Kl\|Id\rangle\delta_{ac} - \langle Kl\|Ic\rangle\delta_{ad} - \langle al\|cd\rangle\delta_{IK}. \tag{2.326}$$

There are four terms that contribute to the second order coupling blocks of the CVS-ADC(3) secular matrix

$$M^{(2)}_{Ia,Klcd} = \sum_{x=1}^{4} M^{(2,x)}_{Ia,Klcd} \tag{2.327}$$

with

$$M^{(2,1)}_{Ia,Klcd} = \delta_{ac} \sum_{bj} t_{ljdb}\langle Kb\|jI\rangle - \delta_{ad} \sum_{bj} t_{ljcb}\langle Kb\|jI\rangle \tag{2.328}$$

$$M^{(2,2)}_{Ia,Klcd} = -\delta_{IK}\sum_{bj} t_{ljdb}\langle ab\|jc\rangle + \delta_{IK}\sum_{bj} t_{ljcb}\langle ab\|jd\rangle \tag{2.329}$$

$$M^{(2,3)}_{Ia,Klcd} = -\frac{1}{2}\delta_{IK}\sum_{jm} t_{jmcd}\langle la\|jm\rangle \tag{2.330}$$

$$M^{(2,4)}_{Ia,Klcd} = -\sum_{j} t_{ljcd}\langle aK\|jI\rangle. \tag{2.331}$$

The **2p-2h,2p-2h block** is expanded up to the first order and given as

$$M^{(0)}_{Ijab,Klcd} = (\epsilon_a + \epsilon_b - \epsilon_I - \epsilon_j)\,\delta_{ac}\delta_{bd}\delta_{IK}\delta_{jl} \tag{2.332}$$

$$\begin{aligned} M^{(1)}_{Ijab,Klcd} =& \langle ab\|cd\rangle\delta_{IK}\delta_{jl} + \langle Kl\|Ij\rangle\delta_{ac}\delta_{bd} - \langle aK\|cI\rangle\delta_{bd}\delta_{jl} - \langle al\|cj\rangle\delta_{bd}\delta_{IK} \\ &- \langle bK\|dI\rangle\delta_{ac}\delta_{jl} - \langle bl\|dj\rangle\delta_{ac}\delta_{IK} + \langle aK\|dI\rangle\delta_{bc}\delta_{jl} + \langle al\|dj\rangle\delta_{bc}\delta_{IK} \\ &+ \langle bK\|cI\rangle\delta_{ad}\delta_{jl} + \langle bl\|cj\rangle\delta_{ad}\delta_{IK}. \end{aligned} \tag{2.333}$$

2. CVS-ADC Spectral Amplitudes:

The CVS-ADC spectral amplitudes up to second order in perturbation theory are given as

$$F^{(0)}_{Ia} = D_{Ia} \tag{2.334}$$

$$F^{(2)A}_{Ia} = -\frac{1}{4}\sum_{bjck} \frac{\langle ab\|jk\rangle\langle jk\|cb\rangle}{(\epsilon_a + \epsilon_b - \epsilon_j - \epsilon_k)\,(\epsilon_c + \epsilon_b - \epsilon_j - \epsilon_k)} D_{Ic} \tag{2.335}$$

$$F^{(2,1)}_{Ia} = -\frac{1}{2}\sum_{bjck} \frac{\langle bc\|jk\rangle\langle ja\|bc\rangle}{(\epsilon_b + \epsilon_c - \epsilon_j - \epsilon_k)\,(\epsilon_a - \epsilon_k)} D_{Ik} \tag{2.336}$$

$$F^{(2,2)}_{Ia} = \frac{1}{2}\sum_{bjkl} \frac{\langle ba\|jk\rangle\langle jk\|bl\rangle}{(\epsilon_a + \epsilon_b - \epsilon_j - \epsilon_k)\,(\epsilon_a - \epsilon_l)} D_{Il} \tag{2.337}$$

$$F^{(1)}_{Ijab} = -\sum_{k} \frac{\langle ab\|kj\rangle}{(\epsilon_a + \epsilon_b - \epsilon_k - \epsilon_j)} D_{Ik}. \tag{2.338}$$

3. CVS-ISR for a General One-Particle Operator:

Starting with the **p-h,p-h block**, the CVS-ISR equations up to second order in perturbation theory are defined as

$$D^{(0)}_{Ia,Jb} = \delta_{IJ}d_{ab} - \delta_{ab}d_{JI} \tag{2.339}$$

$$D^{(2)}_{Ia,Jb} = \sum_{x=1}^{3} D^{(2,x)}_{Ia,Jb}. \tag{2.340}$$

There are three second-order terms contributing to the p-h,p-h block:

$$D^{(2,1)}_{Ia,Jb} = -\delta_{IJ}\sum_{k} (\rho_{kb}d_{ak} + \rho_{ak}d_{kb}) \tag{2.341}$$

$$D^{(2,2)}_{Ia,Jb} = -\frac{1}{4}\delta_{IJ}\sum_{cdkl}\left(t_{klcd}t^{\star}_{klad}d_{cb} + t^{\star}_{klcd}t_{klbd}d_{ac}\right) \tag{2.342}$$

$$D^{(2,3)}_{Ia,Jb} = -\delta_{IJ}\left(\frac{1}{2}\sum_{cdkl}t_{klbc}t^{\star}_{klad}d_{cd} - \sum_{dklm}t_{klbd}t^{\star}_{mlad}d_{mk}\right), \tag{2.343}$$

with ρ_{pq} describing the second order corrections to the one-particle ground state density matrix. The **coupling elements** are given as

$$D^{(0)}_{Ia,Klcd} = \delta_{ad}\delta_{IK}d_{lc} - \delta_{ac}\delta_{IK}d_{ld} \tag{2.344}$$

$$D^{(2)}_{Ia,Klcd} = \delta_{ac}\delta_{IK}\sum_{bj}t_{ljdb}d_{bj} - \delta_{ad}\delta_{IK}\sum_{bj}t_{ljcb}d_{bj} - \delta_{IK}\sum_{j}t_{jlcd}d_{aj}. \tag{2.345}$$

Note that, due to the real Hermitian matrix, only the equations of $D_{Ia,Klcd}$ are shown, because $D_{Ijab,Kc}$ is just the complex conjugate counterpart. Finally, the equation for the **2p-2h,2p-2h block** is listed below as

$$\begin{aligned} D^{(0)}_{Ijab,Klcd} = {} & \delta_{IK}\delta_{lj}\left(\delta_{bd}d_{ac} - \delta_{bc}d_{ad} - \delta_{ad}d_{bc} + \delta_{ac}d_{bd}\right) \\ & - \delta_{ac}\delta_{bd}\left(\delta_{lj}d_{IK} + \delta_{IK}d_{lj}\right). \end{aligned} \tag{2.346}$$

2.5.8 Analysis of Excited State Densities

Next, the descriptors and densities used for a qualitative and quantitative description of excitation processes are briefly reviewed. A detailed derivation can be found in the literature.[84,86–88] To understand core-excitation processes in detail, it is not sufficient to only analyze excitation energies and the transition moments of core-excited states. Excited-state densities are also important physical properties, which help to proper determine excited-state characters, in particular, when the excited-state vectors consist of a mixture of different MO transitions and no dominant amplitude can be identified. In the scope of my thesis, I extended the formalism to the CVS-ADC/CVS-ISR approaches. Let me start with the calculation of state densities that helps to characterize and interpret the nature of electronically excited states.

Generally, a density matrix of the state I of the type

$$\boldsymbol{\gamma}^{II}(x,x') = n\int \Psi^{I}(x,x_2,...,x_n)\Psi^{I}(x',x_2,...,x_n)\,dx_2...dx_n \tag{2.347}$$

with the spatial coordinates x can be constructed using the ISR formalism of a general one-particle operator as shown in Section 2.5.2. Using the CVS-ISR approach, the total density of a core-excited state is calculated as the diagonal part of the density matrix

$$\rho^{II}(x) = \gamma^{II}(x,x). \tag{2.348}$$

However, plotting the total density does not help to characterize an excited state. Therefore, the concept of attachment/detachment densities based on the one-particle difference density matrix (1DDM) $\boldsymbol{\Delta}^{0I}(x,x') = \boldsymbol{\gamma}^{II}(x,x') - \boldsymbol{\gamma}^{00}(x,x')$ between the ground state 0 and an excited state I was introduced.[85] Within this concept, the 1DDM is diagonalized according to

$$\mathbf{W}^{T}\boldsymbol{\Delta}^{0I}(x,x')\mathbf{W} = \mathrm{diag}(\kappa_1,\kappa_2,...,\kappa_n) \tag{2.349}$$

and the diagonal elements κ_i are sorted and separated due to their sign

$$\begin{aligned} d_i &= \min(\kappa_i, 0) \\ a_i &= \max(\kappa_i, 0). \end{aligned} \tag{2.350}$$

Hence, the negative eigenvalues establish the detachment matrix, while the positive eigenvalues correspond to the attachment matrix. The back-transformations

$$\begin{aligned} \mathbf{D}_D &= \mathbf{W}\mathrm{diag}(d_1, d_2, ...)\mathbf{W}^T \\ \mathbf{D}_A &= \mathbf{W}\mathrm{diag}(a_1, a_2, ...)\mathbf{W}^T \end{aligned} \tag{2.351}$$

lead to the detachment $\mathbf{D}_D$ and attachment $\mathbf{D}_A$ (D/A) densities, respectively. To determine the number of detached/attached electrons (promotion number p_{DA}), the integrals over all space of $\mathbf{D}_D$ and $\mathbf{D}_A$ have to be calculated leading to

$$p_D = \sum_i d_i \qquad \text{and} \qquad p_A = \sum_i a_i. \tag{2.352}$$

For excitation processes, where no electrons are gained or lost, the relation $-p_D = p_A = p_{\mathrm{DA}}$ is valid. There are two distinct reasons for a rise of p_{DA} using a correlated wave function model: double excitation character and orbital relaxation effects.[87] Hence, using uncorrelated methods like CIS, p_{DA} is always one. Within the ADC method, orbital relaxation effects are treated indirectly via the double excitations. Since core-excited states exhibit a large amount of doubly excited amplitudes and are strongly effected by orbital relaxation effects, the promotion number can be used as a quantitative descriptor of orbital relaxation effects, while plotting the (D/A) densities visualize these effects. In chapter 2.5.9, a detailed discussion about relaxation effects is given.

Since the (D/A) densities contain relaxation effects, it is more convenient to use hole/electron (h/e) densities for characterizing excited states. The (h/e) densities are based on the one-particle transition density matrix (1TDM), which is defined as an exciton wave function represented in an atomic orbital basis set $\{\psi\}$ according to equation 2.174:

$$\gamma^{0I}(r_h, r_e) = \sum_{r,s} \rho^{0I}_{rs} \psi_r(r_h)\psi_s(r_e). \tag{2.353}$$

r_h and r_e describe the coordinates of the hole and excited electron, respectively. The (h/e) densities are then given straightforwardly as

$$\begin{aligned} \rho_h(r_h) &= \int \gamma^{0I}(r_h, r_e)^2 dr_e \\ \rho_e(r_e) &= \int \gamma^{0I}(r_h, r_e)^2 dr_h. \end{aligned} \tag{2.354}$$

Plotting the (h/e) densities visualizes the pure excitation process without relaxation effects.

Furthermore, the 1TDM can be used to calculate exciton sizes by combining the exciton wave function of the 1TDM with statistical analysis in terms of multipole moments.[84,88] In this picture, the size σ of the holes and the excited electrons can be evaluated as root-mean-square deviation of the position operator $\vec{x}$ of the hole and electron, respectively:

$$\begin{aligned} \sigma_h &= \sqrt{\langle \vec{x}_h^2 \rangle - \langle \vec{x}_h \rangle^2} \\ \sigma_e &= \sqrt{\langle \vec{x}_e^2 \rangle - \langle \vec{x}_e \rangle^2}. \end{aligned} \tag{2.355}$$

Straightforwardly, the distance between the centroids of the hole and electron densities can be formulated as

$$d_{h\to e} = |\vec{d}_{h\to e}| = |\langle \vec{x}_e \rangle - \langle \vec{x}_h \rangle|. \tag{2.356}$$

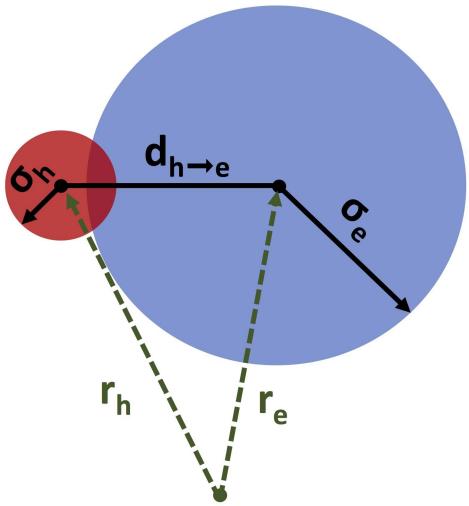

Figure 2.5: Scheme of the hole (red) and electron (blue) densities together with the definition of the hole (r_h) and electron (r_e) position coordinates. Additionally, the corresponding hole (σ_h) and electron (σ_e) sizes are given with the distance between their centroids ($d_{h\to e}$). Due to the generally small core-hole, this scheme indicates the proportion of the core-hole and electron sizes. Furthermore, this illustration can also be transferred to the (D/A) picture with the equivalent descriptors σ_D, σ_A and $d_{D\to A}$.

Figure 2.5 shows a graphical representation of the introduced exciton sizes. As a last step, the dynamic charge separation distance as

$$d_{\text{exc}} = \sqrt{\langle |\vec{x}_e - \vec{x}_h|^2 \rangle} \tag{2.357}$$

is introduced. Here, additional information about correlated electron-hole motions are considered, while $d_{h\to e}$ only quantifies the charge separation of an excited state.[84,88] The exciton sizes are connected via the covariance (COV) between the hole and electron position vectors:

$$\text{COV}(\vec{x}_e, \vec{x}_h) = \langle \vec{x}_e \cdot \vec{x}_h \rangle - \langle \vec{x}_e \rangle \cdot \langle \vec{x}_h \rangle \tag{2.358}$$

$$d^2_{\text{exc}} = d^2_{h\to e} + \sigma^2_h + \sigma^2_e - 2\text{COV}(\vec{x}_e, \vec{x}_h). \tag{2.359}$$

Since the COV does not have an intuitive meaning, this value is normalized against the standard deviation that leads to the Pearson correlation coefficient R_{eh}[84]:

$$R_{eh} = \frac{\text{COV}(\vec{x}_e, \vec{x}_h)}{\sigma_e \sigma_h}. \tag{2.360}$$

The Pearson correlation coefficient ranges from -1 to 1 and can be interpreted as follows: if $R_{eh} > 0$, a positive correlation between the hole and electron exists that can be understood as a concerted motion of the electron and hole quasi-particles. $R_{eh} < 0$ indicates a negative correlation, i.e. the electron and the hole avoid each other dynamically. Pearson correlation values close to 0 denote an independent behavior of the hole and electron.

Since it is not possible to construct a correlated two-body function from the 1DDM, the whole formalism, which was applied to the 1TDM to construct the different exciton sizes and the COV, cannot be translated to the 1DDM. However, with the evaluation of

the multipole moments, one can formulate expressions for the detachment size (σ_D), the attachment size (σ_A) and the distance between the centroids of the charges ($d_{D\to A}$).[84,87]

2.5.9 The Role of Relaxation Effects

Finally, I would like to conclude the theoretical method chapter with a discussion about orbital relaxation effects. The information given in this chapter have already been published by me and my co-authors in *Journal of Chemical Physics, 142 (2015), 214104.*[98] Here, the topic is explained in more detail.

As mentioned before in chapter 2.4, orbital relaxation effects play a crucial role in the description of core-excited states, because a large amount of energy is needed to excite electrons that occupy 1s orbitals to a virtual level. The reason is that core electrons are strongly bound due to the strong Coulomb interaction with the nucleus. This excitation process is accompanied by a rearrangement of the valence electrons due to the reduced shielding of the nucleus.[46–50] Hence, the induced hole leads to a spatial contraction of the electronic wave function that is formally mentioned as orbital relaxation. As a result, a significant lowering in the final state energy is observed compared to cases where the valence electron arrangement of the initial state is maintained.[49] Another typical observation is the scaling of the gross charge rearrangement with the number of valence electrons. The more valence electrons are available, the stronger is the rearrangement of the valence electrons, thus the influence of relaxation effects to the core-excitation energy increases when going to heavier elements.[46,47]

Relaxation Effects in Correlated Core-Excited States

According to the discussion of *Schirmer et al.*[49,76], the contribution of orbital relaxation effects in wave function based post-HF methods can be simply identified. Starting with a CI ansatz, the application of a general excitation operator ($\hat{C}$) to the correlated ground state wave function $|\Psi_0\rangle$ generates a correlated excited state $|\Psi_J^0\rangle$. To truncate the excitation space, the second order of general Rayleigh-Schrödinger perturbation theory can be exploited. In combination with the CVS approximation, the excitation energy ω_{cv} of a core-excited state based on the unperturbed singly core-excited configuration $|\Psi_{cv}\rangle = \hat{c}_v^\dagger \hat{c}_c |\Psi_0\rangle$ is then given in second order as

$$\omega_{cv} = \epsilon_v - \epsilon_c - \langle cv||cv\rangle + U_{cv}(p-h) + U_{cv}(2p-2h) + R_{cv}, \tag{2.361}$$

where v describes virtual orbitals and c refers to the core space. $\langle cv||cv\rangle$ is the first order Coulomb-exchange contribution and ϵ_v and ϵ_c refer to the energies of valence and core orbitals, respectively. R_{cv} contains a partial compensation of 3p-3h contributions in the excited state energy and the ground state correlation energy in second order. For the analysis of relaxation effects, the $U_{cv}(np-nh)$ terms with $n = 1, 2$ are the relevant parts. They describe the interactions of the $|\Psi_{cv}\rangle$ excited configuration with the $np-nh$ excitations, respectively. In quantum chemical methods, relaxation effects can be included indirectly via couplings of $\mathrm{n^{th}}$ excited determinants to higher excited configurations. Since the $U_{cv}(p-h)$ term contains only second order contributions of singly-excited configurations, the remaining $U_{cv}(2p-2h)$ term includes the orbital relaxation information in second order of perturbation theory.[49] Accordingly, a perturbation expansion in higher orders n would result in more $U_{cv}(np-nh)$ terms that contain these contributions via couplings to lower excitation classes. However, I will stay in the second order picture in this discussion.

$U_{cv}(2p-2h)$ can be formulated as

$$U_{cv}(2p-2h) = -2\sum_{c'rs} \frac{\left(1-\frac{1}{2\delta_{vr}}\right)}{\epsilon_r - \epsilon_s} \left(\langle c's|cr\rangle - \delta_{cc'}\langle vs|vr\rangle\right)^2 + MBE, \tag{2.362}$$

where r and s refer to valence occupied or virtual orbitals, while MBE correspond to the remaining genuine many-body effects that will not be discussed here. After expanding equation 2.362 and neglecting the MBE part, one can decompose the term into three parts that exhibit a distinct physical meaning:

$$U_{cv}(2p-2h) = 4S - 2R - 2P. \tag{2.363}$$

For simplicity, the prefactor is defined as

$$A_{vrs} = \frac{\left(1-\frac{1}{2\delta_{vr}}\right)}{\epsilon_r - \epsilon_s}. \tag{2.364}$$

R can be regarded as the relaxation energy for the core-excited state. It contains integrals of the type $\langle c'r|cq\rangle$ and is given as

$$R = \sum_{c'rs} A_{vrs}\langle c's|cr\rangle^2. \tag{2.365}$$

P can be associated with polarization effects induced by the excited electron in the virtual level. Since the integral $\langle vr|vq\rangle$ is contained in P, it is therefore of the same type as R, where v and c are interchanged:

$$P = \sum_{rs} A_{vrs}\langle vs|vr\rangle^2. \tag{2.366}$$

At last, there is the screening term S, which contains the product of both integral types $\langle c'r|cq\rangle$ and $\langle vr|vq\rangle$. S describes the relaxation-induced screening energy of the virtual and core orbitals on each other, which arises from the core-hole interaction with the excited electron:

$$S = \sum_{c'rs} A_{vrs}\langle vs|vr\rangle\langle c's|cr\rangle. \tag{2.367}$$

According to equation 2.363, R and P have negative signs, while the sign of S is positive. Therefore, R and P reduce the excitation energy, while S acts in the opposite way. Since the Coulomb integrals in R, P and S are not independent from each other, the relation between the three parts must be described via the Schwarz inequality ansatz for a suitably defined scalar product, leading to the result

$$|R||P| \geq \frac{S^2}{4}. \tag{2.368}$$

Hence, R and P must be described in a balanced way, otherwise the core excitation energy is not lowered due to the screening S.

Relaxation Effects within the CVS-ADC Scheme

At last, the ansatz for the description of relaxation effects in correlated core-excited states is adapted to the CVS-ADC method. With respect to equation 2.361, the excitation energies

at the ADC level are by construction exact up to second order.[76] Hence, orbital relaxation, polarization and screening effects are already included within the CVS-ADC(2) approach. According to *Schirmer*, the R, P and S contributions are identified to be included in the terms belonging to the coupling blocks p-h,2p-2h and 2p-2h,p-h of the ADC secular matrix.[76] This is straightforward, because these effects are associated with couplings between different excitation classes. In other words, orbital relaxation and polarization effects are included indirectly within the CVS-ADC method via couplings between the excited configurations. Since both CVS-ADC(2) and CVS-ADC(3) comprise only two excitation classes, only the singly excited configurations are relaxed via couplings to the doubly excited configurations and the doubly excited excitations remain unrelaxed. Triply excited configurations that would relax the doubles are first included in CVS-ADC(4).

Comparing the strict and extended second order CVS-ADC approximations, only the first order terms of the 2p-2h-diagonal-block is added in the extended variant and the coupling blocks that provide the R, P and S contributions are unchanged (see Figure 2.2). As a consequence, the description of the doubles is improved in CVS-ADC(2)-x, which results in an increased amount of doubly excited amplitudes (R2). This usually leads to a lowering of the excitation energies[79,181] in CVS-ADC(2)-x compared to CVS-ADC(2)-s, which improves the core-excitation energy towards experimental values.

Going to the third order CVS-ADC level, the 2p-2h-diagonal-block remains the same compared to CVS-ADC(2)-x. Hence, the doubly excited amplitudes are not improved any further within CVS-ADC(3). However, the matrix equations that describe the other remaining blocks are expanded one order higher in perturbation theory compared to CVS-ADC(2)-x. The single excitations are thus improved in CVS-ADC(3), since the p-h-diagonal-block is expanded in third order instead of second order going from CVS-ADC(2)-x to CVS-ADC(3). As a consequence, the interaction of the ground state correlation with higher excitation classes is improved considering the simple Rayleigh-Schrödinger ansatz (equation 2.361). The crucial expansion of CVS-ADC(3) compared to CVS-ADC(2)-x are the coupling elements between singles and doubles, which are now treated in second order of perturbation theory. Evaluating the types of integrals of the added second order contributions of the coupling block (see equations 2.328 – 2.331), there are only two integrals, which can be assigned to the types included in P ($\langle vr|vq\rangle$) and three integrals to the types in R ($\langle c'r|cq\rangle$), i.e.

$$\begin{aligned} M^{(2,1)}_{Ia,Klcd} &\rightarrow 2\langle Kb\|jI\rangle \\ M^{(2,2)}_{Ia,Klcd} &\rightarrow \langle ab\|jc\rangle,\ \langle ab\|jd\rangle \\ M^{(2,4)}_{Ia,Klcd} &\rightarrow \langle aK\|jI\rangle. \end{aligned} \tag{2.369}$$

The matrix element $M^{(2,3)}_{Ia,Klcd}$ contains no integrals of the types included in P or R. In contrast, all of the three contributing first order terms of the coupling blocks in the case of CVS-ADC(2)-x (equation 2.326) can be assigned to P or R. As a consequence, the second order expansion of the coupling blocks in CVS-ADC(3) results in a decreased effective coupling. Since the energy level of the double excitations is not changed compared to CVS-ADC(2)-x, the core excitation energies thus should become higher compared to CVS-ADC(2)-x. Eventually, it can be assumed that the inequality according to (2.368) is unbalanced in the CVS-ADC(2)-s and CVS-ADC(3) schemes, while at the CVS-ADC(2)-x level the description of P and R seems optimal. To give this information beforehand, this assumption will be proven true as shown in chapters 4 and 5.

To quantitatively determine the contribution of relaxation effects, there are two possibilities available. One the one hand, the amount of doubly excited amplitudes (R2)

can be used as a rough indirect indicator to quantify the influence of orbital relaxation effects. However, using the R2 value is theoretically not proper, because it just counts the number of doubly excited amplitudes, while the relaxation effects are included in the couplings between singles and doubles. In addition, the quantitative interpretation of the R2 value is only valid for the CVS-ADC method itself, thus there is no possibility for a comparison with other methods. An alternative to R2 are quantification tools based on the core-excited state density, which gives also access to visualizing these effects, i.e. detachment/attachment densities (D/A), the corresponding promotion numbers p_{DA} and exciton sizes (see chapter 2.5.8). Since the (D/A) densities can be generally obtained independently of the employed quantum chemical method, a direct comparison between different methods is quantitatively possible. Chapter 5 provides an analysis and visualization of relaxation effects by means of chosen molecules.

Chapter 3

Implementation of the CVS-ADC/CVS-ISR Approaches

In this chapter I describe the implementation of the CVS-ADC methods up to third order and the CVS-ISR approach up to second order into a development version of the `adcman`[93] program, which is part of the `Q-Chem`[94] program package. Therefore, I give an overview of the general structure of the interface and introduce important external libraries that are used by the routines in `adcman`. As the next step, I explain the necessary modifications and transformations of the CVS-ADC and CVS-ISR working equations into an efficient C++ code. The discussion about the implementation is concluded with an overview of the implemented CVS-ADC/CVS-ISR features.

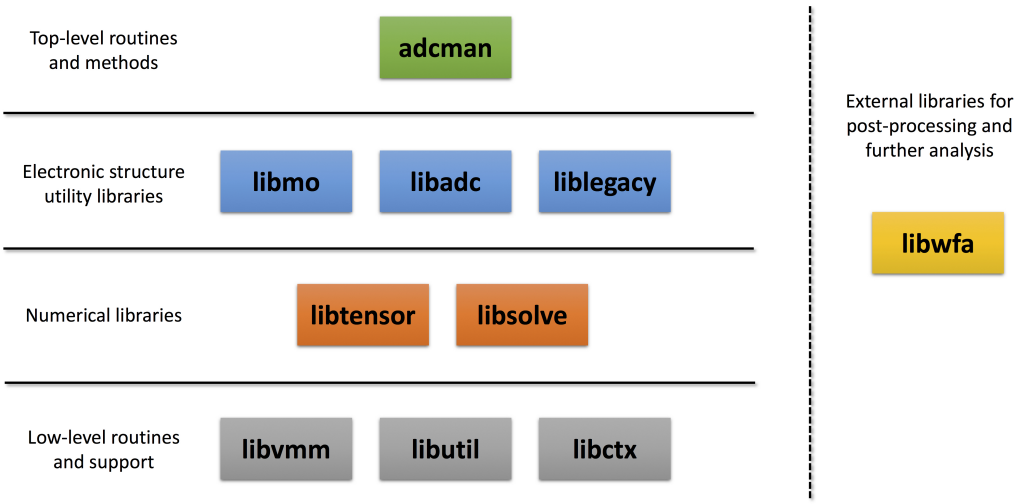

Figure 3.1: Overview of the implementation of ADC methods in the `Q-Chem` package.[84,93,182] The lower two levels contain general supporting and numerical libraries, which are not related directly to electronic structure theory. Only the upper levels contain ADC and electronic structure specific code.

3.1 General Structure and Interface

Being part of the `Q-Chem` program package, `adcman` takes advantage of available interfaces that perform numerical processes and provide principle support for low-level subroutines, e.g. memory management. Here, I introduce these modules briefly. For detailed information, I refer to the literature.[93,94,182] In Figure 3.1, the general structure of the code is summarized. All modules are written in the object-oriented C++ programming language. On the top, there is the `adcman` module, which contains all top-level routines and methods necessary for an ADC calculation. Here, the implemented code coordinates the calculation process, sets up the solver and writes the results into an output file. Besides the fundamental routines of the CVS-ADC/CVS-ISR variants at specific order, changes corresponding to the integral symmetry due to the additional core space as well as a modified output handler were implemented in `adcman`.

The next sub-level contains electronic structure related libraries and utilities. In the `libadc` module, all ADC and ISR equations are implemented explicitly. Here, I added all CVS-ADC/CVS-ISR equations, which are summarized in chapter 3.2. `liblegacy` is the gateway between the ADC code and the `Q-Chem` interface. These routines help to import data from other `Q-Chem` modules, for example all SCF results and MOs, which are needed for the CVS-ADC calculation. Furthermore, with the `liblegacy` functions it is possible to export data from `adcman`, e.g. density matrices, which can be post-processed in external modules like the `libwfa`[84,86–88] library. The `libwfa` module is a wave function analysis package, which amongst others is responsible for the calculation of exciton sizes, detachment/attachment densities and all other descriptors described in chapter 2.5.8. The `libmo` module contains routines to set up the MO spaces, integrals and symmetry using the information imported from `Q-Chem` via the `liblegacy` interface. Hence, both `libmo` and `liblegacy` are important for CVS-ADC calculations, because all integrals and Fock-matrix elements are indexed and created corresponding to the additional restriction

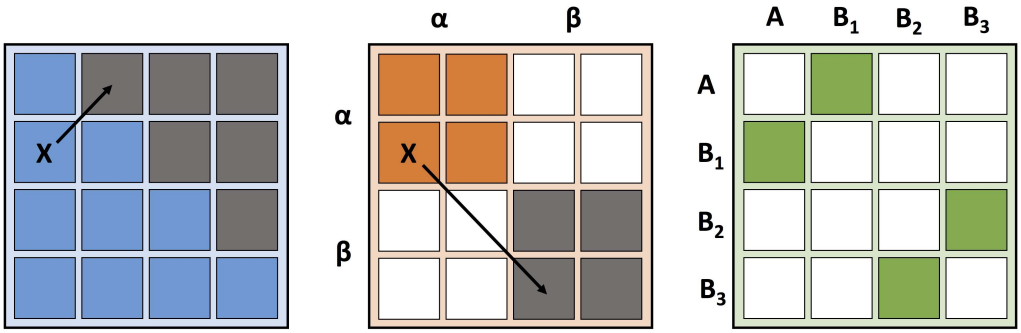

Figure 3.2: Schematic illustration of the symmetry elements available in the `libtensor` library.[182] In these examples, tensors of the rank 2 are shown, whose storage is simplified due to symmetry elements, i.e. permutational symmetry (blue), spin symmetry (orange) and point group symmetry (green). The colored blocks represent the canonical blocks, which are stored, while the white blocks are zero due to respective symmetry elements. The grey blocks are non-zero, but they do not have to be stored, because they can be constructed from the canonical blocks due to symmetry.

of the core space.

Furthermore, `libmo` transforms the imported data in a format being compatible to the `libtensor`[182] interface, which can be called "the heart" of the code, since it contains all numerical routines to perform tensor algebra. Basically, `libtensor` is an open-source C++ object-oriented library for block-tensors, which has been developed for post-HF electronic structure methods. The tensor operations that are required to solve the CVS-ADC eigenvalue problem are fully parallelized and efficiently implemented. Tensors of arbitrary order and size are stored in a blockwise manner, exploiting different kinds of symmetry to limit the amount of required memory. These symmetry properties are permutation symmetry, Abelian point group symmetry and spin symmetry. Figure 3.2 illustrates the different symmetry elements and how they influence the block-tensor structure. Only non-zero elements, which cannot be created due to symmetry operations, are stored in memory or on disk. An example for permutation symmetry are two-electron integrals, which exhibit the following permutational symmetry:

$$\langle ij||ab\rangle = -\langle ji||ab\rangle = -\langle ij||ba\rangle = \langle ji||ba\rangle. \tag{3.1}$$

The spin-symmetry is adapted by partitioning the tensor blocks into $\alpha\alpha$, $\beta\beta$, $\alpha\beta$ and $\beta\alpha$ sub-blocks and mapping identical entries between them. In the case of closed-shell restricted calculations, the spin-orbitals are stored only once for the *alpha*-electrons. Furthermore, the mapping between the blocks allows for unrestricted calculations of closed-shell systems, which has been straightforwardly exploited for the CVS-ADC implementation. Besides creation and storage simplifications, the `libtensor` suite contains a plethora of functions for numerical operations between and on block-tensors. Most important for CVS-ADC equations are contractions of block-tensors X and Y to a resulting tensor Z. If X and Y consist of smaller tensors, e.g. indicated by outer indices i and j, the contraction can be written as the sum of pairwise block contractions:

$$Z_{ij} = \sum_k X_{ik} Y_{kj}, \tag{3.2}$$

where k corresponds to all inner tensor indices. Since the `libtensor` interface is based on

object-oriented templates, the implementation of post-HF equations is thus very simple. The following C++ code snippet shows parts of the CVS-ADC implementation of the second order p-h,p-h block in the `libadc` module. Algebraically, this equation is given in matrix-vector product form (see chapter 3.2 for further explanations) as

$$r^{(2)}_{Ia} = \sum_b v_{Ib} \left(f_{ab} + I^{(2)}_{ab} \right) - \sum_J f_{IJ} v_{Ja} - \sum_{Jb} \langle Ja \| Ib \rangle v_{Jb}. \tag{3.3}$$

```
class cvs_adc2_u11 : public adc_timings<cvs_adc2_u11> {
//Definition of the class
public:
    static const char k_clazz[]; // Class name

private: //Definition of the integrals and elements
    any_tensor<2, double> &f_cc; //!< Fock matrix (CC)
    any_tensor<2, double> &f_vv; //!< Fock matrix (VV)
    any_tensor<4, double> &i_cvcv; //!< Integral \f$<Ia||Jb>\f$
    any_tensor<2, double> &i1; //!< Intermediate \f$ I^{(2)}_{ab} \f$
    any_tensor<2, double> &u1; //!< Input vector (CV)

public: //Constructor to initialize private elements with real data
    //! constructor
    cvs_adc2_u11(
        any_tensor<2, double> &f_cc_,
        any_tensor<2, double> &f_vv_,
        any_tensor<4, double> &i_cvcv_,
        any_tensor<2, double> &i1_,
        any_tensor<2, double> &u1_ ) :
        f_cc(f_cc_), f_vv(f_vv_), i_cvcv(i_cvcv_),
        i1(i1_), u1(u1_) { }

    /** \brief Performs the computation
        \param[out] r1 Result vector
     **/
    void compute(expr_lhs<2, double> &r1) {

        cvs_adc2_u11::start_timer();

        letter I, J, a, b;

        r1(I|a) =
            contract(b, u1(I|b), f_vv(a|b) + 0.25 * i1(a|b))
            - contract(J, f_cc(I|J), u1(J|a))
            - contract(J|b, i_cvcv(J|a|I|b), u1(J|b));

        cvs_adc2_u11::stop_timer();
    }
};
```

Hence, the implementation of CVS-ADC equations is straightforward using the `libtensor` interface. For further detailed information about the `libtensor` library, I recommend the publication by *Epifanovsky* and *co-workers.*[182]

The second important numerical library is `libsolve`, which contains all routines of generic solvers, e.g the Davidson algorithm, which are called from the top-level `adcman` routines. `libsolve` is also based on the `libtensor` interface. At last, there are low-level routines, which are responsible for support and operations in the background. The `libvmm` routines manage the virtual memory, while `libctx` is a context manager based on key-value mapping of data objects. All imported or generated objects, e.g. integrals, keywords, tensors, vectors, etc., are stored in the context and can be easily accessed by other routines. The `libutil` library contains further low-level machine-dependent routines.

Eventually, the general procedure of a CVS-ADC calculation can be summarized as follows:

1. A HF ground state SCF calculation is performed in `Q-Chem` and all results, i.e. integrals, orbitals and property matrices are imported via the `liblegacy` interface. Furthermore, general information about basis sets, point group symmetry and other settings are imported as well.
2. The general block-tensor spaces are set up.
3. The `Q-Chem` integral code is used to calculate all antisymmetrized two-electron integrals and the results are imported into the interface. Therefore, transformations from an atomic orbital (AO) basis into an MO basis and vice versa are performed using the `libmo` module.
4. A MP ground state calculation in `adcman` is performed, the results are saved in the context and printed out.
5. Setting up all necessary prerequisites in the `adcman` program depending on the chosen CVS-ADC order.
6. Generating guess vectors for the Davidson solver and initialize the settings, e.g. number of iterations and convergence criteria.
7. Starting the solver and printing out a summary for each iteration step to the output.
8. After convergence, the CVS-ADC eigenvectors and eigenvalues are stored.
9. Properties, i.e. transition-density matrices, density matrices and state-to-state transition matrices are calculated using the converged CVS-ADC eigenvectors and in the case of the last two the CVS-ISR implementation. All results are stored in the context.
10. If desired, the densities are exported to the `libwfa` module to perform an advanced wave function analysis.
11. All results are summarized and printed, which is controlled by the `adcman` module.

3.2 CVS-ADC and CVS-ISR Equations Implemented as Matrix-Vector Products

As mentioned before, the implementation of the ADC working equations in `adcman/libadc` using the `libtensor` interface is straightforward. In chapter 2.5.7, the CVS-ADC and CVS-ISR working equations as matrix elements are summarized. Using these equations, the CVS-ADC secular matrix, transition moment matrix and CVS-ISR property matrix

can be constructed directly. However, diagonalizing the whole CVS-ADC matrix is computationally demanding and often impossible for medium-sized chemically relevant systems. As mentioned before, the core-excited states of interest are usually the energetically lowest, thus an iterative diagonalization scheme, i.e. the Davidson algorithm, is employed to solve the CVS-ADC eigenvalue problem. Within the Davidson procedure, the subspace diagonalization of large sparse matrices is obtained via appending modified preconditioned residue vectors to the subspace iteratively. Therefore, the CVS-ADC/CVS-ISR matrix equations have to be transformed into matrix-vector products:

$$\begin{aligned} r_{Ia} &= \sum_{Jb} M_{Ia,Jb} v_{Jb} + \sum_{c<d} M_{Ia,Klcd}\, v_{Klcd} \\ r_{Ijab} &= \sum_{Kc} M_{Ijab,Kc} v_{Kc} + \sum_{c<d} M_{Ijab,Klcd}\, v_{Klcd} \end{aligned} \tag{3.4}$$

where r_{Ia} is the resulting vector for single core excitations and r_{Ijab} refers to the resulting vector for double excitations, where one occupied orbital is restricted to correspond to the core space. Arbitrary single- and double-excitation vectors, which are multiplied with the CVS-ADC matrix elements, are denoted, for example, as v_{Ia} and v_{Klcd}, respectively. The initial guess for the Davidson solver can be constructed from the diagonal elements of the CVS-ADC matrix. Concerning the computational cost, this procedure has a large advantage, because the formal scaling of the CVS-ADC matrices are reduced due to matrix-vector multiplications instead of full matrix-matrix operations. Regarding CVS-ADC(3), which scales formally with the order (M^8) where M is the number of basis functions, the scaling is reduced to (M^6) using the Davidson solver. This effect is due to the multiple Kronecker deltas, which vanish when a matrix element is multiplied with an arbitrary excitation vector, e.g.

$$r^{(0)}_{Ia} = \sum_{Jb} M^{(0)}_{Ia,Jb} v_{Jb} = \sum_{Jb} (\epsilon_a - \epsilon_I)\, \delta_{ab}\delta_{IJ} v_{Jb} = \sum_{b} \epsilon_a v_{Ib} - \sum_{J} \epsilon_I v_{Ja}. \tag{3.5}$$

Furthermore, it is not necessary to store the whole CVS-ADC matrix on disk.

Next, strategies to reduce the prefactor of the computational scaling are employed. At first, it is advantageous to transform the ADC equations into a non-canonical basis of orthonormal occupied and virtual orbitals via unitary transformations on the respective orbital spaces. As a consequence, the working equations have to be modified:

1. The restrictions ($c < d$) of the spin-orbitals in real space have to be lifted. Therefore, the following terms are scaled as

   - $M^{(1)}_{Ia,Klcd} \rightarrow \frac{1}{\sqrt{2}} M^{(1)}_{Ia,Klcd}$
   - $M^{(1)}_{Ijab,Kc} \rightarrow \frac{1}{\sqrt{2}} M^{(1)}_{Ijab,Kc}$
   - $M^{(1)}_{Ijab,Klcd} \rightarrow \frac{1}{2} M^{(1)}_{Ijab,Klcd}$.

   After the restrictions are lifted, the double excitation guess and eigenvectors as well as the t- amplitudes, anti-symmetrized two-electron integrals and diagonal elements possess the following symmetry

   - $v_{Ijab} = -v_{jIab} = v_{jIba} = -v_{Ijba}$

   Furthermore, the lifting of the restriction leads to the condition

- $M^{(1)}_{Ijab,Klcd} \begin{cases} = 0 & \text{if } a = b \text{ or } c = d \\ \neq 0 & \text{all other cases} \end{cases}$

  Note that for general ADC, restrictions that correspond to the occupied space, e.g. $i < j$, have to be lifted as well. However, in the case of CVS-ADC, one index corresponds to the core space, thus I can never be equal to j and the corresponding restriction is not necessary.

2. Terms that contain orbital energy differences in the denominator, e.g. t-amplitudes, have to be transformed as well, since the Fock-matrix is non-orthogonal in a non-canonical basis and it thus has to be inverted. In the canonical form, a t-amplitude is given as

   - $t_{ijab} = \frac{\langle ij||ab\rangle}{K_{Ijab,Klcd}}$ with $K_{Ijab,Klcd} = (\epsilon_a + \epsilon_b - \epsilon_I - \epsilon_j)\,\delta_{ac}\delta_{bd}\delta_{IK}\delta jl$ as diagonal matrix

   One can avoid the inversion of $K_{Ijab,Klcd}$ via constructing a new four-index entity $\tilde{t} := K^{-1}I$, where I is the antisymmetrized two-electron integral, and then solve $K\tilde{t} = I$, which can be easily transformed into a new basis.

As a next step, the scaling prefactor can be further reduced using certain expressions, which can be stored on disk or in memory and can be used in the remaining calculations without reevaluating the respective terms. This saves computational effort. Table 3.1 summarizes these implemented expressions. Here, ρ^0_{rs} corresponds to the MP2 density

Table 3.1: Summary of expressions used to describe the CVS-ADC and transition density matrix equations. $\mathcal{P}_{rs}$ is a general permutation operator that interchanges the orbitals r and s.

$$T^2_{ijab} = \sum_{kc} t_{ikac} t_{jkbc}$$

$$T^D_{ijab} = [1 - \mathcal{P}_{ij}] \left[[1 - \mathcal{P}_{ab}] \left[\frac{\sum_{kc} t_{ikac}\langle kb||jc\rangle - \frac{1}{2}\sum_{cd} t_{ijcd}\langle ab||cd\rangle - \frac{1}{2}\sum_{kl}\langle ij||kl\rangle t_{klab}}{\epsilon_a + \epsilon_b - \epsilon_i - \epsilon_j} \right] \right]$$

$$\rho^0_{ij} = -[1 + \mathcal{P}_{ij}] \left[\frac{1}{4} \sum_{kab} t_{ikab} t_{jkab} \right]$$

$$\rho^0_{ia} = -\frac{1}{2(\epsilon_a - \epsilon_i)} \left(\sum_{jbc} t_{ijbc}\langle ja||bc\rangle + \sum_{jkb}\langle jk||ib\rangle t_{jkab} \right)$$

$$\rho^0_{ab} = [1 + \mathcal{P}_{ab}] \left[\frac{1}{4} \sum_{ijc} t_{ijac} t_{ijbc} \right]$$

matrix corrections of the one-particle HF ground state density matrix, which is in the case of CVS-ADC(3) not always an adequate treatment.[81] A better expression can be obtained using the Dyson expansion method.[183] Here, the explicit density that appears in certain third order expressions in the CVS-ADC(3) matrix can be obtained iteratively with respect to the so-called self-energy

$$\Sigma_{pq}(\infty) = \sum_{rs} \langle pq||qs\rangle \rho^{(i)}_{sr}, \tag{3.6}$$

where the difference between the exact one-particle density matrix and the HF ground-state density matrix is defined as the correlation density $\rho^{(i)}_{sr}$. An implementation of the Dyson expansion is not available yet, but can be added in the future.

Further simplifications that result in computational savings are obtained using intermediates of the $M^{(2)}_{Ia,Jb}$ and $M^{(3)}_{Ia,Jb}$ matrix elements. They can be constructed using terms that are multiplied with the same vector and contracted over the same indices, thus the result has to be calculated once and can be stored. In the following sections, the CVS-ADC and CVS-ISR working equations as optimized matrix-vector products, which I implemented in the `libadc` module are summarized.

3.2.1 CVS-ADC up to Third Order

p-h,p-h block:

The implementation of the zeroth and first order terms is straightforward. The orbital energies are represented in the non-canonical Fock-matrix elements f_{rs}, which are imported from the `Q-Chem/liblegacy` interface.

$$r^{(0)}_{Ia} = \sum_b v_{Ib} f_{ab} - \sum_J f_{IJ} v_{Ja} \tag{3.7}$$

$$r^{(1)}_{Ia} = -\sum_{Jb} \langle Ja \| Ib \rangle v_{Jb} \tag{3.8}$$

The second order contributions of the p-h,p-h block can be merged into the intermediate I_{ab}, which has to be calculated once and then can be stored in memory or on disk.

$$r^{(2)}_{Ia} = \frac{1}{4} \sum_b v_{Ib}\ I^{(2)}_{ab} \tag{3.9}$$

with

$$I^{(2)}_{ab} = \sum_{ijc} t_{ijac} \langle ij \| bc \rangle + \sum_{ijc} t_{ijbc} \langle ij \| ac \rangle \tag{3.10}$$

The third order terms are summarized in three intermediates as

$$r_{Ia} = \sum_b v_{Ib}\ I^{(3)}_{ab} + \sum_J I^{(3)}_{IJ}\ v_{Ja} + \sum_{Jb} I^{(3)}_{IaJb}\ v_{Jb}, \tag{3.11}$$

where the intermediates are given as

$$\begin{aligned} I^{(3)}_{ab} = {} & [1 + \mathcal{P}_{ab}] \frac{1}{4} \sum_{ijc} \left(t_{ijac} + T^D_{ijac} \right) \langle ij || bc \rangle \\ & - [1 + \mathcal{P}_{ab}] \left[\frac{1}{2} \sum_{ijc} t_{ijac} \left(\sum_{kd} t_{ikcd} \langle kb || jd \rangle - \frac{1}{4} \sum_{de} t_{ijde} \langle cb || de \rangle \right) \right] \\ & - [1 + \mathcal{P}_{ab}] \left[\sum_{ic} \langle ia || bc \rangle \rho^0_{ic} \right] \\ & + \sum_{ij} \langle ia || jb \rangle \rho^0_{ij} + \sum_{cd} \langle ac || bd \rangle \rho^0_{cd} \end{aligned} \tag{3.12}$$

$$I^{(3)}_{IJ} = [1 + \mathcal{P}_{IJ}] \left[\sum_{ka} \langle kI || Ja \rangle \rho^0_{ka} \right] - \sum_{kl} \langle kI || lJ \rangle \rho^0_{kl} - \sum_{ab} \langle Ia || Jb \rangle \rho^0_{ab} \tag{3.13}$$

$$
\begin{aligned}
I^{(3)}_{IaJb} = [1 + \mathcal{P}_{Ia,Jb}] \Bigg(& \frac{1}{2} \sum_{c} \langle Ja || Ic \rangle \rho^{0}_{bc} - \sum_{k} \langle kI || Ja \rangle \rho^{0}_{kb} \Bigg) \\
& + \frac{1}{2} \sum_{cd} \langle Ic || Jd \rangle \sum_{kl} t_{klac} t_{klbd} - \sum_{kl} \langle lI || kJ \rangle T^{2}_{klab}.
\end{aligned}
\tag{3.14}
$$

In the first intermediate $I^{(3)}_{ab}$, the terms related to the δ_{IJ} expressions are merged, i.e. the full equations 2.313 – 2.316 and parts of 2.317 – 2.320. The remaining parts of the equations 2.317 – 2.320 are related to δ_{ab} and are summarized in intermediate $I^{(3)}_{IJ}$. The third intermediate contains the remaining third order expressions (equations 2.321 – 2.325), which do not contain any Kronecker delta term and are thus merged to $I^{(3)}_{IaJb}$.

p-h,2p-2h block:

Regarding the p-h,2p-2h coupling elements, further simplifications due to the hermicity and symmetry properties of the CVS-ADC matrix can be applied. Since the matrix elements are multiplied with an arbitrary vector, the arbitrary virtual orbital indices c and d can be defined to be equal, thus the first two integrals of equation 2.326 can be merged and the resulting first order term of the p-h,2p-2h coupling block is given as

$$
r^{(1)}_{Ia} = \frac{1}{\sqrt{2}} \left(2 \sum_{jKb} \langle jK \| Ib \rangle v_{jKab} - \sum_{jbc} v_{jIbc} \langle ja \| bc \rangle \right). \tag{3.15}
$$

Similar simplifications can be applied to the second order expressions, where the terms included within the equations 2.328 and 2.329 are merged, respectively.

$$
\begin{aligned}
r^{(2)}_{Ia} = \frac{1}{\sqrt{2}} \Bigg[& 2 \sum_{\substack{cdl \\ bj}} t_{ljdb} \langle jc \| ab \rangle v_{lIcd} - 2 \sum_{\substack{cKl \\ bj}} t_{ljcb} \langle jI \| Kb \rangle v_{lKac} \\
& + \frac{1}{2} \sum_{\substack{cdl \\ jm}} t_{jmcd} \langle jm \| la \rangle v_{lIcd} - \sum_{\substack{cdKl \\ j}} t_{ljcd} \langle jI \| Ka \rangle v_{lKcd} \Bigg].
\end{aligned}
\tag{3.16}
$$

2p-2h,p-h block:

In the case of the 2p-2h,p-h block, the simplifications applied to the p-h,2p-2h block equations cannot be adapted and thus the first and second order expressions are given as

$$
r^{(1)}_{jIab} = \frac{1}{\sqrt{2}} \left(\sum_{K} [\langle jI \| Kb \rangle v_{Ka} - \langle jI \| Ka \rangle v_{Kb}] - \sum_{c} v_{Ic} \langle jc \| ab \rangle \right) \tag{3.17}
$$

$$
\begin{aligned}
r^{(2)}_{jIab} = \frac{1}{\sqrt{2}} \Bigg[& [1 - \mathcal{P}_{ab}] \sum_{Klc} t_{jlac} \langle lK \| Ic \rangle v_{Kb} + \sum_{c} v_{Ic} \Bigg[[1 - \mathcal{P}_{ab}] \sum_{kd} t_{jkbd} \langle ka \| cd \rangle + \\
& \frac{1}{2} \sum_{kl} \langle kl \| jc \rangle t_{klab} \Bigg] - \sum_{Klc} \langle lK \| Ic \rangle t_{jlab} v_{Kc} \Bigg].
\end{aligned}
\tag{3.18}
$$

2p-2h,2p-2h block:

The zeroth-order matrix-vector products of the 2p-2h,2p-2h block can be constructed straightforwardly as

$$r^{(0)}_{jIab} = \sum_c \left(v_{jIbc} f_{ac} - v_{jIac} f_{bc}\right) - \sum_l f_{jl} v_{lIab} - \sum_K f_{IK} v_{jKab}. \tag{3.19}$$

In the case of the first order contributions, a few simplifications can be introduced similar to the first order p-h,2p-2h block equations. Here, permutation symmetry as described above can be exploited to merge certain integrals when defining the arbitrary indices c and d to be equal. The resulting first order vector is then given as

$$\begin{aligned} r^{(1)}_{jIab} = &\frac{1}{2}\sum_{cd} v_{jIcd}\langle ab\|cd\rangle + \frac{1}{2}\sum_{Kl}\langle jI\|lK\rangle v_{lKab} \\ &- \sum_{Kc}\left[v_{jKac}\langle Kb\|Ic\rangle - v_{jKbc}\langle Ka\|Ic\rangle\right] \\ &+ \sum_{lc}\left[\langle jc\|la\rangle v_{lIbc} - \langle jc\|lb\rangle v_{lIac}\right]. \end{aligned} \tag{3.20}$$

Diagonal Elements:

The initial guess for the Davidson algorithm is constructed using the diagonal elements of the respective CVS-ADC matrix. These are

$$D^{(0)}_{Ia} = f_{aa} - f_{II} \tag{3.21}$$

$$D^{(1)}_{Ia} = -\langle Ia\|Ia\rangle \tag{3.22}$$

$$D^{(2)}_{Ia} = \frac{1}{2}\sum_{ijc} t_{ijac}\langle ij\|ac\rangle \tag{3.23}$$

$$D^{(3)}_{Ia} = I^{(3)}_{aa} + I^{(3)}_{II} + I^{(3)}_{IaIa} \tag{3.24}$$

$$D^{(0)}_{jIab} = f_{aa} + f_{bb} - f_{II} - f_{jj} \tag{3.25}$$

$$D^{(1)}_{jIab} = \langle ab\|ab\rangle + \langle Ij\|Ij\rangle - \langle Ia\|Ia\rangle - \langle ja\|ja\rangle - \langle Ib\|Ib\rangle - \langle jb\|jb\rangle. \tag{3.26}$$

The final guess vectors used at a specific CVS-ADC level are given in Table 3.2.

3.2.2 Second Order CVS-ADC Transition Moments

The equations for the spectral amplitudes are implemented in the transition density matrix (TDM) form using the non-canonical orbital basis as well. Therefore, the spectral amplitudes, which are summarized in chapter 2.5.7, are multiplied with the p-h and 2p-2h components of the respective excited state eigenvectors. This results in a scalar product, i.e the transition moment T, as

$$T = \sum_{Ia} F_{Ia} v_{Ia} + \sum_{Ijab} F_{Ijab} v_{Ijab}. \tag{3.27}$$

To obtain the TDM elements, this expression needs to be solved for the matrix representation of an arbitrary one-particle operator D_{cp}. Using the definition of the one-particle

Table 3.2: Summary of the CVS-ADC guess vectors used for the Davidson algorithm. The contributions correspond to a specific CVS-ADC order in perturbation theory.

CVS-ADC(1):	$v^{1}_{\text{singles}} = D^{(0)}_{Ia} + D^{(1)}_{Ia}$
CVS-ADC(2)-s:	$v^{2s}_{\text{singles}} = D^{(0)}_{Ia} + D^{(1)}_{Ia} + D^{(2)}_{Ia}$
	$v^{2s}_{\text{doubles}} = D^{(0)}_{jIab}$
CVS-ADC(2)-x:	$v^{2x}_{\text{singles}} = v^{2s}_{\text{singles}}$
	$v^{2x}_{\text{doubles}} = D^{(0)}_{jIab} + D^{(1)}_{jIab}$
CVS-ADC(3):	$v^{3}_{\text{singles}} = D^{(0)}_{Ia} + D^{(1)}_{Ia} + D^{(2)}_{Ia} + D^{(3)}_{Ia}$
	$v^{3}_{\text{doubles}} = v^{2x}_{\text{doubles}}$

MP2 ground state density matrix elements (see Table 3.1), the resulting CVS-ADC TDM elements in second order are then simply given as

$$\rho_{aI} = v_{Ia} - \sum_{b} \rho^{0}_{ab} v_{Ib} \tag{3.28}$$

and

$$\rho_{jI} = -\sum_{a} \rho^{0}_{ja} v_{Ia} + \frac{1}{\sqrt{2}} \sum_{kab} v_{kIab} t_{jkab}. \tag{3.29}$$

The spectral amplitudes of equations 2.334 and 2.335 are merged in ρ_{aI}, while ρ_{jI} contains the contributions of equations 2.336 - 2.338.

3.2.3 Second Order CVS-ISR Property Elements

The implementation of the CVS-ISR properties up to second order is similar to the one of the TDM. Here, the property equations (see chapter 2.5.7) are transformed into the one-particle density matrix (DM) form (see equation 2.174). Due to the ISR formalism, the operator representation needs to be multiplied from the left and from the right with excited state eigenvectors $\mathbf{X}$ and $\mathbf{Y}$, in this case the one obtained after solving the CVS-ADC eigenvalue problem, to obtain the corresponding excited state property P_{XY} as

$$\begin{aligned} P_{XY} = &\sum_{Ia,Jb} X^{\star}_{Ia} D_{Ia,Jb} Y_{Jb} + \sum_{Ia,Klcd} X^{\star}_{Ia} D_{Ia,Klcd} Y_{Klcd} \\ &+ \sum_{Ijab,Kc} X^{\star}_{Ijab} D_{Ijab,Kc} Y_{Kc} + \sum_{Ijab,Klcd} X^{\star}_{Ijab} D_{Ijab,Klcd} Y_{Klcd}. \end{aligned} \tag{3.30}$$

The final equations for the DM are obtained via sorting all terms by the respective one-particle matrix representation elements d_{pq}. Table 3.3 contains further definitions of intermediates, which simplify the final CVS-ISR working equations. They have to be calculated once and can then be stored.

Table 3.3: Summary of expressions used to describe the CVS-ISR property equations. X and Y correspond to elements of CVS-ADC eigenvectors.

$dp^1_{IJ} = -\sum_a X^*_{Ja} Y_{Ia}$	$dp^2_{IJ} = -\sum_{abk} X^*_{kJab} Y_{kIab}$
$dp^2_{kl} = -\sum_{abJ} X^*_{kJab} Y_{lJab}$	$dp^1_{ab} = \sum_I X^*_{Ia} Y_{Ib}$
$dp^2_{ab} = 2\sum_{cIk} X^*_{kIac} Y_{kIbc}$	$dp_{bk} = \sum_{Ia} X^*_{kIab} Y_{Ia}$
$dp_{kb} = \sum_{Ia} X^*_{Ia} Y_{kIab}$	

Zeroth order:

The zeroth-order expressions, which only consist of the CVS-ADC eigenvectors, are given below.

$$\rho^{XY(0)}_{IJ} = dp^1_{IJ} + dp^2_{IJ} \tag{3.31}$$

$$\rho^{XY(0)}_{kl} = dp^2_{kl} \tag{3.32}$$

$$\rho^{XY(0)}_{kb} = \sqrt{2} dp_{kb} \tag{3.33}$$

$$\rho^{XY(0)}_{bk} = \sqrt{2} dp_{bk} \tag{3.34}$$

$$\rho^{XY(0)}_{ab} = dp^1_{ab} + dp^2_{ab} \tag{3.35}$$

Second order:

The second order terms are simplified using the definitions summarized in Tables 3.1 and 3.3. The first DM element contains the second term of equation 2.343 and is given as

$$\rho^{XY(2)}_{kl} = \sum_{cb} \left[dp^1_{cb} \sum_{dm} t^*_{lmbd} t_{kmcd} \right]. \tag{3.36}$$

The matrix element $\rho^{XY(2)}_{ab}$ is given as

$$\rho^{XY(2)}_{ab} = -\frac{1}{2} \sum_c \left[dp^1_{ac} \rho^0_{cb} + \rho^0_{ac} dp^1_{cb} \right] - \frac{1}{2} \sum_{ckl} t_{klbc} \left[\sum_d t^*_{klad} dp^1_{cd} \right], \tag{3.37}$$

where all terms of equation 2.342 and the first term of equation 2.343 are included. The last two elements, i.e. $\rho^{XY(2)}_{kb}$ and $\rho^{XY(2)}_{bk}$, both contain the remaining second order terms of equations 2.341 and 2.345:

$$\rho^{XY(2)}_{kb} = -\sum_a dp^1_{ab} \rho^0_{ka} - \sqrt{2} \sum_{dl} t_{lkdb} dp_{dl} + \sqrt{2} \left[\frac{1}{2} \sum_I Y_{Ib} \sum_{adl} t_{klad} X^*_{lIad} \right] \tag{3.38}$$

$$\rho^{XY(2)}_{bk} = -\sum_a dp^1_{ab} \rho^0_{ka} - \sqrt{2} \sum_{dl} t_{lkdb} dp_{ld} + \sqrt{2} \left[\frac{1}{2} \sum_I X^*_{Ib} \sum_{adl} t_{klad} Y_{lIad} \right]. \tag{3.39}$$

Regarding state densities, where $\mathbf{X} = \mathbf{Y}$, both matrix elements are identical due to the hermicity of the CVS-ADC matrix. For transition-density matrices between two core-excited states, the results are different, thus both elements have to be implemented.

3.3 Overview of the Implemented CVS-ADC and CVS-ISR Features

At last, I summarize the features of my implementation of the CVS-ADC/CVS-ISR approaches in the `Q-Chem` program package within the `adcman` interface. Besides the general ADC related keywords, two additional keywords in the input file are necessary to control CVS-ADC calculations in `Q-Chem`:

- ***ADC_CVS*** = **true** switches on the CVS-ADC calculation
- ***CC_REST_OCC*** = ***n*** controls the number of core orbitals included in the excitation space. The integer n corresponds to the n energetically lowest core orbitals.

Let me give a short example: cytosine with the molecular formula $C_4H_5N_3O$ includes one oxygen atom. To calculate O 1s core-excited states, *CC_REST_OCC* has to be set to 1, because the 1s orbital of oxygen is the energetically lowest. To obtain the N 1s core excitation, the integer has to be set to 4, because the 1s orbital of the oxygen atom is included as well, since it is energetically below the three 1s orbitals of the nitrogen atoms. Accordingly, to simulate the C 1s XAS spectrum of cytosine, *CC_REST_OCC* must be set to 8. Since the core orbitals of the different kinds of atoms are energetically well-separated, this procedure is justified according to the CVS approximation. For all other related keywords, e.g. properties, I refer to the `Q-Chem` manual (see *www.q-chem.com* for the recent version).

For the simulation and advanced analysis of XA spectra, the following features were implemented in the scope of this thesis.

- Calculations of **core-excited states** with the **CVS-ADC method up to third** order in perturbation theory:
  - Restricted and unrestricted calculations of closed- and open-shell systems, respectively.
  - Core-excitation energies of singlet and triplet core-excited states.
  - Oscillator strengths and transition moments to describe the spectral absorption.
  - Exploiting Abelian point group symmetries to speed up computational timings.
  - Analysis of the excited state configurations in the MO basis that contribute to a core-excited state.
- Calculations of **core-excited state one-particle properties** via the **CVS-ISR** approach:
  - Static dipole moments of core-excited states.
  - Advanced wave function analysis, e.g. exciton sizes, in combination with the `libwfa` library.
  - Visualization of state densities, e.g. detachment/attachment densities.
- Calculations of **core-excited state absorption** processes between two core-excited states via the **CVS-ISR** approach:
  - State-to-state absorption energies and oscillator strengths.

Chapter 4

Benchmarking CVS-ADC up to Third Order

In this chapter, I present benchmark calculations of the CVS-ADC methods up to third order. The calculated results are compared with experimental data or in the case of the CVS-ISR approach with values obtained at the SAC-CI level of theory. For this purpose, a set of the small molecules carbon monoxide (CO), ammonia (NH_3), the methyl radical (CH_3), water (H_2O) and fluoroethene (CH_2CHF) was chosen. The correlated consistent basis set series converges systematically towards a complete basis set (CBS) limit, which for ground state correlation energies can be estimated using

$$E_X = E_{CBS} + Ae^{-(X-1)} + Be^{-(X-1)^2}, \tag{4.1}$$

where X is the cardinal number of the basis set (for example 2 for DZ), E_{CBS} is the resulting estimated energy of the CBS limit, and E_X is the calculated energy using the basis set with the cardinal number X.[120,121] This equation gives the possibility to extrapolate the results systematically, thereby avoiding basis set truncation errors. To the best of my knowledge, such a convergent behavior has not been shown for excited states, yet. In this chapter, I am going to demonstrate that this estimation can also be applied to core-excited states. In the literature there are a few other regression models, where some tend to underestimate or overestimate the CBS limit.[120,121,184,185] Regarding core-excited states at the CVS-ADC levels investigated in this chapter, the employed regression model provides very accurate results, where the coefficient of determination (R^2) is almost 1.00 in all calculations of the CBS limit, indicating that the regression model excellently fits the data.

Furthermore, the general influence of basis sets is evaluated and the influence of pure and Cartesian versions of the basis functions is investigated. Here, I concentrate on the use of standard common basis sets as introduced in chapter 2.1.3. Special variants like the addition of bond-centered or molecule-centered diffuse functions are also known to provide accurate spectral features[100], but they are not considered in this work, because the potential of CVS-ADC(2)-x as a black-box method in combination with standard basis sets is emphasized in this study. Employing such special basis functions requires proper analysis of the type of basis function to be added depending on the atom types, which would destroy the black-box specification.

All structures of the small molecules in the electronic ground state were optimized at the CCSD[51] level using the def2-QZVPPD[119] basis set. These geometry optimizations

were performed with the `Q-Chem 4.2` program.[94] Core-excited states were calculated with my implementation of CVS-ADC up to third order of perturbation theory as well as with my CVS-ISR implementation as described in chapter 3. The core-excited states at the SAC-CI SD-R level were computed using the implementation available in the `Gaussian09` program.[145,155] Note that both ground and core-excited state calculations of the CH_3 radical were always performed using the unrestricted variants of the respective methods. For clarity, I do not mention this fact explicitly in the discussion, thus calculations of the CH_3 radical are also denoted as CVS-ADC calculations instead of CVS-UADC calculations. Furthermore, note that for consistency, the method for calculating oscillator strengths and excited state properties at the third order CVS-ADC level is denoted as CVS-ADC(3,2) as explained in chapter 2.5.3. All computed values shown in this chapter are absolute without any level shift or consideration of relativistic effects.

The following basis sets were employed in this chapter: the series of correlation-consistent polarized valence basis sets (cc-pVX)[115] as well as the augmented (aug)[116] and doubly augmented (d-aug)[116,117] versions with the cardinal number X ranging from double-ζ (DZ) to quintuple-ζ (5Z). Due to computational cost, the d-aug-cc-pVX series ranges only from DZ to quadruple-ζ (QZ). Furthermore, calculations using the series of correlation-consistent polarized core-valence basis sets (cc-pCVX)[186] with X ranging from DZ to 5Z and without (X ranging from DZ to QZ) augmentation were performed. The Ahlrichs series is represented with def2-SVP, def2-TZVP and def2-QZVP with and without diffuse functions denoted with the suffix D.[118,119] Since Pople-type basis sets provided accurate results compared to experimental data as shown in former work[33,89,187], representatives with and without diffuse and polarization functions were chosen from this series, i.e. 6-31G, 6-31G**, 6-31++G**, 6-31G(3df,3pd), 6-311G, 6-311G**, 6-311++G** and 6-311++G(3df,3pd).[109,111–114] If not otherwise stated, all calculations were performed using the Cartesian 6D/10F version of the respective basis sets. Finally, note that the content of this chapter has already been published by me and my co-authors in *Journal of Chemical Physics, 142 (2015), 214104* or has been submitted for publication in *Journal of Chemical Theory and Computation, (2016).*[98,99]

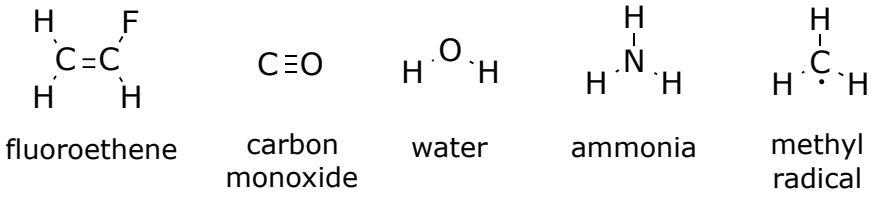

Figure 4.1: Structures of fluoroethene (CH_2CHF), carbon monoxide (CO), water (H_2O), ammonia (NH_3) and the methyl radical (CH_3).

4.1 Convergence of Core-Excitation Energies Towards the Complete Basis Set Limit

Let me start with the estimation of the complete basis set (CBS) limit. Since the series of correlation consistent basis sets provide a systematic convergence against the CBS limit, I focus on the cc-pVX series (with X ranging from DZ to 5Z) and its augmented and doubly-augmented versions. Here, only the strict and extended second order as well as the third order approaches are benchmarked. CVS-ADC(1), which is actually CVS-CIS, has no correlation and orbital relaxation included, thus provides a strong overestimation of core-excitation energies in every case compared to experiments. In the case of NH_3 and CO, the first three core-excited states are discussed and compared to the experiment, while for the methyl radical only one bright core-excited state can be directly matched with experiments. Note that CO and NH_3 exhibit doubly degenerated states due to the p-orbital symmetry. These states are only given once. It should be noted that the computational cost hampers the use of the d-aug-cc-pV5Z basis set, thus the calculation of the CBS limit based on the aug-series should be more exact. The structures of all molecules used in chapter 4 are summarized in Figure 4.1.

4.1.1 CVS-ADC(2)-s

At first, the core-excitation energies obtained at the CVS-ADC(2)-s level are given in Table 4.1. Starting with the carbon 1s excitations of CO, the calculated CBS limits based on the different series are almost identical. The only exception is the CBS limit of state 2 estimated at the cc-pVX level. Here the difference is 0.84 eV compared to the aug-cc-pVX series. Furthermore, the CBS limits of the state 3 cannot be determined using the standard cc-series, because this core-excited state cannot be matched with experiments using the small cc-pVDZ basis. When employing at least the cc-pV5Z basis, state 3 can be obtained. However, state 1 also exists when using cc-pVDZ and the CBS limit is comparable to the ones at the aug and d-aug levels. To explain these result, one has to consider the character of these states. Looking at MO contributions and according to the literature, state 1 is a bright s,π^* core excitation, which exhibits a large oscillator strength, while state 2 and state 3 are dark and were determined to possess a strong core-Rydberg character.[100] As a consequence, one needs a large diffuse basis to describe the Rydberg-type states correctly. Obviously, the aug-cc-pVDZ basis set is already sufficient to obtain these states, thus the addition of diffuse basis functions is necessary to describe the C 1s spectrum of CO correctly.

Going to the O 1s excitations of CO and the N 1s excitations of ammonia, the same statements can be made. In both examples, the Rydberg-type state 3 cannot be characterized using a cc-pVX (even not at the 5Z level) basis set and the CBS limit of state

Table 4.1: Core-excitation energies (ω_{ex}) of the first three singlet core-excited states of CO (C 1s and O 1s) and NH_3 (N 1s) and the first C 1s excited state of CH_3. The energies were calculated using CVS-ADC(2)-s and CVS-UADC(2)-s with different basis sets, respectively. The calculated values and the CBS limits for every series of basis sets are compared with experimental data taken from the literature.[16,188,189] This table has already been published by me and my co-authors.[98]

	CO C 1s			CO O 1s			NH_3 N 1s			CH_3 C 1s
	States ω_{ex} [eV]			States ω_{ex} [eV]			States ω_{ex} [eV]			States ω_{ex} [eV]
Basis set/Expt.	1	2	3	1	2	3	1	2	3	1
cc-pVDZ	291.68	301.98	—	537.38	545.45	—	405.09	407.10	—	285.25
cc-pVTZ	290.26	298.56	—	535.70	541.63	—	403.21	405.25	—	283.78
cc-pVQZ	290.05	297.39	—	535.42	540.27	—	402.82	404.78	—	283.54
cc-pV5Z	289.98	296.67	297.72	535.33	539.47	—	402.55	404.35	—	283.47
CBS (cc)	289.95	296.47	—	535.28	539.23	—	402.50	404.30	—	283.43
aug-cc-pVDZ	291.24	296.70	297.63	536.97	539.83	—	403.29	404.70	—	284.94
aug-cc-pVTZ	290.19	295.84	296.73	535.53	538.48	—	402.33	403.70	404.77	283.69
aug-cc-pVQZ	290.03	295.70	296.58	535.37	538.30	—	402.26	403.62	404.47	283.52
aug-cc-pV5Z	289.97	295.65	296.48	535.31	538.23	539.03	402.24	403.59	404.23	—
CBS (aug)	289.95	295.63	296.50	535.29	538.21	—	402.24	403.58	—	283.45
d-aug-cc-pVDZ	291.16	296.30	297.09	536.93	539.35	540.08	403.25	404.56	404.92	284.91
d-aug-cc-pVTZ	290.18	295.66	296.45	535.52	538.22	538.96	402.32	403.63	403.99	283.68
d-aug-cc-pVQZ	290.02	295.61	296.40	535.37	538.16	538.89	402.26	403.58	403.94	283.51
CBS (d-aug)	289.94	295.59	296.38	535.32	538.16	538.88	402.25	403.58	403.94	283.45
Experiment	287.4	292.5	293.4	534.1	538.8	539.8	400.66	402.33	402.86	281.35

2 differs about 1 eV from the result obtained with the augmented series. Actually, in the case of the O 1s excitations of CO, state 3 cannot be obtained at the augmented level (only 5Z) and the doubly augmented series is necessary. In the case of NH_3, only aug-cc-pVDZ fails to describe this state. The results for the CBS limits of state 1 with s,π^* character calculated with different series of basis sets are again almost identical for CO (O 1s) and NH_3 (N 1s). The CBS limits for state 1 of the methyl radical are almost constant with values of 283.43 eV, 283.45 eV and 283.45 eV, respectively. Due to technical limitations, the calculation using the aug-cc-pV5Z basis set was not possible. Eventually, for all investigated molecules the core-excitation energies are almost converged using a triple-ζ basis set with diffuse basis functions. The standard cc-series provides reasonable results for non-Rydberg states at triple-ζ level, but fails completely in the description of Rydberg states. Furthermore, the improvement towards the CBS limit regarding the s,π^*-states by using augmented diffuse basis functions is only important in the case of double-ζ functions. However, the Rydberg states are strongly improved by diffuse functions.

Compared to the experimental values, the CVS-ADC(2)-s method shows a trend to overestimate carbon and nitrogen 1s excitation energies, while the O 1s excitation energies are both over- and underestimated depending on the state character. The reason is due to the neglect of relativistic effects and the description of relaxation effects (see chapter 2.5.9). The heavier the element, the stronger the underestimation. Going to the C 1s excitations of CO, the bright s,π^* state 1 based on the CBS limit of the aug-cc-pVX series is overestimated by 2.55 eV and the higher-lying Rydberg states are overestimated by 3.13 eV and 3.10 eV, respectively. The bright state 1 of the CH_3 radical, which is also an electron promotion into a π^*-orbital, is overestimated by 2.1 eV. The nitrogen 1s excitations of NH_3 based on the CBS limit of the d-aug-cc-pVX series are overestimated by 1.59 eV, 1.25 eV and 1.08 eV, respectively. Regarding the O 1s excitations of CO, the bright s,π^* state 1 is overestimated by 1.22 eV, which is at the same level as the nitrogen results. However, the Rydberg-type states are underestimated by 0.64 eV and 0.92 eV, respectively. Since the absolute core-excitation energies rise strongly with heavier elements, it is reasonable to express the errors compared to experiment in relative values. The three core-excited states of the C 1s excitation of CO exhibit errors of 0.88%, 1.06% and 1.06%, while the three O 1s excitations differ about 0.23%, -0.12% and -0.17% from experiment, respectively. In the case of the N 1s excitation of NH_3, the relative errors of the three states are 0.4%, 0.31% and 0.27%, respectively. Hence, in the case of the C 1s and N 1s excitations, an absolute shift would thus lead to an excellent quantitative result, because the relative errors are almost constant. Qualitatively, the results obtained at the CVS-ADC(2)-s level are acceptable. However, the relative errors for the lighter C 1s excitations are larger than for the heavier O 1s ones.

4.1.2 CVS-ADC(2)-x

Next, the CVS-ADC(2)-x method is investigated. The results are summarized in Table 4.2. Besides the values of the results, similar conclusions about the CBS limits as the ones of the CVS-ADC(2)-s method can be stated at the CVS-ADC(2)-x level. The calculated CBS limits based on the different series are almost identical for the bright s,π^* state 1 for all investigated systems. The only exceptions are the CBS limits of state 1 of the O 1s excitation of CO and the N 1s excitation of NH_3 estimated at the cc-pVX level. Here the differences are 0.05 eV and 0.12 eV compared to the aug-cc-pVX series, respectively. Furthermore, the CBS limits of the Rydberg-type state 2 and 3 of CO (C 1s and O 1s) as well as state 3 of NH_3 cannot be determined using the standard cc-series, because these core-excited states cannot be matched with experiments using the smaller cc-pVX basis

Table 4.2: Core-excitation energies (ω_{ex}) of the first three singlet core-excited states of CO (C 1s and O 1s) and NH_3 (N 1s) and the first C 1s excited state of CH_3. The energies were calculated using CVS-ADC(2)-x and CVS-UADC(2)-x with different basis sets, respectively. The calculated values and the CBS limits for every series of basis sets are compared with experimental data taken from the literature.[16,188,189] This table has already been published by me and my co-authors.[98]

	CO C 1s			CO O 1s			NH_3 N 1s			CH_3 C 1s
	States ω_{ex} [eV]			States ω_{ex} [eV]			States ω_{ex} [eV]			States ω_{ex} [eV]
Basis set/Expt.	1	2	3	1	2	3	1	2	3	1
cc-pVDZ	289.10	—	—	535.25	—	—	402.62	404.68	—	283.13
cc-pVTZ	287.19	294.99	—	532.87	—	—	400.32	402.39	—	281.18
cc-pVQZ	286.91	293.83	—	532.50	538.40	—	399.96	401.97	—	280.90
cc-pV5Z	286.85	293.18	294.50	532.42	537.73	539.15	399.78	401.69	—	280.84
CBS (cc)	286.80	—	—	532.35	—	—	399.73	401.64	—	280.79
aug-cc-pVDZ	288.53	293.95	295.11	534.87	539.28	540.49	401.38	403.09	404.46	282.73
aug-cc-pVTZ	287.09	292.57	293.68	532.70	537.11	538.24	399.77	401.45	402.45	281.08
aug-cc-pVQZ	286.89	292.41	293.49	532.48	536.91	538.00	399.64	401.31	402.14	280.88
aug-cc-pV5Z	286.84	292.37	293.41	532.42	536.85	537.89	—	—	—	—
CBS (aug)	286.81	292.35	293.39	532.40	536.83	537.87	399.61	401.28	402.01	280.81
d-aug-cc-pVDZ	288.42	293.63	294.63	534.81	538.99	539.99	401.33	403.01	403.54	282.68
d-aug-cc-pVTZ	287.07	292.46	293.46	532.68	536.98	537.97	399.76	401.42	401.95	281.06
d-aug-cc-pVQZ	286.88	292.36	293.37	532.47	536.85	537.84	399.64	401.30	401.84	280.88
CBS (d-aug)	286.80	292.34	293.34	532.40	536.83	537.82	399.62	401.28	401.82	280.81
Experiment	287.4	292.5	293.4	534.1	538.8	539.8	400.66	402.33	402.86	281.35

sets due to lack of diffuse basis functions. While state 3 of the N 1s excitations of NH_3 cannot be obtained using the cc-pVX basis sets, only cc-pVDZ fails to describe state 2 of both CO core excitations and cc-pV5Z is able to describe state 3 of both CO excitations. Note that, due to technical limitations, the calculation of NH_3 and the CH_3 radical were not possible using the aug-cc-pV5Z basis set. Eventually, as already mentioned in the scope of CVS-ADC(2)-s discussion, the core-excitation energies are almost converged using a triple-ζ basis set with diffuse basis functions. The standard cc-series provides reasonable results for non-Rydberg states at triple-ζ level, but fails in the description of Rydberg states. Furthermore, the improvement towards the CBS limit regarding the s,π^*-states by using augmented diffuse basis functions is only significant in the case of double-ζ functions. However, the Rydberg states are strongly improved by diffuse functions.

More important is the comparison of the CBS limits at the aug-cc-pVX level with experimental values. Here, CVS-ADC(2)-x tends to underestimate the core-excitation energies slightly, thereby providing excellent results for both s,π^* and Rydberg-type states. The absolute and relative errors for the carbon 1s excitations regarding the three core-excited states of CO are -0.59 eV (-0.21%), -0.15 eV (-0.05%) and -0.01 eV (-0.003%), respectively, while the bright core-excited state of the CH_3 radical is overestimated by 0.54 eV (0.19%). Hence, the Rydberg-type states are almost perfectly described at the CVS-ADC(2)-x level. Going to the oxygen 1s excitations of CO, the errors are -1.7 eV (-0.32%), -1.97 eV (-0.37%) and -1.93 eV (-0.36%), respectively. This indicates that an absolute shift would lead to an excellent quantitative result, because the errors are almost constant. The same applies for the N 1s excitations of NH_3, where the errors for the three core-excited states are -1.05 eV (-0.26%), -1.05 eV (-0.26%) and -0.85 eV (-0.21%), respectively. These results show the trend of an increased underestimation when going to heavier atoms due to the neglect of relativistic effects and the description of relaxation effects (see chapter 2.5.9). Since relativistic contributions are essentially just a positive shift of the absolute energy and can be estimated to be about 0.1 eV for C 1s, 0.2 eV for N 1s, and 0.4 eV for O 1s excitations[100], the trend of the underestimations of the CVS-ADC(2)-x results is correct. Furthermore, the relative errors are very similar, independent of the core type. The heavier the element, the larger is the absolute error, but relatively this influence is small. Overall, very accurate results compared to experiment are provided at the CVS-ADC(2)-x level using at least an augmented triple-ζ basis set. Note that the CH_3 radical is investigated at the CVS-ADC(2)-x level in more detail in chapter 6.3.1.

4.1.3 CVS-ADC(3)

Let me turn to the CVS-ADC(3) results, which are summarized in Table 4.3. Since there are no new insights concerning the CBS limits, this discussion will be omitted. In principle, the same trends of the CBS limits and differences between s,π^* and core-Rydberg-type states as already discussed in the scope of CVS-ADC(2)-s and CVS-ADC(2)-x are given for CVS-ADC(3).

However, the comparison with experimental values provides significant differences compared to both second order approaches, because the CVS-ADC(3) method shows a clear trend to overestimate the core-excitation energies. The only exception is the bright s,π^* state 1 of the C 1s excitation of CO, which almost excellently matches the experimental value with an error of 0.3 eV (0.10%). The higher-lying Rydberg states, in contrast, are overestimated by about 1.2 eV (0.40%) and 1.3 eV (0.44%), respectively. The bright state of the CH_3 radical, which is also an electron promotion into a π^*-orbital, is overestimated by about 0.5 eV, i.e. 0.17%. Going to core-excitations of heavier atoms,

Table 4.3: Core-excitation energies (ω_{ex}) of the first three singlet core-excited states of CO (C 1s and O 1s) and NH_3 (N 1s) and the first C 1s excited state of CH_3. The energies were calculated using CVS-ADC(3) and CVS-UADC(3) with different basis sets. The calculated values and the CBS limits for every series of basis sets are compared with experimental data taken from the literature.[16,188,189] This table has already been published by me and my co-authors.[98]

	CO C 1s			CO O 1s			NH_3 N 1s			CH_3 C 1s
	States ω_{ex} [eV]			States ω_{ex} [eV]			States ω_{ex} [eV]			States ω_{ex} [eV]
Basis set/Expt.	1	2	3	1	2	3	1	2	3	1
cc-pVDZ	289.96	—	—	541.38	—	—	406.27	407.90	—	284.40
cc-pVTZ	288.11	296.30	—	538.82	547.04	—	404.09	405.73	—	282.33
cc-pVQZ	287.82	295.12	—	538.37	545.62	—	403.73	405.36	—	281.98
cc-pV5Z	287.74	294.49	295.74	538.28	544.91	546.99	403.60	405.21	407.64	281.90
CBS (cc)	287.69	—	—	538.19	—	—	403.54	405.15	—	281.83
aug-cc-pVDZ	289.45	295.33	296.45	541.32	547.33	549.15	405.95	407.55	408.89	284.09
aug-cc-pVTZ	288.02	293.95	295.04	538.74	544.66	546.29	403.92	405.48	406.59	282.24
aug-cc-pVQZ	287.80	293.75	294.83	538.38	544.32	545.86	403.61	405.17	406.17	281.96
aug-cc-pV5Z	287.74	293.70	294.74	538.28	544.22	545.68	—	—	—	—
CBS (aug)	287.70	293.67	294.71	538.23	544.17	545.62	403.47	405.03	405.97	281.84
d-aug-cc-pVDZ	289.35	295.01	296.04	541.26	547.13	548.57	405.91	407.49	408.35	284.04
d-aug-cc-pVTZ	288.01	293.84	294.86	538.72	544.57	545.97	403.90	405.46	406.31	282.22
d-aug-cc-pVQZ	287.79	293.70	294.72	538.38	544.28	545.68	403.61	405.16	406.02	281.96
CBS (d-aug)	287.69	293.65	294.67	538.24	544.17	545.57	403.48	405.03	405.90	281.85
Experiment	287.4	292.5	293.4	534.1	538.8	539.8	400.66	402.33	402.86	281.35

Table 4.4: Summary of the statistical error analysis of the calculated core-excitation energies of the first three singlet C 1s, N 1s and O 1s core-excited states of CO and NH_3 as well as the first core-excited state of the CH_3 radical at the CVS-ADC(2)-s, CVS-ADC(2)-x and CVS-ADC(3) levels of theory, respectively. The relative errors in [%] are given using the experimental values as reference data. Besides the Mean value, the standard deviation σ and the minimal and maximal errors are given. This table has already been published by me and my co-authors.[98]

	Relative error [%]		
	CVS-ADC(2)-s	CVS-ADC(2)-x	CVS-ADC(3)
aug-cc-pVX (CBS)			
Min / Max	-0.11 / 1.06	0.00 / -0.37	0.11 / 1.07
Mean	0.57	-0.22	0.61
σ	0.43	0.12	0.32
d-aug-cc-pVX (CBS)			
Min / Max	-0.17 / 1.05	-0.02 / -0.37	0.10 / 1.06
Mean	0.46	-0.23	0.60
σ	0.44	0.12	0.32

the overestimation increases. The absolute errors obtained for the three states of the O 1s excitations of CO are 4.1 eV (0.77%), 5.4 eV (1.0%) and 5.8 eV (1.0%), respectively. In the case of the N 1s excitation of NH_3, the errors of the three core-excited states are 2.81 eV (0.70%), 2.7 eV (0.67%) and 3.11 eV (0.77%), respectively. The overestimation is indeed large, but the errors are almost constant, thus an absolute shift would lead to an excellent quantitative result. Overall, the results obtained at the CVS-ADC(3) level are acceptable, showing a trend to overestimate the Rydberg states more strongly than the s,π^*-states.

4.1.4 Comparison

After discussing the results obtained at the different CVS-ADC levels, I present a direct comparison between them. Table 4.4 summarizes a statistical error analysis and comparison between the three CVS-ADC levels based on the results of the C 1s excitations of CO and CH_3, the O 1s excitations of CO and the N 1s excitations of NH_3. Only the relative errors with respect to experimental values are given for better comparison between the different kinds of cores. Analyzing the statistical data based on the CBS limits compared to experiment reveals a clear trend. CVS-ADC(2)-x slightly underestimates the core-excitation energies of the C, N and O 1s excited states by about 0.2%, while CVS-ADC(3) and CVS-ADC(2)-s provide an overestimation with a mean value of about 0.6% in both cases. Furthermore, the standard deviation of the CVS-ADC(2)-x results is the smallest with only 0.12%, while the strict second and third order approaches exhibit a large σ of 0.43% and 0.32%, respectively. Looking at the Min/Max values confirms these findings. While CVS-ADC(2)-x yields errors between 0.00% and -0.37%, the magnitude of the other two methods is around 1.1%. Note that larger errors are related to the core excitations of heavier elements in all cases due to stronger relativistic and relaxation effects. However, CVS-ADC(2)-x provides accurate quantitative and qualitative results for all elements

investigated here, thus the results at the extended second order level are less affected by this phenomenon. Since relativistic effects would shift the core-excitation energies to larger numbers, the underestimation provided by CVS-ADC(2)-x shows a "correct" trend that may be explained by the neglect of these effects.

To visualize the difference between CVS-ADC(2)-x and CVS-ADC(3), Figure 4.2 illustrates the trend of the core-excitation energies at the CVS-ADC(2)-x and CVS-ADC(3) levels against the basis set ζ-size, thereby showing the convergence against the CBS limit. Starting with the O 1s excitation of CO, all core-excited states are slightly underestimated constantly by CVS-ADC(2)-x, while CVS-ADC(3) provides a significant overestimation. Going to the "lighter" N 1s excitations of NH_3, the underestimation by CVS-ADC(2)-x is smaller than for the O 1s excitations, while CVS-ADC(3) still provides a large overestimation of all states. Relatively, this overestimation is also smaller than for the heavier O 1s excitations of CO. Regarding the carbon 1s excitations of CO, state 1 with s,π^* character is slightly underestimated using CVS-ADC(2)-x, while the two Rydberg states are in excellent agreement with the experiment. In contrast, CVS-ADC(3) overestimates the Rydberg states, but provides an excellent match of the s,π^*-state 1. However, the shifts in energy between the states are almost perfectly described with both CVS-ADC(2)-x and CVS-ADC(3).

Eventually, the results calculated with both methods almost show a convergence at the triple-ζ level independent of the type of core excitation, but CVS-ADC(2)-x provides the best agreement with experiments and is in addition computationally much cheaper than the third order approach. The reason for the trends provided at the different CVS-ADC levels is explained in chapter 2.5.9. It seems that at the CVS-ADC(2)-x level, a fortuitous error compensation of basis set truncation, neglect of relativistic effects, electron correlation and orbital relaxation and polarization effects is given. This error compensation is broken at the third order level, because the ratio between terms describing relaxation and polarization effects is shifted in a way that the excitation energy increases. Furthermore, the doubles are not further improved at the third order level. CVS-ADC(2)-s overestimates the core-excitation energies, because the doubly excited amplitudes are less improved than in the extended second order approach. In chapter 5, the influence of orbital relaxation effects is investigated in detail.

4.2 Influence of Basis Sets on the Accuracy of the CVS-ADC Approaches

After analyzing results obtained with the correlation consistent basis set series, the influence of other commonly available basis sets on the accuracy of the CVS-ADC approaches is investigated. Furthermore, the use of Cartesian basis functions is analyzed, which were employed in previous publications.[16,90,100]

4.2.1 Comparison of Particular Basis Sets

Besides the basis set dependence of the cc-pVX series and its augmented and doubly augmented versions, other common basis sets are available and their influence on core-excitation energies at the CVS-ADC levels is investigated in this chapter. For this purpose, I present results obtained using selected Ahlrichs- and Pople-type basis sets. Furthermore, the basis sets from the cc- and aug-cc-series are augmented by core-valence functions that are well known to provide an enhanced description of core-valence correlation effects.[186] For the core-valence versions, the CBS limit were estimated, too. Table 4.5 contains the

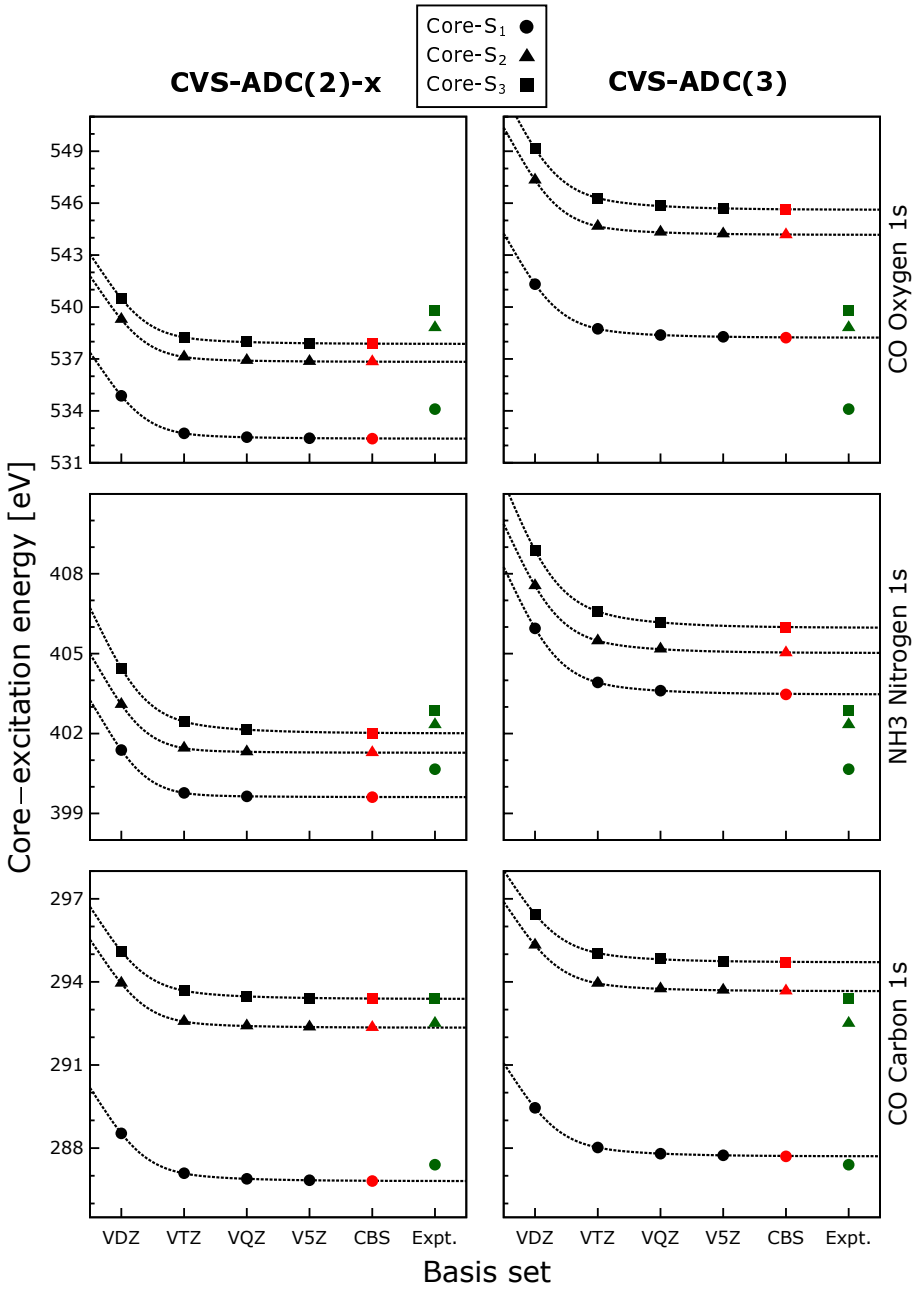

Figure 4.2: Plots of the core-excitation energy against the basis set for the first three core-excited states of CO (C 1s and O 1s) and NH_3 (N 1s). Left: results obtained at the CVS-ADC(2)-x level, Right: results calculated at the CVS-ADC(3) level. The series of the aug-cc-pVXZ was used for the calculation, where X describes the ζ level. The calculated CBS limits are shown in red and the dashed lines represent the fitting function (see equation 4.1). Furthermore, the calculated values are compared with experimental data (green).[16,188]

detailed results of the C 1s excitations of CO obtained with the various basis sets at different CVS-ADC levels.

Let me start this discussion with the core-valence basis set series cc-pCVX and aug-cc-pCVX. The estimated CBS limits are at the same level as the ones obtained using the cc-pVX series and its augmented and doubly augmented versions (see chapter 4.1). Using the cc-pCVDZ basis set significantly improves the core-excitation energy compared to cc-pVDZ towards the CBS limit, for example 0.48 eV in the case of state 1 calculated with the CVS-ADC(2)-x method. However, the addition of the core-valence functions is not sufficient to properly describe the Rydberg-type states 2 and 3. Particularly, state 3 can only be obtained using at least the 5Z basis set. Hence, employing augmented functions is still necessary, which can be confirmed looking at the aug-cc-pCVX results. Overall, employing the core-valence functions improves the results towards the CBS limit, but not more than the aug- or d-aug-functions, which in addition provide access to core-Rydberg states.

Next, the Ahlrichs def2-series is analyzed. The results show in principle the same trends as the cc-series. Diffuse functions (D) are necessary to obtain the Rydberg-type states properly. However, using the triple-ζ def2-TZVP does not provide almost converged results. The differences between def2-TZVP and def2-QZVP are still around 0.3 eV and even at the def2-QZVP level, the values are still above the CBS limit obtained with the comparable cc-series. State 1, for example, calculated with CVS-ADC(2)-x/def2-QZVP is 0.13 eV above the respective CBS limit obtained with the cc-pVX series. The core-excitation energies of the s,π^*-state 1 are not improved significantly using diffuse functions. The difference between def2-SVP and def2-SVPD is 0.21 eV using CVS-ADC(2)-x, while the core-excitation energies obtained using def2-QZVP and def2-QZVPD are almost the same. However, in the case of the Rydberg-type states 2 and 3, the influence of the diffuse functions becomes obvious. Here, the differences between def2-QZVP and def2-QZVPD are about 1 eV.

The Pople-basis sets show similar trends. Here, besides the diffuse functions (+), the influence of polarization functions (*) is investigated, too. Looking at the results reveals that these polarization functions indeed improve the core-excitation energies towards the CBS limits of the cc-series and experimental data. However, diffuse functions are mandatory to describe the Rydberg states. As an alternative, the addition of 3df and 3pd functions also significantly improve the core-excitation energies toward the CBS limits in conjunction with a proper description of the Rydberg states. Within the Pople series, the effect of + functions on the bright s,π^* state 1 is also very small, but the Rydberg-type states are strongly improved. However, the description of state 1 depends strongly on the use of polarization functions.

To evaluate the quality of the results, a comparison with experimental data is necessary. Figure 4.3 summarizes the results obtained with triple-ζ basis functions using the CVS-ADC(2)-x and CVS-ADC(3) methods. In general, the same conclusions can be drawn as discussed in chapter 4.1. At the CVS-ADC(3) level, the core-excitation energies are overestimated, while CVS-ADC(2)-x provides an excellent agreement with the experiment. As expected, large basis sets with diffuse functions provide the best results and in the case of the Pople-series it is advantageous to employ polarized and diffuse functions. Otherwise, the error in core excitation-energies can be large even at the triple-ζ level. Hence, the 6-311G basis does not provide reasonable results compared to the 6-311++G** basis set. At the CVS-ADC(2)-x level, state 1 is slightly underestimated using the Ahlrichs- and cc-series, while the Pople-type basis sets slightly overestimate this s,π^*-state. Since the Rydberg states are slightly overestimated using the 6-311++G** basis, they are best described employing diffuse basis sets from the cc-series. Note that in this CO C 1s

Table 4.5: Comparison of core-excitation energies (ω_{ex}) of the first three C 1s singlet excited states of carbon monoxide. The energies were calculated using CVS-ADC at strict second (2s), extended second (2x) and third order (3) in combination with different basis sets. The calculated values and the CBS limits for the cc-pC and aug-cc-pC series are compared with experimental data.[188] This table has already been published by me and my co-authors.[98]

	State 1 ω_{ex} [eV]			State 2 ω_{ex} [eV]			State 3 ω_{ex} [eV]		
Basis Set/Expt.	2s	2x	3	2s	2x	3	2s	2x	3
cc-pCVDZ	291.37	288.62	289.50	301.52	298.35	—	—	—	—
cc-pCVTZ	290.19	287.07	287.99	298.48	294.86	296.16	—	—	—
cc-pCVQZ	290.03	286.88	287.78	297.24	293.69	294.97	—	—	—
cc-pCV5Z	289.98	286.84	287.73	296.67	293.17	294.48	297.70	294.48	295.72
CBS (cc-pC)	289.95	286.81	287.70	296.42	292.94	—	—	—	—
aug-cc-pCVDZ	291.09	288.28	289.21	296.56	293.67	295.05	297.49	294.84	296.18
aug-cc-pCVTZ	290.15	287.03	287.97	295.82	292.52	293.90	296.71	293.63	294.99
aug-cc-pCVQZ	290.01	286.87	287.78	295.69	292.40	293.73	296.57	293.48	294.81
CBS (aug-cc-pC)	289.94	286.80	287.69	295.63	292.35	293.66	296.50	293.42	294.73
def2-SVP	291.54	288.83	289.62	301.35	298.37	—	—	—	—
def2-TZVP	290.28	287.28	288.19	297.69	294.27	295.56	—	—	—
def2-QZVP	290.05	286.93	287.83	297.05	293.52	294.87	298.00	294.80	296.01
def2-SVPD	291.37	288.62	289.44	297.30	294.51	295.66	298.76	295.98	297.27
def2-TZVPD	290.27	287.27	288.18	295.96	292.81	294.13	297.15	294.07	295.48
def2-QZVPD	290.04	286.93	287.83	295.74	292.47	293.78	296.83	293.66	295.04
6-31G	292.61	290.20	290.75	303.65	—	—	—	—	—
6-31G**	291.43	288.78	289.48	302.17	—	—	—	—	—
6-31++G**	291.37	288.72	289.45	296.90	294.23	295.34	297.96	295.50	296.57
6-31G(3df,3pd)	290.48	287.57	288.46	299.21	295.98	296.98	—	—	—
6-311G	291.42	288.48	289.11	301.49	—	—	—	—	—
6-311G**	290.56	287.50	288.40	300.41	296.76	—	—	—	—
6-311++G**	290.54	287.49	288.40	296.18	292.89	294.17	297.22	294.16	295.40
6-311++G(3df,3pd)	290.15	287.03	287.94	295.90	292.58	293.91	296.98	293.88	295.16
Experiment		287.4			292.5			293.4	

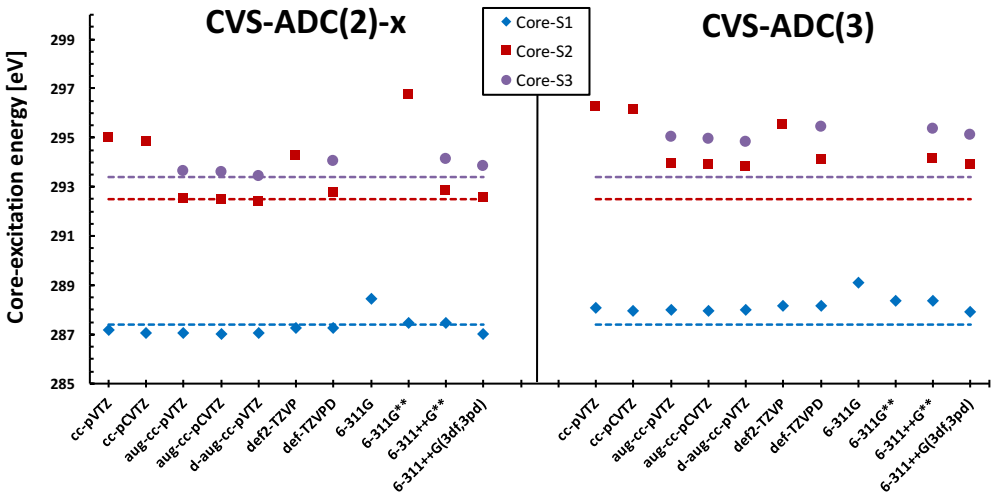

Figure 4.3: Plots of the core-excitation energy against chosen triple-ζ basis sets for the first three C 1s singlet excited states of CO. Left: results obtained at the CVS-ADC(2)-x level, Right: results obtained at the CVS-ADC(3) level. The dashed lines represent the experimental values.[188]

example, the 6-311++G(3df,3pd) basis set performs better than the smaller 6-311++G** basis set, because polarization effects are better described with the additional 3df and 3pd functions.

Besides the quality of the results, the choice of the "right" basis set also depends on the computational time. Both CVS-ADC(2)-x and CVS-ADC(3) methods scale with the order (M^6), where M is the number of basis functions. Since computational time is often limited, the computational effort usually prevents the use of large basis sets, especially for the calculation of chemically relevant molecules with more than 15 atoms. Let me give an example: in the case of the small CO molecule, the aug-cc-pVTZ basis comprises 110 Cartesian basis functions, while the 6-311++G** basis set, which is also at the triple-ζ level and includes diffuse functions, only consists of 46 basis functions. In other words, a calculation of CO at the CVS-ADC(2)-x or CVS-ADC(3) level takes 187 times longer when employing aug-cc-pVTZ instead of 6-311++G**. Considering the excellent quality of the results when using the 6-3111++G** basis set, employing basis sets from the larger aug-cc-series is not necessary, although the results would be more accurate. The same applies for the 6-311++G(3df,3pd) basis set, which comprises 90 Cartesian basis functions in the case of CO. Eventually, employing the 6-311++G** basis set provides an excellent computational cost/performance ratio.

4.2.2 Influence of Cartesian and Pure Basis Functions

Next, the influence of Cartesian 6D/10F basis functions is investigated. Since the Cartesian functions form the space of a reducible representation of the rotation group, the decomposition of Cartesian into pure spherical functions leads to a reduction in the number of basis functions from six d- and 10 f-functions into five d- and seven f-functions. Hence, employing pure basis functions affords computational savings. As shown in chapters 4.1 and 4.2.1, the influence of diffuse and extended basis functions on the core-excitation energies is significant, especially in the case of core Rydberg states. Since Cartesian basis

Table 4.6: Core-excitation energies (ω_{ex}) of the first three C 1s singlet excited states of carbon monoxide. The energies were calculated using CVS-ADC(2)-x in combination with different basis sets in their pure (P) and Cartesian (C) version. The calculated values are compared with experimental data[188] and the difference between C and P δ(P-C) is averaged for every basis set ($\overline{\delta}$). This table has already been published by me and my co-authors.[98]

	State 1 ω_{ex} [eV]			State 2 ω_{ex} [eV]			State 3 ω_{ex} [eV]			$\overline{\delta}$ [eV]
Basis set/Expt.	P	C	δ(P-C)	P	C	δ(P-C)	P	C	δ(P-C)	
6-311++G**	287.76	287.49	0.27	293.21	292.89	0.32	294.48	294.16	0.32	0.30
aug-cc-pVTZ	287.22	287.09	0.14	292.73	292.57	0.16	293.82	293.68	0.14	0.15
d-aug-cc-pVTZ	287.22	287.07	0.14	292.59	292.46	0.14	293.60	293.46	0.13	0.14
aug-cc-pCVTZ	287.06	287.03	0.03	292.57	292.52	0.05	293.67	293.63	0.04	0.04
def2-TZVPD	287.49	287.27	0.22	293.12	292.81	0.31	294.31	294.07	0.23	0.26
Experiment		287.4			292.5			293.4		—

functions are larger due to the additional diffuse d- and f-orbitals, using them should be advantageous. To show this influence, Table 4.6 contains a comparison of the first three C 1s excited states of CO calculated with pure and Cartesian versions of different triple-ζ basis sets.

Overall, employing Cartesian d- and f-functions lowers the core-excitation energies, because the basis is larger and due to the variational principle, the calculated energies are upper bounds of the exact ones. The averaged difference of core-excitation energies between Cartesian and pure functions ($\overline{\delta}$) depends strongly on the chosen basis set. Regarding aug-cc-pCVTZ, the difference is only 0.04 eV, thus the use of Cartesian basis functions has hardly any influence. In contrast, the core-excitation energies differ by about 0.3 eV using 6-311++G** and def2-TZVPD, while $\overline{\delta}$ is around 0.15 eV in the case of aug- and d-aug-cc-pVTZ. Looking at the different states, the difference between Cartesian and pure functions is almost constant within the respective basis sets. The only exception is state 2 using the def2-TZVPD basis set, where the difference between Cartesian and pure variants is 0.31 eV, while it is around 0.22 eV in the case of states 1 and 3. The use of Cartesian basis functions seems advantageous, especially, in the case of the 6-311++G** and def2-TZVPD basis sets, because the influence is large and compared to experimental values, the results are shifted towards the right direction. Eventually, Cartesian 6D/10F should be used whenever it is computationally possible.

4.3 The Accuracy of Oscillator Strengths

To further describe the spectral features of XA spectra, the strength of the absorption, which is represented by the oscillator strength, needs to be calculated properly, too. General ADC(2) methods are well known to provide accurate transition moments for valence-excited states, but the quantitative accuracy in combination with the CVS approximation has not been determined yet.[79,93] Since in the case of CVS-ADC(3,2) no algebraic expressions for the transition moments at third order are available yet, the second order terms are used instead and the quality of the oscillator strength compared to experiment is therefore an interesting question. In Table 4.7, the calculated oscillator strengths of the first three C 1s excitations of the CO molecule calculated at the CVS-ADC(2)-s, CVS-ADC(2)-x and

Table 4.7: Oscillator strengths (f_{osc}) of the first three C 1s singlet excited states of carbon monoxide. The f_{osc} were calculated using CVS-ADC at strict second (2s), extended second (2x) and third order with different basis sets. The mean values and the standard deviations σ are given and the calculated values are compared with experimental data.[188] The doubly degenerated states are given once and their f_{osc} values are given as sum. This table has already been published by me and my co-authors.[98]

	State 1 f_{osc}			State 2 f_{osc}			State 3 f_{osc}		
Basis Set/Expt.	2s	2x	3	2s	2x	3	2s	2x	3
aug-cc-pVDZ	0.162	0.134	0.150	0.004	0.004	0.006	0.014	0.017	0.017
aug-cc-pVTZ	0.177	0.141	0.157	0.004	0.003	0.005	0.012	0.015	0.015
aug-cc-pVQZ	0.179	0.143	0.159	0.004	0.003	0.005	0.010	0.013	0.013
aug-cc-pV5Z	0.179	0.143	0.159	0.004	0.003	0.004	0.009	0.012	0.012
6-31G	0.171	0.141	0.157	0.009	—	—	—	—	—
6-31G**	0.165	0.138	0.152	0.007	—	—	—	—	—
6-31++G**	0.164	0.137	0.151	0.004	0.003	0.005	0.015	0.018	0.017
6-31G(3df,3pd)	0.176	0.143	0.158	0.011	0.008	0.010	—	—	—
6-311G	0.183	0.143	0.160	0.007	—	—	—	—	—
6-311G**	0.178	0.141	0.156	0.006	0.005	—	—	—	—
6-311++G**	0.178	0.141	0.157	0.005	0.003	0.005	0.016	0.020	0.019
6-311++G(3df,3pd)	0.179	0.142	0.158	0.004	0.003	0.005	0.016	0.020	0.019
Mean	0.174	0.141	0.156	0.006	0.004	0.006	0.013	0.016	0.016
σ	0.007	0.003	0.003	0.002	0.002	0.002	0.003	0.003	0.003
Experiment		0.167			0.003			0.008	

CVS-ADC(3,2) levels are summarized. Here, the aug-cc-pVX series and the Pople-basis set series were chosen for a comparison. Regarding the CO example, the calculated oscillator strengths are almost independent of the employed basis set. This can be confirmed with the standard deviations for all CVS-ADC orders and investigated states, which are very small with values between 0.002 and 0.007. Looking at the results of the aug-cc-pVX series, only the double-ζ values differ from the other ζ-levels about 0.01 in the case of state 1. Comparable double-ζ basis sets from the Pople-series show a similar deviation.

Comparing the values obtained at different CVS-ADC levels, the higher-lying core-Rydberg states are almost identical at every investigated CVS-ADC level, while the bright s,π^*-state 1 shows large discrepancies. The smallest oscillator strength for state 1 is provided at the extended second order level, followed by CVS-ADC(3,2). At the CVS-ADC(2)-s level, the oscillator strength of state 1 has the largest value. These numbers differ by 0.3 and more, depending on the chosen basis set. The difference between the CVS-ADC orders can be explained by means of the core-excitation energies provided at the particular CVS-ADC levels. Generally, oscillator strengths depend on the excitation energy and the norm of the transition dipole moment ($|\mu_t|$). As shown in chapter 4.1, the calculated core-excitation energies differ strongly between the CVS-ADC levels. The $|\mu_t|$ value in atomic units (a.u.) of state 1 computed at the different CVS-ADC levels using, for example,

the aug-cc-pV5Z basis set, is 0.225, 0.202 and 0.212 at the CVS-ADC(2)-s, CVS-ADC(2)-x and CVS-ADC(3,2) level, respectively. Hence, the transition dipole moments vary much less than the corresponding oscillator strengths. Since the core-excitation energies differ between the CVS-ADC orders, the absolute values of the oscillator strengths follow the same trend as the core-excitation energies. This phenomenon is not dominant in the case of the Rydberg states, because the oscillator strength is very small compared to the bright state 1.

Looking again at the bright state 1, CVS-ADC(3,2) provides the most accurate result compared to experiment, while CVS-ADC(2)-x underestimates the experimental absorption by about 0.25. It seems that this is a large number, but it does not reduce the quality of the CVS-ADC(2)-x result at all, because compared to the higher-lying Rydberg states, this absorption is still dominant. These findings are in accordance with those presented in previous work, where a specially created basis set for the CO molecule was employed.[100] The oscillator strengths of state 2 and state 3 are in contrast excellently matched by all CVS-ADC methods with errors between 0.001 and 0.008, respectively.

4.4 Evaluation of Core-Excited State Dipole Moments

Finally, calculations of static dipole moments (μ_{ex}) of core-excited states calculated with the CVS-ISR method are discussed. Since experimental data are not available, proper benchmarking is challenging. Using the Full-CI approach would be an alternative, but computationally this is not possible, thus a representative from the CC family was chosen, i.e the SAC-CI SD-R method. Since both CVS-ADC(2)-x and SAC-CI methods are at similar level of theory with similar expected accuracy, the results discussed in this chapter cannot be seen as a real benchmark. However, the SAC-CI results help to demonstrate the correct behavior of the CVS-ADC/CVS-ISR approach. Furthermore, the numerical accuracy of the standard ISR method has already been verified a few times for valence-excited states.[78,93,190] With the knowledge about the accuracy of the CVS-ADC eigenvectors as demonstrated in chapters 4.1 – 4.3 by means of core-excitation energies and oscillator strengths, in principle, one can expect the same accuracy for the CVS-ISR approach. Due to technical and computational limitations of the SAC-CI method, a set of small molecules, which consists of fluoroethene (C 1s), NH_3 (N 1s) and H_2O (O 1s), was chosen for this study. Table 4.8 summarizes the results for the core-excited state dipole moments (μ_{ex}) and core-excitation energies (ω_{ex}) calculated at different CVS-ADC levels compared to data at SAC-CI level of theory. Here, CVS-ADC(1) results are discussed, too.

Since here other systems are investigated compared to the studies of the core-excitation energies and oscillator strengths, I first comment on the trend of the energies. The quality of the core-excitation energies obtained at different CVS-ADC levels, in principle, show the same trends as discussed in the other chapters. The most accurate results are calculated at the CVS-ADC(2)-x level using at least an augmented triple-ζ basis set, while the other CVS-ADC methods overestimate the core-excitation energies compared to experiment. CVS-ADC(1), as expected, provides a strong overestimation due to the lack of ground state correlation and of the description of orbital relaxation effects. Compared to experiments, results at the SAC-CI level are also very accurate. While SAC-CI tends to slightly overestimate the core-excitation energies, CVS-ADC(2)-x underestimates them a little. In the case of the first two oxygen 1s excitations of water, for example, the core-excitation energies at the CVS-ADC(2)-x level are about 1 eV too low, while they are about 1 eV too high at the SAC-CI level. However, the numerical accuracy provided

Table 4.8: Comparison of core-excitation energies (ω_{ex}) and core-excited state dipole moments (μ_{ex}) of the first three singlet states of CH_2CHF (C 1s) and the first five singlet states of NH_3 (N 1s) and H_2O (O 1s). The values are calculated using CVS-ADC at first (1), strict second (2s), extended second (2x) and third (3) order as well as SAC-CI. For all calculations, the 6-311++G** basis set was employed. Furthermore, experimental data (Expt.) of the core-excitation energies are given for comparison.[16,191] The degenerate double π-states of NH_3 are given only once (State 2 and 4), respectively. Sometimes, the energetic order of states differs between the methods. For a direct comparison, the order of states at the CVS-ADC(2)-x level is fixed, while the ones obtained with the other methods are sorted corresponding to the CVS-ADC(2)-x result. This table has already been submitted for publication by me and my co-author.[99]

State	ω_{ex} [eV]						μ_{ex} [D]				
	SAC-CI	1	2s	2x	3	Expt.[16,191]	SAC-CI	1	2s	2x	3
					CH_2CHF C 1s						
S_1	286.04	295.39	288.73	285.05	287.17	285.00	3.04	4.02	3.43	2.73	2.86
S_2	288.52	300.15	290.21	287.09	289.88	—	3.28	2.96	4.77	4.31	4.17
S_3	288.18	296.72	291.01	287.33	289.07	287.10	1.76	2.35	2.24	1.55	1.62
					NH_3 N 1s						
S_1	401.54	416.09	402.50	399.93	404.10	400.66	0.97	1.88	1.20	1.04	1.19
S_2	403.24	416.47	403.98	401.67	405.71	402.33	3.15	1.98	3.39	3.25	2.87
S_3	404.84	419.40	405.84	403.30	407.27	402.86	4.04	6.09	2.48	3.39	4.67
S_4	405.64	421.29	406.73	404.03	408.30	403.50	3.69	1.84	3.72	3.74	3.23
S_5	406.25	421.88	407.13	404.62	408.96	—	1.40	2.97	0.63	1.33	1.87
					H_2O O 1s						
S_1	534.95	551.19	534.83	532.90	538.44	534.00	1.25	1.61	1.70	1.38	1.35
S_2	536.74	551.83	536.42	534.76	540.05	535.90	0.90	0.22	1.31	1.18	0.70
S_3	539.48	556.58	539.25	537.42	543.06		3.83	6.26	0.71	2.35	5.35
S_4	539.65	556.21	539.76	537.70	543.01	537.00	2.88	2.19	2.69	2.76	2.60
S_5	539.79	558.01	539.62	537.71	543.69		2.23	0.62	1.77	2.26	1.75

by both methods is influenced by the type of the element, respectively. The heavier the atom, the larger the absolute error.

Let me turn to the static dipole moments of the core-excited states and start with the C 1s excitation of fluoroethene. The μ_{ex} values of the states S_1 and S_3 provided at the CVS-ADC(2)-x, CVS-ADC(3,2) and SAC-CI levels are in good agreement with each other, while CVS-ADC(2)-s and CVS-ADC(1) overestimate the static dipole moments of the core-S_1 and S_3 states by about 0.5 D and 1.0 D, respectively. The difference of the core-S_1 μ_{ex} value between CVS-ADC(3,2) and SAC-CI is only 0.18 D, while CVS-ADC(2)-x and SAC-CI differ by 0.31 D. On the other hand, the μ_{ex} value of the core-S_2 state, which exhibits almost no oscillator strength, is described differently at the SAC-CI level compared to the CVS-ADC methods. The SAC-CI value is around 1.0 D above the one of CVS-ADC(2)-x value, whereas CVS-ADC(3,2) and CVS-ADC(2)-x are again at the same level. For the core-S_2 state of fluoroethene, the dipole moment obtained by CVS-ADC(1) is only 0.32 D above the SAC-CI result and the CVS-ADC(2)-s value is slightly above the one provided by CVS-ADC(2)-x.

The next example are the N 1s excitations of ammonia. Here, again a good agreement between SAC-CI and CVS-ADC(2)-x/CVS-ADC(3,2) results is given. However, there is one exception, i.e. the core-S_3 state. The difference between SAC-CI and CVS-ADC(2)-x values are only 0.07 D, 0.10 D, 0.05 D and 0.07 D for the core-S_1, S_2, S_4 and S_5 states, respectively, whereas the difference of dipole moments for the S_3 state is 0.65 D. The values provided by the other CVS-ADC methods are shifted without any identifiable regularity, sometimes overestimating and sometimes underestimating the SAC-CI results slightly or strongly. The CVS-ADC(1) results, in particular, show the largest deviations compared to the other approaches.

As the last example, the O 1s excitations of water are discussed. Here, the results are comparable to the ones of NH_3. There is again one spike, i.e. the core-S_3, for which the deviation between the CVS-ADC(2)-x method is significantly larger compared to the SAC-CI result. The differences of the μ_{ex} values between SAC-CI and CVS-ADC(2)-x are 0.13 D, 0.28 D, 1.48 D, 0.12 D and 0.03 D for the first five core-excited singlet states, respectively. The other CVS-ADC approaches show again shifts without any identifiable regularity.

Eventually, this investigation demonstrates the accuracy of the CVS-ADC/CVS-ISR approaches in spite of the lack of experimental data. Between the CVS-ADC(2)-x and SAC-CI levels of theory, a qualitative and quantitative agreement of static core-excited state dipole moments is given in most of the cases. CVS-ADC(3,2) and CVS-ADC(2)-s results often show deviations without any identifiable regularity, while CVS-ADC(1) values strongly differ compared to the others. Hence again, CVS-ADC(2)-x could be identified as the most accurate CVS-ADC approach, but the results at the CVS-ADC(3,2) level are adequate, too. The larger discrepancies between SAC-CI and CVS-ADC(2)-x results, i.e the core-S_3 states of the ammonia and water examples, cannot be explained at the moment. This might be due to slight differences within the core-excited state vectors provided by the SAC-CI and CVS-ADC methods.

Chapter 5

The Contribution of Orbital Relaxation Effects

As explained in chapter 2.5.9, orbital relaxation effects play an important role in the description of core-excited states. In this chapter, the contribution of this effect on core-excitation energies is discussed by means of CVS-ADC calculations up to third order. For this purpose, two quantitative descriptors are available. One is the amount of doubly excited amplitudes (R2) and the other is the electron promotion number (p_{DA}), which is calculated by means of detachment/attachment (D/A) densities (see chapter 2.5.8). Other descriptors like exciton sizes, which also help to identify orbital relaxation effects, are discussed as well. Furthermore, plotting (D/A) densities visualizes these effects and comparisons with plotted hole/electron (h/e) densities provides a qualitative picture of the influence of orbital relaxation effects on the core-excitation process. To demonstrate the contribution of orbital relaxation effects within the CVS-ADC methods, the first core-excited singlet states and their properties of the small molecules CO, CH_2CHF, NH_3, H_2O and the CH_3 radical were calculated using CVS-ADC(1) to CVS-ADC(3,2) (in the case of CH_3 the unrestricted variant was used). Their structures are illustrated in Figure 4.1.

All structures of the small molecules in the electronic ground state were optimized at the CCSD[51] level using the def2-QZVPPD[119] basis set and the `Q-Chem 4.3`[94] program. Core-excited states and the corresponding properties were calculated with my implementation of CVS-ADC up to third order of perturbation theory as well as with my CVS-ISR implementation as described in chapter 3. Exciton sizes and state densities were calculated using the `libwfa` library.[84,86–88] Note that both ground and core-excited state calculations of the CH_3 radical were always performed using the unrestricted variants of the respective methods. The calculations of core-excited states were performed employing the Cartesian 6D/10F version of the 6-311++G**[109,110,113] and aug-cc-pVTZ[115,116] basis sets. All computed values shown in this chapter are absolute without any level shift or consideration of relativistic effects. Finally, note that the content of this chapter has already been published by me and my co-authors in *Journal of Chemical Physics, 142 (2015), 214104* or has been submitted for publication in *Journal of Chemical Theory and Computation, (2016).*[98,99]

5.1 Treatment of Orbital Relaxation Effects

The results presented in chapter 4 lead to the question why CVS-ADC(3) and also CVS-ADC(2)-s perform worse than CVS-ADC(2)-x, although the order of perturbation theory is higher in the case of CVS-ADC(3). Generally, the final result obtained at the CVS-ADC level is based on cancellation of errors of neglecting relativistic effects, description of orbital relaxation effects, basis set truncation, and considering electron correlation. This error cancellation seems optimal in the case of CVS-ADC(2)-x. As explained in chapter 2.5.9, the fortuitous error compensation provided at the CVS-ADC(2)-x level is broken at the CVS-ADC(3) level. This leads to an overestimation of core-excitation energies. The overestimation at the CVS-ADC(2)-s level can be explained due to the lack of improvement of the description of the doubles, which usually leads to a lowering of the excitation energies in CVS-ADC(2)-x compared to CVS-ADC(2)-s.[79,181]

Besides the numerical accuracy of the results, the increased overestimation towards heavier elements in the case of CVS-ADC(3) has also not yet been clarified. Due to the strong Coulomb attraction with the nucleus, the contraction of the core hole becomes larger going to heavier elements, e.g. >100 eV from carbon to nitrogen. Hence, relaxation and polarization effects gain more importance and since these effects are described in an unbalanced way at the CVS-ADC(3) level, this seems to be the reason why the overestimation increases with heavier elements. Actually, the couplings between singles and doubles are evenly disturbed in a way that the CVS-ADC(2)-s method provides better core-excitation energies compared to experiment than CVS-ADC(3) regarding elements heavier than carbon. Since orbital relaxation effects are included indirectly via couplings between the excited configurations, the amount of doubly excited amplitudes contributing to a state (R2) can be seen as an indirect indicator for the relaxation effects in the case of both CVS-ADC(2) variants and CVS-ADC(3). To show this, Table 5.1 contains the correlation between R2 and the core-excitation energy of the first core-excited singlet states of CO, NH_3 and CH_3 at the different CVS-ADC levels.

The ω_{ex} values straightly decrease towards the experimental values going from CVS-ADC(1) to CVS-ADC(2)-x and increase again going further to CVS-ADC(3). In the case of both C 1s excitations (CO and CH_3), the core-excitation energies stay below the one obtained with CVS-ADC(2)-s. However, this is not the case for heavier elements, where the core-excitation energies are larger than those obtained at the CVS-ADC(2)-s level. This observation is independent of the employed 6-311++G** and aug-cc-pVTZ basis sets.

Let me now take a look at the R2 values. CVS-ADC(1) does not include doubly excited amplitudes, thus the R2 value is exactly zero inherently. From the strict second order to the extended second order, the R2 value increases, while it decreases again at the CVS-ADC(3) level. Hence, the trend of the R2 values is opposite to the trend of ω_{ex}. In the case of the C 1s excitation, the R2 value obtained with CVS-ADC(3) is between the values of the strict and extended second order approaches, which is also comparable to the trend of the core-excitation energies. Due to the stronger relaxation effects of core excitations of heavier elements, the amount of doubly excited amplitudes for the N 1s and O 1s excitations provided at the CVS-ADC(2)-s level is larger than at the third order level, because the disturbed relationship between the couplings in CVS-ADC(3) leads to a underestimation of R2 for heavier elements.

Eventually, a distinct relative correlation between R2 and ω_{ex} can be confirmed. Hence, the R2 values can be seen as an indirect indicator for the treatment of relaxation and other energy lowering effects at the different CVS-ADC levels.

Table 5.1: Core-excitation energies (ω_{ex}) and amount of double amplitudes (R2) of the first singlet core-excited state of CO (C 1s and O 1s) and NH_3 (N 1s) and the first C 1s excited state of CH_3 calculated using CVS-ADC at first, strict second (2s), extended second (2x), and third order and employing the 6-311++G** and aug-cc-pVTZ basis sets. The calculated values are compared with experimental data.[16,188,189] This table has already been published by me and my co-authors.[98]

	CO C 1s		CO O 1s		NH_3 N 1s		CH_3 C 1s	
ADC order	ω_{ex} [eV]	R2 [%]	ω_{ex} [eV]	R2 [%]	ω_{ex} [eV]	R2 [%]	ω_{ex} [eV]	R2 [%]
6-311++G**								
1	294.47	—	550.17	—	416.47	—	288.47	—
2s	290.54	7	535.80	17	403.98	19	284.00	6
2x	287.49	19	532.98	22	401.67	22	281.44	14
3	288.40	13	539.18	16	405.71	16	282.65	11
aug-cc-pVTZ								
1	294.41	—	550.09	—	416.46	—	288.45	—
2s	290.19	7	535.53	19	403.70	17	283.69	6
2x	287.09	19	532.70	22	401.45	22	281.08	14
3	288.02	13	538.74	16	405.48	16	282.24	11
Experiment								
	287.4	—	534.1	—	402.33	—	281.35	—

5.2 Quantification and Visualization of Orbital Relaxation Effects via State Densities

Next, the study in the last chapter is extended by visualization and quantification of relaxation effects based on the CVS-ISR approach. For this purpose, the set of the representative small molecules CH_2CHF, H_2O, NH_3 and the CH_3 radical are investigated. The first core-excited singlet state of these molecules were calculated using CVS-ADC(1) to CVS-ADC(3,2), respectively. The results are summarized in Table 5.2.

The core-excitation energies and R2 values follow the same trend as explained in chapters 4 and 5.1. The CVS-ADC(2)-x results are almost in perfect agreement with experimental values, while CVS-ADC(2)-s and CVS-ADC(3) overestimate the ω_{ex} values slightly. CVS-ADC(1), in contrast, provides a significant overestimation. In all investigated examples, the R2 value at the CVS-ADC(2)-x level is the largest. Furthermore, CVS-ADC(3,2) provides larger values than CVS-ADC(2)-s regarding the C 1s excitations ($CH_2CHF$and CH_3), while the opposite is the case for the core excitations of heavier elements.

Let me take a look at the promotion numbers p_{DA}, which are based on the (D/A) densities. The same relation as the one between ω_{ex} and R2 can be identified analyzing the promotion numbers. At the CVS-ADC(1) level, the p_{DA} value is always 1.0, because no higher excited configurations are available. As a consequence, the 1TDM and the 1DDM are identical at the CVS-ADC(1) level, thus the respective descriptors and properties based on these densities are equal, too. CVS-ADC(2)-x results exhibit the highest promotion

Table 5.2: Comparison of core-excitation energies (ω_{ex}), amount of doubly excited amplitudes (R2), and various descriptors (see chapter 2.5.8 for definitions) of the respective first core-excited singlet state of CH_2CHF (C 1s), NH_3 (N 1s), H_2O (O 1s), and the CH_3 radical (C 1s) calculated using CVS-ADC at different order with the 6-311++G** basis set. This table has already been submitted for publication by me and my co-author.[99]

Method	ω_{ex} [eV]	R2 [%]	p_{DA}	σ_D [Å]	σ_h [Å]	σ_A [Å]	σ_e [Å]	$d_{D\to A}$ [Å]	$d_{h\to e}$ [Å]
CH_2CHF C 1s									
CVS-ADC(1)	295.39	—	1.00	0.17	0.17	1.24	1.24	0.61	0.61
CVS-ADC(2)-s	288.73	11.64	1.69	0.97	0.17	1.29	1.46	0.31	0.64
CVS-ADC(2)-x	285.05	23.89	1.87	1.00	0.17	1.20	1.45	0.19	0.59
CVS-ADC(3,2)	287.17	19.55	1.75	0.92	0.17	1.15	1.37	0.22	0.61
NH_3 N 1s									
CVS-ADC(1)	416.09	—	1.00	0.14	0.14	1.81	1.81	0.77	0.77
CVS-ADC(2)-s	402.50	18.47	1.84	0.95	0.14	2.11	2.72	0.34	0.72
CVS-ADC(2)-x	399.93	22.19	1.90	0.89	0.14	1.89	2.50	0.31	0.70
CVS-ADC(3,2)	404.10	17.15	1.79	0.83	0.14	1.75	2.24	0.34	0.72
H_2O O 1s									
CVS-ADC(1)	551.19	—	1.00	0.12	0.12	1.48	1.48	0.80	0.80
CVS-ADC(2)-s	534.83	19.06	1.84	0.84	0.12	1.90	2.40	0.44	0.91
CVS-ADC(2)-x	532.90	20.68	1.85	0.79	0.12	1.67	2.13	0.40	0.86
CVS-ADC(3,2)	538.44	15.53	1.73	0.72	0.12	1.48	1.82	0.42	0.84
CH_3 C 1s									
CVS-UADC(1)	288.47	—	1.00	0.17	0.17	0.82	0.82	0.00	0.00
CVS-UADC(2)-s	284.00	6.20	1.47	0.78	0.17	0.89	0.98	0.00	0.00
CVS-UADC(2)-x	281.44	13.85	1.71	0.89	0.17	0.89	1.04	0.00	0.00
CVS-UADC(3,2)	282.65	10.58	1.61	0.82	0.17	0.84	0.97	0.00	0.00

numbers (larger than 1.7) as well as the largest R2 values, which indicates strong orbital relaxation effects. To put this in relation, typical p_{DA} values for "ordinary" low-lying valence-excited states at the ADC(2) level are below 1.7.[86] However, the trend of the promotion numbers going from the lighter carbon to the heavier oxygen element does not show an expected increase due to the stronger Coulomb attraction of heavier atoms, which results in stronger relaxation effects. The same applies for the R2 values. From carbon to nitrogen (CH_2CHF to NH_3), for example, the p_{DA} values increase slightly from 1.87 to 1.9 at the CVS-ADC(2)-x level, but decrease in the water example to 1.85. The R2 values straightly decrease from carbon to oxygen. Since orbital relaxation effects are only included indirectly within the CVS-ADC methods via couplings to higher excited amplitudes, promotion numbers and the amount of doubly excited amplitudes are not appropriate descriptors to capture this effect. Promotion numbers just count the number of attached and detached electrons due to a core-excitation process based on an initial and final state picture, while R2 only counts the amount of the doubles. In other words, both tools describe the final results after the relaxation process, which must neither necessarily depend on the dynamics of the process itself, nor on the excited element. Nevertheless, promotion numbers and R2 values are adequate tools for the description of the strength of the final relaxation process. An alternative way to analyze the stronger influence of heavier cores on the created holes is provided via the exciton size of the hole (σ_h) based on

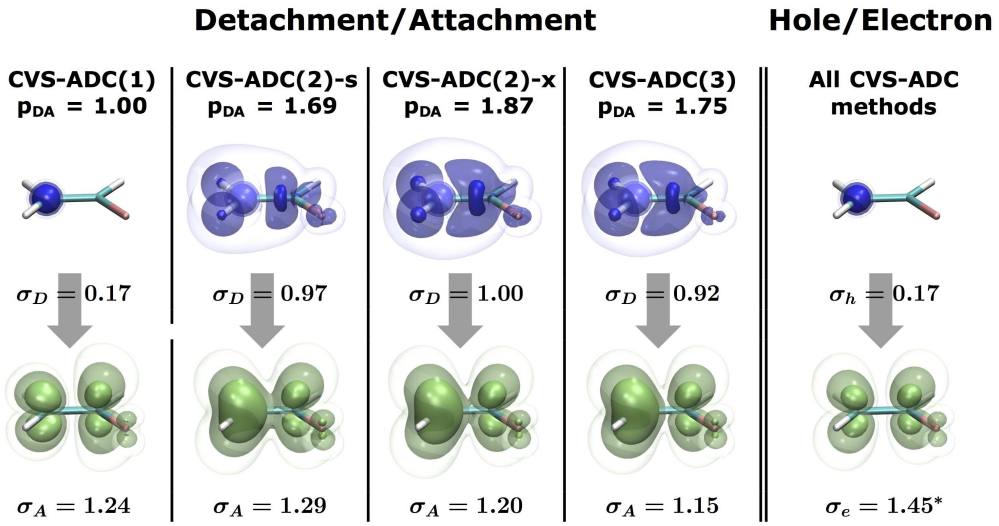

Figure 5.1: Comparison of detachment(blue)/attachment(lime) densities based on the 1DDM with hole(blue)/electron(lime) densities based on the 1TDM. The first C 1s core-excited singlet state of CH_2CHF is shown as example. The densities are calculated at different CVS-ADC levels employing the 6-311++G** basis set. The isosurfaces of the densities were rendered with the isovalues 0.0256 (opaque), 0.0064 (colored transparent), and 0.0016 (transparent). The promotion numbers p_{DA} and the respective exciton sizes σ_x (Å) are shown, too.
*(In the case of the electron density, only the CVS-ADC(2)-x isosurface and corresponding σ_e value are shown. The shapes of the electron isosurfaces at the other CVS-ADC levels are very similar.)

the 1TDM. Since all investigated core-excited states in Table 5.2 are characterized by an excitation from one contracted 1s orbital located on one specific atom, the hole sizes grow from 0.12 Å to 0.17 Å going from oxygen to carbon due to reduced Coulomb attraction.

Besides promotion numbers, another practical benefit of the CVS-ISR method is the possibility to visualize relaxation effects via state densities, i.e (D/A) densities. Figure 5.1 illustrates the differences obtained at the investigated CVS-ADC levels by means of the first C 1s excited singlet state of CH_2CHF, which is characterized by the promotion of one electron from the doubly hydrogen substituted carbon atom (C_{2H}) to a delocalized π^* level. Note that the (h/e) densities based on the 1TDM look practically identical at all CVS-ADC levels, thus only one example is shown. The hole size of 0.17 Å is very small, which indicates the excitation from one contracted carbon 1s orbital. As mentioned above, CVS-ADC(1) provides no difference between (D/A) or (h/e) density properties, which can be seen when comparing both types of densities illustrated in Figure 5.1. Note that the electron densities slightly differ between the CVS-ADC levels, but the shape is almost identical. σ_e is in the case of the CVS-ADC(1) calculation 1.24 Å, which is identical to the σ_A value. Orbital relaxation effects are apparently visible when investigating the (D/A) densities at the higher CVS-ADC levels, particularly, in a direct comparison with the (h/e) densities. Generally, all higher-order CVS-ADC methods show the same effect: while the attachment densities exhibit only slight effects compared to the (h/e) densities, the detachment densities contain strong relaxation effects. These can be described as an expansion from the C_{2H} atom to the neighboring atoms, which results in a strong diffuse

delocalization over the whole molecule. Thereby, the detachment density is mostly relaxed to the other carbon atom, but the two connected hydrogen atoms are influenced, too. In contrast to the detachment density, the attachment density is mainly located on the C_{2H} atom.

Visually, the relaxation effects of the (D/A) densities are largest at the CVS-ADC(2)-x level. To quantify this observation, exciton sizes can be helpful tools (see Table 5.2). In the case of CVS-ADC(2)-x, σ_D is with 1.00 Å almost 6 times larger than σ_h with 0.17 Å. σ_A, in contrast, is about 0.25 Å smaller than the corresponding σ_e value. Comparing these values provided by the other CVS-ADC methods, respectively, one can generalize this observation: σ_e is for all investigated systems slightly larger than σ_A, while σ_D is much larger than σ_h. Hence, the relaxation effects of core excitations lead to a slight contraction of the attachment density and a strong expansion of the detachment density. These effects are largest using CVS-ADC(2)-x, which confirms the analysis of promotion numbers and R2 values. Note that the exciton sizes just describe the extent of the exciton in a center of charge picture defined via root-mean-square deviation of the respective position operators (see chapter 2.5.8). Hence, one has to compare the exciton sizes based on the 1DDM with the ones based on the 1TDM to recognize the influence of relaxation effects to the (D/A) densities. As a consequence of this description, σ_D at the CVS-ADC(2)-s level, for example, is larger than at the CVS-ADC(3,2) level, although the effects are visually larger at the third order level, because the centers of charges are shifted differently. Another example is that the σ_A values are smaller than the σ_e values, although the attachment density has a significant contribution located at the C_{2H} atom. Hence, promotion numbers are better suited for a general quantification of relaxation effects.

Next, let me take a look at the center of charge exciton sizes $d_{D\rightarrow A}$ and $d_{h\rightarrow e}$ (see Table 5.2). A direct comparison reveals that $d_{h\rightarrow e}$ is significantly larger than $d_{D\rightarrow A}$ for all investigated systems using higher order CVS-ADC methods. This can also be explained by inspecting the (D/A) and (h/e) densities visually. Since the investigated states contain only excitations from one contracted 1s orbital, the hole density is localized on one atom. Due to the strong relaxation of the detachment density resulting in the spatial extent of the density over the whole molecule, the center of charge is shifted in the direction of the center of the molecule. Thereby, the attachment density is only slightly affected and also delocalized over the molecule, thus the distance of the center of charges of the (D/A) density is reduced. Finally, note that R2 and p_{DA} values of the organic radical CH_3 are smaller compared to the closed-shell systems. I show in the following chapter that this is often the case for core-excited states with s,π^* character of small open-shell systems (see chapter 6.3). An explanation of this observation is the local character of these core excitations. Looking at both exciton sizes d (center of charges) of the CH_3 radical with values of 0.00 Å independent of the applied CVS-ADC order confirms the local character of this state. The d_{exc} value, which includes the dynamic charge separation contribution, is with 1.04 Å at the CVS-ADC(2)-x level larger than the values based on the center of charge picture, indicating strong dynamic effects within the open-shell CH_3 system.

Chapter 6

Calculations of X-ray Absorption Spectra of Small and Medium-Sized Molecules

After benchmarking the CVS-ADC methods, I present in this chapter calculated X-ray absorption (XA) spectra of chosen medium-sized molecules and small organic radicals. From the field of organic electronics, acenaphthenequinone (ANQ), 3,4,9,10-perylentetracarboxylic dianhydride (PTCDA) and 2,2'-bithiophene (BT) are investigated, while the biologically relevant molecules porphin, thymine and cytosine are studied to demonstrate the capabilities of my CVS-ADC(2)-x implementation. Furthermore, first calculations of XA spectra of radicals ever calculated with the CVS-UADC method are presented. Therefore, a set consisting of the methyl (CH_3) radical, hydroxyl (OH) and allyl radicals as well as the triplet dioxygen diradical (O_2) was chosen. All calculated X-ray absorption spectra are discussed at the level of CVS-(U)ADC(2)-x and compared with experimental data. In the case of the ANQ and cytosine systems, the CVS-ISR method is employed to obtain core-excited state densities, which are used for a further wave function analysis. These results are discussed as well in this chapter. Since most of the other studies presented in this chapter were performed before I have implemented the CVS-ISR approach and combined the CVS-ADC implementation with the `libwfa` package, discussions of state characters are based on the MO configurations using the MO expansion coefficients. There is often no dominant configuration that characterizes a core-excited state adequately, because an electronic core-excited state in terms of CVS-ADC(2)-x is represented by combinations of singly and doubly excited configurations. Hence, only the most dominant configurations with a contribution larger than 6.25% are shown and only pictures of relevant MOs are presented to keep a clear view. Furthermore, only spectroscopically relevant bright core-excited states are given in some cases to avoid discussions of dark core excitations, which are usually not relevant. In the case of the unrestricted calculations, virtual orbitals are labeled according to their spin (α or β). $\pi^*_{\beta 1}$, for example, denotes the lowest unoccupied orbital with β-spin and π^*-character.

Besides PTCDA and cytosine, ground state geometry optimizations of the molecules were performed with MP2 employing the def2-TZVPP[118] basis set in combination with the resolution-of-the-identity (RI)[192,193] approximation and the respective auxiliary TZVPP[194] basis set. Due to technical limitations, the ground state structure of the PTCDA molecule was optimized at the level of DFT, employing the B3LYP xc functional[125–127] and the

def2-TZVPP basis set. The ground state geometry of cytosine was also optimized at the MP2 level of theory, but the SV(P)[195] basis set was employed to be in accordance with another work.[84] For all geometry optimization calculations, the `TURBOMOLE 6.3.7` program[196] was used. Core-excited states and the corresponding properties were calculated with my implementation of CVS-ADC(2)-x as well as the CVS-ISR implementation as described in chapter 3. Exciton sizes and state densities were calculated using the `libwfa` library.[84,86–88] Note that both ground and core-excited state calculations of the small organic radicals are always performed using the unrestricted variants of the respective methods. To save computational time, molecular point group symmetry was exploited in the calculations of BT (C_2), ANQ (C_{2v}), porphin (D_{2h}) and PTCDA (D_{2h}). A special case is the ANQ molecule, where the calculations of C 1s XA spectra were performed using C_{2v} point group symmetry, while the O 1s spectra were computed with and without exploiting point group symmetry. For the calculations of core-excited states, the following basis sets were employed: 6-311++G**[109,110,113] (thymine, BT, ANQ, CH_3, OH, O_2, allyl radical), 6-31++G**[111–113] (porphin) and 6-31G**[111,112] (PTCDA). The optically allowed B_{1u} core-excited states of porphin were also calculated with the larger 6-311++G** basis set to show that the deviations in the results are mostly due to basis set incompleteness. If not otherwise stated, all calculations were performed using the Cartesian 6D/10F version of the respective basis sets. All computed values shown in this chapter are absolute without any level shift or consideration of relativistic effects. Finally, note that the whole content of this chapter has already been published by me and my co-authors. Calculations of the closed-shell systems are published in *Journal of Computational Chemistry, 35 (2014), pages 1900-1915*, while the XA spectra of the open-shell systems are published in *Journal of Chemical Theory and Computation, 10 (2014), pages 4583-4598.*[96,97] Furthermore, the state properties and wave function analyzes of ANQ and cytosine have been submitted for publication in *Journal of Chemical Theory and Computation, (2016).*[99]

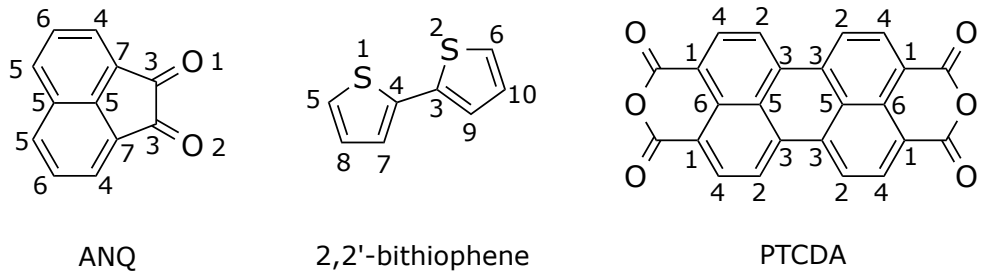

Figure 6.1: Structures of acenaphthenequinone (ANQ), 2,2'-bithiophene (BT) and 3,4,9,10-perylentetracarboxylic dianhydride (PTCDA). In the case of ANQ and PTCDA the atoms are numbered in groups. Each group consists of equivalent atoms due to point group symmetry, whose 1s orbitals form the respective linear combinations of electron donor orbitals.

6.1 Molecules in the Field of Organic Electronics

Electronic devices based on organic materials like organic light emitting devices (OLED) or photovoltaic materials are of high interest to the current applied research.[2,197–199] To investigate and understand charge transport mechanisms depending on intermolecular interactions, XAS techniques are often employed.[11] This is due to the intermolecular interactions, which define the charge transport properties of the semiconducting materials that are correlated with the electronic structure and the levels of the lowest unoccupied molecular orbitals (LUMO) of the molecules. In principle, there are two types of molecules needed for organic solar cells: electron acceptors and electron donors. Thiophenes have been recognized as good donor molecules, while perylene derivatives like 3,4,9,10-perylentetracarboxylic dianhydride (PTCDA) and acenaphthenequinone (ANQ) are widely used as electron acceptors.[95,200–204] Therefore, I chose ANQ, 2,2'-bithiophene (BT) and PTCDA as example systems to demonstrate the potential of CVS-ADC(2)-x calculations in the field of organic electronics. Figure 6.1 illustrates the structures of these molecules, thereby indicating the numbering of the atoms, respectively.

6.1.1 Acenaphthenequinone

ANQ is a medium-sized quinone with 20 atoms and it represents a model system for electron acceptor molecules in photovoltaic devices. Both carbon and oxygen K-edge spectra are discussed in this section. A significant difference between ANQ and the small systems discussed in the last two chapters is the number of atoms of the same type from which core electrons are excited, which is due to the C_{2v} symmetry. ANQ contains twelve carbon atoms and some of them are equivalent (see Figure 6.1) as well as two equivalent oxygen atoms. As a consequence, the 1s orbitals form linear combinations that describe the core-excited states, respectively. Illustrations of the relevant virtual MOs are given in Figure 6.2.

Let me start with the CVS-ADC(2)-x results of the O 1s excitations, which are shown in Table 6.1. Triplet core-excited states are also included to demonstrate that my implementation is capable of calculating such states in general. Experimentally, there is only one broad peak in the low O 1s excitation energy domain between 529.2 eV and 531.4 eV.[205] Since C_{2v} symmetry was not exploited in this example, the first eight core-excited states are almost pairwise degenerate. Each pair of the singlet states consists of one

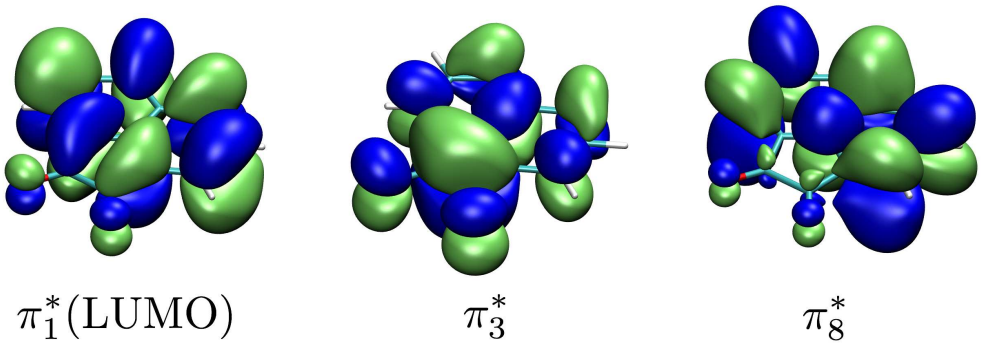

Figure 6.2: Illustration of the relevant virtual molecular orbitals of ANQ at the level of HF in combination with the 6-311++G** basis set. The isosurfaces of the MOs are rendered with an isovalue of 0.02.

Table 6.1: Core-excitation energies (ω_{ex}), oscillator strengths (f_{osc}), character and amount of double amplitudes (R2) of the first eight O 1s singlet and triplet excited states of ANQ calculated using CVS-ADC(2)-x and the 6-311++G** basis set. The calculated values are compared with experimental data.[205] Only the main transitions are shown and the numbering of the atoms complies with Figure 6.1. This table has already been published by me and my co-authors.[96]

State	ω_{ex} [eV]	f_{osc}	Main transition (1s $\rightarrow$)	R2 [%]	ω_{ex} [eV] (Expt.)
T_1	528.99	—	O1,O2 $\rightarrow \pi_3^*$	21	
T_2	528.99	—	O1,O2 $\rightarrow \pi_3^*$	21	
S_1	529.45	0.0002	O1,O2 $\rightarrow \pi_3^*$	23	529.2 - 531.4
S_2	529.45	0.0689	O1,O2 $\rightarrow \pi_3^*$	23	
S_3	533.08	0.0000	O1,O2 $\rightarrow \pi_1^*$	27	
S_4	533.08	0.0003	O1,O2 $\rightarrow \pi_1^*$	27	
T_3	533.09	—	O1,O2 $\rightarrow \pi_1^*$	27	
T_4	533.09	—	O1,O2 $\rightarrow \pi_1^*$	27	

state which is optically allowed, while the other exhibits no significant oscillator strength. The CVS-ADC(2)-x result with 529.45 eV is very close to the experiment, exhibiting an error of 0.85 eV, i.e. a relative error of 0.1%. The optically allowed core-S_2 state is mainly characterized by 51.7% of an electron promotion from a linear combination of the two O 1s orbitals to the π_3^* (LUMO+2) orbital, which exhibits a strong π^* fraction located on the oxygen atoms. Hence, a significant overlap with the O 1s orbitals exists, resulting in a localized state with a strong oscillator strength of 0.0689. The amount of double excitations contributing to this state is considerable with 23%, indicating strong relaxation effects. Reinvestigations with additionally calculating (h/e) state densities provide an improved picture of the state character of the core-S_2 state (see Figure 6.3). Here, it is obvious that the electron is promoted from the oxygen 1s orbitals to a π^*-level, which is localized on the C=O bonds, whereas the LUMO+2 orbital has also a delocalized fraction on the carbon ring. Since the transition into the LUMO+2 orbital only contributes with 51.7%, it is not sufficient to define the state character by only considering the main MO transitions. This demonstrates the advantage of inspecting state densities rather than MO transitions to determine the character of a core-excited state.

Next, the calculated C 1s spectrum of ANQ is discussed. The calculated results of the first 18 singlet states and the experimental comparison are given in Table 6.2. Henceforward, triplet states are neglected, because they are optically forbidden and do not contribute to the absorption spectra. Within the first 18 core-excited states, all optically allowed states are of B_2 symmetry and exhibit s,π^* character based on the MO transition contributions. Some states are doubly degenerate due to the C_{2v} symmetry and all states exhibit large R2 values ranging from 24% to 28%. The first experimental[13] peak is at 284.1 eV, which corresponds to the 1 $^1B_2$ state. The difference of the calculated state to the experiment is only 0.3 eV (0.1%) and based on the MO transitions, this core excitation is dominated by an electron promotion from the C7 atoms to the π_1^* and π_3^* virtual MOs. The next two higher $^1B_2$ states that exhibit oscillator strength are energetically separated by only 0.03 eV, thus both correspond to the second experimentally observed peak at 284.45 eV. Here, the difference between calculation and experiment is 0.36 eV. Both 2 $^1B_2$ and 3 $^1B_2$ states can be characterized by transitions to the π_1^* and the π_3^* orbitals, but in contrast to the 1 $^1B_2$ state, the C4 and C5 carbons are the electron donor atoms. Since the first optically allowed state has an error of 0.3 eV compared to the experiment, the calculated energy difference between the first and second/third bright core-excited states is in perfect agreement with the experiment. The third bright state (4 $^1B_2$) with a calculated core-excitation energy of 284.96 eV exhibits an error of 0.16 eV compared to the experiment. Hence, this error is slightly lower than for the previous two states and therefore the spacing between the second and third optically allowed states is slightly worse described than the first one. The 4 $^1B_2$ state is characterized by a core excitation from the C6 carbons to the π_1^* and π_8^* orbitals. The fourth optically allowed core-excited state is 5 $^1B_2$, which exhibits an oscillator strength of 0.024. Compared to the experimental value of 285.0 eV, the error is 0.27 eV, which is again of similar magnitude as the one of the first two bright states. This state is characterized by a core excitation from the C5 carbons to the π_3^* and π_8^* orbitals. The fifth bright experimental peak at 285.6 eV is broad and can be described as a mixture of different core-excited states. The calculated excitation energies range from 285.6 eV to 285.92 eV, where the degenerate states 8 $^1B_2$ and 9 $^1B_2$ exhibit the highest oscillator strength among these states. Hence, the error to the experiment is 0.32 eV, which is again of the same magnitude as the first one.

Eventually, all excitation energies of the core-excited states of ANQ calculated with CVS-ADC(2)-x/6-311++G** exhibit almost constant absolute and very small relative errors. Therefore, they are in almost perfect agreement with the experimental spectrum,

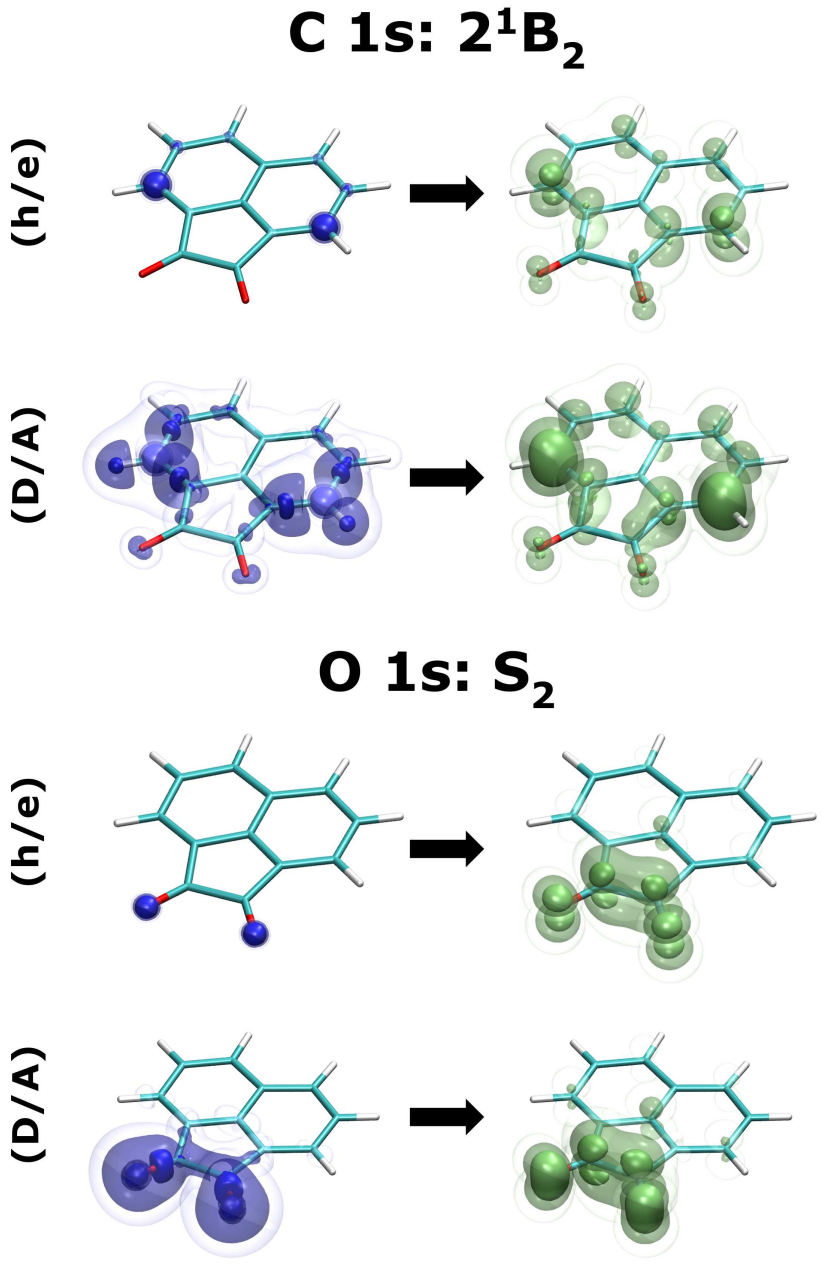

Figure 6.3: Comparison of (h/e) and (D/A) densities of the 2^1B_2 C 1s and O 1s core-S_2 excited states of ANQ computed with CVS-ADC(2)-x using the 6-311++G** basis set. The isosurfaces were rendered with the isovalues 0.0128 (opaque), 0.0064 (colored transparent), and 0.0008 (transparent).

Table 6.2: Core-excitation energies (ω_{ex}), oscillator strengths (f_{osc}), character and amount of double amplitudes (R2) of the first 18 C 1s singlet excited states of ANQ calculated using CVS-ADC(2)-x and the 6-311++G** basis set exploiting C_{2v} point group symmetry. The calculated values are compared with experimental data.[13] Only the main transitions are shown and the numbering of the atoms complies with Figure 6.1. This table has already been published by me and my co-authors.[96]

State	ω_{ex} [eV]	f_{osc}	Main transition (1s $\rightarrow$)	R2 [%]	ω_{ex} [eV] (Expt.)
$1\ ^1A_2$	284.40	0.000	C7 $\rightarrow \pi_1^*, \pi_3^*$	26	284.1
$1\ ^1B_2$	284.40	0.038	C7 $\rightarrow \pi_1^*, \pi_3^*$	26	
$2\ ^1A_2$	284.78	0.000	C4 $\rightarrow \pi_1^*, \pi_3^*$	25	
$2\ ^1B_2$	284.78	0.041	C4 $\rightarrow \pi_1^*, \pi_3^*$	25	284.45
$3\ ^1A_2$	284.81	0.000	C5 $\rightarrow \pi_1^*, \pi_3^*$	25	
$3\ ^1B_2$	284.81	0.086	C5 $\rightarrow \pi_1^*, \pi_3^*$	25	
$4\ ^1A_2$	284.96	0.000	C6 $\rightarrow \pi_1^*, \pi_8^*$	26	
$4\ ^1B_2$	284.96	0.036	C6 $\rightarrow \pi_1^*, \pi_8^*$	26	284.8
$5\ ^1B_2$	285.27	0.024	C5 $\rightarrow \pi_3^*, \pi_8^*$	24	285.0
$5\ ^1A_2$	285.42	0.000	C5 $\rightarrow \pi_1^*$	28	
$6\ ^1A_2$	285.47	0.000	C5 $\rightarrow \pi_1^*$	28	
$7\ ^1A_2$	285.60	0.000	C7 $\rightarrow \pi_3^*, \pi_1^*$	27	
$6\ ^1B_2$	285.60	0.014	C7 $\rightarrow \pi_3^*, \pi_1^*$	27	
$7\ ^1B_2$	285.74	0.028	C5 $\rightarrow \pi_3^*, \pi_8^*$	25	
$8\ ^1A_2$	285.90	0.000	C3 $\rightarrow \pi_3^*, \pi_1^*$	23	285.6
$9\ ^1A_2$	285.92	0.000	C6 $\rightarrow \pi_8^*, \pi_3^*$	26	
$8\ ^1B_2$	285.92	0.034	C6 $\rightarrow \pi_8^*, \pi_3^*$	26	
$9\ ^1B_2$	285.92	0.089	C3 $\rightarrow \pi_3^*, \pi_1^*$	24	

Table 6.3: Comparison of excitation energies (ω_{ex}), oscillator strengths (f_{osc}), amount of doubly excited amplitudes (R2), the character (γ) and various descriptors (see chapter 2.5.8 for definitions) of the first five and three core-excited singlet states with B_2 symmetry of ANQ (C 1s and O 1s). The results were computed using CVS-ADC(2)-x and the 6-311++G** basis set. Exciton sizes and distances are given in Å. This table has already been submitted for publication by me and my co-author.[99]

State	ω_{ex} [eV]	f_{osc}	R2 [%]	p_{DA}	σ_D	σ_h	σ_A	σ_e	$d_{D\to A}$	$d_{h\to e}$	d_{ex}	R_{eh}	γ
ANQ C 1s													
1^1B_2	284.40	0.038	25.53	1.99	1.75	1.19	2.06	2.51	0.05	0.22	2.22	0.47	1s-π^*
2^1B_2	284.78	0.041	25.29	1.96	2.56	2.41	2.57	2.58	0.06	0.11	2.38	0.55	1s-π^*
3^1B_2	284.81	0.086	25.21	1.94	1.87	1.31	2.18	2.45	0.40	1.06	2.44	0.45	1s-π^*
4^1B_2	284.96	0.036	26.45	1.97	2.58	2.43	2.57	2.53	0.19	0.42	2.60	0.47	1s-π^*
5^1B_2	285.27	0.024	24.41	2.18	1.55	0.19	1.91	2.25	0.43	1.00	2.47	0.00	1s-π^*
ANQ O 1s													
1^1B_2	529.45	0.069	22.70	1.85	1.75	1.48	1.96	1.95	0.37	0.90	2.05	0.46	1s-π^*
2^1B_2	533.08	0.000	26.94	2.05	2.04	1.48	2.60	2.67	1.01	2.67	4.22	-0.16	1s-π^*
3^1B_2	534.78	0.001	27.00	2.23	2.18	1.48	2.79	2.68	1.29	3.64	4.65	0.13	1s-π^*

in particular when considering the errors due to the neglected relativistic effects. Before I go on to the next molecule, I would like to present further results of the reinvestigation of ANQ using the CVS-ISR approach and wave function analysis tools to provide deeper insight into the XA spectra. Table 6.3 contains exciton sizes, promotion numbers and correlation coefficients (R_{eh}) for the C 1s and O 1s excitations of ANQ. As mentioned above, the largest difference between the C 1s/O 1s core excitations of ANQ and the small systems discussed in the last chapters is the number of atoms of the same type from which core electrons are excited due to the C_{2v} symmetry. This has also influences on the state densities and corresponding exciton sizes. Let me start with an example, i.e. the (h/e) and (D/A) densities of the 2^1B_2 C 1s core-excited state, which are illustrated in Figure 6.3. This state is characterized by an electron promotion from the linear combination of two symmetrical identical C4 carbon atoms to a π^* level, which is also confirmed by the dominant MO transitions (see Table 6.2). Both hole and detachment densities are mostly located on both C4 atoms, but the detachment density shows typical relaxation effects with the expansion of the density to the neighboring atoms, while the hole density is almost strictly localized on the C4 atoms. Since core orbitals are strongly contracted and localized, electrons are promoted from one specific 1s orbital located on one atom in experiments, because real systems are not perfectly symmetric. However, the results above prove that the theoretical description of core-excitation energies and oscillator strengths exploiting point group symmetry is not problematic, leading to perfect agreement with experimental spectra. One should interpret these states as core excitations located on all symmetrically identical atoms, respectively.

Exciton sizes that contain information about the generated electron hole, however, might provide a wrong picture of the real situation. The σ_h values of the first five $^1B_2$ states of ANQ (C 1s) differ significantly, which depends on the distance or spacing between the symmetric identical carbon atoms. Looking at the example of the 2^1B_2 state, a large σ_h value of 2.41 Å is calculated. This value is twice the intramolecular distance of the two C4 atoms of 4.81 Å, because the exciton hole size is defined as the root-mean-square deviation of the position operator of the hole (center of charges). Hence, the σ_h values fit

perfectly to the distance of the respective identical carbon atoms. In contrast, the σ_h value of the 5^1B_2 state is 0.19 Å indicating a core excitation from a single 1s orbital located on one carbon atom, i.e. the one in the center of the molecule (C5). Here, another advantage of the (h/e) analysis is revealed. In the MO picture, the C5 group consists of four carbon 1s orbitals, thus the characters of the corresponding core excitations are defined with respect to the whole group. The densities of the 5^1B_2 state show that this state, for example, is only dominated by one of the C5 atoms. However, the other states are indeed characterized by linear combinations of equivalent carbon atoms, which is also observable in the exciton distances $d_{D\rightarrow A}$. These are very small with values < 0.5 Å for all C 1s excited states, because the center of charge of the holes is located between the equivalent carbon atoms, which is close to the center of charge of the delocalized attachment densities. As a consequence, one has to be careful with the interpretation of exciton sizes in the case of molecules that contain equivalent atoms due to point group symmetry.

Turning to the promotion numbers, both C 1s and O 1s excitations of ANQ exhibit large values around 2.0 and higher, which fits to the large amount of doubly excited amplitudes contributing to the core-excited states of ANQ. Hence, promotion numbers and a direct comparison between 1DDM and 1TDM properties are still valid tools for analyzing the influence of relaxation effects. Regarding the correlation coefficient R_{eh}, which describes dynamical correlation effects, an influence of the symmetric equivalent atoms can be identified, too. R_{eh} is exactly zero if the electron is promoted from only one localized 1s orbital, for example in the case of the 5^1B_2 state of the C 1s excitation, while the R_{eh} values are $\neq 0$ if the state is characterized by linear combinations of equivalent 1s orbitals. These observations can be explained by the compactness of a localized 1s orbital, while in cases of equivalent atoms the core excitation is theoretically delocalized.

6.1.2 Bithiophene

Thiophene derivatives feature strong absorption bands in the UV region and corresponding fluorescence properties, thus they are often used as electron donors in the field of organic photovoltaic devices.[95,204,206] In combination with appropriate electron acceptors, high energy transfer as well as high charge transfer rates can be yielded. Figure 6.4 illustrates the relevant virtual orbitals of BT. The MOs that mainly participate in the bright core-excited states show a clear π^*-character and should be described reasonably well in any basis set. However, note that, due to the strong diffuse and polarized 6-311++G** basis set, the orbitals d_1^*, d_2^*, d_{10}^* and d_{18}^* do not have a clear π^*-character. They are dominated by the diffuse functions showing the characteristics of an additional weakly bound electron rather than an excited electron. As shown in previous work[207–210], the BT molecule is not planar in the ground state. At the level of RI-MP2 using the def2-TZVPP basis set and exploiting C_2 point group symmetry, the central dihedral angle is -150.1°. In chapter 9.2.3, the torsion around this dihedral angle is investigated in more detail.

Let me first take a look at the S 1s excitations, the results are summarized in Table 6.4. Here, only the first bright experimental peak[36], which is located at 2474 eV, is discussed. The CVS-ADC(2)-x results show that this band is described as a mixture of the first four S 1s core-excited states. Due to the C_2 symmetry, they are pairwise degenerate with core-excitation energies of 2468.83 eV and 2468.97 eV, respectively. Hence, the bright excitation is underestimated by 0.2% (5.1 eV), compared to the experiment, which corresponds to the estimated magnitude of the missing relativistic effects of about 8.0 eV for S 1s excitations.[179] Note that crystal powder of oligothiophenes was used for the experiments.[36] The R2 values of these states are 15%, which is less than the ones for the C 1s and O 1s core excitations of ANQ (see Tables 6.1 and 6.2). Hence, it seems

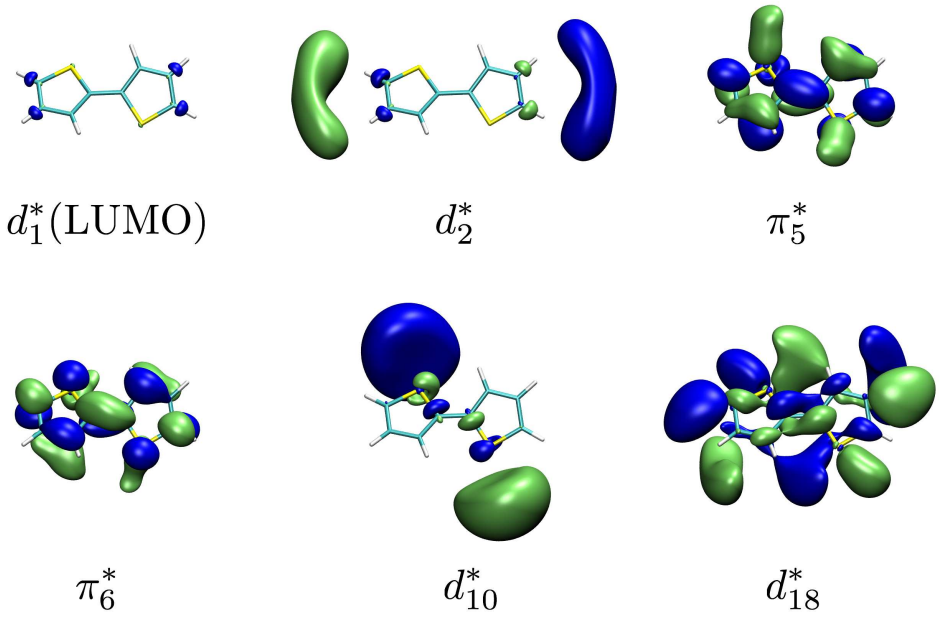

Figure 6.4: Illustration of the relevant virtual molecular orbitals of BT at the level of HF in combination with the 6-311++G** basis set. The isosurfaces of the MOs are rendered with an isovalue of 0.02.

Table 6.4: Core-excitation energies (ω_{ex}), oscillator strengths (f_{osc}), character and amount of double amplitudes (R2) of the first six S 1s singlet excited states of BT calculated using CVS-ADC(2)-x and the 6-311++G** basis set exploiting C_2 point group symmetry. The calculated values are compared with experimental data of oligothiophenes (crystal powder).[36] Only the main transitions are shown and the numbering of the atoms complies with Figure 6.1. This table has already been published by me and my co-authors.[96]

State	ω_{ex} [eV]	f_{osc}	Main transition (1s $\rightarrow$)	R2 [%]	ω_{ex} [eV] (Expt.)
1 ^{1}B	2468.83	0.0057	S1,S2 $\rightarrow \pi_5^*, \pi_6^*$	15	
1 ^{1}A	2468.83	0.0023	S1,S2 $\rightarrow \pi_5^*, \pi_6^*$	15	2474
2 ^{1}B	2468.97	0.0057	S1,S2 $\rightarrow \pi_6^*, d_{18}^*$	15	
2 ^{1}A	2468.97	0.0031	S1,S2 $\rightarrow \pi_6^*, d_{18}^*$	15	
3 ^{1}A	2470.69	0.0001	S1,S2 $\rightarrow d_1^*, d_{10}^*$	15	
3 ^{1}B	2470.69	0.0006	S1,S2 $\rightarrow d_1^*, d_{10}^*$	15	

Table 6.5: Core-excitation energies (ω_{ex}), oscillator strengths (f_{osc}), character and amount of double amplitudes (R2) of the first 14 C 1s singlet excited states of BT calculated using CVS-ADC(2)-x and the 6-311++G** basis set exploiting C_2 point group symmetry. The calculated values are compared with experimental data of BT monolayer adsorbed on a Ag(111) surface.[34] Only the main transitions are shown and the numbering of the atoms complies with Figure 6.1. This table has already been published by me and my co-authors.[96]

State	ω_{ex} [eV]	f_{osc}	Main transition (1s $\rightarrow$)	R2 [%]	ω_{ex} [eV] (Expt.)
1 ^{1}B	285.19	0.004	C7-C10 $\rightarrow \pi_5^*, \pi_6^*$	26	
1 ^{1}A	285.19	0.041	C7-C10 $\rightarrow \pi_5^*, \pi_6^*$	26	
2 ^{1}B	285.42	0.008	C5,C6 $\rightarrow \pi_5^*, \pi_6^*$	26	
2 ^{1}A	285.42	0.115	C5-C6 $\rightarrow \pi_5^*, \pi_6^*$	26	
3 ^{1}A	285.44	0.000	C5-C10 $\rightarrow \pi_5^*, \pi_6^*$	26	285.7
3 ^{1}B	285.44	0.000	C5-C10 $\rightarrow \pi_5^*, \pi_6^*$	26	
4 ^{1}B	285.67	0.003	C3,C4 $\rightarrow \pi_5^*, \pi_6^*$	25	
4 ^{1}A	285.70	0.056	C3,C4 $\rightarrow \pi_5^*, \pi_6^*$	25	
5 ^{1}B	287.08	0.001	C7-C10 $\rightarrow \pi_5^*, \pi_6^*$	25	
5 ^{1}A	287.08	0.038	C7-C10 $\rightarrow \pi_5^*, \pi_6^*$	25	
6 ^{1}B	287.14	0.008	C7-C10 $\rightarrow d_1^*, d_2^*$	26	
6 ^{1}A	287.14	0.003	C7-C10 $\rightarrow d_1^*, d_2^*$	26	286.7
7 ^{1}A	287.19	0.000	C7-C10 $\rightarrow d_1^*, d_2^*$	26	
7 ^{1}B	287.19	0.010	C7-C10 $\rightarrow d_1^*, d_2^*$	26	

that relaxation effects influence the final S 1s excited states less than other examples investigated so far in this thesis. Going to the state characters, the first two transitions are dominated by an electron promotion to the π_5^* and π_6^* orbitals, while the two next higher states are mostly characterized by transitions to the π_6^* and d_{18}^* orbitals. Besides d_{18}^*, all of these virtual orbitals have a distinct π^*-character and are delocalized over the whole BT molecule. The donor orbitals are $\pm$ linear combinations of the two sulfur 1s orbitals due to the C_2 symmetry.

Turning to the C 1s spectrum of the BT, the results are given in Table 6.5. Here, the experiments are performed with BT molecules adsorbed on a Ag(111) surface, while the calculations do not consider environmental influences.[34] I would like to discuss the first two experimental peaks of the C 1s spectrum at 285.7 eV and 286.7 eV. The first peak can be described as a superposition of the first eight core-excited states. Due to the C_2 point group symmetry, some of the core-excited states are doubly degenerate. The core-excitation energies of these states range from 285.19 eV to 285.70 eV, where the 2 ^{1}A state located at 285.42 eV exhibits the largest oscillator strength of 0.115. Hence, the first core-excited experimental peak is slightly underestimated by about 0.1% (0.3 eV). The first eight calculated C 1s core-excited states are characterized by transitions to the π_5^* and π_6^* orbitals including linear combinations of all eight carbon 1s orbitals as donor orbitals. The next six higher core-excited states with core-excitation energies from 287.08 eV to 287.19 eV can be assigned to the second experimental peak. Here, the 5 ^{1}A state at

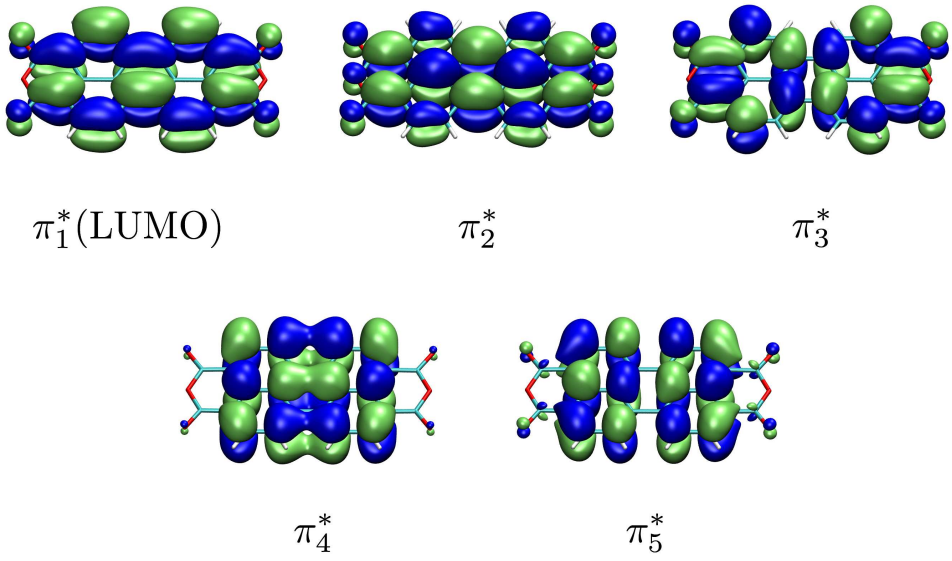

Figure 6.5: Illustration of the relevant virtual molecular orbitals of PTCDA at the level of HF in combination with the 6-31G** basis set. The isosurfaces of the MOs are rendered with an isovalue of 0.02.

287.08 eV exhibits the largest oscillator strength of 0.038, thus the error compared to experiment is 0.13% (0.38 eV). In contrast to the first bright excitation, the energy of this state is slightly overestimated. Hence, the energy spacing between these first two peaks is 1.66 eV at the CVS-ADC(2)-x level, which is larger compared to the experimental energy difference of 1 eV. However, taking into account the lack of the Ag surface interactions, this spacing may still be acceptable. All of the six states contributing to the second peak can be characterized as transitions from the linear combinations of the C7, C8, C9 and C10 1s orbitals to the π_5^*/π_6^* and d_1^*/d_2^* orbitals. In contrast to the S 1s excitations, the amount of double amplitudes contributing to all C 1s excited states is between 25% and 26%, indicating significant orbital relaxation effects.

6.1.3 PTCDA

Due to its electronic structure, PTCDA is a dark red pigment. Its derivatives or nitrogen variants like MePTCDI are often used in organic photovoltaic devices and organic semiconductors as electron acceptors.[95,204,206] Since the molecular size of PTCDA is with 38 atoms quite large, the smaller 6-31G** basis set had to be used for the CVS-ADC(2)-x calculations. In Figure 6.5 the relevant MOs for the core-excited states are shown at the HF/6-31G** level, while the results of the first eight B_{1u} C 1s singlet excited states are given in Table 6.6. Due to the spectroscopic selection rules of the D_{2h} point group, only states belonging to the irreducible representations B_{1u}, B_{2u} and B_{3u} are one photon allowed and can possess oscillator strength.

In general, B_{1u} states exhibit significantly larger oscillator strengths than B_{2u} and B_{3u}, thus only the first eight B_{1u} states will be discussed, which contribute to the first two experimental peaks at 284.4 eV and 285.6 eV. Based on the CVS-ADC(2)-x calculation, the first experimental peak is described by a mixture of the first four core-excited B_{1u} states

Table 6.6: Core-excitation energies (ω_{ex}), oscillator strengths (f_{osc}), character and amount of double amplitudes (R2) of the first eight B_{1u} C 1s singlet excited states of PTCDA calculated using CVS-ADC(2)-x and the 6-31G** basis set exploiting D_{2h} point group symmetry. The calculated values are compared with experimental data.[13] Only the main transitions are shown and the numbering of the atoms complies with Figure 6.1. This table has already been published by me and my co-authors.[96]

State	ω_{ex} [eV]	f_{osc}	Main transition (1s $\rightarrow$)	R2 [%]	ω_{ex} [eV] (Expt.)
1 $^1B_{1u}$	285.36	0.072	C1 $\rightarrow \pi_1^*, \pi_3^*$	26	
2 $^1B_{1u}$	285.44	0.058	C2 $\rightarrow \pi_1^*$	27	284.4
3 $^1B_{1u}$	285.72	0.073	C3 $\rightarrow \pi_1^*$	26	
4 $^1B_{1u}$	285.75	0.090	C4 $\rightarrow \pi_1^*, \pi_3^*$	26	
5 $^1B_{1u}$	287.11	0.061	C5 $\rightarrow \pi_2^*, \pi_4^*$	23	
6 $^1B_{1u}$	287.19	0.090	C2 $\rightarrow \pi_4^*, \pi_5^*, \pi_3^*$	25	285.6
7 $^1B_{1u}$	287.23	0.095	C6 $\rightarrow \pi_4^*, \pi_5^*, \pi_2^*$	22	
8 $^1B_{1u}$	287.30	0.076	C4 $\rightarrow \pi_4^*, \pi_5^*, \pi_1^*$	26	

with energies ranging from 285.36 eV to 285.75 eV, while the second peak corresponds to the next four higher core-excited B_{1u} states with energies ranging from 287.11 eV to 287.30 eV. For a better overview, the carbon atoms are collected in groups according to the D_{2h} symmetry (see Figure 6.1). The states contributing to the first peak are characterized as transitions from C1, C2, C3 and C4 to the π_1^* and π_3^* orbitals, while in the case of the states that describe the second peak, the transitions are dominated by electron promotions from C2, C4, C5 and C6 to the first five virtual π^*-orbitals. The amount of doubly excited amplitudes is large with values between 22% and 27% for all investigated $^1B_{1u}$ states, thus strong orbital relaxation effects contribute to the C 1s core excitations of PTCDA. Looking at the errors compared to experiment, the influence of the small 6-31G** basis set becomes obvious. The 4 $^1B_{1u}$ state, which exhibits the largest oscillator strength with 0.090 in the case of the first bright excitation, has a computed core-excitation energy of 285.75 eV, thus the error compared to the experiment is 0.5% (1.35 eV). In the case of the second experimental peak, the 7 $^1B_{1u}$ state possesses the largest oscillator strength with 0.095. Hence, the error with respect to the experiment is 0.6% (1.63 eV). Eventually, the use of the smaller, non-diffuse 6-31G** basis set results in larger relative errors than in the case of the diffuse 6-311++G** basis set used for ANQ and BT, but the peak structure of the experimental spectrum is still very well reproduced, because the errors of both peaks are of the same magnitude.

6.2 Molecules with Biological Relevance

Porphin can be seen as a representative molecule of interest in both biology and organic electronics. Just to mention a few examples, Porphin and porphyrine derivatives are building blocks in the oxygen transport center of hemoglobin and are relevant in light-harvesting pigments in photosynthetic proteins. Furthermore, they are studied to understand energy transfer processes in photosynthetic systems and they are employed in chemical sensors.[211,212] Additionally, I present investigations of the XA spectra of the

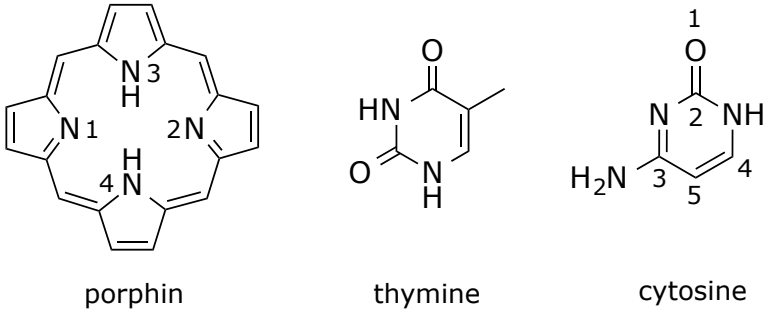

Figure 6.6: Structures of porphin and the DNA bases thymine and cytosine.

deoxyribonucleic acid (DNA) nucleobases thymine and cytosine, because recent research in cancer therapy concentrates on an enhancement of radio-therapies via ICD after a resonant core excitation that results in a low energy electron generation with the nucleobases as potential targets.[7,8] Both DNA bases were investigated in previous work by *Trofimov et al.*, but small basis sets had to be employed.[33,89] To demonstrate the basis set influence, the C 1s, N 1s and O 1s excited spectra of thymine were recomputed with the larger and more diffuse 6-311++G** basis set. In the case of cytosine, the CVS-ISR implementation was used to calculate state densities and accompanied with an enhanced wave function analysis, a deeper insight into the nature of the C 1s and O 1s excited states of cytosine is presented. The structures of porphin, thymine and cytosine are shown in Figure 6.6.

6.2.1 Porphin

Starting with the N 1s core excitations of porphin, the relevant MOs are illustrated in Figure 6.7. Extremely diffuse virtual MOs occur in the low-energy regime, e.g. d^*_{16} and d^*_{19}, which correspond to weakly bound additional electrons due to the polarized and diffuse functions of the 6-311++G** basis set.

Similar to the PTCDA molecule, which also exhibits D_{2h} point group symmetry, only excited states with the irreducible representations B_{1u}, B_{2u} and B_{3u} are optically allowed and can possess oscillator strength. Here, the B_{1u} states have much larger oscillator strengths than the others. Hence, only the B_{1u} states are discussed and the CVS-ADC(2)-x results are given in Table 6.7. For comparison, results obtained with the 6-31++G** and 6-311++G** basis sets are shown to demonstrate the influence of the larger 6-311++G** basis set on the core-excitation energies of the B_{1u} states.

Let me start with the first two experimental[212] peaks at 398.2 eV and 400.3 eV. The experimental XA spectrum is obtained from a solid film of porphin, thus one can expect differences to the calculations. However, the first two experimental peaks are perfectly reproduced by CVS-ADC(2)-x using the larger 6-311++G** basis set. The absolute errors of the $1\ ^1B_{1u}$ and $2\ ^1B_{1u}$ states are only 0.03 eV and 0.05 eV compared to the experiment, while using the smaller 6-31++G** basis set leads to significantly larger errors of 1.69 eV and 1.82 eV, respectively. The energy spacing between these two states, however, is excellently described using both basis sets. Looking at the MO transitions reveals that the $1\ ^1B_{1u}$ state is characterized by an electron promotion from a linear combination of the N 1s orbitals located on the deprotonated nitrogens to the LUMO, while the $2\ ^1B_{1u}$ state is dominated by transitions from the 1s orbitals of the protonated nitrogens to the LUMO+1. The third and fourth peaks at 402.3 eV and 403.9 eV are experimentally not well resolved, because they are included in a broad absorption band. According to the CVS-ADC(2)-x

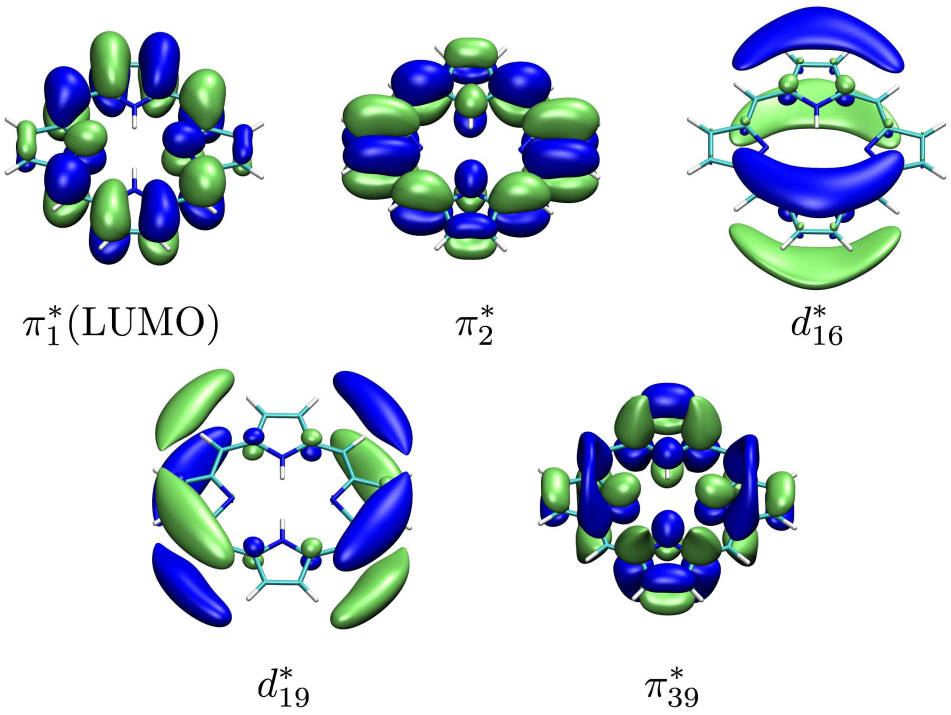

Figure 6.7: Illustration of the relevant virtual molecular orbitals of porphin at the level of HF in combination with the 6-311++G** basis set. The isosurfaces of the MOs are rendered with an isovalue of 0.02.

calculations, the third peak can be described as a mixture of the 3 $^1B_{1u}$ and 4 $^1B_{1u}$ states, while the fourth peak corresponds to the 8 $^1B_{1u}$ state. Using the 6-311++G** basis set leads to an underestimation of 1.12 eV and 0.53 eV compared to the experiment, respectively. Since the third peak exhibits a large error, the energy spacing between the second and third states is underestimated by 0.83 eV at the CVS-ADC(2)-x/6-311++G** level, while the experimental value is 2 eV. The fourth peak, however, is in principle well described. Inspecting the characters of these states reveals that the third and fourth peak correspond to Rydberg-type states. The transitions of the 3 $^1B_{1u}$ and 4 $^1B_{1u}$ states are characterized as 1s excitations of the deprotonated nitrogens into the π_{39}^*, d_{16}^* and d_{19}^* MOs, which exhibit diffuse fractions. The main transition of the 8 $^1B_{1u}$ state can be characterized as an electron promotion from the protonated nitrogen 1s orbitals to the π_{39}^* and d_{16}^* MOs. The strongly diffuse character of theses states can explain the larger errors at the CVS-ADC(2)-x level compared to experiment. Furthermore, one should consider that the experimental spectrum of the solid species features a broad absorption, where peaks three and four are embedded. Hence, the error analysis of the calculated values should be taken with a grain of salt. The R2 values of all $^1B_{1u}$ states are large with values between 25% and 27%, indicating again strong orbital relaxation effects.

Table 6.7: Core-excitation energies (ω_{ex}), oscillator strengths (f_{osc}), character and amount of double amplitudes (R2) of the first eight B_{1u} C 1s singlet excited states of porphin calculated using CVS-ADC(2)-x exploiting D_{2h} point group symmetry. The calculated values are compared with experimental data of a solid porphin film.[212] The calculations were performed using the 6-31++G** and 6-311++G** basis sets. Only the main transitions are shown and the numbering of the atoms complies with Figure 6.6. This table has already been published by me and my co-authors.[96]

	6-31++G**		6-311++G**				Expt.
State	ω_{ex} [eV]	f_{osc}	ω_{ex} [eV]	f_{osc}	R2 [%]	Main transition (1s $\rightarrow$)	ω_{ex} [eV]
$1\ ^1B_{1u}$	399.89	0.0338	398.07	0.0351	26	N1,N2 $\rightarrow \pi_1^*$	398.2
$2\ ^1B_{1u}$	402.12	0.0268	400.35	0.0280	25	N3,N4 $\rightarrow \pi_2^*$	400.3
$3\ ^1B_{1u}$	403.03	0.0263	401.18	0.0257	26	N1,N2 $\rightarrow \pi_{39}^*$	402.3
$4\ ^1B_{1u}$	403.59	0.0079	401.73	0.0095	26	N1,N2 $\rightarrow d_{16}^*, d_{19}^*, \pi_{39}^*$	
$5\ ^1B_{1u}$	404.29	0.0012	402.47	0.0011	27	N1,N2 $\rightarrow d_{19}^*, \pi_{24}^*, \pi_{23}^*$	
$6\ ^1B_{1u}$	404.82	0.0019	402.97	0.0027	27	N1,N2 $\rightarrow \pi_{23}^*, d_{16}^*$	
$7\ ^1B_{1u}$	404.90	0.0008	403.08	0.0003	27	N1,N2 $\rightarrow \pi_{26}^*, d_{19}^*, \pi_{24}^*$	
$8\ ^1B_{1u}$	405.18	0.0187	403.37	0.0178	25	N3,N4 $\rightarrow \pi_{39}^*, d_{16}^*$	403.9
$9\ ^1B_{1u}$	405.37	0.0001	403.51	0.0001	27	N1,N2 $\rightarrow \pi_{24}^*, \pi_{23}^*$	
$10\ ^1B_{1u}$	405.74	0.0085	403.91	0.0005	27	N1,N2 $\rightarrow \pi_{35}^*, \pi_{60}^*, \pi_{39}^*$	

6.2.2 Thymine

The K-shell absorption spectra of thymine were investigated at the CVS-ADC(2)-x level in detail in previous work.[89] Since my efficient implementation of the CVS-ADC methods allows for the treatment of about 500 basis functions in an adequate computational time, I concentrate here on the improvement of the results by using the larger 6-311++G** basis set, whereas before only the small 6-31+G basis set had been employed. The former work also provides a comparison of the computed oscillator strengths with experimentally measured intensities. It turned out that the calculated oscillator strengths are in a good agreement to experimental intensities, independent of the size of the basis set.

The first 15 C 1s states calculated at the CVS-ADC(2)-x level are summarized in Table 6.8, including the previous results using the 6-31+G basis set. Generally, the results can be summarized by the following statements:

- When the larger basis set is employed, the relative error in the C 1s core-excitation energies is reduced from about 1% to only 0.2%, i.e. approximately 2.5 eV to at most 0.65 eV.
- Thereby, the order of the states changes slightly.
- Oscillator strengths do not differ much when employing the different basis sets, which confirms the investigation in chapter 4.3.
- No constant shifting of the computed core-excitation energies is necessary to achieve agreement with the experiment, when the larger 6-311++G** basis set is employed.

Table 6.8: Core-excitation energies (ω_{ex}), oscillator strengths (f_{osc}) and relative errors of the first 15 C 1s singlet excited states of thymine calculated using CVS-ADC(2)-x. The calculated values are compared with experimental data and previous work.[89] My calculations were performed using the 6-311++G** basis set, while in the previous work the 6-31+G basis set had been used. This table has already been published by me and my co-authors.[96]

	Previous work			Our work			Expt.
State	ω_{ex} [eV]	f_{osc}	Error [%]	ω_{ex} [eV]	f_{osc}	Error [%]	ω_{ex} [eV]
1	287.02	0.024	0.74	284.84	0.024	-0.02	284.9
2	288.54	0.045	0.92	286.36	0.045	0.16	285.9
3	288.97	0.000		286.90	0.000		
4	289.05	0.004		287.11	0.003		
5	289.38	0.000		287.29	0.000		
6	289.98	0.007		287.95	0.015	0.23	287.3
7	290.06	0.015	0.96	288.03	0.007		
8	290.23	0.001		288.07	0.002		
9	290.37	0.007		288.24	0.053	0.15	287.8
10	290.40	0.013		288.34	0.000		
11	290.42	0.056	0.91	288.39	0.004		
12	290.46	0.000		288.45	0.013	0.02	288.4
13	290.62	0.000		288.63	0.000		
14	290.95	0.010	0.88	288.88	0.008		
15	291.00	0.001		289.11	0.002		

Table 6.9: Core-excitation energies (ω_{ex}), oscillator strengths (f_{osc}) and relative errors of the seven energetically lowest N 1s singlet excited states of thymine calculated using CVS-ADC(2)-x. The calculated values are compared with experimental data and previous work.[89] My calculations were performed using the 6-311++G** basis set, while in the previous work the 6-31+G basis set had been used. This table has already been published by me and my co-authors.[96]

	Previous work			Our work			Expt.
State	ω_{ex} [eV]	f_{osc}	Error [%]	ω_{ex} [eV]	f_{osc}	Error [%]	ω_{ex} [eV]
1	404.06	0.0119	0.59	401.50	0.0111	-0.05	
2	404.43	0.0085		401.82	0.0070		401.7
3	404.61	0.0079		402.21	0.0078		
4	405.03	0.0069		402.54	0.0035		
5	405.11	0.0035		402.60	0.0066		
6	405.49	0.0098	0.69	403.03	0.0106	0.08	402.7
7	405.91	0.0055		403.42	0.0050		

Eventually, this comparison confirms the excellent accuracy of the CVS-ADC(2)-x/6-311++G** approach due to fortuitous error compensation.

Let me turn to the N 1s spectrum of thymine, the results are given in Table 6.9. Based on the analysis of the first two bright experimental peaks, the observations are similar to the C 1s results. The CVS-ADC(2)-x calculations with the larger 6-311++G** basis set exhibit again a remarkable agreement with the experiment, while a constant shift of about 2.6 eV had to be applied to the core-excitation energies computed with the smaller basis set. Employing the larger 6-311++G** basis set reduces the error to less than 0.2 eV, e.g. 0.1%, while when using the smaller basis set relative errors of 0.59% and 0.69% are obtained (2.36 eV, 2.79 eV).

Going to the analysis of the O 1s spectrum of thymine confirms the results of the other K-edge spectra. The results are given in Table 6.10. The previous work with the smaller basis set shows relative errors between 0.31% and 0.42% for the first three bright O 1s excited states of thymine. This is an absolute error of about 2.2 eV. My calculations with the 6-311++G** basis set provides an underestimation between 0.14% and 0.29% (0.76 eV – 1.56 eV), thus a better quantitative agreement with the experiment is given. The energy spacing between the first two experimental peaks is 0.9 eV and therefore almost perfectly described at the CVS-ADC(2)-x level with both basis sets (1 eV).

Eventually, the study of the thymine molecule confirms the benchmark results in chapter 4. CVS-ADC(2)-x in combination with a diffuse triple-ζ basis set benefits significantly from the fortuitous error compensation and the remaining error has about the size of the neglected relativistic effects.

6.2.3 Cytosine

The XA spectra of cytosine were investigated in previous work at the CVS-ADC(2)-x level.[33] Here I would like to expand this investigation with information provided using the CVS-ISR formalism and the wave function analysis tools. Let me start with the C 1s excitations, the results are summarized in Table 6.11. Here, only density information

Table 6.10: Core-excitation energies (ω_{ex}), oscillator strengths (f_{osc}) and relative errors of the first 15 O 1s singlet excited states of thymine calculated using CVS-ADC(2)-x. The calculated values are compared with experimental data and previous work.[89] My calculations were performed using the 6-311++G** basis set, while in the previous work the 6-31+G basis set had been used. This table has already been published by me and my co-authors.[96]

	Previous work			Our work			Expt.
State	ω_{ex} [eV]	f_{osc}	Error [%]	ω_{ex} [eV]	f_{osc}	Error [%]	ω_{ex} [eV]
1	533.55	0.0310	0.40	530.52	0.0282	-0.17	531.4
2	534.53	0.0293	0.42	531.54	0.0268	-0.14	532.3
3	536.52	0.0001		533.30	0.0001		
4	536.67	0.0004		533.43	0.0003		
5	536.97	0.0002		533.73	0.0003		
6	537.32	0.0016		534.10	0.0012		
7	537.35	0.0026	0.31	534.14	0.0027	-0.29	
8	537.47	0.0000		534.20	0.0002		
9	537.73	0.0020		534.37	0.0013		
10	537.75	0.0006		534.56	0.0006		535.7
11	537.80	0.0019		534.71	0.0019		
12	538.09	0.0011		534.77	0.0007		
13	538.17	0.0011		534.90	0.0009		
14	538.33	0.0020		534.94	0.0018		
15	538.60	0.0001		535.26	0.0001		

Table 6.11: Core-excitation energies (ω_{ex}), oscillator strengths (f_{osc}), character, amount of double amplitudes (R2) and various descriptors (see chapter 2.5.8 for definitions) of the first five C 1s excited singlet states of cytosine calculated using CVS-ADC(2)-x and the 6-311++G** basis set. The calculated values are compared with experimental data.[33] This table has already been published by me and my co-authors.[84]

State	ω_{ex} [eV]	f_{osc}	R2 [%]	σ_h (Å)	σ_e (Å)	d_{ex} (Å)	character	Exp. ω_{ex} [eV]
S_1	284.98	0.017	24.9	0.166	1.72	1.93	1s-π^*	285.04
S_2	286.57	0.050	22.8	0.166	1.60	1.70	1s-π^*	285.98
S_3	286.86	0.005	24.9	0.166	2.95	3.31	1s-Ryd.	
S_4	287.33	0.014	25.3	0.167	2.14	2.48	1s-π^*	
S_5	287.70	0.053	21.0	0.167	1.70	1.77	1s-π^*	287.30

provided by the 1TDM is considered. At the CVS-ADC(2)-x/6-311++G** level an excellent agreement with experimental data[33] is provided. The first three experimental peaks at 285.04 eV, 285.98 eV and 287.30 eV are almost perfectly reproduced with computed core-excitation energies of 284.98 eV, 286.57 eV and 287.70 eV, respectively. These bright excitations correspond to the C 1s excited S_1, S_2 and S_5 states. To determine the characters of these states, the computed (h/e) densities are illustrated in Figure 6.8. All of the three optically allowed C 1s core-excited states are characterized by transitions into π^*-levels, which are delocalized over the cytosine ring. Since there is no point group symmetry and the carbon atoms are not chemically identical, the carbon 1s orbitals are energetically separated, which leads to very localized core excitations. Regarding the S_1, the electron is promoted from the 1s orbital of the C5 atom, while it is the C4 atom in the case of the S_2 and the C3 atom that characterizes the S_5. Hence, all carbon 1s orbitals are each localized on only one carbon atom and therefore all core-exited states are dominated by transitions including one carbon 1s orbital. The hole sizes (σ_h) confirm this observation with very small values of about 0.17 Å for all investigated C 1s core excitations. Looking at the electron sizes (σ_e) and the dynamic charge separation values (d_{ex}), they follow the same trend. States exhibiting s,π^*-character show significantly smaller σ_e and d_{ex} values than the Rydberg state S_3, which has a spatially diffuse character. The correlation coefficient (R_{eh}) values are always 0.000, because the core excitation proceeds from very compact 1s orbitals, leading to a total lack of correlation. However, the R2 values are between 21.0% and 25.3%, which indicates strong orbital relaxation effects. These are further analyzed by means of the oxygen 1s excitations of cytosine.

Cytosine exhibits only one oxygen atom, thus there is only one localized O 1s orbital from which the electron can be promoted into various virtual levels. The CVS-ADC(2)-x results of the O-1s excitations are summarized in Table 6.12. Experimentally, there is only one significant peak at 532.00 eV in the low energy region[33], which corresponds to the core-S_1 state with a computed excitation energy of 531.04 eV. The next four higher core-excited states are optically forbidden, because they possess no oscillator strength. Inspecting the promotion numbers (p_{DA}) shows that values are around 2.0 or even larger, thus strong relaxation effects are included within all O 1s core-excited states. This is confirmed with R2 values larger than 22%. The hole size is with 0.12 Å constant for all core-excited states, because there is only a single oxygen atom. Note that this value is slightly smaller when compared to the C 1s states, which follows from the increased nuclear charge. Similar to the results shown in chapter 5.2, the σ_D values are at least 10

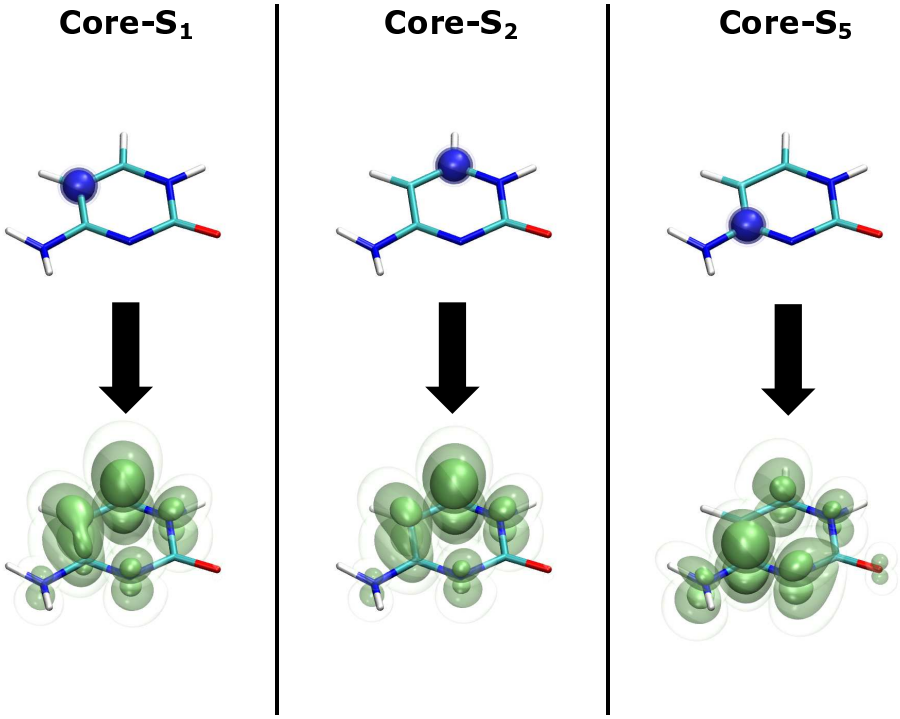

Figure 6.8: Illustration of hole(blue)/electron(lime) densities based on the 1TDM of the first, second and fifth C 1s core-excited singlet states of cytosine computed with CVS-ADC(2)-x using the 6-311++G** basis set. The isosurfaces were rendered with the isovalues 0.0064 (opaque), 0.0016 (colored transparent) and 0.0004 (transparent).

Table 6.12: Comparison of excitation energies (ω_{ex}), oscillator strengths (f_{osc}), amount of doubly excited amplitudes (R2), the character (γ) and various descriptors (see chapter 2.5.8 for definitions) of the first five O 1s excited singlet states of cytosine. The results were computed using CVS-ADC(2)-x and the 6-311++G** basis set. Exciton sizes and distances are given in Å. This table has already been submitted for publication by me and my co-author.[99]

State	ω_{ex} [eV]	f_{osc}	R2 [%]	p_{DA}	σ_D	σ_h	σ_A	σ_e	$d_{D\to A}$	$d_{h\to e}$	d_{ex}	R_{eh}	γ
S_1	531.04	0.027	22.16	1.95	1.15	0.12	1.64	1.74	0.58	1.36	2.22	0.00	1s-π^*
S_2	532.31	0.001	25.83	2.21	1.52	0.12	2.11	1.99	1.09	3.07	3.66	0.00	1s-π^*
S_3	532.63	0.000	23.70	2.18	1.51	0.12	2.57	3.10	0.98	2.46	3.96	0.00	1s-Dip.
S_4	533.59	0.000	24.10	2.22	1.62	0.12	3.32	4.27	1.20	3.32	5.41	0.00	1s-Ryd.
S_5	533.64	0.000	23.86	2.23	1.65	0.12	3.43	4.17	1.51	3.98	5.76	0.00	1s-Ryd.

times larger due to the strong expansion of the detachment density. In Figure 6.9 the (h/e) and (D/A) densities of the first, third and fourth core-excited singlet states of cytosine are illustrated. Again, the (h/e) densities help to characterize the core-excited states, thereby demonstrating the advantage of plotting (h/e) and (D/A) densities over looking at MO transition amplitudes. The S_1 state is a core excitation from the 1s orbital to a delocalized π^* level. The MO transition amplitude with the highest contribution to this state (MO1 to MO48) has only a percentage of 21.3%. The remaining contribution consists of a mixture of different MO transition amplitudes, thus it is very hard to characterize states being represented by such strong mixtures of amplitudes. Since all contributions are collected in one picture, inspecting the (D/A) or (h/e) densities is therefore significantly more advantageous. The O 1s core-S_3 state is a dipole bound state, because its electron density is localized around the excited oxygen, possessing diffuse character in space. In contrast, the core-S_4 state has a diffuse Rydberg character, because the core-excited electron is delocalized over and beyond the whole molecule in space. The detachment densities of all three examples show, as expected, a strong expansion of the hole due to relaxation effects. The dominant fraction of the density is relaxed to the neighboring nitrogen and carbon atoms with an additional contribution, which is delocalized over the molecule. The corresponding σ_e and σ_A values give hints for the character of the states, too. S_1 and S_2, which have a distinct s,π^*-character, exhibit σ_e values smaller than 2.0 Å. Due to its diffuse character, the dipole bound S_3 state has a σ_e value of 3.10 Å, while the Rydberg-type states (S_4 and S_5) provide electron sizes larger than 4.0 Å, because their electron densities are even more diffuse than the one of the dipole bound S_3 state. Similar to the C 1s excited states of cytosine, the d_{ex} values show a similar trend as the electron sizes. Furthermore, since the excitation proceeds from one localized 1s orbital, the R_{eh} values for all investigated O 1s excited states are exactly zero.

6.3 Small Organic Radicals

After discussing medium-sized closed-shell systems, the capabilities of the unrestricted CVS-UADC(2)-x are presented in this chapter by means of its application to a set of small organic radicals. For this purpose, the methyl and hydroxyl radicals are investigated followed by the triplet dioxygen diradical and the allyl radical. Their structures are illustrated in Figure 6.10. The methyl and allyl radicals occur as intermediates and precursors in the petroleum cracking industry and additionally, the allyl radical also serves as model system to study chemical dynamics of radicals.[42,213–215] The OH radical generally participates in combustion reactions and is a rife molecule in the Earth's atmosphere, where it is involved in oxidation reactions.[216,217]

6.3.1 Methyl and Hydroxyl Radicals

Both experiments of the methyl and OH radicals compared to were performed in gas phase, in which the OH radical is produced directly via the reaction H + NO_2 → OH + NO, while the CH_3 radical was generated in a supersonic molecular beam by flash pyrolysis of azomethane seeded in helium.[189,218] The relevant spin-orbitals of these systems are summarized and illustrated in Figure 6.11, while the CVS-UADC(2)-x results are given in Table 6.13. In the case of the CH_3 radical, the geometry optimization at the level of RI-UMP2/def2-TZVPP exhibits a planar equilibrium structure. The optimized C–H distances are 1.072 Å, while the H–C–H bond angles have values of 120.0°. The geometry optimization of the OH radical results in an equilibrium O–H distance of 0.966 Å, which is in excellent agreement with experimental data of 0.970 Å.[218] For both CH_3 and OH

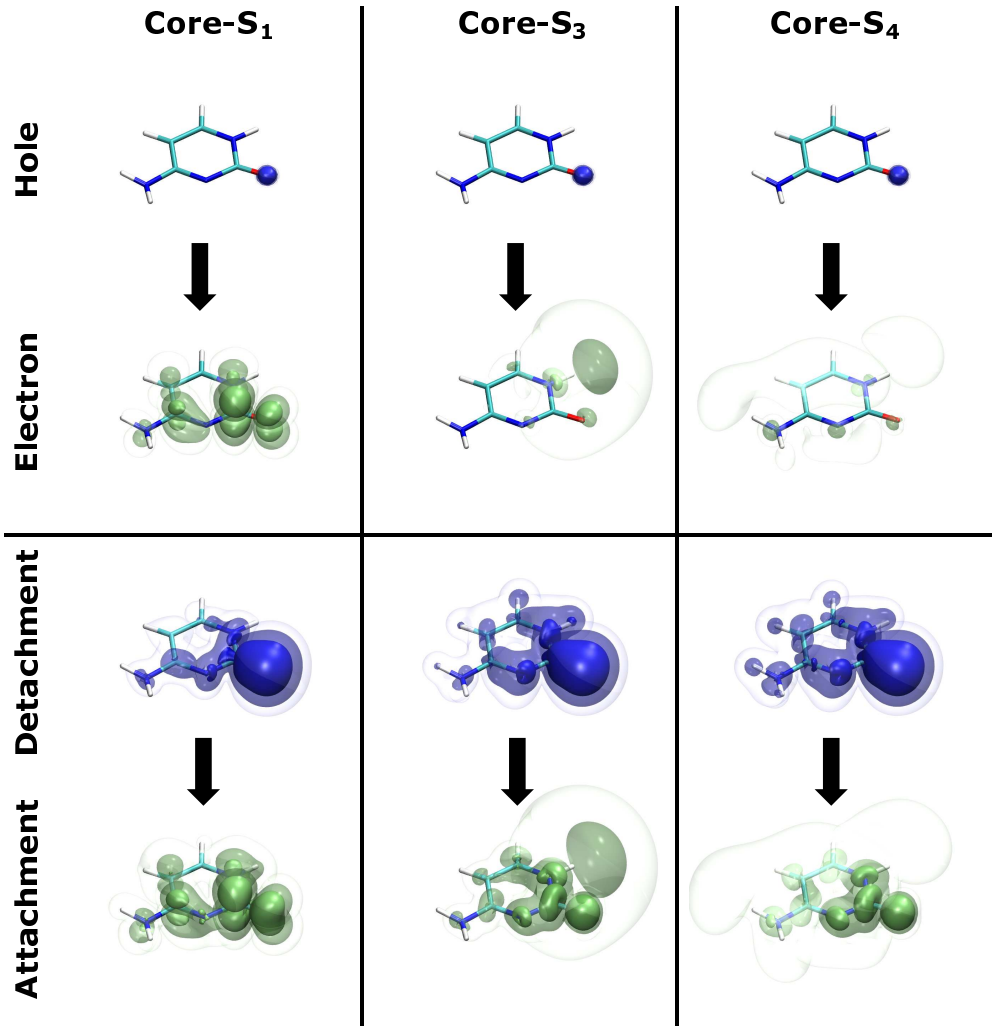

Figure 6.9: Comparison of detachment/attachment densities (bottom) based on the 1DDM with electron/hole densities (top) based on the 1TDM of the first, third and fourth O 1s core-excited singlet states of cytosine computed with CVS-ADC(2)-x using the 6-311++G** basis set. The isosurfaces were rendered with the isovalues 0.0064 (opaque), 0.0016 (colored transparent) and 0.0004 (transparent).

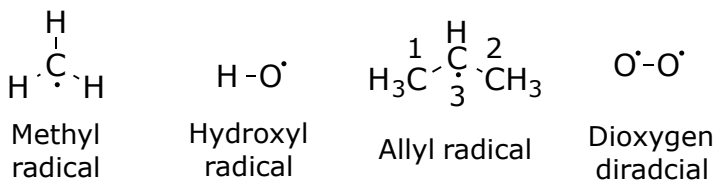

Figure 6.10: Structures of the methyl, hydroxyl and allyl radicals as well as the triplet dioxygen diradical.

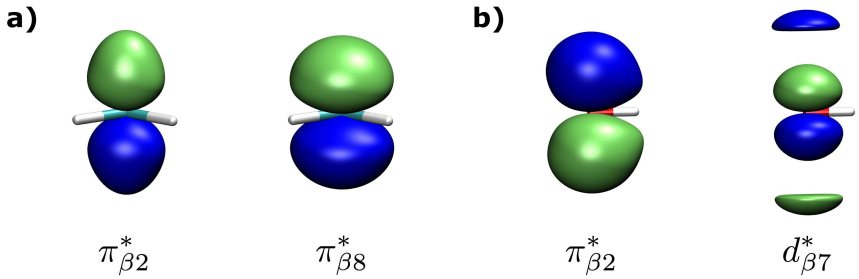

Figure 6.11: Illustration of the relevant virtual molecular spin-orbitals of a) the CH_3 radical and of b) the OH radical at the level of UHF in combination with the 6-311++G** basis set. The isosurfaces of the spin orbitals are rendered with an isovalue of 0.06.

Table 6.13: Core-excitation energies (ω_{ex}), oscillator strengths (f_{osc}), character and amount of double amplitudes (R2) of the first five C 1s excited states of the CH_3 radical and the O 1s excited states of the OH radical calculated using CVS-UADC(2)-x and the 6-311++G** basis set. The calculated values are compared with experimental data.[189,218] Only the main transitions are shown. This table has already been published by me and my co-authors.[97]

State	ω_{ex} [eV]	f_{osc}	Main transition (C 1s $\rightarrow$)	R2 [%]	ω_{ex} [eV] (Expt.)
			CH_3 radical (C 1s)		
1	281.42	0.036	$\pi^*_{\beta 2}, \pi^*_{\beta 8}$	14	281.35
2	286.83	0.000	$\pi^*_{\beta 1}, \pi^*_{\beta 9}$	22	
3	287.72	0.000	$\pi^*_{\alpha 1}, \pi^*_{\alpha 8}$	23	
4	288.23	0.005	$\pi^*_{\beta 4}, \pi^*_{\beta 11}$	22	
5	288.23	0.005	$\pi^*_{\beta 3}, \pi^*_{\beta 20}$	22	
			OH radical (O 1s)		
1	525.17	0.0449	$\pi^*_{\beta 2}, d^*_{\beta 7}$	11	525.85
2	534.86	0.0041	$\pi^*_{\beta 1}, \pi^*_{\beta 5}, \pi^*_{\beta 3}$	19	
3	536.19	0.0115	$\pi^*_{\alpha 1}, \pi^*_{\alpha 3}, \pi^*_{\alpha 5}$	20	
4	538.81	0.0077	$\pi^*_{\beta 3}, \pi^*_{\beta 1}$	19	
5	539.77	0.0070	$\pi^*_{\beta 4}$	19	

radicals, the $\langle \hat{S}^2 \rangle$ value of the UHF ground state is 0.76 and therefore close to the optimum value of 0.75, indicating hardly any spin-contamination of the ground state reference determinants.

Let me start with the discussion of the C 1s excited states of the CH_3 radical. The experimental XA spectrum provides a vibrational structure, which consists of four peaks between 281 and 283 eV. These peaks belong to a single bright electronic transition with a core-excitation energy of 281.35 eV, which at the CVS-UADC(2)-x level corresponds to the first core-excited state with a computed excitation energy of 281.42 eV. Hence, this absorption is excellently described with the CVS-UADC(2)-x method, exhibiting an error of only 0.02% (0.07 eV). This first core-excited state is mostly characterized by transitions from the carbon 1s orbital to the carbon 2p-spin-orbitals, which are denoted as $\pi^*_{\beta 2}$ and $\pi^*_{\beta 8}$. Both transitions have a contribution of about 40%, respectively. Since the overlap between the carbon 1s and 2p orbitals is large, the resulting oscillator strength of the first core-excited state is with 0.036 significantly larger compared to the next higher states, which are optically forbidden. The amount of doubly excited amplitudes is 14% in the case of the bright core-excited state 1, while the higher-lying dark states have R2 values around 22%. The R2 value of 14% is approximately 10% smaller than the ones of closed shell systems investigated in chapters 6.1 and 6.2, indicating smaller relaxation effects.

Turning to the O 1s excitations of the OH radical, a similar picture as for the CH_3 radical is provided. The vibrationally resolved peak structure of the experimental XA spectrum is between 525 eV and 527.5 eV and belongs to a single bright electronic transition with the experimental value of 525.85 eV. With an oscillator strength of 0.0449, this state is matched with the first core-excited state that exhibits a computed core-excitation energy of 525.17 eV. Hence, the CVS-UADC(2)-x calculation provides an absolute error of only 0.68 eV compared to the experiment, which is only 0.1%. The character of the first core-excited state is dominated by a transition from the oxygen 1s orbital to the oxygen 2p-orbitals $\pi^*_{\beta 2}$ and $d^*_{\beta 7}$ with contributions of 63.1% and 21.2%, respectively. Note that the orbital $d^*_{\beta 7}$ does not have a distinct π^*-character, because it is dominated by the diffuse functions due to the 6-311++G** basis set, which correspond to weakly bound, additional electrons at the UHF level. Regarding the R2 values, the same trend is observed as for the CH_3 radical. The amount of double excitations included in the first bright state is with 11% again much lower than for non-radical molecules. The R2 values of the next higher core-excited states are again significantly larger with values around 20%. However, they also exhibit oscillator strength, but since no experimental data is available for a comparison, I neglect the discussion of these states.

6.3.2 Allyl Radical

The experiments of the allyl free radical compared to were performed in gas phase by flash pyrolysis of allyl iodide and 1,5-hexadiene.[42] The relevant spin-orbitals are shown in Figure 6.12 and the results of the CVS-UADC(2)-x/6-311++G** calculation are given in Table 6.14. Experimental data of the structure of the ally radical is available, which shows C–C bond lengths of 1.428 Å and a C–C–C angle of 124.6°.[219] At the RI-MP2/def2-TZVPP level, the equilibrium C–C bond length is with 1.371 Å underestimated, while the calculated C–C–C angle of 124.3° is in good agreement with the experiment. Furthermore, a small spin contamination of the ground state reference can be identified. The $\langle \hat{S}^2 \rangle$ value of the UHF reference determinant is 0.94, but since previous work reported acceptable UADC(2) results for valence excited-states of doublet radicals with $\langle \hat{S}^2 \rangle$ values below 1.25, the CVS-UADC(2)-x method can be used for the allyl radical.[82]

Turning to the XA spectrum, the states 1 and 2 as well as the states 5 and 6 are almost

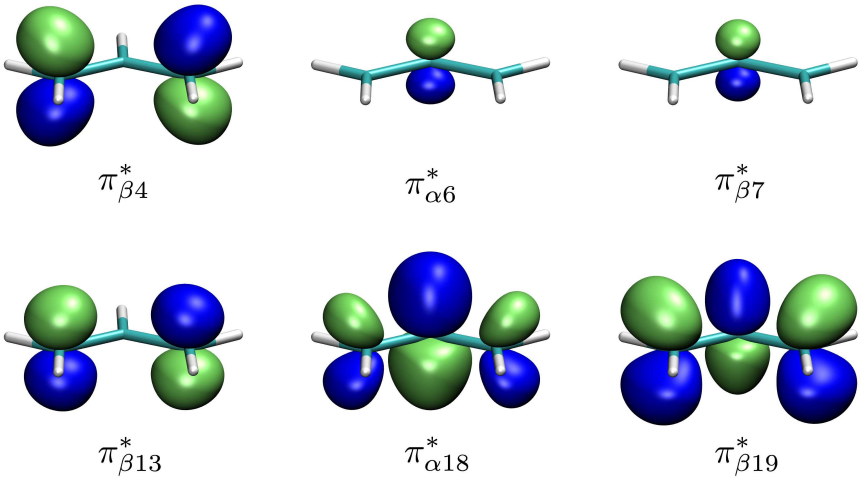

Figure 6.12: Illustration of the relevant virtual molecular spin-orbitals of the allyl radical at the level of UHF in combination with the 6-311++G** basis set. The isosurfaces of the spin orbitals are rendered with an isovalue of 0.06.

Table 6.14: Core-excitation energies (ω_{ex}), oscillator strengths (f_{osc}), character and amount of double amplitudes (R2) of the first eight C 1s excited states of the allyl radical calculated using CVS-UADC(2)-x and the 6-311++G** basis set. The calculated values are compared with experimental data.[42] Only the main transitions are shown and the numbering of the atoms complies with Figure 6.10. This table has already been published by me and my co-authors.[97]

State	ω_{ex} [eV]	f_{osc}	Main transition (C 1s $\rightarrow$)	R2 [%]	ω_{ex} [eV] (Expt.)
1	282.37	0.001	C3 $\rightarrow \pi^*_{\beta 4}, \pi^*_{\beta 13}$	16	281.99
2	282.37	0.056	C1,C2 $\rightarrow \pi^*_{\beta 4}, \pi^*_{\beta 13}$	16	
3	284.40	0.000	C1,C2 $\rightarrow \pi^*_{\beta 4}, \pi^*_{\beta 13}$	29	
4	284.78	0.022	C3 $\rightarrow \pi^*_{\alpha 18}, \pi^*_{\alpha 6}$	16	285.27
5	286.70	0.000	C3 $\rightarrow \pi^*_{\beta 1}, \pi^*_{\beta 2}$	24	
6	286.70	0.001	C1,C2 $\rightarrow \pi^*_{\beta 1}, \pi^*_{\beta 2}$	24	
7	286.90	0.026	C1,C2 $\rightarrow \pi^*_{\beta 19}, \pi^*_{\beta 7}$	27	287.50
8	286.93	0.002	C3 $\rightarrow \pi^*_{\alpha 1}, \pi^*_{\alpha 3}$	23	

degenerate due to symmetry. Note that point group symmetry was not exploited explicitly in these calculations, thus the states are only almost degenerate. The first state that is dipole allowed is state 2, which exhibits oscillator strength of 0.056. The experimental core-excitation energy of 281.99 eV is slightly overestimated by 0.1% (0.38 eV) at the CVS-UADC(2)-x level. The character of this state is dominated by transitions from linear combinations of the terminal carbon 1s orbitals to the $\pi^*_{\beta 4}$ and $\pi^*_{\beta 13}$ spin-orbitals, which are linear combinations of the empty 2p-orbitals of the terminal C1/C2 atoms. The second state possessing oscillator strength is state 4 with a core-excitation energy of 284.78 eV. Compared to the experimental value of 285.27 eV, this state is underestimated by 0.2%, leading to a poor energy gap of 2.41 eV between the two first bright states (experimentally 3.28 eV). This state is characterized by a transition from the middle carbon atom (C3) 1s orbital to the delocalized $\pi^*_{\alpha 18}$ and $\pi^*_{\alpha 6}$ spin-orbitals. The third experimental peak at 287.50 eV corresponds to state 7, which is again underestimated by 0.6 eV at the CVS-ADC(2)-x level, leading to a relative error to the experiment of -0.2%. However, since the second bright state is underestimated as well, the energy spacing between the second and third bright states is calculated to be 2.12 eV and therefore matches the experimental one of 2.23 eV. The character of state 7 is dominated by transitions from the 1s orbitals located at the terminal carbon atoms C1/C2 to the delocalized $\pi^*_{\beta 19}$ and $\pi^*_{\beta 7}$ spin-orbitals, which correspond to the π^*_{α}-spin-orbitals of state 4. The R2 values of all states are between 16% and 27%, where the lower values belong to the lowest two bright states. The amount of double configurations is thus about 10% lower compared to the closed-shell systems.

Eventually, the XA spectrum of the allyl radical is not described with the same excellent quality at the CVS-ADC(2)-x/6-311++G** level as the examples discussed before. This might be due to the ground state structure optimized with RI-MP2, which exhibits larger deviations from experimental data.

6.3.3 Triplet Dioxygen Diradical

As the last example of this chapter, the triplet O_2 radical is investigated. The O–O bond length was determined experimentally to be 1.21 Å[220], which is in excellent agreement with the computed RI-UMP2 equilibrium value of 1.222 Å. Furthermore, the UHF reference wave function exhibits hardly any spin contamination with a $\langle \hat{S}^2 \rangle$ value of 2.05. Figure 6.13 illustrates the relevant virtual and singly occupied molecular spin orbitals (SOMO). Due to the diffuse basis functions of the 6-311++G** basis set, $d^*_{\alpha 1}$, $d^*_{\beta 3}$, $d^*_{\beta 7}$, $d^*_{\alpha 9}$ and $d^*_{\beta 11}$ do not have a distinct π^* character, showing strongly diffuse fractions.

Let me turn to the results of the CVS-UADC(2)-x calculation, which are summarized in Table 6.15. Below the ionization limit, the experimental spectrum exhibits three significant peaks.[221,222] The first one is located at 530.7 eV, which is described with the first two core-excited states at the CVS-ADC(2)-x level. Due to the half-filled $\pi^*_{\beta 1}$ and $\pi^*_{\beta 2}$ orbitals, which are identical with respect to rotation and characterize these transitions, state 1 and 2 are degenerate, exhibiting core-excitation energies of 529.82 eV. Hence, the computed core-excitation energy is close to the experimental value with an error of only 0.17% (0.88 eV). The sum of their oscillator strengths yields a significant value of 0.1062. The next higher experimental peak at 538.8 eV can be assigned to the eighth core-excited state, which exhibits an excitation energy of 538.69 eV and a significant oscillator strength of 0.0706. The error is only 0.02% (0.11 eV) compared to experiment, thus the energy spacing between the degenerate states 1/2 and state 8 is 8.87 eV at the CVS-UADC(2)-x level, which is an overestimation by 0.77 eV compared to the experiment. State 8 is mainly dominated by electron promotions to the diffuse $d^*_{\beta 3}$, $d^*_{\beta 11}$, $d^*_{\alpha 9}$ and $d^*_{\alpha 1}$ orbitals, indicating the characteristics of a Rydberg-type state. The third experimental

Table 6.15: Core-excitation energies (ω_{ex}), oscillator strengths (f_{osc}), character and amount of double amplitudes (R2) of the first 25 O 1s excited states of the triplet dioxygen diradical calculated using CVS-UADC(2)-x and the 6-311++G** basis set. The calculated values are compared with experimental data.[221] Only the main transitions are shown and the α and β spin-orbitals s_1 refer to the positive linear combination of the two oxygen 1s orbitals, while s_2 denotes the negative linear combination. This table has already been published by me and my co-authors.[97]

State	ω_{ex} [eV]	f_{osc}	Main transition (1s $\rightarrow$)	R2 [%]	ω_{ex} [eV] (Expt.)
1	529.82	0.0531	$s_{\beta 2} \rightarrow \pi^*_{\beta 2}$	21	530.7
2	529.82	0.0531	$s_{\beta 2} \rightarrow \pi^*_{\beta 1}$	21	
3	529.85	0.0000	$s_{\beta 1} \rightarrow \pi^*_{\beta 2}$	21	
4	529.85	0.0000	$s_{\beta 1} \rightarrow \pi^*_{\beta 1}$	21	
5	536.85	0.0000	$s_{\alpha 2} \rightarrow d^*_{\alpha 9}, d^*_{\alpha 1}$; $s_{\beta 2} \rightarrow d^*_{\beta 11}, d^*_{\beta 3}$	26	
6	536.87	0.0017	$s_{\alpha 1} \rightarrow d^*_{\alpha 9}, d^*_{\alpha 1}$; $s_{\beta 1} \rightarrow d^*_{\beta 11}, d^*_{\beta 3}$	26	
7	538.68	0.0000	$s_{\beta 2} \rightarrow \pi^*_{\beta 2}, d^*_{\beta 11}$; $s_{\alpha 2} \rightarrow d^*_{\alpha 9}, d^*_{\alpha 1}$	26	
8	538.69	0.0706	$s_{\beta 1} \rightarrow d^*_{\beta 3}, d^*_{\beta 11}$; $s_{\alpha 1} \rightarrow d^*_{\alpha 9}, d^*_{\alpha 1}$	26	538.8
9	539.17	0.0003	$s_{\beta 2} \rightarrow \pi^*_{\beta 4}$	24	
10	539.21	0.0000	$s_{\beta 1} \rightarrow \pi^*_{\beta 4}$	24	
11	540.27	0.0002	$s_{\alpha 2} \rightarrow \pi^*_{\alpha 2}$	27	
12	540.29	0.0000	$s_{\alpha 1} \rightarrow \pi^*_{\alpha 2}$	27	
13	540.71	0.0000	$s_{\beta 2} \rightarrow \pi^*_{\beta 5}$	24	
14	540.71	0.0000	$s_{\beta 2} \rightarrow \pi^*_{\beta 6}$	24	
15	540.75	0.0050	$s_{\beta 1} \rightarrow \pi^*_{\beta 5}$	24	
16	540.75	0.0050	$s_{\beta 1} \rightarrow \pi^*_{\beta 6}$	24	
17	541.52	0.0000	$s_{\beta 2} \rightarrow d^*_{\beta 3}, d^*_{\beta 11}$	26	
18	541.55	0.0185	$s_{\beta 1} \rightarrow d^*_{\beta 3}, d^*_{\beta 11}$	26	
19	541.78	0.0000	$s_{\alpha 2} \rightarrow \pi^*_{\alpha 4}$	27	
20	541.78	0.0000	$s_{\alpha 2} \rightarrow \pi^*_{\alpha 3}$	27	
21	541.80	0.0056	$s_{\alpha 1} \rightarrow \pi^*_{\alpha 4}$	27	541.7
22	541.80	0.0056	$s_{\alpha 1} \rightarrow \pi^*_{\alpha 3}$	27	
23	542.51	0.0000	$s_{\alpha 2} \rightarrow d^*_{\alpha 1}, d^*_{\alpha 9}$	27	
24	542.51	0.0209	$s_{\alpha 1} \rightarrow d^*_{\alpha 1}, d^*_{\alpha 9}$; $s_{\beta 2} \rightarrow d^*_{\beta 7}$	27	
25	542.60	0.0090	$s_{\beta 2} \rightarrow d^*_{\beta 7}$; $s_{\alpha 1} \rightarrow d^*_{\alpha 1}$	25	

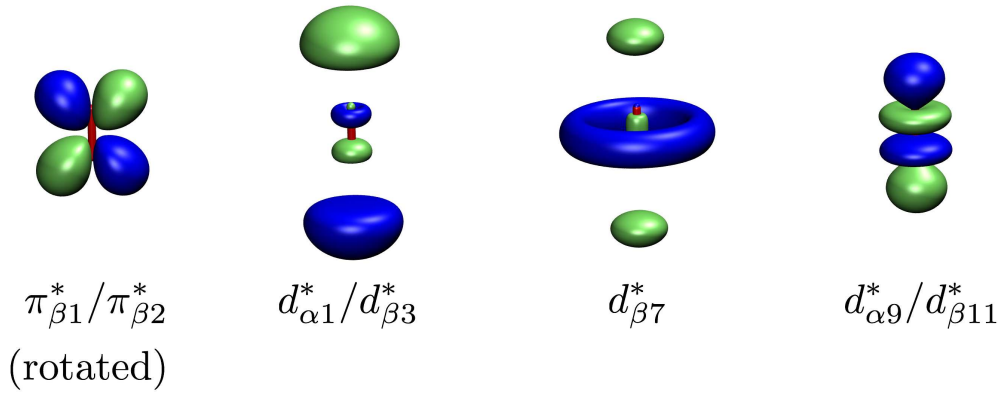

Figure 6.13: Illustration of the relevant virtual molecular spin-orbitals of the triplet dioxygen diradical at the level of UHF in combination with the 6-311++G** basis set. The isosurfaces of the spin orbitals are rendered with an isovalue of 0.06.

peak located at 541.7 eV can be matched with state 18, exhibiting a core-excitation energy of 541.55 eV. Hence, the CVS-UADC(2)-x calculation yields an error of only 0.03% compared to the experiment. Furthermore, the energy difference of 2.9 eV between the second and third peaks is also excellently computed with a value of 2.86 eV. State 18 is mainly characterized by transitions to the diffuse $d^*_{\beta 3}$ and $d^*_{\beta 11}$ orbitals. However, the experimentally resolved third bright excitation is generally very broad, which indicates a series of Rydberg states. State 24, for example, with a core-excitation energy of 542.51 eV exhibits an oscillator strength of 0.0209, but cannot be assigned properly to the experiment. It is dominated by transitions to the $d^*_{\alpha 1}$, $d^*_{\alpha 9}$ and $d^*_{\beta 7}$ spin-orbitals, thus it has a strong Rydberg-character, too. In contrast to the other open-shell examples, the ratio of double excitations contributing to all O 1s excited states is considerable with values between 21% and 27%, indicating strong orbital relaxation effects.

Eventually, the XA spectrum of the triplet O_2 diradical is excellently reproduced with the CVS-UADC(2)-x method using the 6-311++G** basis set.

6.4 Interim Summary

The results presented in this chapter demonstrate the capability of CVS-ADC(2)-x in combination with the 6-311++G** basis set to successfully simulate XA spectra of medium-sized molecules as well as small organic radicals. Furthermore, in combination with the CVS-ISR approach and wave function analysis packages, a deeper insight into the nature of core-excited states can be provided. Generally, the ADC formalism provides a balanced description of electron correlation in both ground and excited state. In the case of core excitations, neglecting relativistic contributions to the K-shell excitations reduce the error produced at the level of CVS-ADC(2)-x/6-311++G**. The combination of the CVS-ADC(2)-x method and the 6-311++G** basis set potentially provides a fortuitous error compensation of orbital relaxation, electron correlation, basis set truncation and relativistic effects, resulting in core-excitation energies close to experiments.

Chapter 7

Comparison of CVS-ADC and TD-DFT

In this chapter, core-excitation energies at the CVS-ADC(2)-x level presented in chapter 6 are compared with TD-DFT and CVS-ADC(2)-s results to demonstrate the self-interaction error (SIE) problem inherent in pure TD-DFT, thereby clarifying the accuracy at the CVS-ADC(2)-x level. In the case of the ANQ, thymine and allyl radical systems, a comparison with CVS-ADC(3,2) results is discussed, too. The structures of all molecules are illustrated in Figures 6.1, 6.6 and 6.10.

The computational details (geometry optimizations, basis sets, methods and programs) of this study are identical to the ones of chapter 6. Additionally, TD-DFT calculations of the core-excited states were performed employing the B3LYP xc functional and using the REW implementation in the `ORCA 2.8` program.[223] Hence, to selectively obtain 1s XA spectra, only excitations from the respective 1s orbitals were included in the REW-TD-DFT calculations (see chapter 2.4.3).[161,224] I chose the B3LYP xc functional, because TD-DFT has proven now several times to yield quite accurate results for core excitation spectra in combination with the B3LYP functional.[15,37,75,175] CVS-ADC(3,2) results were obtained with my implementation described in chapter 3. Note that, due to technical reasons, the REW-TD-DFT calculations were performed employing the pure 5D/7F versions, while the CVS-ADC results were computed using the Cartesian 6D/10F version of the respective basis sets. However, the influence of the additional Cartesian d and f orbitals on the core-excitation energies at the REW-TD-DFT level are relatively small compared to the inherent SIE, thus a direct comparison with CVS-ADC values is justified. All computed values shown in this chapter are absolute without any level shift or consideration of relativistic effects. Finally, note that the whole content of this chapter has already been published by me and my co-authors. Calculations of the closed-shell systems are published in *Journal of Computational Chemistry, 35 (2014), pages 1900-1915*, while the XA spectra of the open-shell systems are published in *Journal of Chemical Theory and Computation, 10 (2014), pages 4583-4598.*[96,97] The discussion about CVS-ADC(3,2) results is published in *Journal of Chemical Physics, 142 (2015), 214104.*[98]

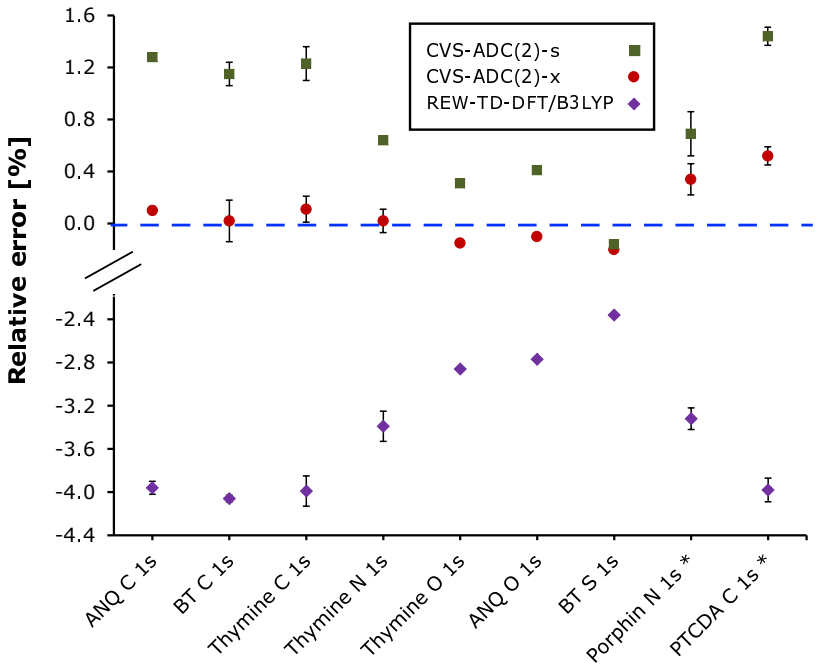

Figure 7.1: Illustration of the calculated relative arithmetic mean errors of the core-excitation energies calculated with different methods compared to experimental values. The dashed line in blue indicates a discrepancy of 0% to the experiment. The means are calculated for each type of core excitation (element specific) and every molecule using all core-excited states of the respective element that can be assigned to experimental data. The vertical bars represent the standard deviation. Note that the values marked with a * are not directly comparable to the others, because smaller basis sets were used for these calculations.

7.1 Closed-Shell Systems

Let me start with the discussion of the closed-shell molecules presented in chapters 6.1 and 6.2. Figure 7.1 summarizes and illustrates the arithmetic mean errors of the computed core-excitation energies with respect to experimental values for the CVS-ADC(2)-x, CVS-ADC(2)-s and REW-TD-DFT/B3LYP approaches, which were evaluated for each molecule and every core excitation (element specific) separately.

At first, the results of the O 1s core-excited states of ANQ are discussed and the results are summarized in Table 7.1. Comparison with the experiments reveals that B3LYP underestimates the fourth-lowest bright core-excited state by 2.8% (∼14.3 eV), while CVS-ADC(2)-s overestimates the core-excitation energy by 0.4% (∼2.2 eV). CVS-ADC(2)-x exhibits the most accurate result of the O 1s excited state of ANQ with an error of only 0.1% (0.85 eV). Furthermore, the trend of R2 values confirms the analysis in chapter 5. The bright singlet state, for example, has only 18% of double excitation character at the CVS-ADC(2)-s level, while CVS-ADC(2)-x yields 23%. Comparing the three methods, the respective states are almost degenerate for all methods ($\Delta\omega \leq 0.02$ eV $\sim 7 \cdot 10^{-4}$ a.u.). The first four states are in identical order, while the subsequent states exhibit a slightly different order due to the small energy differences between them. The differences in the

Table 7.1: Comparison of core-excitation energies (ω_{ex}) and oscillator strengths (f_{osc}) of the first eight O 1s singlet and triplet as well as the first spectroscopically bright C 1s singlet excited states of ANQ, calculated with CVS-ADC(2)-s/x and REW-TD-DFT/B3LYP with experimental values.[13,205] The calculations were performed employing the 6-311++G** basis set and in the case of the carbon 1s excitations, C_{2v} point group symmetry was exploited. This table has already been published by me and my co-authors.[96]

	B3LYP		CVS-ADC(2)-s		CVS-ADC(2)-x		Expt.
State	ω_{ex} [eV]	f_{osc}	ω_{ex} [eV]	f_{osc}	ω_{ex} [eV]	f_{osc}	ω_{ex} [eV]
				O 1s			
1	514.97 (T)	—	531.58 (T)	—	528.99 (T)	—	
2	514.97 (T)	—	531.58 (T)	—	528.99 (T)	—	
3	515.69 (S)	0.0284	532.17 (S)	0.0002	529.45 (S)	0.0002	529.2 - 531.4
4	515.70 (S)	0.0338	532.17 (S)	0.0640	529.45 (S)	0.0689	
5	517.33 (T)	—	534.21 (T)	—	533.08 (S)	—	
6	517.34 (S)	0.0005	534.21 (T)	—	533.08 (S)	0.0003	
7	517.34 (T)	—	534.21 (S)	0.0001	533.09 (T)	—	
8	517.35 (S)	0.0005	534.21 (S)	0.0006	533.09 (T)	—	
				C 1s			
1	273.28	0.015	287.76	0.051	284.40	0.038	284.1
2	273.53	0.040	288.10	0.155	284.78	0.041	284.45
3	273.63	0.058			284.81	0.086	
4	273.75	0.007	288.33	0.029	284.96	0.036	284.8
5	273.77	0.026	288.36	0.060			
6	274.02	0.023	288.63	0.011	285.27	0.024	285
7			288.71	0.030			
8					285.60	0.014	
9	274.59	0.060	289.10	0.029	285.74	0.028	
10	274.96	0.016	289.30	0.015	285.92	0.034	
11	274.97	0.045	289.45	0.112	285.92	0.089	285.6
12	275.06	0.023			286.13	0.014	
13					286.34	0.007	

order may be due to numerical accuracy, especially since no point group symmetry was used for the calculations. This is corroborated by the fact that for B3LYP the states 3 and 4, which should be degenerate, show an energy difference of the same order of magnitude.

Next, the ANQ C 1s excitation spectra calculated at the three levels of theory are discussed and the results are shown as well in Table 7.1. In principle, the results are similar to the O 1s spectra. However, compared to the O 1s result, the relative errors of the first bright state calculated with both REW-TD-DFT/B3LYP and CVS-ADC(2)-s are with 4.0% and 1.3% significantly larger, respectively. Since there are five bright experimental peaks, the absolute errors between the calculated states and the experimental values can be compared as well to judge the quality of the spectral features. At the REW-TD-DFT/B3LYP level, the spacings between the states are essentially constant with values ranging from 10.6 eV to 11.0 eV. The overestimation of the CVS-ADC(2)-s method is also practically constant with absolute errors between 3.7 eV an 3.9 eV. Hence, by addition of an absolute, constant energy shift to the REW-TD-DFT and CVS-ADC(2)-s results, good agreement of the calculated spectra with the experiment is achieved. Note that the number of states matching an experimental peak varies between the three methods, e.g. the fourth experimental peak is described by one bright state using the CVS-ADC(2)-x and REW-TD-DFT/B3LYP methods, while CVS-ADC(2)-s yields two states contributing to this peak. Nevertheless, both CVS-ADC(2) methods are in the case of ANQ more precise than REW-TD-DFT/B3LYP with respect to absolute errors in core-excitation energies, as well as energy differences between the states.

Going to the S 1s excitations of the BT molecule (see Table 7.2), there is a smaller difference between CVS-ADC(2)-x and -s compared to the ANQ molecule. Due to strong relaxation and relativistic effects, both second order CVS-ADC approaches underestimate the core-excitation energies. Furthermore, the relative error for both methods is almost the same with -0.2% and CVS-ADC(2)-s is actually closer to the experiment. Considering relativistic effects of about 8.0 eV[179], which would shift the results above the experimental value, the CVS-ADC(2)-x result would be slightly better compared to experiment. REW-TD-DFT/B3LYP provides a relative error of 2.4%, which is in the same order of magnitude as the ANQ (O 1s) results.

The result of the C 1s excitations of BT are also given in Table 7.2. Here, REW-TD-DFT/B3LYP again shows a strong underestimation of both experimental peaks by large values of 4.0% (11.08 eV) and 4.1% (11.24 eV), respectively. Since these errors are almost constant, the energy difference between the two bright states are better described with REW-TD-DFT/B3LYP than with CVS-ADC(2)-x. At the CVS-ADC(2)-s level, a larger overestimation of 1.1% (3.13 eV) and 1.2% (3.51 eV) can be identified, respectively. In the case of the C 1s excitations of BT, the energy difference between the first two bright core-excited states is better reproduced with CVS-ADC(2)-s than with CVS-ADC(2)-x, but the extended variant provides better absolute values compared to the experiment.

Turning to the C 1s excitations of the PTCDA molecule, the results are given in Table 7.3. Since a smaller 6-31G** basis set was employed due to computational cost, the energy difference between the first two spectroscopically bright states is discussed. Experimentally, this value is 1.2 eV. The calculations using the CVS-ADC(2)-x method are closest to this value with 1.48 eV, while REW-TD-DFT/B3LYP provides an energy spacing of 1.57 eV and the value at the CVS-ADC(2)-s level is 1.51 eV. In spite of employing a smaller basis set, the absolute value of the core-excitation energies are practically at the same level as shown for the other examples. REW-TD-DFT provides an underestimation of about 4.1% and the overestimation of CVS-ADC(2) is about 1.4%. CVS-ADC(2)-x shows the best absolute and relative results for the C 1s excitations of PTCDA.

Let me continue with the thymine molecule. The results of the C 1s, N 1s and O 1s

Table 7.2: Comparison of core-excitation energies (ω_{ex}) and oscillator strengths (f_{osc}) of the first six S 1s and first spectroscopically bright C 1s singlet excited states of BT, calculated using CVS-ADC(2)-s/x and REW-TD-DFT/B3LYP with experimental values of oligothiophenes (crystal powder) or BT monolayer on Ag(111) surface.[34,36] The calculations were performed employing the 6-311++G** basis set and exploiting C_2 point group symmetry. This table has already been published by me and my co-authors.[96]

	B3LYP		CVS-ADC(2)-s		CVS-ADC(2)-x		Expt.
State	ω_{ex} [eV]	f_{osc}	ω_{ex} [eV]	f_{osc}	ω_{ex} [eV]	f_{osc}	ω_{ex} [eV]
S 1s							
1	2415.76	0.0031	2469.80	0.0039	2468.83	0.0057	2474
2	2415.76	0.0006	2469.80	0.0017	2468.83	0.0023	
3	2416.85	0.0059	2470.08	0.0085	2468.97	0.0057	
4	2416.85	0.0004	2470.08	0.0010	2468.97	0.0031	
5	2417.46	0.0002	2471.28	0.0000	2470.69	0.0001	
6	2417.46	0.0007	2471.28	0.0003	2470.69	0.0006	
C 1s							
1	274.12	0.003	288.58	0.005	285.19	0.004	285.7
2	274.12	0.032	288.58	0.053	285.19	0.041	
3	274.38	0.009	288.83	0.007	285.42	0.008	
4	274.38	0.010	288.83	0.095	285.42	0.115	
5	274.62	0.004	288.93	0.003	285.67	0.003	
6	274.62	0.055	288.93	0.043	285.70	0.056	
7	274.89	0.002	289.02	0.004			
8	274.90	0.043	289.05	0.067			
9	275.46	0.003	290.21	0.004	287.08	0.001	286.7
10	275.46	0.057	290.21	0.046	287.08	0.038	
11			290.28	0.006	287.14	0.008	
12			290.28	0.001	287.14	0.003	
13					287.19	0.010	

Table 7.3: Comparison of core-excitation energies (ω_{ex}) and oscillator strengths (f_{osc}) of the first spectroscopically bright C 1s singlet excited states of PTCDA, calculated using CVS-ADC(2)-s/x and REW-TD-DFT/B3LYP with experimental values.[13] The calculations were performed employing the 6-31G** basis set and exploiting D_{2h} point group symmetry. This table has already been published by me and my co-authors.[96]

	B3LYP		CVS-ADC(2)-s		CVS-ADC(2)-x		Expt.
Bright state	ω_{ex} [eV]	f_{osc}	ω_{ex} [eV]	f_{osc}	ω_{ex} [eV]	f_{osc}	ω_{ex} [eV]
1	273.23	0.031	287.87	0.069	285.36	0.072	
2	273.31	0.063	288.01	0.060	285.44	0.058	284.4
3	273.32	0.024	288.32	0.072	285.72	0.073	
4	273.64	0.041	288.41	0.091	285.75	0.090	
5	274.88	0.105	289.71	0.069	287.11	0.061	
6	275.07	0.032	289.87	0.094	287.19	0.090	
7	275.11	0.043	289.92	0.203	287.23	0.095	285.6
8	275.20	0.073	289.95	0.019	287.30	0.076	
9			290.01	0.020			

excitations are summarized in Table 7.4. As usual, a large error of the core-excitation energies at the REW-TD-DFT/B3LYP level can be identified. In the case of the C 1s excitations, the underestimation is about 4%, while it is 3.5% and 2.9% for the N 1s and O 1s excitations, respectively. CVS-ADC(2)-x provides again the best results compared to experiment, with errors of about 0.12%, 0.05% and 0.2% for the carbon, nitrogen and oxygen 1s excitations, respectively. In the case of the strict second order CVS-ADC approach, these errors are about 1.3%, 0.6% and 0.3%. Since some experimental signals are available, I can analyze the spacings between the states that provide information about the quality of the calculated spectra. Going to the C 1s excitations, the experimental value for the energy difference between the first two bright states is 1 eV. This value is best matched at the REW-TD-DFT/B3LYP level with a value of 1.14 eV, while CVS-ADC(2)-x yields 1.52 eV and the strict variant provides 1.38 eV. However, the experimental difference of 1.4 eV between the second and third spectroscopically bright states is best described at the CVS-ADC(2)-s level with a value of 1.38 eV, while REW-TD-DFT/B3LYP strongly underestimates this shift with 0.76 eV. CVS-ADC(2)-x provides also an acceptable value of 1.59 eV. The next energy difference is between the states 3 and 4, which is experimentally found to be 0.5 eV. This value is again best matched with REW-TD-DFT/B3LYP (0.48 eV). With a value of 0.1 eV, CVS-ADC(2)-s underestimates this spacing, while CVS-ADC(2)-x provides only a slight underestimation (0.29 eV). The energy difference between state 4 and 5 is experimentally found to be 0.6 eV, which is also too small at the CVS-ADC(2)-s level with a value of 0.11 eV. Here, CVS-ADC(2)-x and REW-TD-DFT/B3LYP give better results with values of 0.21 eV and 0.26 eV, respectively, but this shift is also strongly underestimated compared to the experiment. Turning to the energy difference between the first two bright N 1s core-excited states of thymine, CVS-ADC(2)-s provides the best result with 1.15 eV compared to the experimental value of 1 eV, while CVS-ADC(2)-x and REW-TD-DFT-B3LYP yield 1.53 eV and 1.6 eV, respectively. Regarding the energy

Table 7.4: Comparison of core-excitation energies (ω_{ex}) and oscillator strengths (f_{osc}) of the first spectroscopically bright C 1s, N 1s and O 1s singlet excited states of thymine, calculated using CVS-ADC(2)-s/x and REW-TD-DFT/B3LYP with experimental values.[89] The calculations were performed employing the 6-311++G** basis set. This table has already been published by me and my co-authors.[96]

	B3LYP		CVS-ADC(2)-s		CVS-ADC(2)-x		Expt.
Bright state	ω_{ex} [eV]	f_{osc}	ω_{ex} [eV]	f_{osc}	ω_{ex} [eV]	f_{osc}	ω_{ex} [eV]
C 1s							
1	274.24	0.019	288.45	0.032	284.84	0.024	284.9
2	275.38	0.042	289.83	0.058	286.36	0.045	285.9
3	276.14	0.014	291.21	0.012	287.95	0.015	287.3
4	276.62	0.038	291.31	0.013	288.24	0.053	287.8
5	276.88	0.008	291.42	0.072	288.45	0.013	288.4
N 1s							
1	388.17	0.0111	404.20	0.0098	401.50	0.0111	
2	388.57	0.0090	404.49	0.0069	401.82	0.0070	401.7
3	389.40	0.0028	404.59	0.0056	402.21	0.0078	
4	389.77	0.0067	404.91	0.0026	402.54	0.0035	
5	389.79	0.0008	405.35	0.0041	402.60	0.0066	402.7
6	389.86	0.0084	405.46	0.0027	403.03	0.0106	
7					403.42	0.0050	
O 1s							
1	516.63	0.0243	532.95	0.0240	530.52	0.0282	531.4
2	517.53	0.0142	534.01	0.0218	531.54	0.0268	532.3

Table 7.5: Comparison of core-excitation energies (ω_{ex}) and oscillator strengths (f_{osc}) of the first spectroscopically bright N 1s singlet excited states of porphin, calculated using CVS-ADC(2)-s/x and REW-TD-DFT/B3LYP with experimental values of a solid porphin film.[212] The calculations were performed employing the 6-31++G** basis set and exploiting D_{2h} point group symmetry. This table has already been published by me and my co-authors.[96]

	B3LYP		CVS-ADC(2)-s		CVS-ADC(2)-x		Expt.
Bright state	ω_{ex} [eV]	f_{osc}	ω_{ex} [eV]	f_{osc}	ω_{ex} [eV]	f_{osc}	ω_{ex} [eV]
1	385.83	0.0169	401.50	0.0212	399.89	0.0338	398.2
2	387.64	0.0115	403.63	0.0169	402.12	0.0268	400.3
3	389.01	0.0115	404.56	0.0050	403.03	0.0263	402.3
4	389.01	0.0249	404.90	0.0317	403.59	0.0079	
5	390.68	0.0273	405.81	0.0056	405.18	0.0187	403.9

spacing between the first two spectroscopically bright O 1s core excitations, the REW-TD-DFT/B3LYP value is with 0.9 eV in perfect agreement with the experiment (0.9 eV), while both CVS-ADC(2) variants slightly overestimate this shift with an value of 1.0 eV.

The last closed-shell example is the porphin molecule. The results of the N 1s excitations are given in Table 7.5. Here, only the energy differences between the states are investigated, because the smaller 6-31++G** basis set was employed due to technical reasons. The energy difference between the first two experimental peaks is 2.1 eV, which is best reproduced using the CVS-ADC(2)-s method with a value of 2.13 eV. At the REW-TD-DFT/B3LYP level, this value is 1.81 eV, while the extended second order CVS-ADC variant provides a value of 2.23 eV. Hence, all methods describe this shift very well. As already mentioned in chapter 6.2.1, the bright core-excited state 3 is poorly reproduced at the CVS-ADC(2)-x level. This is also the case for the REW-TD-DFT/B3LYP and CVS-ADC(2)-s approaches, which can be identified when looking at the energy differences between the second and third state. These are 1.37 eV in the case of REW-TD-DFT/B3LYP and 0.93 eV regarding CVS-ADC(2)-s. The latter result is therefore at the same level as the result obtained with the extended variant. These results are thus a further hint that calculations that correspond to a vacuum environment might not be adequate for the description of the third peak, because the experimental spectrum is obtained in the solid state.

Finally, I evaluate the results obtained for the closed-shell systems statically. Table 7.6 contains the arithmetic mean errors of the core-excitation energies with respect to experimental data for each element averaged over all molecules investigated in this chapter with the 6-311++G** basis set. Note that the statistics are collected on the basis of only a few selected examples, thus they cannot be taken as general. Going from oxygen to the lighter carbon, the mean error at the CVS-ADC(2)-x level changes from -0.73 eV to 0.25 eV. Core-excitation energies from the carbon 1s levels are on average slightly overestimated, while the calculated values for nitrogen and oxygen are slightly underestimated. The range of the relative errors is between -0.14% and 0.09%, thus they are close to zero. A similar trend is observed at the REW-TD-DFT level. Here, the absolute value of the mean error decreases from -14.62 eV to -10.97 eV, while the relative error increases by approximately 1.1%. Hence, the absolute errors are about 50 times larger compared to CVS-ADC(2)-x

Table 7.6: Comparison of the calculated mean errors and the standard deviations σ of the core-excitation energies obtained with the 6-311++G** basis set with respect to experimental data for the different types of core excitations and different methods. The means are taken over all closed-shell molecules, which are discussed in this chapter, and all core excitations of the respective type. The mean errors are given in eV. Additionally, relative errors in % are shown in parentheses. This table has already been published by me and my co-authors.[96]

	B3LYP		CVS-ADC(2)-s		CVS-ADC(2)-x	
Core	Mean	σ	Mean	σ	Mean	σ
O 1s	-14.62 (-2.83)	0.27 (0.05)	1.81 (0.34)	0.32 (0.06)	-0.73 (-0.14)	0.17 (0.03)
N 1s	-13.19 (-3.39)	0.49 (0.14)	2.58 (0.64)	0.11 (0.02)	-0.27 (-0.07)	0.51 (0.13)
C 1s	-10.97 (-3.99)	0.29 (0.10)	3.58 (1.24)	0.28 (0.10)	0.25 (0.09)	0.25 (0.09)

as well as the range of relative errors from -2.83% to -3.99%. CVS-ADC(2)-s provides an opposite trend with the smallest mean error of 1.81 eV for O 1s core-excitation energies and 3.58 eV for the C 1s ones. Therefore, the relative error increases from 0.34% to 1.24% going from oxygen to carbon. Compared to the CVS-ADC(2)-x results, the absolute values are larger at the strict second order level. As explained in previous chapters, the reason for the differences between the elements is due to the larger relativistic effects for heavier atoms, which are neither included in the REW-TD-DFT calculations nor in the CVS-ADC ones.

Eventually, this study confirms the conclusions obtained in the investigation of the small systems in chapter 4, thereby demonstrating the accuracy of the CVS-ADC(2)-x method in combination with Pople-type basis sets, in particular, the 6-311++G** basis. CVS-ADC(2)-x in combination with the 6-311++G** basis set reproduces the experimental results most accurately with relative errors between -0.14% and 0.09%. The reason for this is the fortuitous compensation of errors due to basis set truncation, orbital relaxation, electron correlation, and neglect of relativistic effects. While core excitations from the carbon 1s levels are on average slightly overestimated, the results for oxygen and nitrogen are slightly underestimated. REW-TD-DFT/B3LYP, in contrast, strongly underestimates the core-excitation energies compared to the experimental values up to 14.62 eV in the case of oxygen 1s excitations. This underestimation is most likely due to an unbalanced SIE, which results in a much too small energy gap between core and valence orbitals. Since the absolute errors at the REW-TD-DFT/B3LYP level are comparatively constant, absolute shifts of the core-excitation energies are mandatory to provide accurate results. The strict second order CVS-ADC variant slightly overestimates the core-excitation energies compared to the experimental values. However, the mean errors are significantly smaller than the ones at the REW-TD-DFT/B3LYP level. Since the standard deviations are very similar for all three methods, the XA spectra are in general adequately described with all investigated methods.

7.2 Open-Shell Systems

Next, I would like to show that the unrestricted REW-TD-DFT and CVS-ADC variants exhibit the same trends as the restricted approaches. For this purpose, the results of XA spectra of the small organic radicals (see chapter 6.3) are recalculated with the CVS-

Table 7.7: Comparison of core-excitation energies (ω_{ex}) and oscillator strengths (f_{osc}) of the first spectroscopically bright C 1s excited state of the CH_3 and the O 1s excited state of the OH radicals as well as of the first three spectroscopically bright C 1s excited states of the allyl radical and the first five spectroscopically bright O 1s excited states of the triplet O_2 diradical, calculated using CVS-UADC(2)-s/x and REW-TD-DFT/B3LYP with experimental values.[42,189,218,221] The calculations were performed employing the 6-311++G** basis set and the values of the core-excitation energies are given relative to the first core-excited state of the respective molecule. This table has already been published by me and my co-authors.[97]

	B3LYP		CVS-UADC(2)-s		CVS-UADC(2)-x		Expt.
Bright state	ω_{ex} [eV]	f_{osc}	ω_{ex} [eV]	f_{osc}	ω_{ex} [eV]	f_{osc}	ω_{ex} [eV]
			CH_3				
1	270.91	0.034	283.97	0.043	281.42	0.036	281.35
			OH				
1	511.42	0.0444	527.67	0.0497	525.17	0.0449	525.85
			Allyl				
1	271.55	0.039	285.09	0.068	282.37	0.056	281.99
2	+2.91	0.011	+2.39	0.028	+2.41	0.022	+3.28
3	+4.08	0.038	+5.35	0.032	+4.52	0.026	+5.51
			O_2				
1	516.51	0.0575	533.52	0.0602	529.82	0.0531	530.7
2	516.51	0.0575	533.52	0.0602	529.82	0.0531	
3	+8.72	0.0392	+8.90	0.0383	+8.87	0.0706	+8.1
4	+11.55	0.0109	+11.02	0.0319	+11.74	0.0185	+11.0
5	+11.80	0.0783	+12.28	0.0661	+12.69	0.0209	

UADC(2)-s and the unrestricted REW-TD-DFT/B3LYP methods. Table 7.7 summarizes all results with respect to experimental values.

Let me start with the results of the C 1s and O 1s excited spectroscopically bright peaks of the CH_3 and OH radicals. REW-TD-DFT/B3LYP underestimates both dipole allowed core-excited states by 3.9% (10.44 eV) and 2.8% (14.43 eV), respectively, while CVS-UADC(2)-s overestimates these core-excitation energies by 0.9% (2.62 eV) and 0.3% (1.82 eV). For both systems, the CVS-UADC(2)-x results are in almost perfect agreement with the experiment as shown in chapter 6.3.1. In the case of CVS-UADC(2)-s, the bright states of the OH and CH_3 radicals exhibit an R2 value of 6%, respectively. This is compared to the CVS-UADC(2)-x results only about half of the contribution, indicating a too weak consideration of orbital relaxation effects.

Going to the results of the allyl radical (C 1s excitations), the core-excitation energies at the CVS-UADC(2)-s level are overestimated as usual. The energy differences between the three core-excited states obtained with CVS-UADC(2)-s with values of 2.39 eV and 2.96 eV, respectively, are inaccurate compared to the experiment, too. REW-TD-DFT/B3LYP underestimates the core-excitation energies of the bright peaks by about 4% (10.44 - 11.87 eV). Furthermore, the energy spacing between the bright core-excited states is also

inaccurately described. The energy difference between the first and second bright state is experimentally found to be 3.28 eV. Here, REW-TD-DFT/B3LYP provides a value of 2.9 eV, which is more accurate than at the CVS-UADC(2)-x level (2.41 eV). The second energy spacing of 2.23 eV between state 2 and 3, in contrast, is better described at the CVS-UADC(2)-x level with a value of 2.12 eV, while REW-TD-DFT exhibits 1.18 eV. Hence, in summary, CVS-UADC(2)-x provides the best results for the tested methods.

The last example corresponds to the O 1s excitations of the triplet O_2 diradical. The typical underestimation at the REW-TD-DFT/B3LYP level is considerable with values for the first three spectroscopically bright O 1s core-excited states of 14.19 eV, 13.58 eV and 13.65 eV, respectively, compared to experiment, which is approximately 2.6%–2.7%. These deviations are almost constant, thus by addition of an absolute, constant energy shift the calculated spectrum would be in good agreement with the experiment. Similarly, CVS-UADC(2)-s overestimates these states almost constantly with errors between 0.5% and 0.7%, thus by subtraction of a constant shift, the agreement with experimental data would be achieved. However, taking account of the results discussed in chapter 6.3.3, CVS-UADC(2)-x provides the best agreement with experiment, because the energy spacing as well as the absolute core-excitation energies are almost perfectly reproduced. Note that the fourth state with large oscillator strength (bright state 5, Table 7.7) cannot be properly assigned to experiment by all three methods.

Eventually, this study reveals that the results for the small organic radicals exhibit similar quality as the ones for closed-shell molecules investigated in chapter 7.1. In combination with the 6-311++G** basis set, CVS-UADC(2)-x provides a very good agreement with experiments, exhibiting relative errors between -0.2% and 0.1% and accurate absolute values in the case of the examples investigated in this chapter. In contrast, CVS-UADC(2)-s slightly overestimates the core-excitation energies up to 1.1% compared to experiments and REW-TD-DFT/B3LYP strongly underestimates them by up to 4%. Since the energy spacing between the core-excited states are accurately described, the relative spectra are well reproduced by CVS-UADC(2)-s and REW-TD-DFT/B3LYP. However, a constant shift to the core-excitation energies is mandatory using these methods to simulate core excitation spectra correctly.

7.3 Comparison Between the Extended Second Order and Third Order CVS-ADC Approaches

Finally, the O 1s excitations of ANQ, the N 1s and O 1s excitations of thymine and the C 1s excitations of the allyl radical were recalculated using the CVS-(U)ADC(3,2) method, thereby checking the capability of the third-order approach to describe spectral features correctly, although core-excitation energies are strongly overestimated. The results are compared directly with CVS-ADC(2)-x and experimental values (see Table 7.8). Here, I do not present the complete results obtained at the CVS-ADC(3,2) level, because they provide no further insights. Tables containing the whole data have been published by me and my co-authors in the supplementary information in *Journal of Chemical Physics, 142 (2015), 214104.*[98]

Let me start with the bright O 1s excitation of ANQ, which is denoted as S_4. The absolute difference of 5.62 eV between the two CVS-ADC levels is significantly large. Compared to the experiment CVS-ADC(2)-x underestimates the core-excitation energy by only 0.85 eV, while CVS-ADC(3,2) provides an overestimation of 4.77 eV. This is a further hint that core-excitation energies are strongly overestimated at the CVS-ADC(3,2) level.

Table 7.8: Comparison of core-excitation energies (ω_{ex}) of the spectroscopically bright excited states of ANQ (O 1s), thymine (N 1s and O 1s), and the allyl radical (C 1s), calculated using CVS-(U)ADC(2)-x and CVS-(U)ADC(3,2) in combination with the 6-311++G** basis set with experimental data.[42,89,205] δ(3-2x) denotes the differences of core-excitation energies between CVS-ADC(2)-x and CVS-ADC(3,2), δ(3-Expt.) describes the differences of core-excitation energies between CVS-ADC(3,2) and experimental values, and δ(2x-Expt.) is the differences of core-excitation energies between CVS-ADC(2)-x and experimental values. This table has already been published by me and my co-authors.[98]

State	ω_{ex} [eV]					
	CVS-(U)ADC(2)-x	CVS-(U)ADC(3,2)	Expt.	δ(3-2x)	δ(3-Expt.)	δ(2x-Expt.)
ANQ O 1s						
S_4	529.45	535.07	529.2 - 531.4	5.62	4.77	-0.85
Thymine N 1s						
A	401.50	405.81	401.7	4.31	4.11	-0.20
B	401.82	406.39				
C	402.21	406.57				
D	402.54	406.80 (E)	402.7	4.29	4.62	0.33
E	402.60	407.32 (D)				
F	403.03	407.73				
G	403.42	408.29				
Thymine O 1s						
A	530.52	536.48	531.4	5.96	5.08	-0.88
B	531.54	537.52	532.3	5.98	5.22	-0.76
Allyl radical C 1s						
B	282.37	283.94	281.99	1.56	1.95	0.38
D	284.78	286.51	285.27	1.73	1.24	-0.49
G	286.90	288.87	287.50	1.98	1.37	-0.60

Turning to the thymine molecule, I start with the O 1s excitations. The two bright states A and B are excellently described at the CVS-ADC(2)-x level with an almost constant error of -0.8/-0.9 eV, respectively. CVS-ADC(3,2) overestimates these states by 5.08 eV and 5.22 eV compared to the experiment, but these errors are almost equal, thus the spacing between the states is correctly described. Since the difference between CVS-ADC(2)-x and CVS-ADC(3,2) is almost identical with 6 eV for both states, the spectral spacing is described almost equally with both methods. The same observations can be made regarding the N 1s excitations of thymine. Note that the order of states D and E are interchanged, when comparing both methods. CVS-ADC(3,2) again overestimates these states by more than 4 eV, while CVS-ADC(2)-x level provides errors of -0.20 eV and 0.33 eV for the two bright states compared to the experiment, respectively. However, the spacing between the states is almost identical using both CVS-ADC approaches.

At last, the C 1s excitations of the allyl radical are investigated. CVS-UADC(3,2) again overestimates the first three bright core-excited states with values of 1.95 eV, 1.24 eV and 1.37 eV, respectively, while these errors are 0.38 eV, -0.49 eV and -0.60 eV in the case of CVS-UADC(2)-x. In this example, the δ(3-2x) values are not constant, thus the spacing between the states is not described equally by both methods. The energy difference between state B and D is 2.41 eV at the CVS-UADC(2)-x level, while CVS-UADC(3,2) provides a spacing of 2.57 eV. Going to the spacing between the states D and G, values of 2.36 eV and 2.12 eV are obtained, respectively. Comparing with the experiment reveals that CVS-UADC(3,2) indeed provides an improvement compared to CVS-ADC(2)-x, since the experimental spacings of 3.28 eV and 2.23 eV are closer to the third order results.

Eventually, this study confirms that core-excitation energies at the CVS-ADC(3,2) level are strongly overestimated compared to experimental data. However, the results are qualitatively better or at the same level as the ones obtained with the CVS-ADC(2)-x method.

Chapter 8

Computational Timings

This chapter contains an analysis of computational timings of my implementation of the CVS-ADC methods up to third order. General timings of the `libtensor` library and the `adcman` program were investigated before and the results can be found in the literature.[93,182] Here, I concentrate on the influence of the CVS approximation and the size of the core space on computational timings of my implementation. Therefore, the cysteine, (E)-1,2-difluoroethene (FE), and the butatriene molecules were chosen as example systems. Without considering hydrogen atoms, cysteine exhibits seven core orbitals, while FE and butatriene have four, respectively. All molecules were calculated at different CVS-ADC levels by restricting all possible numbers of their core orbitals. Using a core space of four in the case of cysteine, for example, means that the four lowest core orbitals in energy are used as active orbitals in the core space (c). The three remaining core orbitals are treated as general non core occupied orbitals and therefore they are part of the occupied space (o). The computational times as a function of the core space are represented as walltime per iteration (W/I) of the Davidson algorithm, which is used to solve the CVS-ADC eigenvalue problem. To provide a direct comparison between the different CVS-ADC levels, the W/I values are given in % of the largest W/I at each CVS-ADC level individually. In the case of CVS-ADC(2)-s and -x calculations, the largest W/I value is for a core space of seven (cysteine), where for CVS-ADC(3) it is the one for one core orbital.

Geometry optimizations of all systems were performed at the level of RI-MP2[192,193] employing the def2-QZVPP[118] basis set and the respective auxiliary QZVPP[194] basis set using the `TURBOMOLE 6.3.7`[196] program. The core-excited states were calculated with my implementation of CVS-ADC up to third order on a machine with an *AMD Opteron (TM) Processor 6620* with 3GHz, 16 cores and 256 GB RAM, employing the 6-31G* basis set[111,112,225] in the pure 5D/7F version. The calculations of cysteine were performed using 16 CPU cores, while the calculations of FE and butatriene were performed using a single CPU core. In every case, 10 core-excited states were calculated to obtain the W/I values. For a direct comparison, 10 excited states of every system were calculated as well with the general ADC method up to third order using the `adcman` program.[81,93] Finally, note that the content of this chapter has already been published by me and my co-authors in *Journal of Chemical Physics, 142 (2015), 214104.*[98]

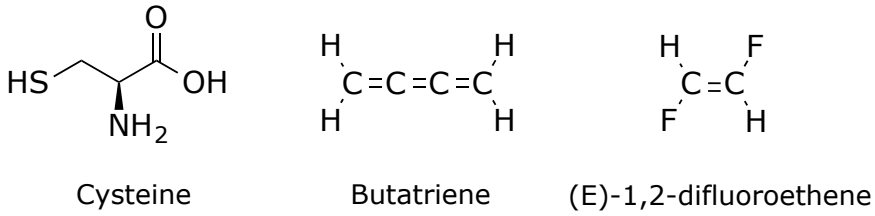

Figure 8.1: Structures of cysteine, butatriene and (E)-1,2-difluoroethene (FE).

8.1 Timings of the CVS-ADC Implementations

The structures of the molecules used in this chapter are summarized in Figure 8.1. The results of the scan of the the computational times as a function of the core space represented as walltime per iteration (W/I) of the Davidson algorithm are given in Table 8.1, while Figure 8.2 illustrates these functions. Furthermore, the functions are linear fitted and the corresponding fit parameters are given in Table 8.1, too. For all investigated cases, the coefficients of determination are between 0.985 and 0.999, which indicates an almost perfect linear correlation between the computational time and the size of the core space. The gradients of both CVS-ADC(2)-s and CVS-ADC(2)-x have a positive sign. Hence, the computational time rises with increasing core space. In contrast, the gradients at the CVS-ADC(3) levels have a negative sign, thus the computational time is larger with a smaller core space.

Relatively, the gradient is larger at the CVS-ADC(2)-x than at the CVS-ADC(2)-s level. In the case of cysteine, for example, the gradients at the extended second order variant is 11.66%, while at the strict second order level it is 6.94%. Since in all examples the absolute values of the gradients at the CVS-ADC(3) level are smaller than the ones of CVS-ADC(2)-s, the influence of the core space on the CVS-ADC(3) timings is relatively the smallest, e.g. -4.34% in the case of cysteine. These trends are valid for all investigated systems. However, the relative change in computational speed depending on the size of the core space is not independent of the chosen system. Let me give an example: in the case of CVS-ADC(2)-x, the gradient is 11.66% for cysteine, 19.52% for FE and 19.54% for butatriene. Since the non-core occupied space influences the computational time as well, the difference of the absolute values of the gradient might be due to the ratio between core and occupied valence orbitals (c/o). These ratios are 0.40 (butatriene), 0.33 (EF) and 0.28 (cysteine), respectively. If one compares the c/o ratios with the trend of the gradient values, a linear correlation cannot be identified. However, a trend can be suggested, i.e. the larger the c/o ratio the larger the absolute value of the gradient. In other words, the acceleration of the computational time depends on the c/o ratio, too. Note that one exception is CVS-ADC(2)-x, where the gradient values of FE and butatriene are almost the same.

The negative trend at the CVS-ADC(3) level can be explained by means of the explicit working equations (see chapter 3.2.1). Compared to CVS-ADC(2)-x, the 2p-2h,2p-2h block is identical, thus the difference can be found in the p-h,p-h and the coupling blocks. The matrix-vector products of both p-h,p-h and coupling blocks at the CVS-ADC(3) level contain many contractions over the o space, which are expensive and time demanding compared to the ones at the CVS-ADC(2)-x level. Regarding the p-h,p-h block, these are the additional 13 third order terms, which are summarized in the intermediates $I^{(3)}_{ab}$, $I^{(3)}_{IJ}$ and $I^{(3)}_{IaJb}$ (see equations 3.11 – 3.14), while the additional second order equations 3.18

Table 8.1: Timings of the CVS-ADC method. Walltime per iteration (W/I) of the Davidson algorithm used to solve the CVS-ADC eigenvalue problem as a function of the space of active core electrons (CS) of cysteine, (E)-1,2-difluoroethene, and butatriene using the CVS-ADC(2)-s, CVS-ADC(2)-x, and CVS-ADC(3,2) methods in combination with the 6-31G* basis set are shown. The functions are linearly fitted with $\mathrm{W/I} = m \cdot CS + b$ and the respective coefficients of determination (R^2) are given, too. The largest W/I values are set to 100% in every case, respectively. This table has already been published by me and my co-authors.[98]

Core space &	CVS-ADC(2)-s		CVS-ADC(2)-x		CVS-ADC(3,2)	
fit parameters	W/I [s]	W/I [%]	W/I [s]	W/I [%]	W/I [s]	W/I [%]
Cysteine						
1	0.33	57.81	1.74	29.19	62.76	100.00
2	0.37	65.72	2.59	43.46	59.69	95.10
3	0.42	73.84	3.41	57.24	56.85	90.59
4	0.45	80.02	4.07	68.34	54.06	86.14
5	0.49	86.96	4.76	79.88	51.39	81.88
6	0.53	93.00	5.32	89.20	48.79	77.74
7	0.57	100.00	5.96	100.00	46.42	73.96
m	0.04	6.94	0.70	11.66	-2.72	-4.34
b	0.29	51.87	1.20	20.11	65.18	103.85
R^2	0.998	0.998	0.995	0.995	0.999	0.999
(E)-1,2-difluoroethene						
1	0.05	59.82	0.57	42.07	15.16	100.00
2	0.07	74.42	0.84	62.70	13.63	89.86
3	0.08	86.60	1.13	84.09	12.16	80.19
4	0.09	100.00	1.35	100.00	10.81	71.31
m	0.01	13.27	0.26	19.52	-1.45	-9.57
b	0.04	47.03	0.32	23.42	16.57	109.28
R^2	0.999	0.999	0.996	0.996	0.999	0.999
Butatriene						
1	0.07	51.93	0.71	41.10	19.27	100.00
2	0.09	69.31	1.15	66.59	16.89	87.63
3	0.12	87.60	1.48	85.33	14.78	76.68
4	0.13	100.00	1.73	100.00	12.83	66.55
m	0.02	16.25	0.34	19.54	-2.15	-11.13
b	0.05	36.58	0.42	24.40	21.30	110.54
R^2	0.994	0.994	0.985	0.985	0.998	0.998

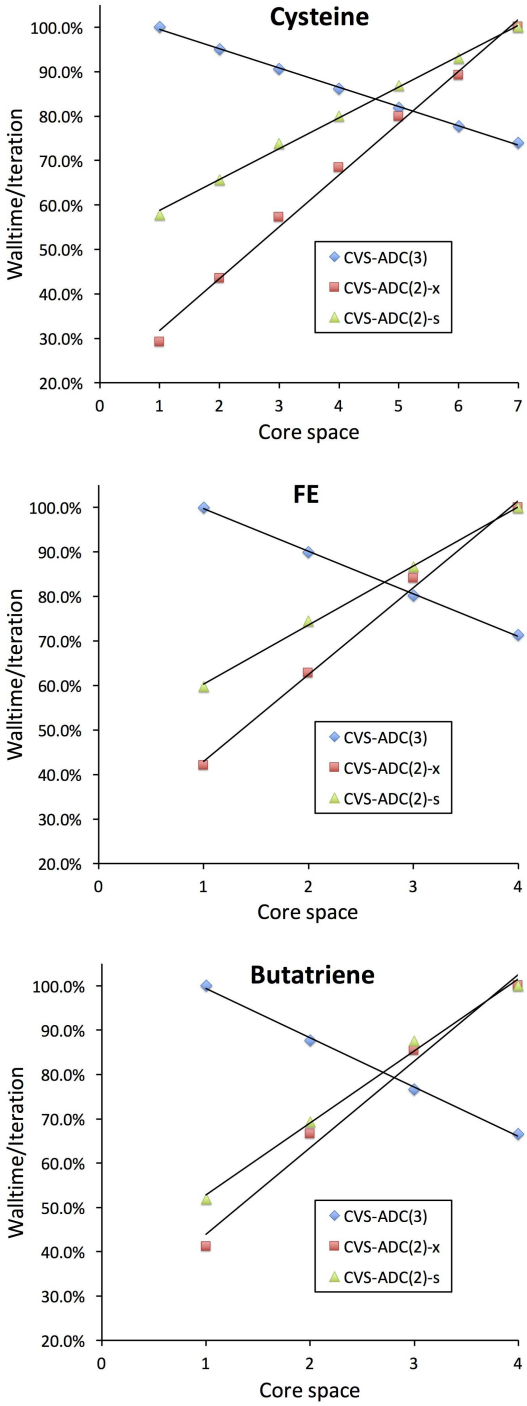

Figure 8.2: Illustration of the relative walltime per iteration (W/I) of the Davidson algorithm used to solve the ADC eigenvalue problem as a function of the space of active core electrons (CS) of cysteine (top), FE (middle) and butatriene (bottom) using the CVS-ADC(2)-s, CVS-ADC(2)-x, and CVS-ADC(3) methods in combination with the 6-31G* basis set. The functions are linearly fitted with $\mathrm{W/I} = m \cdot CS + b$.

and 3.16 are the respective ones of the coupling blocks. As a consequence, the reduction of the o space, which is accompanied by an increase of the c space, leads to computational speed-up.

Finally, let me discuss absolute values and give a comparison to general ADC calculations. Since the ADC method is implemented in a similar way as the CVS-ADC approach in `adcman`, a direct comparison is possible. The absolute W/I values in seconds are discussed instead of the relative ones, because a general ADC calculations does not differ between c and o spaces. In the case of cysteine with a full core space of seven, one iteration at the CVS-ADC(3) level takes 46.42 s, while CVS-ADC(2)-x calculations are eight times faster with 5.96 s and the strict variant needs only 0.57 s for one iteration, which is ten times faster than at the CVS-ADC(2)-x level. For the FE molecule (core space of four), these values are more drastic. Here, CVS-ADC(2)-s provides a value of 0.09 s, while the extended variant needs 15 times longer (1.35 s) for one iteration. With 10.81 s, CVS-ADC(3) takes 8 times longer than the CVS-ADC(2)-x calculation. Compared to the full ADC approach without the CVS approximation, the speed-up is also large. Besides the restriction of the excitation space to correspond to core orbitals, many two-electron integrals are neglected within the CVS approximation, which leads to a significant reduction of the terms in the CVS-ADC working equations as shown in chapter 2.5.7. This reduction leads to computational savings of the Davidson diagonalization scheme. In the case of cysteine, the calculation of 10 valence-excited states using the ADC(2)-x method takes 22.97 s, which is about 3.85 times longer than at the CVS-ADC(2)-x level (seven core orbitals). The CVS-ADC(2)-s calculation with a core space of seven is 3.12 times faster than the respective ADC(2)-s calculation, while it is a factor of 2.37 for the CVS-ADC(3) calculation. In the case of the FE example, the W/I values for ADC(2)-s, ADC(2)-x and ADC(3) are 0.10 s, 5.55 s and 26.10 s, respectively, thus the corresponding CVS calculations with four core orbitals are faster by factors of 1.11, 4.11 and 2.41.

Chapter 9

Application of CVS-ADC Calculations in the Field of Organic Electronics

In this chapter, I present some applications of CVS-ADC calculations in the field of organic electronics. Organic solar cells[197,199] or organic field-effect transistors (OFETs), for example, use organic semiconductors as the active layer, which exhibit a conjugated π-electron system that provides a delocalization of the electronic wave functions in the HOMO/LUMO region.[226,227]

The first study is about pentacene and its derivatives, which are often used in OFETs as hole conductors (p-type). These materials exhibit large charge carrier mobility due to a favorable crystal structure that provides excellent overlap of the frontier molecular orbitals.[228–231] A deeper insight into the charge carrier properties of pentacene systems could be provided by XA spectra of their cations. However, it is very challenging to measure experimental spectra of ionized species. Hence, QC calculations can be performed to predict such spectra and provide the required information. The results of the benchmarks in chapter 4 as well as the successful simulations in chapter 6.3 justify the prediction of XA spectra of not yet measured species with the CVS-UADC(2)-x approach in combination with the 6-311++G** basis set. Since pentacene is a large system and due to technical limitations, anthracene was chosen as a small relative of pentacene. With restricted CVS-ADC(2)-x calculations, the XA spectrum of neutral closed-shell anthracene was calculated and is discussed compared to experimental data. Next, the XA spectrum of the anthracene cation radical (A^+), for which no experimental data is available yet, is predicted based on CVS-UADC(2)-x calculations and compared to the calculated spectrum of the neutral closed-shell species. This analysis is performed for two limiting cases: one using the neutral ground state geometry denoted as A_N^+ and the other one using the equilibrium ground state structure of the anthracene cation (A_C^+). The latter case is chosen to allow for geometry relaxation. The A_N^+ system is suitable for experiments with very short-lived cationic intermediates, while the A_C^+ form requires stable cations.

The second investigation presented in this chapter is about trends of core-excited state properties along potential energy surfaces (PES). For this purpose, ANQ as a model system for an electron acceptor, 2,2'-bithiophene (BT) for an electron donor and phenol as a typical precursor in polymer synthesis were chosen. In the case of BT, the torsion around the central dihedral angle, which connects the two thiophene rings, is analyzed,

while the PES along the distances of the C–O bonds are evaluated in the case of ANQ and phenol. In these calculations, the chosen reaction coordinate was constrained, while all other coordinates were allowed to relax freely.

The ground state geometry optimization of the anthracene cation was performed at the UMP2 level employing the def2-TZVPP[118] basis set combined with the resolution-of-the-identity (RI)[192,193] approximation and the respective auxiliary TZVPP[194] basis set. The geometry of neutral anthracene was optimized using RI-MP2 in combination with the def2-TZVPP basis set and the respective auxiliary TZVPP basis set. Ground state structures of ANQ, phenol and BT were optimized at the MP2 level employing the 6-311++G**[109,110,113] basis set. Geometry optimizations at the RI-MP2 and RI-UMP2 levels were performed using the `TURBOMOLE 6.3.7`[196] program, while the MP2 optimizations for the PES scans were performed with the `Q-Chem 4.2`[94] program. Core-excited states and the corresponding properties were calculated with my implementation of restricted and unrestricted CVS-ADC(2)-x as well as the CVS-ISR implementation as described in chapter 3. Exciton sizes and state densities were calculated using the `libwfa` library.[84,86–88] To save computational time, molecular point group symmetry was exploited in the calculations of anthracene (D_{2h}), ANQ (C_{2v}) and BT (C_2). The anthracene cation was also optimized exploiting D_{2h} point group symmetry, which is justified in the literature.[232–234] All core-excited states in this chapter were computed employing the 6-311++G** basis set in its Cartesian 6D/10F version. As usual, all computed values shown in this chapter are absolute without consideration of relativistic effects. Note that the larger the number of constituting atoms of a molecule the higher is the density of core-excited states within a small energy region. Hence, only spectroscopically bright, relevant core-excited states are given in the case of the anthracene study to keep a clear view. These are states belonging to the irreducible representations B_{1u}, B_{2u} and B_{3u}, which are the only ones being optically allowed and thus possess oscillator strength. State characterizations of the anthracene systems are determined via MO configurations, because these investigations were performed before the CVS-ISR approach was available. As explained in chapter 6, only the most dominant MO configurations with a contribution larger than 6.25% are shown and only pictures of relevant MOs are presented to keep a clear view. Furthermore, note that the PES of ANQ, BT and phenol were optimized in the MP2 ground state and no core-excited state geometry optimizations were performed, because CVS-ADC gradients are not available yet. Finally, note that the content of this chapter has already been published by me and my co-authors. The investigation of the anthracene cation is published in *Journal of Chemical Theory and Computation, 10 (2014), pages 4583-4598*, while the PES scans of ANQ, BT and phenol have been submitted for publication in *Journal of Chemical Theory and Computation, (2016).*[97,99]

Table 9.1: Core-excitation energies (ω_{ex}), oscillator strengths (f_{osc}), character and amount of double amplitudes (R2) of the first ten C 1s excited singlet states of anthracene with B_{1u}, B_{2u} and B_{3u} symmetry, calculated using CVS-ADC(2)-x and the 6-311++G** basis set. The calculated values are compared with experimental data.[236] Only the main transitions are shown and the numbering of the carbon atoms complies with Figure 9.2a and refers to linear combinations of the respective carbon 1s orbitals. This table has already been published by me and my co-authors.[97]

State	ω_{ex} [eV]	f_{osc}	Main transition	R2 [%]	ω_{ex} [eV] (Expt.)
$1\ ^1B_{1u}$	284.63	0.058	C2 $\rightarrow \pi_4^*$	26	
$2\ ^1B_{1u}$	284.76	0.139	C3 $\rightarrow \pi_4^*, \pi_{14}^*$	25	284.5 (A)
$3\ ^1B_{1u}$	284.93	0.092	C3 $\rightarrow \pi_4^*, \pi_{14}^*$	26	
$4\ ^1B_{1u}$	285.34	0.029	C1 $\rightarrow \pi_4^*$	27	
$5\ ^1B_{1u}$	286.21	0.125	C1 $\rightarrow \pi_{10}^*$	24	285.9 (B)
$6\ ^1B_{1u}$	286.57	0.048	C3 $\rightarrow \pi_{10}^*$	27	
$7\ ^1B_{1u}$	286.79	0.003	C3 $\rightarrow \pi_{10}^*$	29	
$1\ ^1B_{2u}$	286.91	0.000	C3 $\rightarrow \pi_1^*, \pi_2^*$	26	
$1\ ^1B_{3u}$	286.93	0.011	C3 $\rightarrow \pi_1^*, \pi_2^*$	26	
$2\ ^1B_{2u}$	286.97	0.024	C3 $\rightarrow \pi_1^*, \pi_2^*, \pi_3^*$	26	

9.1 Prediction of the X-ray Absorption Spectrum of the Anthracene Cation

The first topic of this chapter is the prediction of the XA spectrum of the anthracene cation. Overall, I discuss three different kinds of spectra and structures: neutral anthracene, the anthracene cation using the geometry of the neutral structure and the anthracene cation in the optimized cationic structure. Since this study was performed before the CVS-ISR method and the wave function analysis tool were available, state characterizations are based on MO transitions. The relevant virtual orbitals are illustrated in Figure 9.1. Furthermore, the optimized geometrical parameters of both neutral and cationic structures are given in Figure 9.2b. Note that only the energetically lowest states are discussed in this thesis and the Rydberg states beyond 290 eV are neglected.

9.1.1 Simulation of the Carbon K-edge Spectrum of Neutral Anthracene

Let me begin with a brief analysis of the carbon K-edge XA spectrum of the neutral closed-shell anthracene molecule in gas phase. To judge the quality of the optimized ground state structure at the RI-MP2 level, the calculated geometry parameters are compared to experimental crystal structure data.[235] The optimized structure at the RI-MP2 level of theory reproduces the crystal structure data very well with deviations not exceeding 0.005 Å.

Using this calculated neutral structure of anthracene, the ten lowest core-excited states with B_{1u}, B_{2u} and B_{3u} symmetry were calculated using CVS-ADC(2)-x and the results are summarized in Table 9.1. The experimental spectrum of anthracene in the gas phase

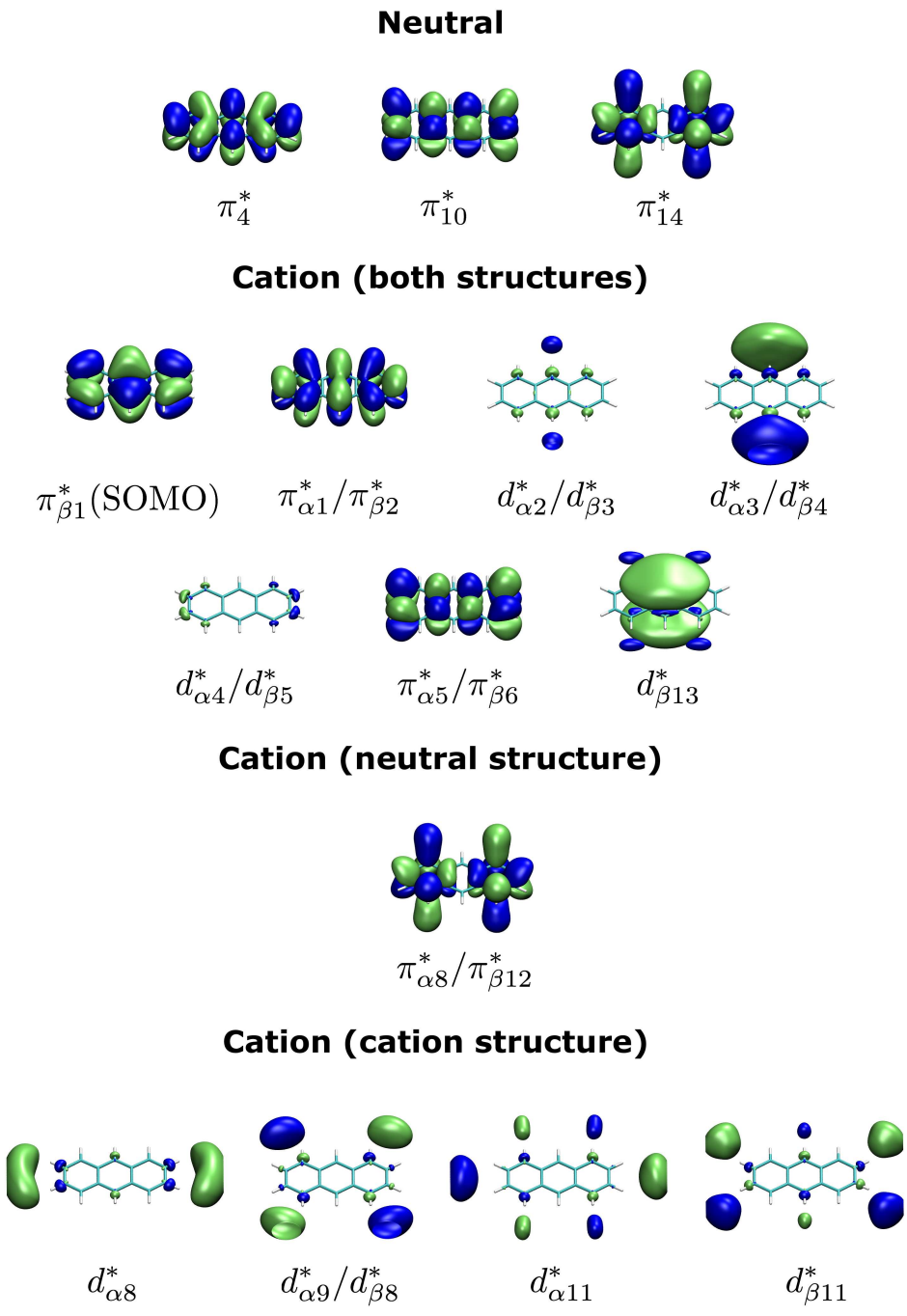

Figure 9.1: Plots of the relevant virtual MOs of neutral anthracene and the anthracene cation in both optimized neutral and cationic structure at the level of (U)HF in combination with the 6-311++G** basis set. The isosurfaces of the MOs are rendered with an isovalue of 0.02. Since character and shape of specific orbitals of the cation variants are identical, they are merged under "Cation (both structures)". Relevant orbitals that differ between the respective structures are given separately.

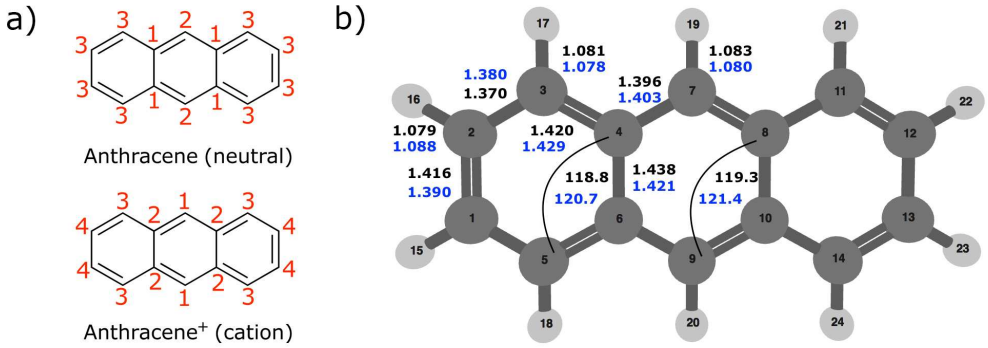

Figure 9.2: a) Structures of anthracene. For a better overview, the numbering of the atoms in the case of anthracene are grouped, because the electron donor orbitals that characterize the transitions are linear combinations of 1s orbitals. Each group consists of similar atoms whose 1s orbitals are linearly combined into the electron donor orbitals ordered by their energy. Due to structural differences, the numbering of the atoms of the neutral and cation species differs as well. b) Comparison of the calculated structures of anthracene (values in black) and its cation radical (values in blue) at the level of RI-(U)MP2 employing the def2-TZVPP basis set and exploiting D_{2h} point group symmetry. Bond distances are in [Å] and bond angles are in [°].

exhibits two significantly strong peaks located at 284.5 eV (A) and 285.9 eV (B). Both signals are excellently reproduced by CVS-ADC(2)-x in combination with the 6-311++G** basis set with errors of only 0.09% (0.26 eV) and 0.1% (0.31 eV), respectively. Hence, the energy spacing between the two peaks, which is experimentally 1.40 eV, is almost perfectly described with a calculated value of 1.45 eV. Peak A can be characterized as a mixture of the first three calculated excited states with B_{1u} symmetry, where the second $^1B_{1u}$ state exhibits the largest oscillator strength, thus the maximum of the peak exhibits a core-excitation energy of 284.76 eV. The 2 $^1B_{1u}$ state is dominated by transitions from the C3 1s orbital group to the π_4^* and π_{14}^* virtual molecular orbitals. Peak B is represented by a mixture of the 5 $^1B_{1u}$ and 6 $^1B_{1u}$ states, of which 5 $^1B_{1u}$ exhibits the largest oscillator strength of 0.125. In the MO transition picture, this state is dominated by electron promotions from the C1 group to the π_{10}^* orbital. All core-excited states exhibit a large R2 value with more than 25%, which indicates strong orbital relaxation effects. To visualize the calculated spectrum and to provide a direct comparison to the experiment, Figure 9.3 illustrates plots of the calculated and experimental spectra, thereby clarifying the excellent accuracy at the CVS-ADC(2)-x level.

9.1.2 Prediction of the Carbon K-edge Spectrum of the Anthracene Cation

With the knowledge of the excellent accuracy of the CVS-ADC(2)-x/6-311++G** approach in the description of the C 1s XA spectrum of neutral anthracene, the prediction of the C 1s XA spectrum of the anthracene cation radical (A^+) is justified. As mentioned above, I investigated two limiting cases, one using the neutral ground state geometry denoted as A_N^+ and the other one using the equilibrium ground state structure of the anthracene cation (A_C^+). In Figure 9.2b the structural parameters of the optimized cation structure at the level of RI-UMP2 are given and compared with the ones of the neutral

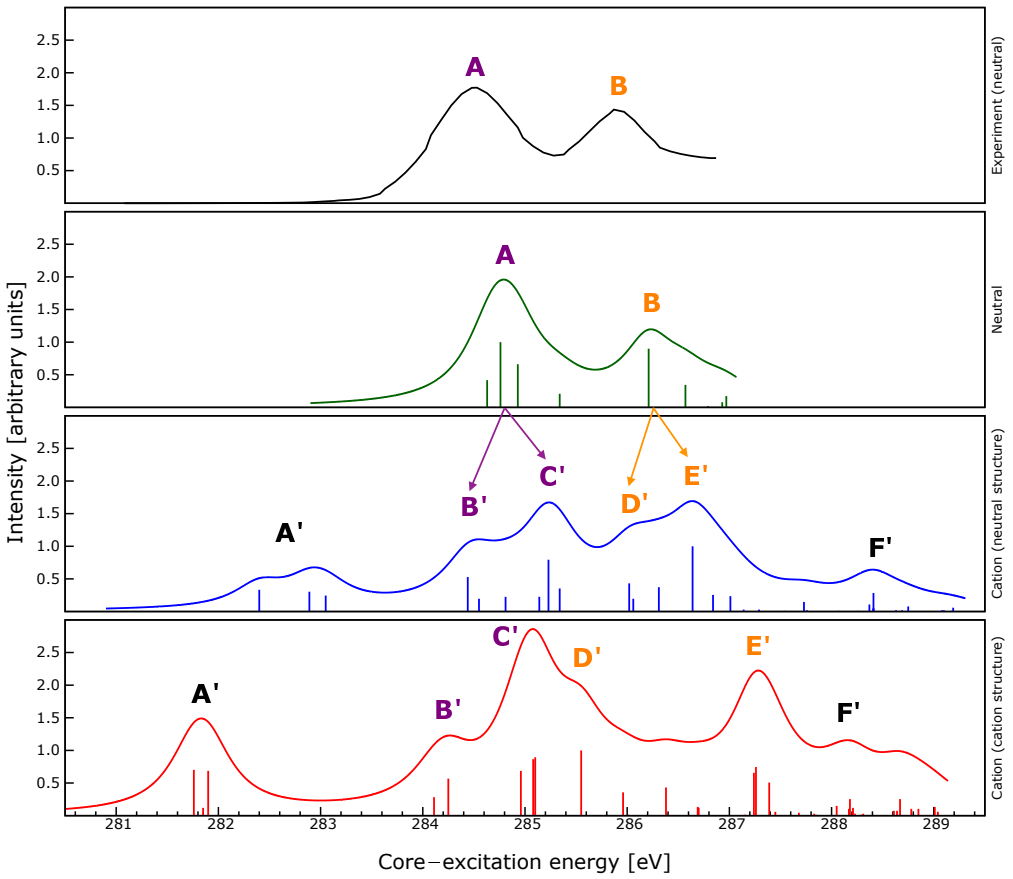

Figure 9.3: Plots of XA spectra of neutral and cationic anthracene as obtained at the CVS-(U)ADC(2)-x/6-311++G** level of theory. For comparison, the experimental spectrum of neutral anthracene is shown, too.[236,237] The theoretical spectra are simulated using a Lorentzian broadening of 0.6 eV full width at half maximum. All calculated core-excitation energies are absolute without a level shift. From top to bottom: experimental spectrum of neutral anthracene in gas phase (black), neutral anthracene using the optimized neutral structure (dark green), anthracene cation using the optimized neutral structure (blue), anthracene cation using the optimized cationic structure (red). To highlight relationships, peaks corresponding to A are marked in purple, while peaks related to B are colored in orange.

species. The following numbering of the carbon atoms also complies with Figure 9.2b, while for the subsequent discussion about state characters the numbering of Figure 9.2a is used. Compared to the experimental[234] determination of the structural parameters of the anthracene cation, the RI-UMP2 approach provides accurate geometry parameters compared to experiment with mean deviations of only 0.009 Å. The dominant differences to the neutral structure are bond-length alternations (BLA) due to the half occupied π-orbital of A^+. The bond length between the C1 and C2 atoms as well as the distance between the C4 and C6 atoms are slightly shortened, while the other bonds are elongated a little. The C-H bond lengths are almost identical (-0.003 Å) in both structures. However, one exception is the distance between C2 and H16, which is in the case of the cation structure elongated by 0.009 Å.

Before I discuss the calculated XA spectra, let me give some further information on the different structures. At first, note that the ground state of both structural conformers belong to different irreducible representations of D_{2h}: $^2B_{2g}$ for A_C^+ and $^2B_{3g}$ for A_N^+, respectively. Furthermore, both ground state reference wave functions of the A_N^+ and A_C^+ systems exhibit little spin contamination with $\langle \hat{S}^2 \rangle$ values of 0.90 and 1.13, respectively. According to *Starcke et al.*, spin contamination below 1.25 provides still reasonable results at the level of UADC(2)-x for doublet valence excited-states, thus both anthracene cation conformers can be treated at the CVS-UADC(2)-x level.[82] Since an unrestricted ground state determinant is employed in the case of the cation structure, the linear combinations of the C 1s orbitals due to point group symmetry differ between the neutral anthracene system and its cationic form, independent of which structure is chosen (see Figure 9.2a). The neutral anthracene molecule has only three groups of linear combinations between the C 1s orbitals, while both A_C^+ and A_N^+ exhibit four groups, respectively. The numbering of the groups of orbitals is ordered according to the respective orbital energies. Turning to the relevant molecular (spin) orbitals (see Figure 9.1), their shapes of both A_C^+ and A_N^+ systems are almost identical. However, there are energetic shifts for higher lying orbitals, which are also necessary to characterize the relevant bright core-excited states. These orbitals are listed separately in Figure 9.1. Furthermore, the structural differences due to the BLA are responsible for different orbital energies between the ones of A_N^+ and A_C^+. The orbital energy of the singly occupied molecular orbital (SOMO, $\pi^*_{\beta 1}$), for example, is -0.217 a.u. regarding the A_C^+ system, while in A_N^+ it has a higher energy of -0.191 a.u. However, the shape of the SOMO is identical in both structural conformers. Note that extremely diffuse virtual spin orbitals occur in the low-energy regime, e.g. $d^*_{\alpha 2}$, which correspond to weakly bound, additional electrons at the UHF level due to the polarized and diffuse basis functions of the 6-311++G** basis set.

Let me turn to the calculation of the XA spectra of the anthracene cation. Tables 9.2 and 9.3 summarize the results of A_C^+ and A_N^+ obtained at the CVS-UADC(2)-x level, respectively. Furthermore, Figure 9.3 illustrates the plots of the calculated spectra. In general, the R2 values of the core-excited states of both A_C^+ and A_N^+ are at the same level as for neutral anthracene with values between 20% and 31%. This is opposite to the results of the small organic radicals in chapter 6.3, where small R2 values are observed. The peaks of both calculated cation spectra are denoted with a prime symbol ('). Since the peaks of the neutral and cationic systems are related to each other based on state characterization, I discuss the spectra peak by peak.

Let me start with the analysis of the first bright peak, which is assigned as A'. In the case of the A_N^+ conformer, A' is a mixture of the first four core-excited states with B_{1u} symmetry and can be characterized by transitions from the C1, C2, C3 and C4 groups to the SOMO. In other words, all carbon 1s orbitals contribute to this peak. Therefore, this peak is broad, ranging from about 282 eV to 283.5 eV and exhibiting a sub-peak

Table 9.2: Core-excitation energies (ω_{ex}), oscillator strengths (f_{osc}), character and amount of double amplitudes (R2) of the first 30 C 1s excited states of the anthracene cation (optimized cation structure) with B_{1u}, B_{2u} and B_{3u} symmetry calculated using CVS-UADC(2)-x and the 6-311++G** basis set. Only the main transitions are shown and the numbering of the carbon atoms complies with Figure 9.2a and refers to linear combinations of the respective carbon 1s orbitals. The assignment complies with Figure 9.3. This table has already been published by me and my co-authors.[97]

State	Symmetry	ω_{ex} [eV]	f_{osc}	Main transition	R2 [%]	Assignment
1 B_{3u}	B_{1u}	281.76	0.047	C2 $\rightarrow \pi^*_{\beta 1}$, $\pi^*_{\beta 2}$	23	
2 B_{3u}	B_{1u}	281.85	0.008	C4 $\rightarrow \pi^*_{\beta 1}$; C1 $\rightarrow \pi^*_{\beta 1}$	28	A'
3 B_{3u}	B_{1u}	281.90	0.046	C1 $\rightarrow \pi^*_{\beta 1}$; C4 $\rightarrow \pi^*_{\beta 1}$	23	
4 B_{3u}	B_{1u}	284.11	0.019	C3 $\rightarrow d^*_{\alpha 2}$	20	B'
5 B_{3u}	B_{1u}	284.25	0.038	C4 $\rightarrow d^*_{\alpha 2}$, $d^*_{\alpha 9}$	20	
6 B_{3u}	B_{1u}	284.96	0.046	C3 $\rightarrow \pi^*_{\beta 2}$	27	
7 B_{3u}	B_{1u}	285.08	0.058	C4 $\rightarrow \pi^*_{\beta 2}$, $d^*_{\beta 11}$	26	C'
8 B_{3u}	B_{1u}	285.10	0.060	C2 $\rightarrow d^*_{\alpha 2}$,$d^*_{\alpha 9}$; C3 $\rightarrow \pi^*_{\alpha 1}$	26	
9 B_{3u}	B_{1u}	285.55	0.067	C2 $\rightarrow \pi^*_{\beta 2}$, $d^*_{\beta 11}$, $d^*_{\alpha 2}$, $\pi^*_{\beta 1}$	28	D'
10 B_{3u}	B_{1u}	285.96	0.024	C2 $\rightarrow \pi^*_{\alpha 1}$; C1 $\rightarrow d^*_{\alpha 2}$	24	
11 B_{3u}	B_{1u}	286.01	0.001	C4 $\rightarrow \pi^*_{\alpha 1}$	28	
12 B_{3u}	B_{1u}	286.38	0.029	C1 $\rightarrow \pi^*_{\beta 2}$, $d^*_{\alpha 2}$	29	
13 B_{3u}	B_{1u}	286.69	0.009	C3 $\rightarrow \pi^*_{\alpha 1}$; C2 $\rightarrow d^*_{\alpha 2}$	29	
14 B_{3u}	B_{1u}	286.70	0.008	C1 $\rightarrow d^*_{\alpha 2}$,$\pi^*_{\beta 2}$; C2 $\rightarrow \pi^*_{\alpha 1}$	29	
15 B_{3u}	B_{1u}	287.15	0.001	C4 $\rightarrow d^*_{\alpha 2}$, $d^*_{\alpha 8}$, $d^*_{\alpha 9}$	28	
16 B_{3u}	B_{1u}	287.24	0.044	C4 $\rightarrow \pi^*_{\beta 2}$, $d^*_{\beta 8}$, $d^*_{\alpha 11}$	28	
17 B_{3u}	B_{1u}	287.26	0.050	C2 $\rightarrow d^*_{\beta 13}$,$\pi^*_{\alpha 1}$; C1 $\rightarrow d^*_{\beta 11}$	26	E'
18 B_{3u}	B_{1u}	287.39	0.034	C3 $\rightarrow d^*_{\beta 13}$,$\pi^*_{\beta 40}$; C2 $\rightarrow \pi^*_{\beta 2}$	27	
19 B_{3u}	B_{1u}	287.45	0.004	C3 $\rightarrow d^*_{\alpha 8}$, $d^*_{\alpha 2}$, $\pi^*_{\alpha 17}$	28	
20 B_{3u}	B_{1u}	287.60	0.000	C4 $\rightarrow d^*_{\beta 13}$, $\pi^*_{\beta 2}$, $\pi^*_{\beta 40}$	30	
21 B_{3u}	B_{1u}	287.68	0.003	C3 $\rightarrow d^*_{\beta 8}$, $\pi^*_{\beta 2}$, $\pi^*_{\beta 16}$	30	
1 B_{1u}	B_{3u}	287.83	0.000	C4 $\rightarrow d^*_{\alpha 3}$, $\pi^*_{\alpha 5}$, $d^*_{\alpha 4}$	25	
1 A_u	B_{2u}	287.83	0.002	C4 $\rightarrow d^*_{\alpha 3}$, $\pi^*_{\alpha 5}$, $d^*_{\alpha 4}$	25	
2 A_u	B_{2u}	287.85	0.001	C3 $\rightarrow d^*_{\alpha 3}$, $d^*_{\alpha 4}$	25	
22 B_{3u}	B_{1u}	288.01	0.000	C2 $\rightarrow d^*_{\beta 11}$, $d^*_{\beta 8}$, $\pi^*_{\beta 2}$,$\pi^*_{\beta 16}$	31	
23 B_{3u}	B_{1u}	288.05	0.010	C1 $\rightarrow d^*_{\alpha 9}$,$d^*_{\alpha 8}$; C2 $\rightarrow \pi^*_{\alpha 1}$	29	
24 B_{3u}	B_{1u}	288.17	0.007	C2 $\rightarrow d^*_{\beta 13}$; C1 $\rightarrow d^*_{\beta 11}$,$d^*_{\beta 8}$	28	F'
3 A_u	B_{2u}	288.18	0.017	C4 $\rightarrow d^*_{\beta 3}$, $d^*_{\beta 5}$, $d^*_{\beta 4}$, $d^*_{\alpha 3}$	26	
2 B_{1u}	B_{3u}	288.18	0.000	C4 $\rightarrow d^*_{\beta 3}$, $d^*_{\beta 5}$, $d^*_{\beta 4}$, $d^*_{\alpha 3}$	26	
4 A_u	B_{2u}	288.21	0.008	C3 $\rightarrow d^*_{\beta 3}$, $d^*_{\beta 5}$, $d^*_{\alpha 3}$	26	

Table 9.3: Core-excitation energies (ω_{ex}), oscillator strengths (f_{osc}), character and amount of double amplitudes (R2) of the first 35 C 1s excited states of the anthracene cation (optimized neutral structure) with B_{1u}, B_{2u} and B_{3u} symmetry calculated using CVS-UADC(2)-x and the 6-311++G** basis set. Only the main transitions are shown and the numbering of the carbon atoms complies with Figure 9.2a and refers to linear combinations of the respective carbon 1s orbitals. The assignment complies with Figure 9.3. This table has already been published by me and my co-authors.[97]

State	Symmetry	ω_{ex} [eV]	f_{osc}	Main transition	R2 [%]	Assignment
1 B_{2u}	B_{1u}	282.40	0.034	C1 $\rightarrow \pi^*_{\beta1}$, $\pi^*_{\beta2}$	20	
2 B_{2u}	B_{1u}	282.89	0.031	C3 $\rightarrow \pi^*_{\beta1}$	24	A'
3 B_{2u}	B_{1u}	282.94	0.001	C2 $\rightarrow \pi^*_{\beta1}$	27	
4 B_{2u}	B_{1u}	283.05	0.025	C4 $\rightarrow \pi^*_{\beta1}$, $\pi^*_{\beta6}$	26	
5 B_{2u}	B_{1u}	284.44	0.054	C4 $\rightarrow \pi^*_{\alpha1}$, $\pi^*_{\alpha8}$	24	B'
6 B_{2u}	B_{1u}	284.55	0.020	C3 $\rightarrow \pi^*_{\alpha1}$, $\pi^*_{\alpha8}$	25	
7 B_{2u}	B_{1u}	284.81	0.023	C2 $\rightarrow \pi^*_{\alpha1}$	25	
8 B_{2u}	B_{1u}	285.14	0.023	C1 $\rightarrow \pi^*_{\alpha1}$	26	
9 B_{2u}	B_{1u}	285.23	0.081	C3 $\rightarrow \pi^*_{\beta2}$, $\pi^*_{\beta12}$	26	C'
10 B_{2u}	B_{1u}	285.34	0.036	C4 $\rightarrow \pi^*_{\beta2}$, $\pi^*_{\beta12}$	26	
11 B_{2u}	B_{1u}	285.73	0.000	C2 $\rightarrow \pi^*_{\beta2}$, $\pi^*_{\alpha5}$, $\pi^*_{\beta6}$, $\pi^*_{\alpha1}$	24	
12 B_{2u}	B_{1u}	286.02	0.044	C1 $\rightarrow \pi^*_{\beta2}$, $\pi^*_{\beta1}$	28	D'
13 B_{2u}	B_{1u}	286.06	0.020	C2 $\rightarrow \pi^*_{\beta2}$, $\pi^*_{\alpha5}$	27	
14 B_{2u}	B_{1u}	286.31	0.038	C4 $\rightarrow \pi^*_{\alpha5}$, $\pi^*_{\alpha1}$, $\pi^*_{\alpha20}$	28	
15 B_{2u}	B_{1u}	286.64	0.102	C2 $\rightarrow \pi^*_{\beta6}$, $\pi^*_{\beta12}$, $\pi^*_{\alpha5}$	25	E'
16 B_{2u}	B_{1u}	286.84	0.026	C3 $\rightarrow \pi^*_{\alpha8}$, $\pi^*_{\alpha9}$, $\pi^*_{\alpha1}$, $\pi^*_{\alpha5}$	29	
17 B_{2u}	B_{1u}	287.01	0.024	C4 $\rightarrow \pi^*_{\beta6}$, $\pi^*_{\beta2}$	29	
18 B_{2u}	B_{1u}	287.14	0.003	C3 $\rightarrow \pi^*_{\alpha5}$	29	
19 B_{2u}	B_{1u}	287.17	0.001	C2 $\rightarrow \pi^*_{\alpha8}$, $\pi^*_{\alpha5}$, $\pi^*_{\alpha9}$	28	
20 B_{2u}	B_{1u}	287.29	0.003	C3 $\rightarrow \pi^*_{\beta6}$	29	
21 B_{2u}	B_{1u}	287.54	0.001	C4 $\rightarrow \pi^*_{\alpha8}$, $\pi^*_{\alpha9}$, $\pi^*_{\alpha1}$	30	
22 B_{2u}	B_{1u}	287.73	0.015	C2 $\rightarrow \pi^*_{\beta12}$,$\pi^*_{\beta6}$,$\pi^*_{\beta9}$; C3 $\rightarrow \pi^*_{\beta2}$	28	
23 B_{2u}	B_{1u}	287.76	0.002	C2 $\rightarrow \pi^*_{\beta12}$,$\pi^*_{\beta6}$,$\pi^*_{\beta9}$; C3 $\rightarrow \pi^*_{\beta2}$	29	
1 B_{1u}	B_{2u}	288.07	0.001	C3 $\rightarrow d^*_{\beta3}$	25	
1 A_u	B_{3u}	288.07	0.000	C3 $\rightarrow d^*_{\beta3}$, $d^*_{\beta4}$	25	
2 B_{1u}	B_{2u}	288.10	0.000	C4 $\rightarrow d^*_{\alpha4}$, $d^*_{\beta5}$	25	
2 A_u	B_{3u}	288.12	0.000	C4 $\rightarrow d^*_{\alpha4}$, $d^*_{\alpha2}$, $d^*_{\beta5}$	25	
24 B_{2u}	B_{1u}	288.26	0.001	C4 $\rightarrow \pi^*_{\beta12}$, $\pi^*_{\beta9}$, $\pi^*_{\beta2}$	31	
3 B_{1u}	B_{2u}	288.34	0.000	C4 $\rightarrow d^*_{\beta3}$, $d^*_{\alpha2}$, $d^*_{\beta5}$, $d^*_{\alpha4}$	26	
3 A_u	B_{3u}	288.37	0.011	C4 $\rightarrow d^*_{\beta3}$, $d^*_{\alpha2}$, $d^*_{\beta5}$, $d^*_{\alpha4}$	26	
4 B_{1u}	B_{2u}	288.41	0.029	C3 $\rightarrow d^*_{\alpha2}$, $d^*_{\beta3}$, $d^*_{\alpha3}$	26	F'
4 A_u	B_{3u}	288.41	0.005	C3 $\rightarrow d^*_{\alpha2}$, $d^*_{\beta3}$, $d^*_{\alpha3}$	26	
25 B_{2u}	B_{1u}	288.63	0.002	C1 $\rightarrow \pi^*_{\alpha9}$, $\pi^*_{\alpha15}$	32	
5 B_{1u}	B_{2u}	288.65	0.000	C2 $\rightarrow d^*_{\alpha3}$, $\pi^*_{\alpha13}$	26	
5 A_u	B_{3u}	288.68	0.000	C2 $\rightarrow d^*_{\alpha3}$, $\pi^*_{\alpha13}$	26	

structure, leading to a shoulder with a core-excitation energy of 283.05 eV. In contrast, peak A' of the A_C^+ conformer is a mixture of the first three core-excited states with B_{1u} symmetry. The transitions are also characterized by electron promotions into the SOMO, but not from the C3 group. Furthermore, A' of A_C^+ is less broad than the one of A_N^+, exhibiting a sharp maximum around 281.85 eV. Compared to the neutral species, the core-excitation energy of A' is with 281.8 eV about 3 eV below peak A. Due to the higher energy of the SOMO and the BLA, A' of A_N^+ is shifted by about 1.1 eV to 282.9 eV compared to A_C^+. Both cation conformers have in common that, due to the energetically low-lying SOMO, peak A' is well separated from the next higher core-excited states. Since the SOMO is filled in the neutral anthracene species, A' is a characteristic attribute of the cation spectrum and therefore denoted as a SOMO-peak. Considering future experiments, a very broad absorption between 281 eV and 283 eV can be expected, because A_N^+ and A_C^+ are limiting cases.

Going to the next higher peaks B' and C', the results obtained with both conformers are similar. Generally, B' can be regarded as a shoulder of the stronger peak C' consisting of a mixture of the two next higher core-excited states, while C' is a mixture of three core-excited states. The core-excitation energies of B' with values of 284.25 eV and 284.44 eV for A_C^+ and A_N^+ are also very similar. The same applies for peak C' with core-excitation energies of about 285.1 eV and 285.23 eV, respectively. However, the characters of the transition differ between both conformers. Peak B' of A_C^+ can be mainly described by an electron promotion from the C3 and C4 groups to the diffuse $d^*_{\alpha 9}$ and $d^*_{\alpha 2}$ orbitals, while B' of A_N^+ is characterized by transitions from C3 and C4 to the $\pi^*_{\alpha 1}$ and $\pi^*_{\alpha 8}$ orbitals. The characters of the states contributing to C' of A_N^+ are the same as the ones of B', but with the corresponding β-spin-orbitals characterizing the transitions. Regarding the strong peak C' of the A_C^+ structure, the dominant contributions are characterized by electron promotions from the C2 – C4 orbital groups to the $\pi^*_{\beta 2}$-orbital, which is comparable to the one of A_N^+. However, transitions to diffuse orbitals like $d^*_{\beta 11}$, $d^*_{\alpha 2}$ and $d^*_{\alpha 9}$ have also a significant contribution. In the case of A_N^+, the virtual orbitals that characterize peaks B' and C' are not diffuse and have the same shape as π^*_4 and π^*_{14} of the neutral species (see Figure 9.1). Hence, B' and C' of A_N^+ correspond exactly to peak A of the neutral species, while this is only the case for peak C' of the A_C^+ conformer. Furthermore, peak C' of A_C^+ exhibits a larger intensity than C' of A_N^+, because states 7 B_{3u} and 8 B_{3u} contributing to the C' peak are almost degenerate. Compared to peak A of the neutral species, the core-excitation energy of C' is blue shifted by about 0.5 eV. Regarding both cation conformers, the absorption of B' and C' together is much broader than the related one of neutral anthracene (only A).

Let me turn to the next higher peaks D' and E'. Here, the differences between A_N^+ and A_C^+ are more significant. Analyzing the results of the the A_N^+ system shows that the core-excited states that contribute to these peaks are characterized by transitions from the C1/C2 groups to the $\pi^*_{\beta 2}$, $\pi^*_{\beta 1}$ and $\pi^*_{\alpha 5}$ spin-orbitals in the case of D', while the core excitations corresponding to E' are dominated by transitions to $\pi^*_{\beta 6}$, $\pi^*_{\beta 12}$ and $\pi^*_{\alpha 5}$. Hence, both peaks correspond to peak B of the neutral species, because these orbitals have the same shape as the ones that characterize the core-excited states contributing to peak B. This is similar to peaks B' and C', which are related to A. With core-excitation energies of 286.0 eV (D') and 286.6 eV (E'), respectively, D' can be seen as the shoulder of peak E', which exhibits the larger absorption. The maximum of peak E' is blue shifted by 0.4 eV compared to B of the neutral species and due to the D' shoulder, E' is broadened compared to B. Looking at the results of the A_C^+ conformer, D' is red shifted by 0.47 eV compared to the A_N^+ conformer and it seems that D' is rather a shoulder of C' than of peak E'. Furthermore, the state characters differ as well. The states contributing to D'

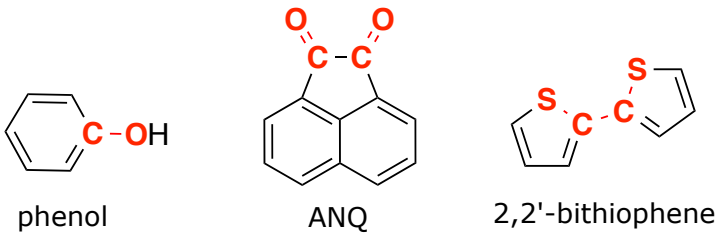

Figure 9.4: Structures of phenol, acenaphthenequinone (ANQ) and 2,2'-bithiophene (BT). Nuclear coordinates of phenol, ANQ and BT, which are investigated in this chapter, are marked in red, respectively.

of the A_C^+ conformer are dominated by transitions from the C2 group to the $\pi^*_{\beta 2}$, $d^*_{\beta 11}$, $\pi^*_{\beta 1}$ and $d^*_{\alpha 2}$ spin-orbitals, while E' contains a mix of transitions into the $\pi^*_{\beta 2}$ and diffuse orbitals. Compared to B of the neutral species, E' of A_C^+ exhibits a large blue shift of 1.05 eV.

Finally, I would like to briefly comment on peaks F' of both A_N^+ and A_C^+ conformers, which correspond to higher-lying core-excited states. These are mostly dominated by transitions from C 1s orbitals into a mixture of strongly diffuse orbitals, thus they can be characterized as Rydberg states. F' of A_C^+ exhibits a core-excitation energy of 288.18 eV, while F' of A_N^+ is slightly blue shifted by 0.23 eV.

Eventually, one can expect the following features for the experimental C 1s XA spectra of anthracene cations. Compared to the neutral species, an additional broad peak with core-excitation energies ranging from 281 eV to 283 eV due to the SOMO exists. Furthermore, one can expect a large peak broadening due to geometry relaxation of the cation (A_C^+). The latter depends on the life-time of the cation. The longer the cation exists, the closer the experiment should be to the calculated results of the A_C^+ conformer. Potentially, these calculations may help in the future to identify anthracene cations or related systems as reactive intermediates in organic materials.

9.2 Trends of Core-Excited State Properties Along Potential Energy Surfaces of ANQ, Bithiophene and Phenol

Let me turn to the second topic of this chapter, which is the investigation of properties of core-excited states along relaxed scans of ground-state potential energy surfaces (PES) of the representative medium-sized model systems phenol, ANQ and BT using the CVS-ADC(2)-x/CVS-ISR approach. ANQ is a simple model for electron-accepting molecules like PTCDA, while derivatives of BT are often employed as electron donors in organic semi-conducting materials.[13,204] Since gradients of the CVS-ADC approaches are not available yet, the PES were optimized in the ground state at the MP2 level and no core-excited state geometry optimizations were performed. In these calculations, the chosen reaction coordinate was constrained, while all other coordinates were allowed to relax freely. Figure 9.4 shows the structures of phenol, ANQ and BT as well as the chosen reaction coordinates.

9.2.1 PES Scan of the C–O Bond Distance in Phenol

Let me start with the scan of the C–O bond length (r_{CO}) of phenol, which was calculated in 0.05 Å steps from 1.10 Å to 1.65 Å. Figure 9.5 illustrates the plots of the scan. As expected for a diatomic internuclear separation, the potential in the S_0 has the typical shape of a Morse potential. The minimum in the S_0 is at 1.37 Å. The relative S_0 energy is 2.47 eV above the minimum at an internuclear distance of 1.10 Å, while at 1.65 Å, the energy is 0.85 eV higher than the one of the minimum, thereby indicating the convergence against the dissociation energy. At the minimum S_0 geometry, the relative core-excitation energy of the bright O 1s excited 1^1A' state is 533.84 eV. The relative energy of the O 1s core-1^1A' state rises strongly at small C–O distances, whereas at the larger distances from 1.37 Å to 1.55 Å, the energy decreases slightly. The shape of the corresponding potential is strongly dissociating. It seems that the potential converges against a stationary point. This indicates an unstable situation, thus one should expect an OH radical dissociation after the core-excitation depending on the lifetime of the O 1s excited 1^1A' state.

In Figure 9.5 the trends of the core-excited state dipole moment μ_{ex} as well as the ground state dipole moment along the distance between C and O are plotted. In principle, the dipole moment in the ground state at the relaxed MP2 level describes a polynomial behavior. The minimum is around the S_0 geometry with a value of almost 1.40 D. This value is in agreement with experiments, where a dipole moment of 1.22 D was determined.[238] Going from smaller to larger internuclear C–O distances, the dipole moment in the S_0 slightly increases to 2.41 D and 2.22 D at 1.10 Å and 1.65 Å, respectively. Compared to the dipole moment in the S_0, the trend of the core-excited state dipole moment differs significantly. Looking at the S_0 minimum at 1.37 Å, the absolute value of μ_{ex} is 4.23 D larger than the ground state dipole moment, which can be explained by an enhanced polarity due to the core hole. From 1.10 Å to 1.45 Å, μ_{ex} increases from 4.5 D to 6.2 D. This observation is in agreement with the expectation of two partial charges that are moved away from each other. However, at 1.50 Å the core-excited state dipole moment breaks down steeply to almost zero at an internuclear distance of 1.65 Å. This phenomenon can be explained when looking at the (D/A) densities of the O 1s excited 1^1A' state of phenol at r_{CO} values of 1.37 Å and 1.6 Å, respectively, which are shown in Figure 9.6. Comparing the shapes of the detachment densities at both C–O distances with each other, one can hardly find any significant differences. The detachment density is strongly broadened around the oxygen atom by extending the hole to the neighboring atoms due to relaxation effects. However, the attachment densities at both C–O distances differ from each other. At the smaller r_{CO} of 1.37 Å, the attachment density is mostly localized at the OH group with small contributions located at the connected carbon. At the larger r_{CO} of 1.60 Å, in contrast, it seems that the C–O bond starts to break, thus the density located at the disconnected carbon atom is enhanced. Thereby, the density contribution on the hydrogen atom of the OH group is reduced. Since the core-excited electron is delocalized over the carbon atom and the OH group at larger C–O distances, the partial charges compensate each other, which leads to a decrease of the core-excited state dipole moment.

The influence of the breaking of the C–O bond can be confirmed by looking at the trends of exciton sizes related to the 1DDM analysis as a function of r_{CO} (see Figure 9.5). From 1.10 Å to 1.50 Å, the exciton sizes increase, while at an internuclear distance of 1.55 Å, they start to decrease. Since at smaller C–O distances the core excitation is mostly localized on the OH group and only a minor part of the density is located at the aromatic ring, the extent of the attachment and detachment parts increases when going to larger r_{CO} values. At larger distances, when the bond breaking starts to occur, the density at the carbon atom expands. As a consequence, the extent of the exciton decreases, because

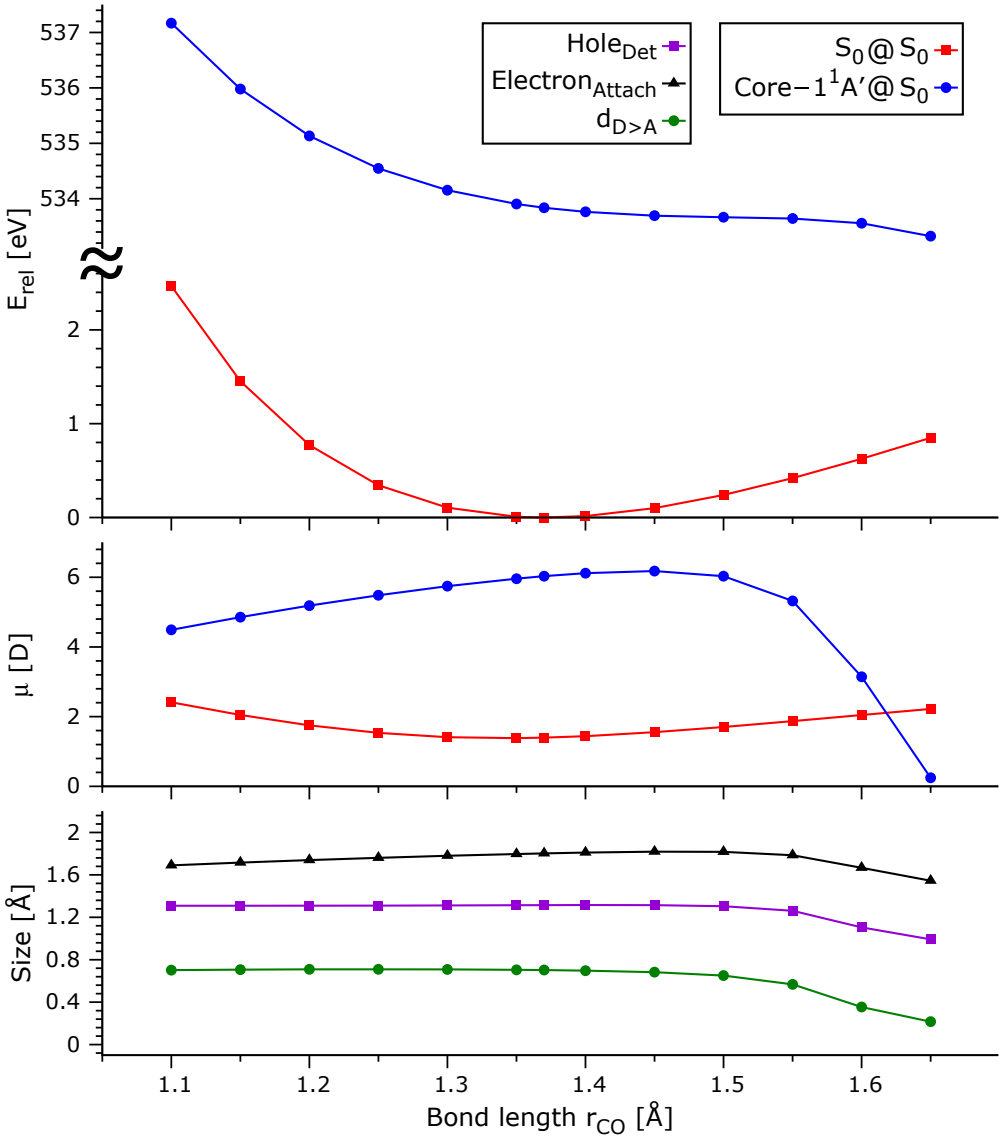

Figure 9.5: Relaxed PES scan along the distance of the C-O bond r_{CO} of phenol in the electronic ground state (S_0). The S_0 calculations were performed at the MP2/6-311++G** level of theory, while the O 1s excited 1^1A' state is calculated using the respective ground state geometries and the CVS-ADC(2)-x/6-311++G** approach. Top: relative energies E_{rel}. The S_0 minimum at 1.37 Å is set to zero. Middle: static dipole moments μ of the S_0 and O 1s excited 1^1A' states. Bottom: different exciton sizes of the 1^1A' state based on the 1DDM, i.e. σ_D, σ_A, and $d_{D\rightarrow A}$.

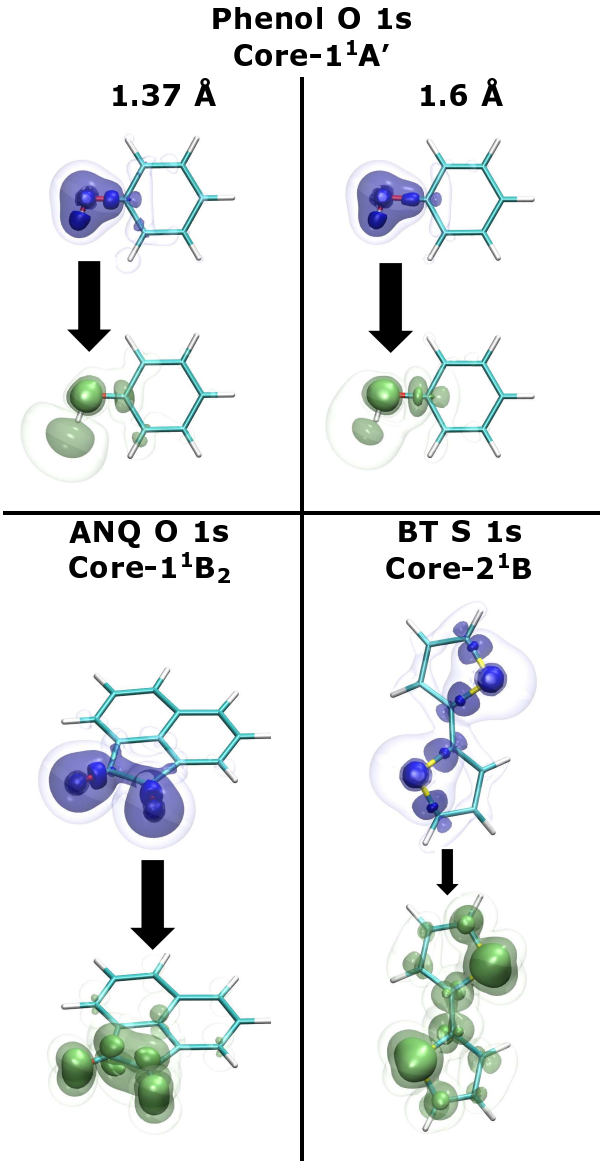

Figure 9.6: Detachment(blue)/attachment(lime) densities of the $1^1A'$ O 1s core-excited state of phenol, the 1^1B_2 O 1s core-excited state of ANQ, and the 2^1B S 1s core-excited state of BT. The calculations were performed at the CVS-ADC(2)-x/6-311++G** level. The isosurfaces were rendered with the isovalues 0.0256 (opaque), 0.0064 (colored transparent), and 0.0016 (transparent) in the case of phenol, while the respective isovalues for ANQ and BT are 0.0128, 0.0032 and 0.0008. For comparison two structures of phenol are shown, which exhibit C–O bond lengths of 1.37 Å (energetic S_0 minimum) and 1.60 Å. The structures of BT and ANQ are in their energetic S_0 minimum, respectively.

the center of charge is shifted towards the aromatic ring.

9.2.2 Symmetric PES Scan of the Two C=O Bond Distances in ANQ

Next, the static dipole moments of the bright O 1s core-excited state of ANQ along the symmetric stretch motion of the two C=O bond distances of ANQ are investigated. In contrast to phenol, this system exhibits two symmetrically equivalent C=O double bonds due to the C_{2v} point group symmetry. Since the O 1s XA spectrum of ANQ is dominated by one broad peak, which was identified as the O 1s excited 1^1B_2 state (see chapter 6.1.1), this coordinate is of special interest. The C=O distance is investigated from 1.10 Å to 1.55 Å and the results are shown in Figure 9.7. The (D/A) densities exhibit the same shape and character at all C=O distances, thus only the (D/A) densities at the S_0 minimum at r_{CO} = 1.21 Å are shown in Figure 9.6.

Both ground and O 1s excited 1^1B_2 state potentials have a typical Morse-type shape, but the potential of the core excitation is less steep than the S_0 one. Going to the static dipole moments, the trends in both S_0 and O 1s excited 1^1B_2 states are similar. This is in contrast to the phenol example, where the dipole moments show a completely different behavior. In the case of ANQ, both investigated dipole moments increase from small r_{CO} values of 1.10 Å to a maximum at 1.55 Å. The absolute μ_{ex} values are in this example smaller than the ground state ones, e.g. at the C=O distance of 1.21 Å the S_0 dipole moment is 6.09 D, while the core-excited state dipole moment is only 2.79 D. Again, these results can be explained by inspecting the (D/A) densities (see Figure 9.6). Due to the double bond character of the C=O bonds, the core excitation is localized on the whole bonds and not on the oxygen atoms themselves. Furthermore, the symmetric treatment of the equivalent C=O bonds leads to a delocalization over both C=O bonds. This means a strong delocalization of the core-excited electron, which is accompanied by significant relaxation effects of the core hole. As a consequence, the polarity of the C=O bonds decreases in the O 1s excited 1^1B_2 state, which results in a smaller dipole moment compared to the ground state.

9.2.3 PES Scan of the Torsion Around the Central Dihedral Angle of Bithiophene

The last example is the PES Scan of the torsion around the central dihedral angle β (S–C–C–S) of BT (see Figure 9.4).
Since C_2 point group symmetry was exploited in all calculations, the two sulfur atoms are equivalent and the S 1s excited states are characterized by transitions from linear combinations of the two 1s orbitals of the sulfur atoms. This dihedral angle plays an important role for the absorption and emission properties in the ultraviolet region of bithiophenes. For example, I showed in a previous work that this torsion angle dominates the most important reaction coordinate in an oligothiophene-based organic solar-cell material.[95] The energy- and charge-transfer processes are strongly influenced by this torsion. In the ground state, BT is usually non-planar[207,209,239], while the first strongly bright valence-excited state, which is dominated by the LUMO, has a planar structure, because the LUMO has a binding character between the two thiophene rings.[95] Hence, the question arises whether the bright S 1s core-excited 2^1B_2 state shows a similar behavior. The results along the scan in a range from 0° to 180° are summarized in Figure 9.8.

The potential in the ground state exhibits the typical shape for BT systems at the MP2 level.[207,209,239] There are three local maxima and two local minima with an absolute

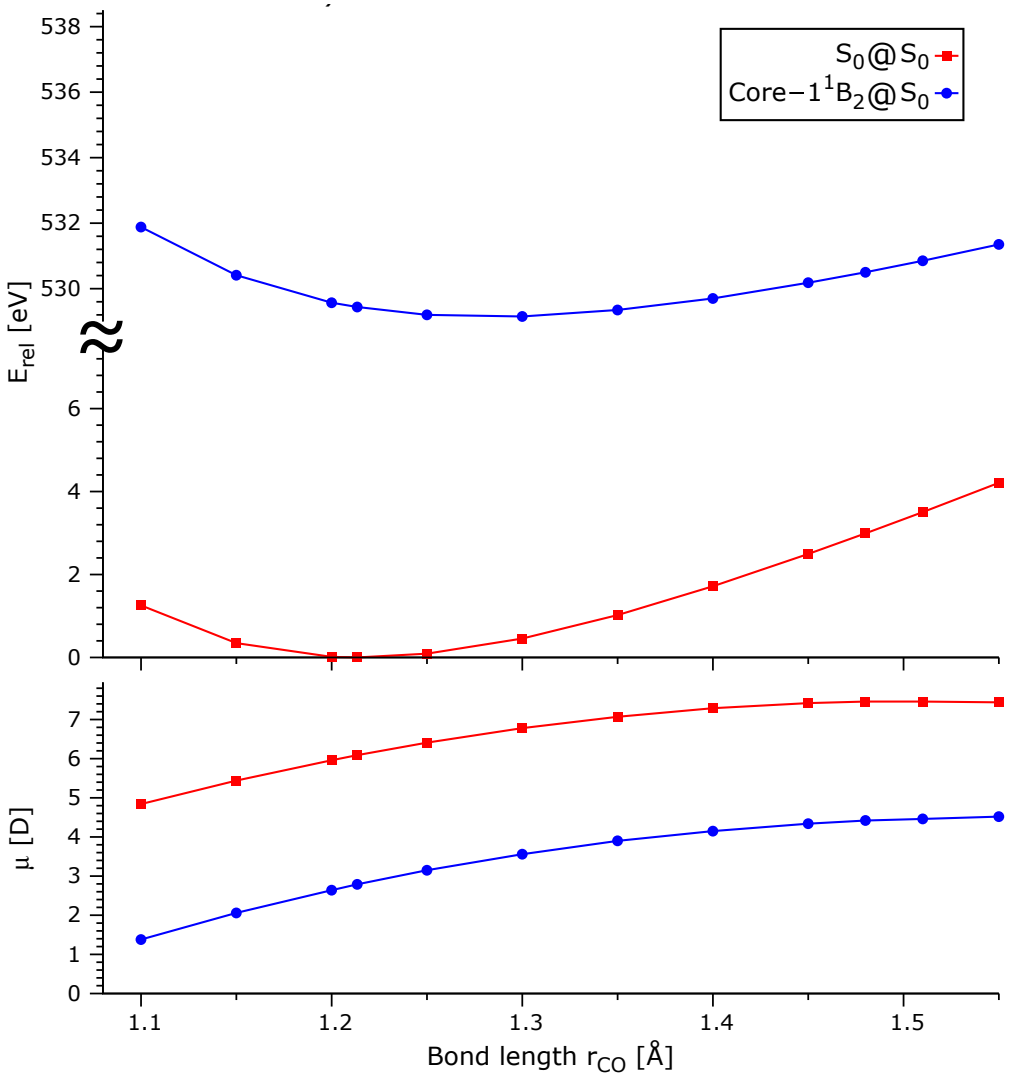

Figure 9.7: Relaxed PES scan along the parallel stretching of the two C=O bonds r_{CO} of the ANQ ground state. The S_0 calculations were performed at the MP2/6-311++G** level of theory, while the vertical O 1s excited 1^1B_2 states were calculated using the respective ground state geometries and the CVS-ADC(2)-x method in combination with the 6-311++G** basis set. Top: relative energies E_{rel}. The energy of the S_0 minimum at 1.21 Å is set to zero. Bottom: static dipole moments μ of the S_0 and core-excited 1^1B_2 states.

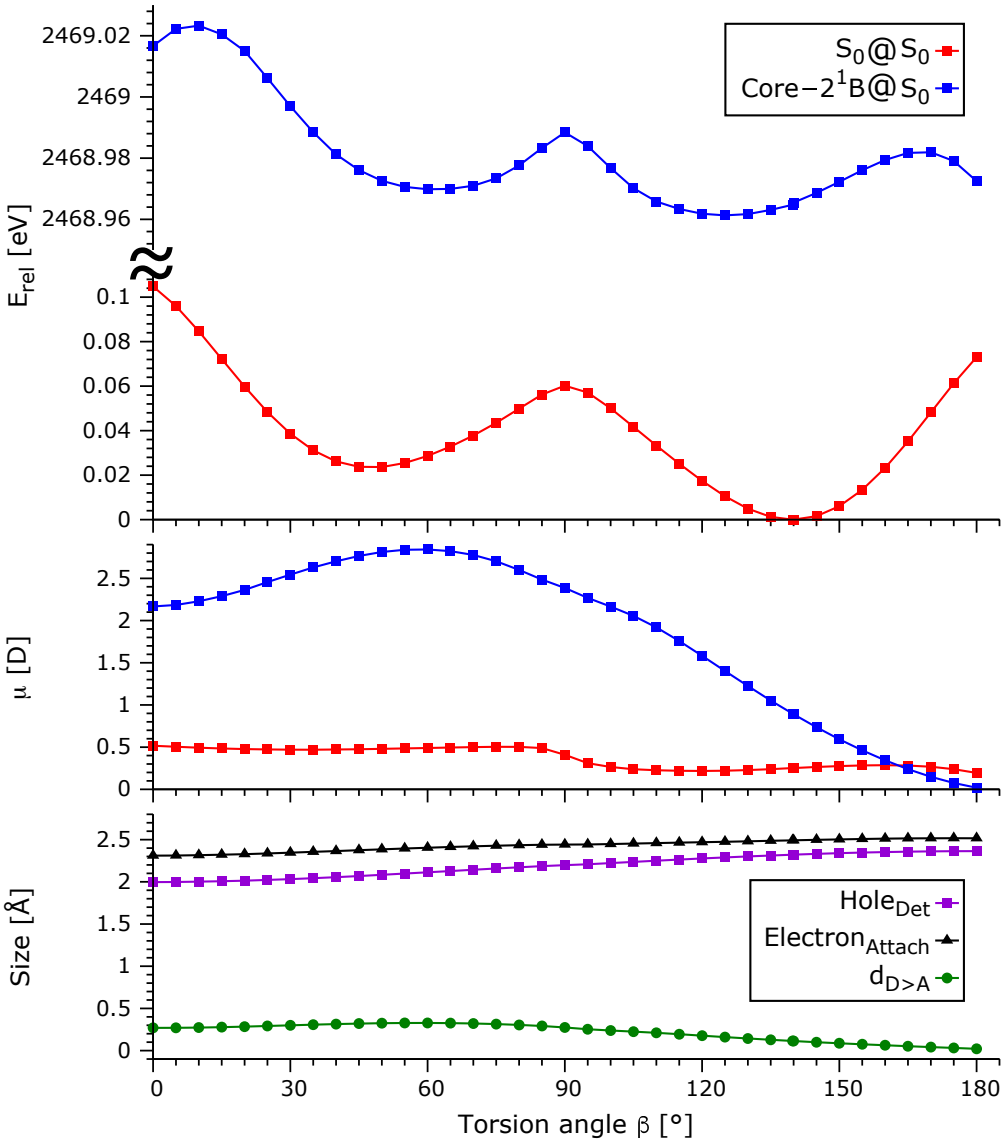

Figure 9.8: Relaxed PES scan along the dihedral angle β of BT in the electronic ground state S_0. The S_0 calculations were performed at the MP2/6-311++G** level of theory, while the vertical S 1s core-excited 2^1B_2 state is calculated using the respective ground state geometries and the CVS-ADC(2)-x method in combination with the 6-311++G** basis set. Top: relative energies E_{rel}. The energy of the S_0 minimum at 139.79° is set to zero. Middle: static dipole moments μ of S_0 and the S 1s core-excited 2^1B_2 state. Bottom: different exciton sizes of the core-2^1B_2 state based on the 1DDM, i.e. σ_D, σ_A and $d_{D\rightarrow A}$.

minimum located at 139.8°. The torsion of β is around a single bond, thus the corresponding energy barrier is very low. The largest maximum is located at 0° with a relative energy of only 0.11 eV compared to the absolute minimum. Going to the S 1s core-excited 2^1B_2 state, there are also three local maxima and two local minima, but with slightly shifted β values compared to the ground state. The barrier of the core-excitation energy is with 0.06 eV at the same level as the ground state potential. Hence, the potential of the S 1s excited 2^1B_2 state along the torsional mode is mostly dominated by the valence electrons and the influence of the torsion around β to the core-2^1B_2 state and vice versa is negligible. Looking at the (D/A) densities (see Figure 9.6) reveals the reason for the small barrier in this core-excited state. Since the attachment density is delocalized over the thiophene rings due to the C_2 point group symmetry, there is no binding character along the central C–C bond, resulting in a low barrier of the torsion around β. Hence, the bright S 1s core-excited 2^1B_2 state does not exhibit the same character as the bright valence-excited state of BT.

Let me turn to the trend of static dipole moments along the torsional mode. The absolute values of the ground state dipole moments are small, ranging from 0.22 D to 0.52 D. From 0° to 75°, they remain practically constant, while they drop constantly to 0.22 D between 75° and 120°, exhibiting a small maximum around 160°. Note that the trend of the dipole moment in the S_0 calculated at the MP2/6-311++G** level differs from former calculations in the literature.[240] There, a smaller cc-pVDZ basis set was employed. Generally, the dipole moment in the S_0 should constantly decrease towards zero going from β values of 0° to 180°, because the distance between the two sulfur atoms (r_{SS}) increases and the charges totally compensate each other at 180°. It seems that the polarization and diffuse functions included in the 6-311++G** basis set enhance the description of the dipole moment in the ground state. Compared to the ground state, the trend of static dipole moments of the S 1s excited 2^1B_2 state differs strongly. μ_{ex} has values between 0.02 D and 2.84 D and increases almost constantly from 0° to 60° and then falls to almost 0 D at 180°. This trend can be explained again by means of the exciton sizes and the C_2 point group symmetry of the BT molecule (see Figure 9.8, bottom). Looking at the trends of σ_D and σ_A, the increase of the internuclear distance of the two sulfur atoms during the torsion around β becomes obvious. r_{SS} ranges between 3.31 Å at 0° and 4.38 Å at 180°, while due to relaxation effects that expand the hole density to the neighboring atoms, σ_D only increases from 2.00 Å to 2.36 Å. The trend of the distance of the center of charges ($d_{D\rightarrow A}$) provides the same shape as μ_{ex}. The maximum is located at $\beta = 60°$ and then $d_{D\rightarrow A}$ drops down to almost zero at 180°, where the two sulfur atoms are opposite to each other and thus the partial charges compensate each other. Since the the (D/A) densities are delocalized due to relaxation effects, μ_{ex} and $d_{D\rightarrow A}$ increase going from 0° to 60°.

Eventually, a significant influence of the torsion around β on the dipole moment and polarization of BT in the S 1s excited core-2^1B_2 state is observed, which differs strongly from the electronic ground state. However, the potential in the S 1s excited core-2^1B_2 state is very similar to the one in the ground state.

Chapter 10

Core-Excited State Absorption Processes

Besides core-excited state properties, an interesting aspect of the CVS-ISR method is the accessibility of transition moments between two states. These can be used for calculating oscillator strengths for excited state absorption (ESA) spectra. Experimentally, time-resolved X-ray absorption techniques are available to probe excitations from a valence-excited state to a core-excited one using ultrafast sequences of vacuum ultraviolet (VUV)/X-ray pulses.[31,241] To the best of my knowledge, no experimental data of an inverse absorption, i.e. core-excited state absorption (CESA) processes from a core-excited state to another using a sequence of X-ray/VUV pulses, are available yet. In principle, all excited states of a molecule can absorb a photon, leading to an ESA process, but only ESA spectra of the lowest excited states, e.g. S_1 or T_1, can usually be measured.[242] Higher-lying states, especially core-excited ones, are meta-stable and undergo fast relaxation or decay processes, making the measurement of ESA difficult. However, such spectroscopic data could exhibit new insights and the theoretical CESA transition moments for comparison are already available using my CVS-ADC/CVS-ISR approach and are presented in this thesis.

Therefore, the set of CO, ANQ, the methyl radical CH_3 and triplet O_2 were chosen (for structures see Figures 4.1, 6.1 and 6.10). The structures of the small molecules CO and the CH_3 radical in the electronic ground state were optimized at the CCSD[51] level using the def2-QZVPPD[119] basis set. For comparison with the results presented in chapters 6.1.1 and 6.3.3, the structures of the molecules ANQ and the triplet O_2 diradical were optimized at the MP2 level in combination with the resolution-of-the-identity (RI)[192,193] approximation and employing the def2-TZVPP[118] basis set combined with the respective auxiliary TZVPP basis set[194]. The CCSD calculations were performed using the `Q-Chem 4.3` program[94], while for the geometry optimizations at the RI-MP2 level the `TURBOMOLE 6.3.7` program[196] was used. For the open shell systems, the unrestricted variants of CCSD and MP2 were used, respectively. Core excitations and the corresponding state-to-state transition moments were calculated with my implementation of the CVS-ADC/CVS-ISR approach. The calculations of the triplet O_2 diradical and the methyl radical were performed using the unrestricted variant of CVS-ADC (CVS-UADC). The calculations of core-excited states were performed employing the Cartesian 6D/10F version of the 6-311++G** basis.[109,110,113] To save computational time, C_{2v} point group symmetry was exploited in all calculations of ANQ.

10.1 CESA Processes Between Core-Excited States

The first calculated results of core-excited state absorption (CESA) events are presented in this chapter and are briefly discussed. Since the calculation of CESA oscillator strengths is straightforward using the CVS-ADC/ISR approach, a theoretical demonstration of such transitions can easily be performed. The results calculated at the CVS-ADC(2)-x level are summarized in Table 10.1. Starting with the C 1s excitations of the CO molecule, the first 10 transitions from the bright dipole allowed core-excited singlet state 1 were calculated. Due to degenerate π^*-orbitals, some core-excited states are also degenerate. The first transitions that exhibit a meaningful oscillator strength are the transitions from state 1 to 3 and 4, which are 5.40 eV and 6.68 eV higher in energy, respectively. The oscillator strength of the transition from state 1 to state 4 can be explained by plotting the (h/e) densities. Figure 10.1 illustrates the plots of some chosen transitions. In the CO example, the transition from 1 to 4 exhibits oscillator strength, because the characters of both states are similar with π^* shapes located on the carbon atom (see electron densities). Hence, an overlap is given. Overall, four bright excitations can be identified within the 10 lowest transitions.

Going to the O 1s excitations of ANQ, transitions from the bright dipole allowed 1 $^1B_2$ core-excited singlet state to the first six $^1B_2$ and $^1A_2$ core-excited singlet states were calculated. All transitions exhibit oscillator strength due to the delocalized π^* system of the ANQ molecule. As an example, the transition from the 1 $^1B_2$ to the 2 $^1A_2$ state is shown in Fig. 10.1.

Finally, there are two open-shell examples that were calculated using the unrestricted CVS-ADC(2)-x variant. Within the first 16 transitions from the C 1s core-excited state 1 of the CH_3 radical, only three exhibit oscillator strength, i.e. to state 2, 3 and 17. Especially, the transition to state 17 exhibits a large oscillator strength of 0.172. In the case of the O_2 diradical, transitions from the core-excited state 8 were chosen, because this state was identified in chapter 6.3.3 to have a large oscillator strength. Here, only four transitions exhibit a meaningful oscillator strength, where the transition to state 23 has the highest value of 0.039. Figure 10.1 illustrates the transition to state 12, which can be characterized as a diffuse Rydberg state. This transition is also dipole allowed with an oscillator strength of 0.016.

Eventually, this investigation demonstrates that CESA processes are theoretically possible, leading to dipole allowed transitions that could be measured hypothetically. CVS-ADC(2)-x in combination with the CVS-ISR approach provides a quantum chemical tool to calculate such events and maybe can be applied in the future to help interpreting experiments.

Table 10.1: List of the calculated CESA transitions from the first core-excited singlet state to the first 11 core-excited singlet states of CO (C 1s), from the 1 $^1B_2$ core-excited singlet state to the first six $^1B_2$ and $^1A_2$ core-excited singlet states of ANQ (O 1s), from the first core-excited state to the first 17 core-excited states of CH_3 (C 1s), and from the eighth core-excited state to the first 24 core-excited states of the triplet O_2 diradical (O 1s). The CESA excitation energies (ω_{ex}) and oscillator strengths (f_{osc}) were calculated using CVS-ADC(2)-x (CO and ANQ) and CVS-UADC(2)-x (CH_3 and O_2), employing the 6-311++G** basis set.

State X	ω_{ex} [eV]	f_{osc}	State X	ω_{ex} [eV]	f_{osc}
CO C 1s (State 1 → State X)			ANQ O 1s (State 1^1B_2 → State X)		
2	0.00	0.000	2 $^1A_2$	3.63	0.054
3	5.40	0.008	2 $^1B_2$	3.63	0.031
4	6.68	0.016	3 $^1B_2$	5.33	0.006
5	6.68	0.000	3 $^1A_2$	5.33	0.008
6	6.87	0.017	4 $^1B_2$	6.25	0.018
7	9.44	0.016	4 $^1A_2$	6.25	0.002
8	10.09	0.000	5 $^1A_2$	6.30	0.021
9	10.09	0.000	5 $^1B_2$	6.30	0.170
10	10.44	0.001	6 $^1B_2$	7.31	0.025
11	10.44	0.000	6 $^1A_2$	7.31	0.071
CH_3 C 1s (State 1 → State X)			O_2 O 1s (State 8 → State X)		
2	5.39	0.018	9	0.48	0.000
3	6.29	0.010	10	0.53	0.010
4	6.80	0.000	11	1.59	0.000
5	6.80	0.000	12	1.60	0.016
6	7.70	0.000	13	2.02	0.001
7	7.70	0.000	14	2.02	0.001
8	7.79	0.000	15	2.07	0.000
9	8.27	0.000	16	2.07	0.000
10	8.27	0.000	17	2.83	0.000
11	8.39	0.000	18	2.86	0.000
12	9.22	0.000	19	3.10	0.003
13	9.22	0.000	20	3.10	0.003
14	9.25	0.000	21	3.12	0.000
15	9.60	0.172	22	3.12	0.000
16	10.09	0.000	23	3.82	0.039
17	10.09	0.000	24	3.82	0.000

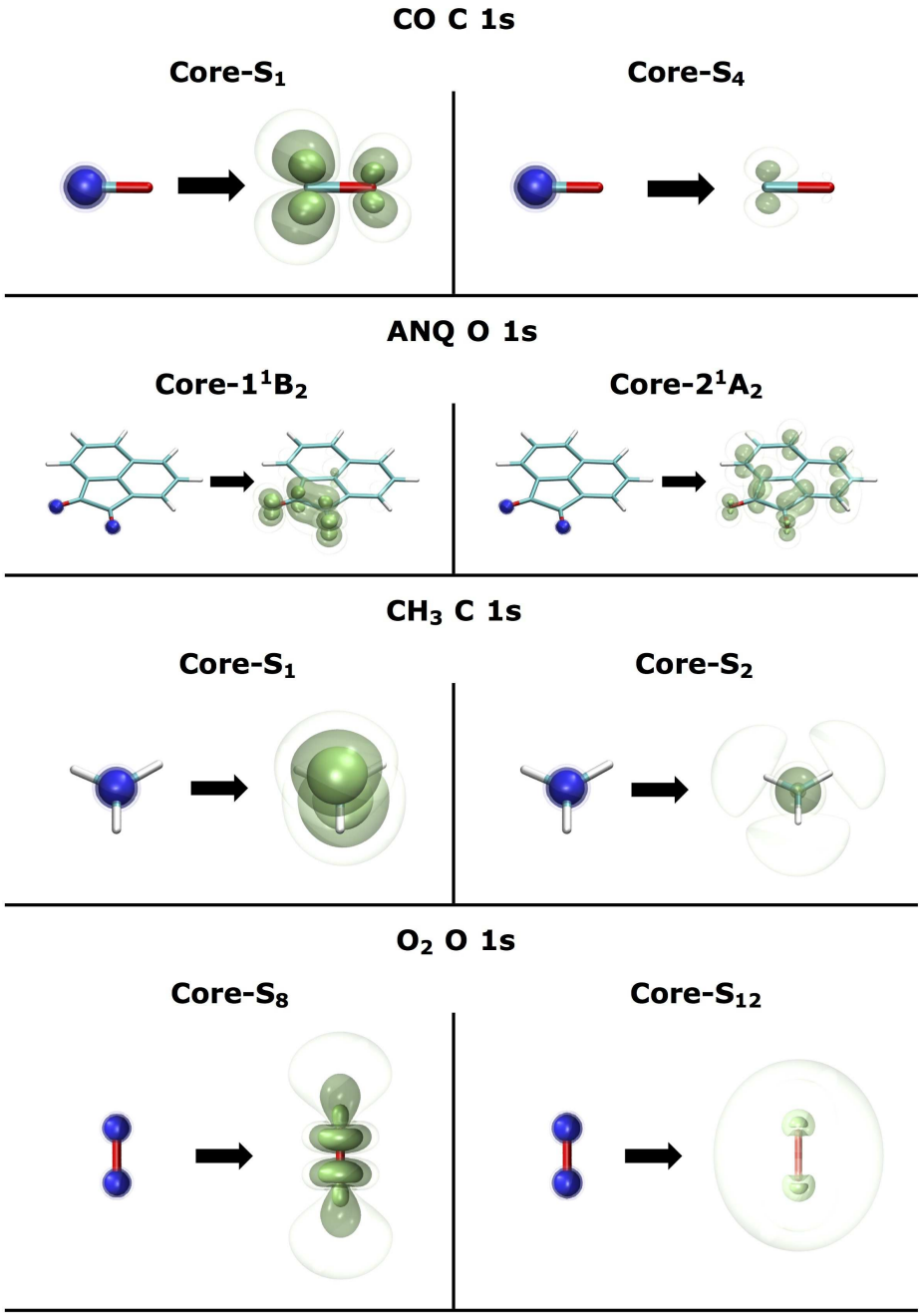

Figure 10.1: Plots of hole (left, blue) and electron (right, lime) densities based on the 1TDM of some CESA related core-excited states of CO (C 1s), ANQ (O 1s), CH_3 (C 1s), and triplet O_2 (O 1s) calculated at the CVS-ADC(2)-x/6-311++G** level. The isosurfaces of ANQ, CH_3 and O_2 were rendered with the isovalues 0.0128 (opaque), 0.0032 (colored transparent), and 0.0008 (transparent), while the ones of CO are rendered with the isovalues 0.0512 (opaque), 0.0128 (colored transparent), and 0.0032 (transparent).

Chapter 11

Conclusion and Outlook

In this thesis, I presented efficient implementations of different variants of the algebraic diagrammatic construction scheme (ADC) in combination with the core-valence separation (CVS) approximation, which allows for the calculation of core-excited states. Due to the CVS approximation, the size of the ADC matrix is reduced and the valence-excited states are strictly decoupled from the core space. This is justified since the interaction between core and valence-excited states is weak as the energy difference between valence and core orbitals is large. As a consequence, the corresponding Coulomb integrals are very small, thus they can be neglected and the core-excited states can be computed directly. The implementation features excitation energies of singlet and triplet core-excited states as well as oscillator strengths and state properties to describe the spectral characteristics, thereby simulating X-ray absorption (XA) spectra. Furthermore, the program allows to exploit point group symmetry.

Besides the efficient implementation of the restricted strict and extended second order CVS-ADC(2) approaches, which can treat about 500 basis functions in an adequate computational time, I developed the unrestricted CVS-UADC approach for the computation of XA spectra of open-shell systems (ions and radicals) for the first time. Subsequently, I derived and implemented the third order CVS-ADC(3) approach by applying the CVS approximation to the ADC(3) working equations. Furthermore, the intermediate state representation (ISR) for a general one-particle operator was combined for the first time with the CVS approximation for the calculation of core-excited state properties, i.e. static dipole moments, core-excited state densities and transition moments between core-excited states. In combination with wave function analysis packages, a deeper evaluation of transition- and density matrices can be performed, providing access to exciton sizes, e.g. hole sizes or distances between hole and electron densities of core-excited states. Since the third order algebraic expressions for the transition moments and ISR properties are not available yet, the second order terms are used to describe the properties and transition moments at the CVS-ADC(3) level, which is denoted as the CVS-ADC(3,2) method.

To demonstrate the accuracy of the CVS-ADC methods and their capabilities to simulate XA spectra, benchmark calculations and different applications were presented in chapters 4 – 10. There, it has been shown by means of miscellaneous sets of small and medium-sized molecules that the restricted and the unrestricted CVS-ADC(2)-x approaches provide an excellent agreement with experimental data. The benchmark calculations on the basis of the C, N and O 1s excitations, where the complete basis set (CBS) limit of the aug-cc-series was estimated, show an error of -0.23%±0.12% for core excitation energies at the CVS-ADC(2)-x level compared to experiments. The CVS-ADC(3,2) and

CVS-ADC(2)-s methods, in contrast, overestimate the core excitation energies with a mean errors of 0.61%±0.32% and 0.57%±0.43%, respectively. This overestimation, in particular in the case of CVS-ADC(3,2), depends significantly on the core-type. The heavier the element, the larger the overestimation at the CVS-ADC(3,2) level. The reason for the larger deviations of heavier elements are stronger relativistic and relaxation effects due to stronger Coulomb interactions between the core and valence electrons. In the case of CVS-ADC(2)-x and -s, core excitations from heavier elements usually lead to a larger underestimation of the corresponding excitation energies. Since relativistic effects, which are not included within the CVS-ADC approaches, would shift the core-excitation energies to larger numbers, the underestimation provided by CVS-ADC(2)-x/-s shows a "correct" trend that may be explained by the neglect of these effects. Energy spacings between core-excited states, oscillator strengths and static dipole moments are well described at both CVS-ADC(2)-x and CVS-ADC(3,2) levels, which justifies the use of the second order transition moments and ISR property equations for CVS-ADC(3).

A detailed investigation of the influence of the chosen basis set on the results revealed that core-excitation energies are almost converged at the triple-ζ level independent of the chosen type of basis set. To successfully describe Rydberg or dipole-bound states, the inclusion of diffuse basis functions is mandatory, while bright s,π^* states can be well described by employing smaller basis sets without augmentation, e.g. the cc-pVDZ basis set. Pople-type basis sets, additionally, show a strong influence of the polarization functions. For a quantitatively adequate result, one should at least apply the 6-311G** basis set. Actually, the correlation consistent series provides better results in combination with the CVS-ADC methods, but the calculations are much faster employing Pople-type basis sets, because they contain less basis functions. Employing the 6-311++G** basis set, for example, is in the case of CO 186 times faster than the respective aug-cc-pVTZ basis. Furthermore, the use of Cartesian 6D/10F basis functions is of advantage compared to pure 5D/7F functions.

Overall, I reach the conclusion that CVS-ADC(2)-x, in combination with a diffuse triple-ζ basis in its Cartesian version, provides a fortuitous compensation of basis set truncation errors, correlation effects, neglect of relativistic effects and orbital relaxation effects resulting in an excellent agreement with experimental data. This error cancellation is broken at the CVS-ADC(3,2) and CVS-ADC(2)-s levels, which I showed in chapters 2.5.9 and 5. Generally, orbital relaxation and polarization effects are included indirectly within the CVS-ADC method via couplings between excited configurations. Since both CVS-ADC(2) and CVS-ADC(3,2) comprise two excitation classes, only the singly excited configurations are relaxed via couplings to the doubly excited configurations, while the double excitations remain unrelaxed. The overestimation at the CVS-ADC(2)-s level can be explained by the fact that the description of the doubles is not improved as in CVS-ADC(2)-x, which usually leads to a lowering of the excitation energies in CVS-ADC(2)-x compared to CVS-ADC(2)-s. At the CVS-ADC(3,2) level, the effective coupling is decreased without further improving doubly-excited amplitudes, which results in an overestimation of core-excitation energies. The influence of relaxation effects on the core-excited states was performed by means of counting the amount of doubly-excited amplitudes (R2) contributing to a state and electron promotion numbers (p_{DA}). In this case, a clear trend between the R2/p_{DA} values and core-excitation energies was identified, which demonstrates the strong influences of relaxation effects on core-excitation energies. Since a p_{DA} value of 1.0 indicates no inclusion of relaxation effects, which is typical for uncorrelated quantum chemical methods like CIS, values larger than 1.0 indicate these many-body effects. In the case of CVS-ADC(2)-x, the promotion numbers are larger than 1.7 (on average around 2.0), which indicates a huge contribution for singly

core-excited states. Furthermore, the CVS-ISR approach gives access to core-excited state densities, thus the subsequent decomposition of the difference density matrix (1DDM) into detachment/attachment (D/A) densities is a useful procedure that provides the possibility to visualize orbital relaxation effects. Typically, the attachment density is less influenced by relaxation effects, while the detachment density shows strong relaxation effects expanding the core hole to neighboring atoms. Besides the analysis of the 1DDM, the evaluation of the transition density matrix (1TDM) provides further information too. Hole and electron (h/e) densities based on the 1TDM do not contain orbital relaxation effects, thus they can be seen as a description of the vertical excitation process itself. Exciton sizes based on either 1TDM or 1DDM can be employed to learn further information about relaxation effects and the extent of the core excitation, in particular, when comparing corresponding exciton sizes obtained with the different densities with each other. I have shown, for example, that the detachment density is strongly expanded in space by relaxation effects, while the attachment density slightly contracts.

With the knowledge about the excellent performance of the restricted and unrestricted CVS-ADC(2)-x approaches, I chose molecules of current interest in the fields of organic electronics (ANQ, bithiophene, PTCDA) and biology (porphin, thymine, cytosine) as well as small organic radicals (CH_3, OH, allyl, triplet O_2) to simulate their XA spectra. Regarding these examples, CVS-ADC(2)-x, in combination with the 6-311++G** basis set, provides a mean error of about 0.1% compared to experimental core-excitation energies. Besides the excellent agreement of the calculated and experimental core-excitation energies, the energy spacing between the states is also well described using the CVS-ADC(2)-x method. By means of ANQ and cytosine, an analysis of state and transition densities was performed to determine state characters and to show, which information can be gained by means of exciton sizes. In the case of cytosine, plotting the (D/A) or (h/e) densities provides a unique and clear picture of the core-excitation process that helps to distinguish between s,π^*-, dipole-bound and Rydberg-states. Furthermore, exciton sizes help to characterize core-excited states. The electron sizes, for example, grow by about 2.0 Å going from s,π^* states to dipole-bound states or Rydberg states in the case of cytosine O 1s excitations. Investigations of correlation effects and dynamic charge separation reveal that core excitations from a single atom exhibit no correlation effects due to the localized contracted 1s orbital, whereas core excitations described via linear combinations of symmetrically equivalent 1s orbitals show slight contributions.

Next, the core-excitation energies at the CVS-ADC(2)-x level presented in chapter 6 were compared with REW-TD-DFT and CVS-ADC(2)-s results to demonstrate the self-interaction error (SIE) problem inherent in pure TD-DFT. I have shown that for both close- and open-shell systems an almost constant underestimation of core-excitation energies ranging from 2% to 4% is provided, employing the B3LYP xc-functional. However, energy spacings between the states are also well described in most cases at the level of REW-TD-DFT/B3LYP. Nevertheless, an experimental comparison is always mandatory for a quantitative interpretation of REW-TD-DFT spectra, because the underestimation of core-excitation energies clearly limits its predictive power. By adding a large constant shift to the absolute core-excitation energies, adequate core-absorption spectra can be obtained with REW-TD-DFT/B3LYP. The restricted and unrestricted strict CVS-ADC(2) variants generally overestimate the excitation energies in combination with the 6-311++G** basis sets up to 1.5%.

The investigation of computational timings with focus on the influence of the CVS approximation and the size of the core space showed a linear dependence of the computational time on the size of the core space. The larger the core space the longer take the calculation in the case of the second order CVS-ADC approaches. At the CVS-ADC(3,2) level, the

opposite dependence was identified. The reason for this are the additional third order terms that are dominated by contractions over the non-core occupied space. Generally, a CVS-ADC(3,2) calculation can take 8 to 10 times longer than a respective CVS-ADC(2)-x calculation. Compared to general ADC(2)-x calculations, the CVS approximation leads to a significant speed-up. In the case of cysteine, the calculation of 10 valence-excited states using the ADC(2)-x method takes about 3.85 times longer than at the CVS-ADC(2)-x level.

Next, two relevant applications of CVS-ADC(2)-x calculations in the field of organic electronics were presented. Since CVS-UADC(2)-x provides accurate absolute core-excitation energies and properties of core-excited states, I used this approach to predict the XA spectrum of the anthracene cation, which has not been measured experimentally yet. First of all, I investigated the neutral anthracene species at the level of restricted CVS-ADC(2)-x, which provides an excellent agreement with the experiment. The following analysis of the anthracene cation species revealed that, due to the half-filled SOMO, a new absorption band appears in the spectrum located approximately 3.5 eV – 1.5 eV below the first peak of neutral anthracene. Furthermore, I expect peak broadening in the cationic spectrum compared to the two first peaks of neutral anthracene. The second application in the field of organic electronics corresponds to core-excited state properties along relevant nuclear coordinates of phenol, ANQ and BT. Regarding these systems, plotting (D/A) densities and evaluating exciton sizes help to understand the behavior of core-excited state dipole moments along the coordinates of interest. Particularly, the torsion around the central dihedral angle of bithiophene has a strong influence on the dipole moment of the bright S 1s excited state.

Finally, the calculation of core-excited state absorption (CESA) spectra was introduced. The CVS-ISR method provides an elegant way to calculate transition moments between core-excited states, although experimental data of CESA events are not available yet. Using test systems, it was shown that CESA is theoretically possible, showing large oscillator strengths in some cases. For example, transitions from the first O 1s singlet excited state of ANQ to the 10 higher-lying states exhibit oscillator strength in every case, due to the delocalized π^*-LUMO level.

Since the CVS-ADC methods, in particular the extended second order approach, can be employed to successfully simulate XA spectra, it is reasonable to extend and further develop these approaches. There are many possible projects that should be considered in the future. Since CVS-ADC(3,2) does not further improve the results compared to CVS-ADC(2)-x, one should consider possible correction schemes to include a better description of orbital relaxation and polarization effects, for example within the doubly-excited configurations. It may be possible to expand the 2p-2h-block via perturbation theory or to only include specific terms of CVS-ADC(4) to describe these missing relaxation and polarization effects. Employing CVS-ADC(4) might entirely fix this problem, but the computational cost would be increased drastically too. Since TD-DFT provides reasonable XA spectra, but fails in the calculation of absolute core-excitation energies due to the SIE, a proper investigation of relaxation effects within the TD-DFT approach would be an interesting topic as well. For this, the wave function analysis tools can be employed and the results can be compared with CVS-ADC data. The resolution-of-the-identity (RI)[192,193] approximation is a potential approach to reduce the computational cost of the CVS-ADC calculations. In combination with the MP2 and CC2 methods, the RI approximation is known to provide small errors compared to the full results, which makes it a promising approach for CVS-ADC. For this purpose, the CVS-ADC equations have to be modified to correspond to the RI scaling. So far, CVS-ADC calculations do not consider any environmental effects. Since NEXAFS spectra are usually regarded for solid state

materials, considering environmental effects would be advantageous for the description of core-excited states. Furthermore, recent investigations of XA spectra of liquid water[166] could be supported with CVS-ADC calculations that include solvent effects. Therefore, the combination of the CVS-ADC approaches with solvation models like the polarizable continuum model (PCM) could provide deeper insights.[243,244] Another possibility to describe environmental effects is the frozen density embedding (FDE)[245,246] approach, which can theoretically be combined with ADC methods. Furthermore, the development of analytic gradients of the energy at the CVS-ADC levels would be favorable, since they provide access to core-excited state geometry optimizations, emission spectra and response properties. Recently, analytic gradients for general ADC have been developed, thus it should be straightforward to derive them for the CVS methods.[247] As mentioned in chapter 10, state-to-state transitions between core-excited states have not been measured yet. However, transitions between valence- and core-excited states have been studied recently.[31,241] Hence, a theoretical description at the CVS-ADC/CVS-ISR level for such excited state absorption processes would be helpful to interpret the experiments. For this purpose, the CVS-ISR approach needs to be combined with the ISR for general valence-excited states. Generally, it is also possible to implement the calculation of two-photon absorption processes using the CVS-ISR approach, which can be done in future work. Since core-excited states are meta-stable leading to fast decay processes like Auger or ICD, the description of such resonances would also be an interesting challenge. Generally, complex-absorption potentials (CAP) can be used to describe resonances beyond the ionization threshold of excited molecules.[248,249] The implementation of CAP-ADC can be realized using the `Q-Chem` framework, provided by *Krylov et al.*[249,250] To calculate ICD decay rates, the implementation of the Fano-Stieltjes-ADC method is necessary.[251,252] This approach was successfully used to describe ICD decay rates after core excitations in ArKr clusters.[7] Finally, the CVS approximation can also be applied to calculate ionization potentials of core-excited states (CVS-IP-ADC).[183] An efficient implementation of this approach would be useful to describe photoelectron spectra of medium-sized molecules.

Closing this thesis, I like to mention again that CVS-ADC(2)-x in combination with a diffuse triple-ζ basis set in its Cartesian version can be seen as a black-box method for the calculation of core-excited states of organic molecules. The 6-311++G** basis set, in particular, provides an excellent ratio of accuracy and computational cost. Furthermore, in combination with the CVS-ISR approach and wave function analysis packages, a deeper insight into the nature of core-excited state can be provided.

Appendix

Bibliography

[1] J. C. Bernède. "Organic Photovoltaic Cells: History, Principle and Techniques". *Journal of the Chilean Chemical Society*, 53 (2008) pages 1549–1564.

[2] A. L. Roes, E. A. Alsema, K. Blok and M. K. Patel. "Ex-ante Environmental and Economic Evaluation of Polymer Photovoltaics". *Progress in Photovoltaics: Research and Applications*, 17 (2009) pages 372–393.

[3] T. M. Clarke and J. R. Durrant. "Charge Photogeneration in Organic Solar Cells". *Chemical Reviews*, 110 (2010) pages 6736–6767.

[4] L. Dou, Y. Liu, Z. Hong, G. Li and Y. Yang. "Low-Bandgap Near-IR Conjugated Polymers/Molecules for Organic Electronics". *Chemical Reviews*, 115 (2015) pages 12633–12665.

[5] M. J. Maul, T. R. M. Barends, A. F. Glas, M. J. Cryle, T. Domratcheva, S. Schneider, I. Schlichting and T. Carell. "Crystal Structure and Mechanism of a DNA (6-4) Photolyase". *Angewandte Chemie International Edition*, 47 (2008) pages 10076–10080.

[6] S. Faraji and A. Dreuw. "Physicochemical Mechanism of Light-Driven DNA Repair by (6-4) Photolyases". *Annual Review of Physical Chemistry*, 65 (2014) pages 275–292.

[7] K. Gokhberg, P. Kolorenč, A. I. Kuleff and L. S. Cederbaum. "Site- and energy-selective slow-electron production through intermolecular Coulombic decay". *Nature*, 505 (2014) pages 661–663.

[8] F. Trinter, M. S. Schöffler, H. K. Kim, F. P. Sturm, K. Cole, N. Neumann, A. Vredenborg, J. Williams, I. Bocharova, R. Guillemin *et al.* "Resonant Auger decay driving intermolecular Coulombic decay in molecular dimers". *Nature*, 505 (2014) pages 664–666.

[9] G. Wedler. *Lehrbuch der Physikalischen Chemie*. Wiley-VCH, Weinheim, fifth edition (**2004**).

[10] J. E. Penner-Hahn. "X-ray Absorption Spectroscopy". In "Comprehensive Coordination Chemistry II", Elsevier (**2003**). pages 159–186.

[11] J. Stöhr. *NEXAFS Spectroscopy*. Springer, Berlin (**1992**).

[12] S. G. Urquhart, H. Ade, M. Rafailovich, J. S. Sokolov and Y. Zhang. "Chemical and vibronic effects in the high-resolution near-edge X-ray absorption fine structure spectra of polystyrene isotopomers". *Chemical Physics Letters*, 322 (2000) pages 412–418.

[13] F. Holch, D. Hübner, R. Fink, A. Schöll and E. Umbach. "New set-up for high-quality soft-X-ray absorption spectroscopy of large organic molecules in the gas phase". *Journal of Electron Spectroscopy and Related Phenomena*, 184 (2011) pages 452–456.

[14] G. W. C. Kaye and T. H. Laby. *Tables of Physical and Chemical Constants and Some Mathematical Functions*. Longman, Essex, England, 16th edition (**1995**).

[15] A. J. Atkins, C. R. Jacob and M. Bauer. "Probing the Electronic Structure of Substituted Ferrocenes with High-Resolution XANES Spectroscopy". *Chemistry - A European Journal*, 18 (2012) pages 7021–7025.

[16] J. Schirmer, A. B. Trofimov, K. J. Randall, J. Feldhaus, A. M. Bradshaw, Y. Ma, C. T. Chen and F. Sette. "K-shell excitation of the water, ammonia, and methane molecules using high-resolution photoabsorption spectroscopy". *Physical Review A*, 47 (1993) pages 1136–1147.

[17] G. HÄHNER. "Near edge X-ray absorption fine structure spectroscopy as a tool to probe electronic and structural properties of thin organic films and liquids". *Chemical Society Reviews*, 35 (2006) pages 1244–1255.

[18] J. A. DE GOUW, J. VAN ECK, A. C. PETERS, J. VAN DER WEG AND H. G. M. HEIDEMAN. "Resonant Auger spectra of the $2p^{-1}$ nl states of argon". *Journal of Physics B: Atomic Molecular and Optical Physics*, 28 (1995) pages 2127–2141.

[19] J. A. DE GOUW, J. VAN ECK, J. VAN DER WEG AND H. G. M. HEIDEMAN. "Threshold effects in the Auger decay of argon photoexcited below the $2_{p3/2}$ threshold". *Journal of Physics B: Atomic Molecular and Optical Physics*, 28 (1995) pages 1761–1775.

[20] G. B. ARMEN, H. AKSELA, T. ÅBERG AND S. AKSELA. "The resonant Auger effect". *Journal of Physics B: Atomic Molecular and Optical Physics*, 33 (2000) pages R49–R92.

[21] N. OTTOSSON, G. ÖHRWALL AND O. BJÖRNEHOLM. "Ultrafast charge delocalization dynamics in aqueous electrolytes: New insights from Auger electron spectroscopy". *Chemical Physics Letters*, 543 (2012) pages 1–11.

[22] P. MORIN AND I. NENNER. "Atomic Antoionization Following Very Fast Dissociation of Core-Excited HBr". *Physical Review Letters*, 56 (1986) pages 1913–1916.

[23] D. COULMAN, A. PUSCHMANN, U. HÖFER, H. P. STEINRÜCK, W. WURTH, P. FEULNER AND D. MENZEL. "Excitation, deexcitation, and fragmentation in the core region of condensed and adsorbed water". *Journal of Chemical Physics*, 93 (1990) pages 58–75.

[24] E. M. GARCÍA, A. KIVIMÄKI, L. G. M. PETTERSSON, J. Á. RUIZ, M. CORENO, M. DE SIMONE, R. RICHTER AND K. C. PRINCE. "Fluorescence Emission of Excited Hydrogen Atoms after Core Excitation of Water Vapor". *Physical Review Letters*, 96 (2006) page 063003.

[25] L. S. CEDERBAUM, J. ZOBELEY AND F. TARANTELLI. "Giant Intermolecular Decay and Fragmentation of Clusters". *Physical Review Letters*, 79 (1997) pages 4778–4781.

[26] S. MARBURGER, O. KUGELER, U. HERGENHAHN AND T. MÖLLER. "Experimental Evidence for Interatomic Coulombic Decay in Ne Clusters". *Physical Review Letters*, 90 (2003) page 203401.

[27] T. JAHNKE, H. SANN, T. HAVERMEIER, K. KREIDI, C. STUCK, M. MECKEL, M. SCHÖFFLER, N. NEUMANN, R. WALLAUER, S. VOSS *et al.* "Ultrafast energy transfer between water molecules". *Nature Physics*, 6 (2010) pages 139–142.

[28] U. HERGENHAHN. "Interatomic and intermolecular Coulombic decay: The early years". *Journal of Electron Spectroscopy and Related Phenomena*, 184 (2011) pages 78–90.

[29] P. H. P. HARBACH, M. SCHNEIDER, S. FARAJI AND A. DREUW. "Intermolecular Coulombic Decay in Biology: The Initial Electron Detachment from $FADH^-$ in DNA Photolyases". *The Journal of Physical Chemistry Letters*, 4 (2013) pages 943–949.

[30] C. GARINO, E. BORFECCHIA, R. GOBETTO, J. A. VAN BOKHOVEN AND C. LAMBERTI. "Determination of the electronic and structural configuration of coordination compounds by synchrotron-radiation techniques". *Coordination Chemistry Reviews*, 277-278 (2014) pages 130–186.

[31] C. J. MILNE, T. J. PENFOLD AND M. CHERGUI. "Recent experimental and theoretical developments in time-resolved X-ray spectroscopies". *Coordination Chemistry Reviews*, 277-278 (2014) pages 44–68.

[32] Y. ZUBAVICHUS, A. SHAPORENKO, M. GRUNZE AND M. ZHARNIKOV. "Innershell Absorption Spectroscopy of Amino Acids at All Relevant Absorption Edges". *The Journal of Physical Chemistry A*, 109 (2005) pages 6998–7000.

[33] V. FEYER, O. PLEKAN, R. RICHTER, M. CORENO, M. DE SIMONE, K. C. PRINCE, A. B. TROFIMOV, I. L. ZAYTSEVA AND J. SCHIRMER. "Tautomerism in Cytosine and Uracil: A Theoretical and Experimental X-ray Absorption and Resonant Auger Study". *The Journal of Physical Chemistry A*, 114 (2010) pages 10270–10276.

[34] P. Väterlein, M. Schmelzer, J. Taborski, T. Krause, F. Viczian, M. Bässler, R. Fink, E. Umbach and W. Wurth. "Orientation and bonding of thiophene and 2,2'-bithiophene on Ag(111): a combined near edge extended X-ray absorption fine structure and Xα scattered-wave study". *Surface Science*, 452 (2000) pages 20–32.

[35] M. Alagia, C. Baldacchini, M. G. Betti, F. Bussolotti, V. Carravetta, U. Ekström, C. Mariani and S. Stranges. "Core-shell photoabsorption and photoelectron spectra of gas-phase pentacene: Experiment and theory". *Journal of Chemical Physics*, 122 (2005) page 124305.

[36] H. Ikeura-Sekiguchi and T. Sekiguchi. "Unoccupied electronic states in polythiophene as probed by XAS and RAS". *Surface and Interface Analysis*, 40 (2008) pages 673–675.

[37] C. Vahlberg, M. Linares, S. Villaume, P. Norman and K. Uvdal. "Noradrenaline and a Thiol Analogue on Gold Surfaces: An Infrared Reflection-Absorption Spectroscopy, X-ray Photoelectron Spectroscopy, and Near-Edge X-ray Absorption Fine Structure Spectroscopy Study". *The Journal of Physical Chemistry C*, 115 (2011) pages 165–175.

[38] C. Vahlberg, M. Linares, P. Norman and K. Uvdal. "Phenylboronic Ester- and Phenylboronic Acid-Terminated Alkanethiols on Gold Surfaces". *The Journal of Physical Chemistry C*, 116 (2012) pages 796–806.

[39] R. C. Nelson and J. T. Miller. "An introduction to X-ray absorption spectroscopy and its in situ application to organometallic compounds and homogeneous catalysts". *Catalysis Science & Technology*, 2 (2012) pages 461–470.

[40] N. Mimura, S. Tsubota, K. Murata, K. K. Bando, J. J. Bravo-Suárez, M. Haruta and S. T. Oyama. "Gas-phase radical generation by Ti oxide clusters supported on silica: application to the direct epoxidation of propylene to propylene oxide using molecular oxygen as an oxidant". *Catalysis Letters*, 110 (2006) pages 47–51.

[41] R. Kakavandi, S.-A. Savu, L. Sorace, D. Rovai, M. Mannini and M. B. Casu. "Core-Hole Screening, Electronic Structure, and Paramagnetic Character in Thin Films of Organic Radicals Deposited on SiO_2/Si(111)". *The Journal of Physical Chemistry C*, 118 (2014) pages 8044–8049.

[42] M. Alagia, E. Bodo, P. Decleva, S. Falcinelli, A. Ponzi, R. Richter and S. Stranges. "The soft X-ray absorption spectrum of the allyl free radical." *Physical Chemistry Chemical Physics*, 15 (2013) pages 1310–1318.

[43] A. Dreuw and M. Head-Gordon. "Single-reference ab initio methods for the calculation of excited states of large molecules." *Chemical Reviews*, 105 (2005) pages 4009–4037.

[44] L. S. Cederbaum, W. Domcke and J. Schirmer. "Many-body theory of core holes". *Physical Review A*, 22 (1980) pages 206–222.

[45] A. Barth and L. S. Cederbaum. "Many-body theory of core-valence excitations". *Physical Review A*, 23 (1981) pages 1038–1061.

[46] L. C. Snyder. "Core-Electron Binding Energies and Slater Atomic Shielding Constants". *Journal of Chemical Physics*, 55 (1971) pages 95–99.

[47] U. Gelius. "Binding Energies and Chemical Shifts in ESCA". *Physica Scripta*, 9 (1974) pages 113–147.

[48] H. Siegbahn and L. Karlsson. "Photoelectron Sprectroscopy". In W. Mehlhorn, editor, "Corpuscles and Radiation in Matter I", Springer, Berlin, Heidelberg (**1982**).

[49] J. Schirmer, M. Braunstein, M.-T. Lee and V. McKoy. "Core Relaxation Effects in Molecular Photoionization". In "VUV and Soft X-Ray Photoionization", Springer US, New York (**1996**). pages 105–133.

[50] M. Kutzner. "Core relaxation effects in inner shell photoionization of atoms". *Radiation Physics and Chemistry*, 70 (2004) pages 95–104.

[51] G. D. Purvis III and R. J. Bartlett. "A full coupled-cluster singles and doubles model: The inclusion of disconnected triples". *Journal of Chemical Physics*, 76 (1982) pages 1910–1918.

[52] S. Coriani, T. Fransson, O. Christiansen and P. Norman. "Asymmetric-Lanczos-Chain-Driven Implementation of Electronic Resonance Convergent Coupled-Cluster Linear Response Theory". *Journal of Chemical Theory and Computation*, 8 (2012) pages 1616–1628.

[53] S. Coriani, O. Christiansen, T. Fransson and P. Norman. "Coupled-cluster response theory for near-edge x-ray-absorption fine structure of atoms and molecules". *Physical Review A*, 85 (2012) page 022507.

[54] S. Coriani and H. Koch. "Communication: X-ray absorption spectra and core-ionization potentials within a core-valence separated coupled cluster framework". *Journal of Chemical Physics*, 143 (2015) page 181103.

[55] J. Geertsen, M. Rittby and R. J. Bartlett. "The equation-of-motion coupled-cluster method: Excitation energies of Be and CO". *Chemical Physics Letters*, 164 (1989) pages 57–62.

[56] A. I. Krylov. "Equation-of-Motion Coupled-Cluster Methods for Open-Shell and Electronically Excited Species: The Hitchhiker's Guide to Fock Space". *Annual Review of Physical Chemistry*, 59 (2008) pages 433–462.

[57] N. A. Besley. "Equation of motion coupled cluster theory calculations of the X-ray emission spectroscopy of water". *Chemical Physics Letters*, 542 (2012) pages 42–46.

[58] R. J. Bartlett. "Coupled-cluster theory and its equation-of-motion extensions". *Wiley Interdisciplinary Reviews: Computational Molecular Science*, 2 (2012) pages 126–138.

[59] B. Peng, P. J. Lestrange, J. J. Goings, M. Caricato and X. Li. "Energy-Specific Equation-of-Motion Coupled-Cluster Methods for High-Energy Excited States: Application to K-edge X-ray Absorption Spectroscopy". *Journal of Chemical Theory and Computation*, 11 (2015) pages 4146–4153.

[60] H. Nakatsuji and K. Hirao. "Cluster expansion of the wavefunction. Pseduo-orbital theory applied to spin correlation". *Chemical Physics Letters*, 47 (1977) pages 569–571.

[61] H. Nakatsuji. "Cluster expansion of the wavefunction. Calculation of electron correlations in ground and excited states by SAC and SAC CI theories". *Chemical Physics Letters*, 67 (1979) pages 334–342.

[62] H. Nakatsuji. "Cluster expansion of the wavefunction. Electron correlations in ground and excited states by SAC (symmetry-adapted-cluster) and SAC CI theories". *Chemical Physics Letters*, 67 (1979) pages 329–333.

[63] K. Kuramoto, M. Ehara and H. Nakatsuji. "Theoretical fine spectroscopy with symmetry adapted cluster–configuration interaction general-R method: First-row K-shell ionizations and their satellites". *Journal of Chemical Physics*, 122 (2005) page 014304.

[64] Y. Ohtsuka and H. Nakatsuji. "Inner-shell ionizations and satellites studied by the open-shell reference symmetry-adapted cluster/symmetry-adapted cluster configuration-interaction method". *Journal of Chemical Physics*, 124 (2006) page 054110.

[65] M. Ehara and H. Nakatsuji. "Development Of Sac-Ci General-R Method For Theoretical Fine Spectroscopy". In "Recent Progress in Coupled Cluster Methods", Springer Netherlands, Dordrecht (**2010**). pages 79–112.

[66] O. Christiansen, H. Koch and P. Jørgensen. "The second-order approximate coupled cluster singles and doubles model CC2". *Chemical Physics Letters*, 243 (1995) pages 409–418.

[67] T. Fransson, S. Coriani, O. Christiansen and P. Norman. "Carbon X-ray absorption spectra of fluoroethenes and acetone: A study at the coupled cluster, density functional, and static-exchange levels of theory". *Journal of Chemical Physics*, 138 (2013) page 124311.

[68] E. Runge and E. K. U. Gross. "Density-functional theory for time-dependent systems". *Physical Review Letters*, 52 (1984) pages 997–1000.

[69] E. K. U. Gross and W. Kohn. "Local density-functional theory of frequency-dependent linear response". *Physical Review Letters*, 55 (1985) pages 2850–2852.

[70] E. K. U. Gross and W. Kohn. "Time-Dependent Density-Functional Theory". *Advances in Quantum Chemistry*, 21 (1990) pages 255–291.

[71] P. Norman, D. M. Bishop, H. J. A. Jensen and J. Oddershede. "Nonlinear response theory with relaxation: The first-order hyperpolarizability". *Journal of Chemical Physics*, 123 (2005) page 194103.

[72] G. Tu, Z. Rinkevicius, O. Vahtras, H. Ågren, U. Ekström, P. Norman and V. Carravetta. "Self-interaction-corrected time-dependent density-functional-theory calculations of x-ray-absorption spectra". *Physical Review A*, 76 (2007) page 022506.

[73] Y. Zhang, W. Hua, K. Bennett and S. Mukamel. "Nonlinear Spectroscopy of Core and Valence Excitations Using Short X-Ray Pulses: Simulation Challenges." In N. Ferré, M. Filatov and M. Huix-Rotllant, editors, "Topics in Current Chemistry 368 - Density-Functional Methods for Excited States", Springer Berlin Heidelberg, Berlin, Heidelberg (**2015**). pages 273–347.

[74] F. A. Asmuruf and N. A. Besley. "Calculation of near-edge X-ray absorption fine structure with the CIS(D) method". *Chemical Physics Letters*, 463 (2008) pages 267–271.

[75] N. A. Besley and F. A. Asmuruf. "Time-dependent density functional theory calculations of the spectroscopy of core electrons". *Physical Chemistry Chemical Physics*, 12 (2010) pages 12024–12039.

[76] J. Schirmer. "Beyond the random-phase approximation: A new approximation scheme for the polarization propagator". *Physical Review A*, 26 (1982) pages 2395–2416.

[77] A. B. Trofimov, G. Stelter and J. Schirmer. "A consistent third-order propagator method for electronic excitation". *Journal of Chemical Physics*, 111 (1999) page 9982.

[78] J. Schirmer and A. B. Trofimov. "Intermediate state representation approach to physical properties of electronically excited molecules". *Journal of Chemical Physics*, 120 (2004) pages 11449–11464.

[79] A. Dreuw and M. Wormit. "The algebraic diagrammatic construction scheme for the polarization propagator for the calculation of excited states". *Wiley Interdisciplinary Reviews: Computational Molecular Science*, 5 (2015) pages 82–95.

[80] C. Møller and M. S. Plesset. "Note on an approximation treatment for many-electron systems". *Physical Review*, 46 (1934) pages 618–622.

[81] P. H. P. Harbach, M. Wormit and A. Dreuw. "The third-order algebraic diagrammatic construction method (ADC(3)) for the polarization propagator for closed-shell molecules: Efficient implementation and benchmarking." *Journal of Chemical Physics*, 141 (2014) page 064113.

[82] J. H. Starcke, M. Wormit and A. Dreuw. "Unrestricted algebraic diagrammatic construction scheme of second order for the calculation of excited states of medium-sized and large molecules". *Journal of Chemical Physics*, 130 (2009) page 024104.

[83] F. Mertins and J. Schirmer. "Algebraic propagator approaches and intermediate-state representations. I. The biorthogonal and unitary coupled-cluster methods". *Physical Review A*, 53 (1996) pages 2140–2152.

[84] F. Plasser, B. Thomitzni, S. A. Bäppler, J. Wenzel, D. R. Rehn, M. Wormit and A. Dreuw. "Statistical Analysis of Electronic Excitation Processes: Quantification of Location, Compactness, and Excitonic Correlation Effects". *Journal of Computational Chemistry*, 36 (2015) pages 1609–1620.

[85] M. Head-Gordon, A. M. Graña, D. Maurice and C. A. White. "Analysis of Electronic Transitions as the Difference of Electron Attachment and Detachment Densities". *The Journal of Physical Chemistry*, 99 (1995) pages 14261–14270.

[86] F. Plasser, S. A. Bäppler, M. Wormit and A. Dreuw. "New tools for the systematic analysis and visualization of electronic excitations. II. Applications". *Journal of Chemical Physics*, 141 (2014) page 024107.

[87] F. Plasser, M. Wormit and A. Dreuw. "New tools for the systematic analysis and visualization of electronic excitations. I. Formalism". *Journal of Chemical Physics*, 141 (2014) page 024106.

[88] S. A. Bäppler, F. Plasser, M. Wormit and A. Dreuw. "Exciton analysis of many-body wave functions: Bridging the gap between the quasiparticle and molecular orbital pictures". *Physical Review A*, 90 (2014) page 052521.

[89] O. Plekan, V. Feyer, R. Richter, M. Coreno, M. de Simone, K. C. Prince, A. B. Trofimov, E. V. Gromov, I. L. Zaytseva and J. Schirmer. "A theoretical and experimental study of the near edge X-ray absorption fine structure (NEXAFS) and X-ray photoelectron spectra (XPS) of nucleobases: Thymine and adenine". *Chemical Physics*, 347 (2008) pages 360–375.

[90] A. B. Trofimov, T. E. Moskovskaya, E. V. Gromov, H. Köppel and J. Schirmer. "Theoretical study of K-shell excitations in formaldehyde". *Physical Review A*, 64 (2001) page 022504.

[91] A. B. Trofimov, T. E. Moskovskaya, E. V. Gromov, N. M. Vitkovskaya and J. Schirmer. "Core-level electronic spectra in ADC(2) approximation for polarization propagator: Carbon monoxide and nitrogen molecules". *Journal of Structural Chemistry*, 41 (2000) pages 483–494.

[92] J. Schirmer and A. B. Trofimov. "Private Communications, 2012".

[93] M. Wormit, D. R. Rehn, P. H. P. Harbach, J. Wenzel, C. M. Krauter, E. Epifanovsky and A. Dreuw. "Investigating excited electronic states using the algebraic diagrammatic construction (ADC) approach of the polarisation propagator". *Molecular Physics*, 112 (2014) pages 774–784.

[94] Y. Shao, Z. Gan, E. Epifanovsky, A. T. B. Gilbert, M. Wormit, J. Kussmann, A. W. Lange, A. Behn, J. Deng, X. Feng *et al.* "Advances in molecular quantum chemistry contained in the Q-Chem 4 program package". *Molecular Physics*, 113 (2015) pages 184–215.

[95] J. Wenzel, A. Dreuw and I. Burghardt. "Charge and energy transfer in a bithiophene perylenediimide based donor-acceptor-donor system for use in organic photovoltaics". *Physical Chemistry Chemical Physics*, 15 (2013) pages 11704–11716.

[96] J. Wenzel, M. Wormit and A. Dreuw. "Calculating Core-Level Excitations and X-Ray Absorption Spectra of Medium-Sized Closed-Shell Molecules with the Algebraic-Diagrammatic Construction Scheme for the Polarization Propagator". *Journal of Computational Chemistry*, 35 (2014) pages 1900–1915.

[97] J. Wenzel, M. Wormit and A. Dreuw. "Calculating X-ray absorption spectra of open-shell molecules with the unrestricted algebraic-diagrammatic construction scheme for the polarization propagator". *Journal of Chemical Theory and Computation*, 10 (2014) pages 4583–4598.

[98] J. Wenzel, A. Holzer, M. Wormit and A. Dreuw. "Analysis and comparison of CVS-ADC approaches up to third order for the calculation of core-excited states". *Journal of Chemical Physics*, 142 (2015) page 214104.

[99] J. Wenzel and A. Dreuw. "Physical properties, exciton analysis and visualization of core-excited states: an intermediate state representation approach". *submitted for publication in Journal of Chemical Theory and Computation*, (2016).

[100] A. Barth and J. Schirmer. "Theoretical core-level excitation spectra of N_2 and CO by a new polarisation propagator method". *Journal of Physics B: Atomic and Molecular Physics*, 18 (1985) pages 867–885.

[101] A. Szabo and N. S. Ostlund. *Modern Quantum Chemistry*. McGraw-Hill Publishing Company, New York, first edition, revised edition (**1989**).

[102] A. D. Becke. "Perspective: Fifty years of density-functional theory in chemical physics". *Journal of Chemical Physics*, 140 (2014) page 18A301.

[103] R. J. Bartlett and M. Musiał. "Coupled-cluster theory in quantum chemistry". *Reviews of Modern Physics*, 79 (2007) pages 291–352.

[104] J. E. D. Bene, R. Ditchfield and J. A. Pople. "Self-Consistent Molecular Orbital Methods. X. Molecular Orbital Studies of Excited States with Minimal and Extended Basis Sets". *Journal of Chemical Physics*, 55 (1971) pages 2236–2241.

[105] W. Thiel. "Semiempirical quantum-chemical methods". *Wiley Interdisciplinary Reviews: Computational Molecular Science*, 4 (2014) pages 145–157.

[106] P. G. Szalay, T. Müller, G. Gidofalvi, H. Lischka and R. Shepard. "Multiconfiguration Self-Consistent Field and Multireference Configuration Interaction Methods and Applications". *Chemical Reviews*, 112 (2012) pages 108–181.

[107] B. O. Roos. "The Complete Active Space Self-Consistent Field Method and its Applications in Electronic Structure Calculations". *Advances in Chemical Physics*, 69 (1987) pages 399–445.

[108] T. Helgaker, P. Jørgensen and J. Olsen. *Molecular Electronic-Structure Theory*. John Wiley & Sons Ltd, Chichester, West Sussex (**2000**).

[109] R. Krishnan, J. S. Binkley, R. Seeger and J. A. Pople. "Self-consistent molecular orbital methods. XX. A basis set for correlated wave functions". *Journal of Chemical Physics*, 72 (1980) pages 650–654.

[110] A. D. McLean and G. S. Chandler. "Contracted Gaussian basis sets for molecular calculations. I. Second row atoms, Z=11–18". *Journal of Chemical Physics*, 72 (1980) pages 5639–5648.

[111] W. J. Hehre, R. Ditchfield and J. A. Pople. "Self-Consistent Molecular Orbital Methods. XII. Further Extensions of Gaussian-Type Basis Sets for Use in Molecular Orbital Studies of Organic Molecules". *Journal of Chemical Physics*, 56 (1972) pages 2257–2261.

[112] P. C. Hariharan and J. A. Pople. "The influence of polarization functions on molecular orbital hydrogenation energies". *Theoretica Chimica Acta*, 28 (1973) pages 213–222.

[113] T. Clark, J. Chandrasekhar, G. W. Spitznagel and P. V. R. Schleyer. "Efficient diffuse function-augmented basis sets for anion calculations. III. The 3-21+G basis set for first-row elements, Li–F". *Journal of Computational Chemistry*, 4 (1983) pages 294–301.

[114] M. J. Frisch, J. A. Pople and J. S. Binkley. "Self-consistent molecular orbital methods 25. Supplementary functions for Gaussian basis sets". *Journal of Chemical Physics*, 80 (1984) pages 3265–3269.

[115] T. H. Dunning Jr. "Gaussian basis sets for use in correlated molecular calculations. I. The atoms boron through neon and hydrogen". *Journal of Chemical Physics*, 90 (1989) pages 1007–1023.

[116] R. A. Kendall, T. H. Dunning Jr and R. J. Harrison. "Electron affinities of the first-row atoms revisited. Systematic basis sets and wave functions". *Journal of Chemical Physics*, 96 (1992) pages 6796–6806.

[117] D. E. Woon and T. H. Dunning Jr. "Gaussian basis sets for use in correlated molecular calculations. IV. Calculation of static electrical response properties". *Journal of Chemical Physics*, 100 (1994) pages 2975–2988.

[118] F. Weigend and R. Ahlrichs. "Balanced basis sets of split valence, triple zeta valence and quadruple zeta valence quality for H to Rn: Design and assessment of accuracy." *Physical Chemistry Chemical Physics*, 7 (2005) pages 3297–3305.

[119] D. Rappoport and F. Furche. "Property-optimized Gaussian basis sets for molecular response calculations". *Journal of Chemical Physics*, 133 (2010) page 134105.

[120] K. A. Peterson, D. E. Woon and T. H. Dunning Jr. "Benchmark calculations with correlated molecular wave functions. IV. The classical barrier height of the $H+H_2 \rightarrow H_2+H$ reaction". *Journal of Chemical Physics*, 100 (1994) pages 7410–7415.

[121] K. A. Peterson and C. Puzzarini. "Systematically convergent basis sets for transition metals. II. Pseudopotential-based correlation consistent basis sets for the group 11 (Cu, Ag, Au) and 12 (Zn, Cd, Hg) elements". *Theoretical Chemistry Accounts: Theory, Computation, and Modeling (Theoretica Chimica Acta)*, 114 (2005) pages 283–296.

[122] J. D. Watts, J. Gauss and R. J. Bartlett. "Coupled-cluster methods with noniterative triple excitations for restricted open-shell Hartree–Fock and other general single determinant reference functions. Energies and analytical gradients". *Journal of Chemical Physics*, 98 (1993) pages 8718–8733.

[123] P. Hohenberg and W. Kohn. "Inhomogeneous Electron Gas". *Physical Review*, 136 (1964) pages B864–B871.

[124] W. KOHN AND L. J. SHAM. "Self-Consistent Equations Including Exchange and Correlation Effects". *Physical Review*, 140 (1965) pages A1133–A1138.

[125] C. LEE, W. YANG AND R. G. PARR. "Development of the Colle-Salvetti correlation-energy formula into a functional of the electron density". *Physical Review B*, 37 (1988) pages 785–789.

[126] A. D. BECKE. "Density-functional thermochemistry. III. The role of exact exchange". *Journal of Chemical Physics*, 98 (1993) pages 5648–5652.

[127] A. D. BECKE. "A new mixing of hartree-fock and local density-functional theories". *Journal of Chemical Physics*, 98 (1993) pages 1372–1377.

[128] R. G. PARR AND W. YANG. *Density-Functional Theory of Atoms and Molecules*. Oxford Science Publication, New York (**1989**).

[129] A. D. BECKE. "Density-functional exchange-energy approximation with correct asymptotic-behavior". *Physical Review A*, 38 (1988) pages 3098–3100.

[130] P. H. P. HARBACH AND A. DREUW. In P. COMBA, editor, "Modeling of Molecular Properties", Wiley-VCH Verlag, Weinheim, Germany (**2011**). pages 29–47.

[131] H. SEKINO AND R. J. BARTLETT. "A linear response, coupled-cluster theory for excitation energy". *International Journal of Quantum Chemistry*, 18 (1984) pages 255–265.

[132] H. J. MONKHORST. "Calculation of properties with the coupled-cluster method". *International Journal of Quantum Chemistry*, 12 (1977) pages 421–432.

[133] E. DALGAARD AND H. J. MONKHORST. "Some aspects of the time-dependent coupled-cluster approach to dynamic response functions". *Physical Review A*, 28 (1983) pages 1217–1222.

[134] A. L. FETTER AND J. D. WALECKA. *Quantum theory of many-particle systems*. McGraw-Hill, New York (**1971**).

[135] Z.-L. CAI, K. SENDT AND J. R. REIMERS. "Failure of density-functional theory and time-dependent density-functional theory for large extended π systems". *Journal of Chemical Physics*, 117 (2002) pages 5543–5549.

[136] S. GRIMME AND M. PARAC. "Substantial errors from time-dependent density functional theory for the calculation of excited states of large π systems". *Chemphyschem : a European journal of chemical physics and physical chemistry*, 4 (2003) pages 292–295.

[137] A. DREUW, J. L. WEISMAN AND M. HEAD-GORDON. "Long-range charge-transfer excited states in time-dependent density functional theory require non-local exchange". *Journal of Chemical Physics*, 119 (2003) pages 2943–2946.

[138] E. R. DAVIDSON. "The iterative calculation of a few of the lowest eigenvalues and corresponding eigenvectors of large real-symmetric matrices". *Journal of Computational Physics*, 17 (1975) pages 87–94.

[139] M. E. CASIDA AND M. HUIX-ROTLLANT. "Progress in time-dependent density-functional theory". *Annual Review of Physical Chemistry*, 63 (2012) pages 287–323.

[140] A. D. LAURENT AND D. JACQUEMIN. "TD-DFT benchmarks: A review". *International Journal of Quantum Chemistry*, 113 (2013) pages 2019–2039.

[141] M. E. CASIDA. "Time-dependent density functional response theory for molecules". In "Recent advances in density functional methods, Part I", World Scientific, Singapore (**1995**).

[142] S. HIRATA AND M. HEAD-GORDON. "Time-dependent density functional theory within the Tamm-Dancoff approximation". *Chemical Physics Letters*, 314 (1999) pages 291–299.

[143] O. CHRISTIANSEN, A. HALKIER, H. KOCH, P. JØRGENSEN AND T. HELGAKER. "Integral-direct coupled cluster calculations of frequency-dependent polarizabilities, transition probabilities and excited-state properties". *Journal of Chemical Physics*, 108 (1998) pages 2801–2816.

[144] M. KÁLLAY AND J. GAUSS. "Calculation of excited-state properties using general coupled-cluster and configuration-interaction models". *Journal of Chemical Physics*, 121 (2004) pages 9257–9269.

[145] H. Nakatsuji. "Description of two-and many-electron processes by the SAC-CI method". *Chemical Physics Letters*, 177 (1991) pages 331–337.

[146] J. Vinson, J. J. Rehr, J. J. Kas and E. L. Shirley. "Bethe-Salpeter equation calculations of core excitation spectra". *Physical Review B*, 83 (2011) page 115106.

[147] M. Head-Gordon, R. J. Rico, M. Oumi and T. J. Lee. "A doubles correction to electronic excited states from configuration interaction in the space of single substitutions". *Chemical Physics Letters*, 219 (1994) pages 21–29.

[148] W. J. Hunt and W. A. I. Goddard. "Excited states of H_2O using improved virtual orbitals". *Chemical Physics Letters*, 3 (1969) pages 414–418.

[149] H. Ågren, V. Carravetta, O. Vahtras and L. G. M. Pettersson. "Direct, Atomic Orbital, Static Exchange Calculations of Photoabsorption Spectra of Large Molecules and Clusters". *Chemical Physics Letters*, 222 (1994) pages 75–81.

[150] C. C. J. Roothaan. "Self-Consistent Field Theory for Open Shells of Electronic Systems". *Reviews of Modern Physics*, 32 (1960) pages 179–185.

[151] A. T. B. Gilbert, N. A. Besley and P. M. W. Gill. "Self-Consistent Field Calculations of Excited States Using the Maximum Overlap Method (MOM)". *The Journal of Physical Chemistry A*, 112 (2008) pages 13164–13171.

[152] P. Norman. "A perspective on nonresonant and resonant electronic response theory for time-dependent molecular properties". *Physical Chemistry Chemical Physics*, 13 (2011) pages 20519–20535.

[153] T. Helgaker, S. Coriani, P. Jørgensen, K. Kristensen, J. Olsen and K. Ruud. "Recent Advances in Wave Function-Based Methods of Molecular-Property Calculations". *Chemical Reviews*, 112 (2012) pages 543–631.

[154] J. Kauczor, P. Norman, O. Christiansen and S. Coriani. "Communication: A reduced-space algorithm for the solution of the complex linear response equations used in coupled cluster damped response theory". *Journal of Chemical Physics*, 139 (2013) page 211102.

[155] M. J. Frisch, G. W. Trucks, H. B. Schlegel, G. E. Scuseria, M. A. Robb, J. R. Cheeseman, G. Scalmani, V. Barone, B. Mennucci, G. A. Petersson *et al.* "Gaussian 09". (2009).

[156] O. Christiansen, P. Jørgensen and C. Hättig. "Response functions from Fourier component variational perturbation theory applied to a time-averaged quasienergy". *International Journal of Quantum Chemistry*, 68 (1998) pages 1–52.

[157] S. R. Gwaltney, M. Nooijen and R. J. Bartlett. "Simplified methods for equation-of-motion coupled-cluster excited state calculations". *Chemical Physics Letters*, 248 (1996) pages 189–198.

[158] P. S. Bagus. "Self-Consistent-Field Wave Functions for Hole States of Some Ne-Like and Ar-Like Ions". *Physical Review*, 139 (1965) pages A619–A634.

[159] H.-l. Hsu, E. R. Davidson and R. M. Pitzer. "An SCF method for hole states". *Journal of Chemical Physics*, 65 (1976) page 609.

[160] A. Naves de Brito, N. Correia, S. Svensson and H. Ågren. "A theoretical study of x-ray photoelectron spectra of model molecules for polymethylmethacrylate". *Journal of Chemical Physics*, 95 (1991) pages 2965–2974.

[161] M. Stener, G. Fronzoni and M. de Simone. "Time dependent density functional theory of core electrons excitations". *Chemical Physics Letters*, 373 (2003) pages 115–123.

[162] N. A. Besley and A. Noble. "Time-Dependent Density Functional Theory Study of the X-ray Absorption Spectroscopy of Acetylene, Ethylene, and Benzene on Si(100)". *The Journal of Physical Chemistry C*, 111 (2007) pages 3333–3340.

[163] Y. Imamura, T. Otsuka and H. Nakai. "Description of core excitations by time-dependent density functional theory with local density approximation, generalized gradient approximation, meta-generalized gradient approximation, and hybrid functionals". *Journal of Computational Chemistry*, 28 (2007) pages 2067–2074.

[164] P. Norman, D. M. Bishop, H. J. A. Jensen and J. Oddershede. "Near-resonant absorption in the time-dependent self-consistent field and multiconfigurational self-consistent field approximations". *Journal of Chemical Physics*, 115 (2001) pages 10323–10334.

[165] U. Ekström, P. Norman, V. Carravetta and H. Ågren. "Polarization Propagator for X-Ray Spectra". *Physical Review Letters*, 97 (2006) page 143001.

[166] T. Fransson, I. Zhovtobriukh, S. Coriani, K. T. Wikfeldt, P. Norman and L. G. M. Pettersson. "Requirements of first-principles calculations of X-ray absorption spectra of liquid water". *Physical Chemistry Chemical Physics*, 18 (2016) pages 566–583.

[167] J. P. Perdew and A. Zunger. "Self-interaction correction to density-functional approximations for many-electron systems". *Physical Review B*, 23 (1981) pages 5048–5079.

[168] Y. Tawada, T. Tsuneda, S. Yanagisawa, T. Yanai and K. Hirao. "A long-range-corrected time-dependent density functional theory". *Journal of Chemical Physics*, 120 (2004) pages 8425–8433.

[169] T. Yanai, D. P. Tew and N. C. Handy. "A new hybrid exchange–correlation functional using the Coulomb-attenuating method (CAM-B3LYP)". *Chemical Physics Letters*, 393 (2004) pages 51–57.

[170] J. D. Biggs, Y. Zhang, D. Healion and S. Mukamel. "Watching energy transfer in metalloporphyrin heterodimers using stimulated X-ray Raman spectroscopy". *Proceedings of the National Academy of Sciences of the United States of America*, 110 (2013) pages 15597–15601.

[171] Y. Zhang, J. D. Biggs, N. Govind and S. Mukamel. "Monitoring Long-Range Electron Transfer Pathways in Proteins by Stimulated Attosecond Broadband X-ray Raman Spectroscopy". *The Journal of Physical Chemistry Letters*, 5 (2014) pages 3656–3661.

[172] J.-W. Song, S. Tokura, T. Sato, M. A. Watson and K. Hirao. "An improved long-range corrected hybrid exchange-correlation functional including a short-range Gaussian attenuation (LCgau-BOP)". *Journal of Chemical Physics*, 127 (2007) page 154109.

[173] J.-W. Song, M. A. Watson, A. Nakata and K. Hirao. "Core-excitation energy calculations with a long-range corrected hybrid exchange-correlation functional including a short-range Gaussian attenuation (LCgau-BOP)". *Journal of Chemical Physics*, 129 (2008) page 184113.

[174] N. A. Besley, M. J. G. Peach and D. J. Tozer. "Time-dependent density functional theory calculations of near-edge X-ray absorption fine structure with short-range corrected functionals". *Physical Chemistry Chemical Physics*, 11 (2009) pages 10350–10358.

[175] A. Nakata, Y. Imamura, T. Otsuka and H. Nakai. "Time-dependent density functional theory calculations for core-excited states: Assessment of standard exchange-correlation functionals and development of a novel hybrid functional". *Journal of Chemical Physics*, 124 (2006) page 094105.

[176] A. Nakata, Y. Imamura and H. Nakai. "Hybrid exchange-correlation functional for core, valence, and Rydberg excitations: Core-valence-Rydberg B3LYP". *Journal of Chemical Physics*, 125 (2006) page 064109.

[177] G. C. Wick. "The evaluation of the collision matrix". *Physical Review*, 80 (1950) pages 268–272.

[178] T. D. Crawford. "Practical Coupled-Cluster Theory". In "An Introduction to Coupled-Cluster Theory", www.uam.es/docencia/quimcursos/Docs/Knowledge/Fundamental_Theory/cc/node13.html and ff, (last accessed online 22.01.2016) (**1996**).

[179] G. Fronzoni, R. De Francesco, M. Stener and P. Decleva. "Spin-orbit relativistic calculations of the core excitation spectra of SO_2". *Journal of Chemical Physics*, 126 (2007) page 134308.

[180] J. Schirmer, A. B. Trofimov and G. Stelter. "A non-Dyson third-order approximation scheme for the electron propagator". *Journal of Chemical Physics*, 109 (1998) pages 4734–4744.

[181] A. B. Trofimov and J. Schirmer. "An Efficient Polarization Propagator Approach to Valence Electron-Excitation Spectra". *Journal of Physics B: Atomic Molecular and Optical Physics*, 28 (1995) pages 2299–2324.

[182] E. Epifanovsky, M. Wormit, T. Kuś, A. Landau, D. Zuev, K. Khistyaev, P. Manohar, I. Kaliman, A. Dreuw and A. I. Krylov. "New implementation of high-level correlated methods using a general block tensor library for high-performance electronic structure calculations". *Journal of Computational Chemistry*, 34 (2013) pages 2293–2309.

[183] J. Schirmer and A. Thiel. "An intermediate state representation approach to K-shell ionization in molecules. I. Theory". *Journal of Chemical Physics*, 115 (2001) pages 10621–10635.

[184] T. Helgaker, W. Klopper, H. Koch and J. Noga. "Basis-set convergence of correlated calculations on water". *Journal of Chemical Physics*, 106 (1997) pages 9639–9646.

[185] A. Halkier, T. Helgaker, P. Jørgensen, W. Klopper, H. Koch, J. Olsen and A. K. Wilson. "Basis-set convergence in correlated calculations on Ne, N_2, and H_2O". *Chemical Physics Letters*, 286 (1998) pages 243–252.

[186] D. E. Woon and T. H. Dunning Jr. "Gaussian basis sets for use in correlated molecular calculations. V. Core-valence basis sets for boron through neon". *Journal of Chemical Physics*, 103 (1995) pages 4572–4585.

[187] I. Bâldea, B. Schimmelpfennig, M. Plaschke, J. Rothe, J. Schirmer, A. B. Trofimov and T. Fanghänel. "C 1s near edge X-ray absorption fine structure (NEXAFS) of substituted benzoic acids - A theoretical and experimental study". *Journal of Electron Spectroscopy and Related Phenomena*, 154 (2007) pages 109–118.

[188] M. Tronc, G. C. King and F. H. Read. "Carbon K-shell excitation in small molecules by high-resolution electron impact". *Journal of Physics B: Atomic and Molecular Physics*, 12 (1979) pages 137–157.

[189] M. Alagia, M. Lavollée, R. Richter, U. Ekström, V. Carravetta, D. Stranges, B. Brunetti and S. Stranges. "Probing the potential energy surface by high-resolution x-ray absorption spectroscopy: The umbrella motion of the core-excited CH_3 free radical". *Physical Review A*, 76 (2007) page 022509.

[190] S. Knippenberg, D. R. Rehn, M. Wormit, J. H. Starcke, I. L. Rusakova, A. B. Trofimov and A. Dreuw. "Calculations of nonlinear response properties using the intermediate state representation and the algebraic-diagrammatic construction polarization propagator approach: Two-photon absorption spectra". *Journal of Chemical Physics*, 136 (2012) page 064107.

[191] R. McLaren, S. Clark, I. Ishii and A. Hitchcock. "Absolute oscillator strengths from K-shell electron-energy-loss spectra of the fluoroethenes and 1,3-perfluorobutadiene". *Physical Review A*, 36 (1987) pages 1683–1701.

[192] F. Weigend and M. Häser. "RI-MP2: first derivatives and global consistency". *Theoretical Chemistry Accounts: Theory, Computation, and Modeling (Theoretica Chimica Acta)*, 97 (1997) pages 331–340.

[193] C. Hättig and F. Weigend. "CC2 excitation energy calculations on large molecules using the resolution of the identity approximation". *Journal of Chemical Physics*, 113 (2000) pages 5154–5161.

[194] F. Weigend, M. Häser, H. Patzelt and R. Ahlrichs. "RI-MP2: optimized auxiliary basis sets and demonstration of efficiency". *Chemical Physics Letters*, 294 (1998) pages 143–152.

[195] A. Schäfer, H. Horn and R. Ahlrichs. "Fully optimized contracted Gaussian basis sets for atoms Li to Kr". *Journal of Chemical Physics*, 97 (1992) pages 2571–2577.

[196] R. Ahlrichs, M. Bär, M. Häser, H. Horn and C. Kölmel. "Electronic structure calculations on workstation computers: The program system turbomole". *Chemical Physics Letters*, 162 (1989) pages 165–169.

[197] N. S. Lewis. "Toward Cost-Effective Solar Energy Use". *Science*, 315 (2007) pages 798–801.

[198] M. Katsuhara, I. Yagi, A. Yumoto, M. Noda, N. Hirai, R. Yasuda, T. Moriwaki, S. Ushikura, A. Imaoka, T. Urabe *et al.* "A flexible OLED display with an OTFT backplane made by scalable manufacturing process". *Journal of the Society for Information Display*, 18 (2010) pages 399–404.

[199] S.-Y. Chang, H.-C. Liao, Y.-T. Shao, Y.-M. Sung, S.-H. Hsu, C.-C. Ho, W.-F. Su and Y.-F. Chen. "Enhancing the efficiency of low bandgap conducting polymer bulk heterojunction solar cells using P3HT as a morphology control agent". *Journal of Materials Chemistry A*, 1 (2013) pages 2447–2452.

[200] J. Cremer, E. Mena-Osteritz, N. G. Pschierer, K. Müllen and P. Bäuerle. "Dye-functionalized head-to-tail coupled oligo(3-hexylthiophenes)—perylene–oligothiophene dyads for photovoltaic applications". *Organic & Biomolecular Chemistry*, 3 (2005) pages 985–995.

[201] A. Petrella, J. Cremer, L. De Cola, P. Bäuerle and R. M. Williams. "Charge transfer processes in conjugated triarylamine-oligothiophene-perylenemonoimide dendrimers." *The Journal of Physical Chemistry A*, 109 (2005) pages 11687–11695.

[202] L. X. Chen, S. Xiao and L. Yu. "Dynamics of photoinduced electron transfer in a molecular donor-acceptor quartet." *The Journal of Physical Chemistry B*, 110 (2006) pages 11730–11738.

[203] L. Huo, J. Hou, S. Zhang, H. Y. Chen and Y. Yang. "A Polybenzo[1,2-b:4,5-b']dithiophene Derivative with Deep HOMO Level and Its Application in High-Performance Polymer Solar Cells". *Angewandte Chemie International Edition*, 49 (2010) pages 1500–1503.

[204] T. Roland, J. Léonard, G. H. Ramirez, S. Méry, O. Yurchenko, S. Ludwigs and S. Haacke. "Sub-100 fs charge transfer in a novel donor–acceptor–donor triad organized in a smectic film". *Physical Chemistry Chemical Physics*, 14 (2012) pages 273–279.

[205] N. Schmidt, T. Clark, S. G. Urquhart and R. H. Fink. "Electron-vibron coupling in halogenated acenaphthenequinone upon O K-edge soft x-ray absorption". *Journal of Chemical Physics*, 135 (2011) page 144301.

[206] T. Roland, G. H. Ramirez, J. Léonard, S. Méry and S. Haacke. "Ultrafast broadband laser spectroscopy reveals energy and charge transfer in novel donor-acceptor triads for photovoltaic applications". *Journal of Physics: Conference Series*, 276 (2011) page 012006.

[207] J. L. Brédas, G. B. Street, B. Thémans and J. M. André. "Organic polymers based on aromatic rings (polyparaphenylene, polypyrrole, polythiophene): Evolution of the electronic properties as a function of the torsion angle between adjacent rings". *Journal of Chemical Physics*, 83 (1985) pages 1323–1329.

[208] C. Quattrocchi, R. Lazzaroni and J. L. Brédas. "Theoretical investigation of the conformational behavior of 2,2-bithiophene". *Chemical Physics Letters*, 208 (1993) pages 120–124.

[209] A. Karpfen, C. H. Choi and M. Kertesz. "Single-bond torsional potentials in conjugated systems: A comparison of ab Initio and density functional results". *The Journal of Physical Chemistry A*, 101 (1997) pages 7426–7433.

[210] P. M. Viruela, R. Viruela and E. Orti. "Difficulties of density functional theory in predicting the torsional potential of 2,2 '-bithiophene". *International Journal of Quantum Chemistry*, 70 (1998) pages 303–312.

[211] S. Narioka, H. Ishii, Y. Ouchi, T. Yokoyama, T. Ohta and K. Seki. "XANES spectroscopic studies of evaporated porphyrin films: Molecular orientation and electronic structure". *The Journal of Physical Chemistry*, 99 (1995) pages 1332–1337.

[212] G. Polzonetti, V. Carravetta, G. Iucci, A. Ferri, G. Paolucci, A. Goldoni, P. Parent, C. Laffon and M. V. Russo. "Electronic structure of platinum complex/Zn-porphyrinato assembled macrosystems, related precursors and model molecules, as probed by X-ray absorption spectroscopy (NEXAFS): theory and experiment". *Chemical Physics*, 296 (2004) pages 87–100.

[213] B. S. Greensfelder, H. H. Voge and G. M. Good. "Catalytic and Thermal Cracking of Pure Hydrocarbons: Mechanisms of Reaction". *Industrial & Engineering Chemistry*, 41 (1949) pages 2573–2584.

[214] K. M. Leung and R. P. Lindstedt. "Detailed kinetic modeling of C1 — C3 alkane diffusion flames". *Combustion and Flame*, 102 (1995) pages 129–160.

[215] I. Fischer and P. Chen. "Allyl-A model system for the chemical dynamics of radicals". *The Journal of Physical Chemistry A*, 106 (2002) pages 4292–4300.

[216] F. J. Comes. "Recycling in the Earth's Atmosphere: The OH Radical—Its Importance for the Chemistry of the Atmosphere and the Determination of Its Concentration". *Angewandte Chemie International Edition*, 33 (1994) pages 1816–1826.

[217] D. J. Hucknall. *Chemistry of hydrocarbon combustion*. Chapman Hall, London (**1985**).

[218] S. Stranges, R. Richter and M. Alagia. "High-resolution inner-shell photoabsorption of the OH and OD free radicals". *Journal of Chemical Physics*, 116 (2002) pages 3676–3680.

[219] E. Vajda, J. Tremmel, B. Rozsondai, I. Hargittai, A. K. Maltsev, N. D. Kagramanov and O. M. Nefedov. "Molecular structure of allyl radical from electron diffraction". *Journal of the American Chemical Society*, 108 (1986) pages 4352–4353.

[220] W. J. Orville-Thomas. "A bond-order/bond-length relation for oxygen-oxygen bonds". *Journal of Molecular Spectroscopy*, 3 (1958) pages 588–591.

[221] P. Glans, K. Gunnelin, P. Skytt, J. H. Guo, N. Wassdahl, J. Nordgren, H. Ågren, F. K. Gel'mukhanov, T. Warwick and E. Rotenberg. "Resonant x-ray emission spectroscopy of molecular oxygen". *Physical Review Letters*, 76 (1996) pages 2448–2451.

[222] N. Kosugi, E. Shigemasa and A. Yagishita. "High-Resolution and Symmetry-Resolved Oxygen K-Edge Spectra of O_2". *Chemical Physics Letters*, 190 (1992) pages 481–488.

[223] F. Neese. "The ORCA program system". *Wiley Interdisciplinary Reviews: Computational Molecular Science*, 2 (2012) pages 73–78.

[224] S. DeBeer George, T. Petrenko and F. Neese. "Prediction of Iron K-Edge Absorption Spectra Using Time-Dependent Density Functional Theory". *The Journal of Physical Chemistry A*, 112 (2008) pages 12936–12943.

[225] M. M. Francl, W. J. Pietro, W. J. Hehre, J. S. Binkley, M. S. Gordon, D. J. DeFrees and J. A. Pople. "Self-consistent molecular orbital methods. XXIII. A polarization-type basis set for second-row elements". *Journal of Chemical Physics*, 77 (1982) pages 3654–3665.

[226] C. D. Dimitrakopoulos and P. R. L. Malenfant. "Organic Thin Film Transistors for Large Area Electronics". *Advanced Materials*, 14 (2002) pages 99–117.

[227] H. Sirringhaus. "25th Anniversary Article: Organic Field-Effect Transistors: The Path Beyond Amorphous Silicon". *Advanced Materials*, 26 (2014) pages 1319–1335.

[228] S. Lee, B. Koo, J. Shin, E. Lee, H. Park and H. Kim. "Effects of hydroxyl groups in polymeric dielectrics on organic transistor performance". *Applied Physics Letters*, 88 (2006) page 162109.

[229] C. G. Choi and B.-S. Bae. "Effects of Hydroxyl Groups in Gate Dielectrics on the Hysteresis of Organic Thin Film Transistors". *Electrochemical and Solid-State Letters*, 10 (2007) pages H347–H350.

[230] H. S. Tan, N. Mathews, T. Cahyadi, F. R. Zhu and S. G. Mhaisalkar. "The effect of dielectric constant on device mobilities of high-performance, flexible organic field effect transistors". *Applied Physics Letters*, 94 (2009) page 263303.

[231] H. Klauk. "Organic thin-film transistors". *Chemical Society Reviews*, 39 (2010) pages 2643–2666.

[232] C. Niederalt, S. Grimme and S. D. Peyerimhoff. "Ab initio theoretical study of the electronic absorption spectra of polycyclic aromatic hydrocarbon radical cations of naphthalene, anthracene and phenanthrene". *Chemical Physics Letters*, 245 (1995) pages 455–462.

[233] S. Hirata, T. J. Lee and M. Head-Gordon. "Time-dependent density functional study on the electronic excitation energies of polycyclic aromatic hydrocarbon radical cations of naphthalene, anthracene, pyrene, and perylene". *Journal of Chemical Physics*, 111 (1999) pages 8904–8912.

[234] A. Matsuura, T. Nishinaga and K. Komatsu. "Structural Studies on the Radical Cations of Benzene, Naphthalene, Biphenylene, and Anthracene Fully Annelated with Bicyclo[2.2.2]octene Frameworks". *Journal of the American Chemical Society*, 122 (2000) pages 10007–10016.

[235] D. W. J. Cruickshank. "A detailed refinement of the crystal and molecular structure of anthracene". *Acta Crystallographica*, 9 (1956) pages 915–923.

[236] M. L. Gordon, D. Tulumello, G. Cooper, A. P. Hitchcock, P. Glatzel, O. C. Mullins, S. P. Cramer and U. Bergmann. "Inner-Shell Excitation Spectroscopy of Fused-Ring Aromatic Molecules by Electron Energy Loss and X-ray Raman Techniques". *The Journal of Physical Chemistry A*, 107 (2003) pages 8512–8520.

[237] A. P. Hitchcock and D. C. Mancini. "Bibliography and database of inner shell excitation spectra of gas phase atoms and molecules". *Journal of Electron Spectroscopy and Related Phenomena*, 67 (1994) pages 1–123.

[238] N. W. Larsen. "Microwave spectra of the six mono-^{13}C-substituted phenols and of some monodeuterated species of phenol. Complete substitution structure and absolute dipole moment". *Journal of Molecular Structure*, 51 (1979) pages 175–190.

[239] J. L. Brédas and A. J. Heeger. "Theoretical investigation of gas-phase torsion potentials along conjugated polymer backbones: polyacetylene, polydiacetylene, and polythiophene". *Macromolecules*, 23 (1990) pages 1150–1156.

[240] V. Lukes, M. Breza and S. Biskupič. "Structure and electronic properties of bithiophenes. I. Torsional dependence". *Journal of Molecular Structure: THEOCHEM*, 618 (2002) pages 93–100.

[241] F. Bencivenga, S. Baroni, C. Carbone, M. Chergui, M. B. Danailov, G. De Ninno, M. Kiskinova, L. Raimondi, C. Svetina and C. Masciovecchio. "Nanoscale dynamics by short-wavelength four wave mixing experiments". *New Journal of Physics*, 15 (2013) page 123023.

[242] S. Grimme. "Calculation of the Electronic Spectra of Large Molecules". In K. B. Lipkowitz, R. Larter and T. R. Cundari, editors, "Reviews in Computational Chemistry", John Wiley & Sons, Inc., Hoboken, NJ, USA (**2004**). pages 153–218.

[243] J. Tomasi, B. Mennucci and R. Cammi. "Quantum Mechanical Continuum Solvation Models". *Chemical Reviews*, 105 (2005) pages 2999–3094.

[244] J.-M. Mewes, Z.-Q. You, M. Wormit, T. Kriesche, J. M. Herbert and A. Dreuw. "Experimental Benchmark Data and Systematic Evaluation of Two a Posteriori, Polarizable-Continuum Corrections for Vertical Excitation Energies in Solution". *The Journal of Physical Chemistry A*, 119 (2015) pages 5446–5464.

[245] T. A. Wesolowski and A. Warshel. "Frozen density functional approach for ab initio calculations of solvated molecules". *The Journal of Physical Chemistry*, 97 (1993) pages 8050–8053.

[246] J. Neugebauer, M. J. Louwerse, E. J. Baerends and T. A. Wesolowski. "The merits of the frozen-density embedding scheme to model solvatochromic shifts". *Journal of Chemical Physics*, 122 (2005) page 094115.

[247] D. R. Rehn. *Inaugural-Dissertation: Development of Quantum Chemical Methods for Excited-State and Response Properties.* Ph.D. thesis, Heidelberg University, Heidelberg (**2015**).

[248] R. Santra and L. S. Cederbaum. "Complex absorbing potentials in the framework of electron propagator theory. I. General formalism". *Journal of Chemical Physics*, 117 (2002) pages 5511–5521.

[249] D. Zuev, T.-C. Jagau, K. B. Bravaya, E. Epifanovsky, Y. Shao, E. Sundstrom, M. Head-Gordon and A. I. Krylov. "Complex absorbing potentials within EOM-CC family of methods: Theory, implementation, and benchmarks". *Journal of Chemical Physics*, 141 (2014) page 024102.

[250] T.-C. Jagau and A. I. Krylov. "Complex Absorbing Potential Equation-of-Motion Coupled-Cluster Method Yields Smooth and Internally Consistent Potential Energy Surfaces and Lifetimes for Molecular Resonances". *The Journal of Physical Chemistry Letters*, 5 (2014) pages 3078–3085.

[251] V. Averbukh and L. S. Cederbaum. "Ab initio calculation of interatomic decay rates by a combination of the Fano ansatz, Green's-function methods, and the Stieltjes imaging technique." *Journal of Chemical Physics*, 123 (2005) page 204107.

[252] S. Kopelke, K. Gokhberg, V. Averbukh, F. Tarantelli and L. S. Cederbaum. "Ab initio interatomic decay widths of excited states by applying Stieltjes imaging to Lanczos pseudospectra". *Journal of Chemical Physics*, 134 (2011) page 094107.

List of Figures

List of Tables

List of Publications

- **Physical properties, exciton analysis and visualization of core-excited states: an intermediate state representation approach**
  Jan Wenzel and Andreas Dreuw
  submitted for publication in Journal of Chemical Theory and Computation, (2016)

- **Statistical Analysis of Electronic Excitation Processes: Quantification of Location, Compactness, and Excitonic Correlation Effects**
  Felix Plasser, Benjamin Thomitzni, Stefanie A. Bäppler, Jan Wenzel, Dirk R. Rehn, Michael Wormit, and Andreas Dreuw
  Journal of Computational Chemistry, 36 (2015), pages 1609-1620

- **Analysis and comparison of CVS-ADC approaches up to third order for the calculation of core-excited states**
  Jan Wenzel, Andre Holzer, Michael Wormit, and Andreas Dreuw
  Journal of Chemical Physics, 142 (2015), pages 214104

- **Advances in molecular quantum chemistry contained in the Q-Chem 4 program package**
  Yihan Shao, Zhengting Gan, Evgeny Epifanovsky, Andrew T. B. Gilbert, Michael Wormit, Joerg Kussmann, Adrian W. Lange, Andrew Behn, Jia Deng, Xintian Feng, Debashree Ghosh, Matthew Goldey, Paul R. Horn, Leif D. Jacobson, Ilya Kaliman, Rustam Z. Khaliullin, Tomasz Ku, Arie Landau, Jie Liu, Emil I. Proynov, Young Min Rhee, Ryan M. Richard, Mary A. Rohrdanz, Ryan P. Steele, Eric J. Sundstrom, H. Lee Woodcock III, Paul M. Zimmerman, Dmitry Zuev, Ben Albrecht, Ethan Alguire, Brian Austin, Gregory J. O. Beran, Yves A. Bernard, Eric Berquist, Kai Brandhorst, Ksenia B. Bravaya, Shawn T. Brown, David Casanova, Chung-Min Chang, Yunquing Chen, Siu Hung Chien, Kristina D. Closser, Deborah L. Crittenden, Michael Diedenhofen, Robert A. DiStasio Jr., Hainam Do, Anthony D. Dutoi, Richard G. Edgar, Shervin Fatehi, Laszlo Fusti-Molnar, An Ghysels, Anna Golubeva-Zadorozhnaya, Joseph Gomes, Magnus W. D Hanson-Heine, Philipp H. P. Harbach, Andreas W. Hauser, Edward G. Hohenstein, Zachary C. Holden, Thomas-C. Jagau, Hyunjun Ji, Ben Kaduk, Kirill Khistyaev, Jaehoon Kim, Jihan Kim, Rollin A. King, Phil Klunzinger, Dmytro Kosenkov, Tim Kowalczyk, Caroline M. Krauter, Ka Un Lao, Adle Laurent, Keith V. Lawler, Sergey V. Levchenko, Ching Yeh Lin, Fenglai Liu, Ester Livshits, Rohini C. Lochan, Arne Luenser, Prashant Manohar, Samuel F. Manzer, Shan-Ping Mao, Narbe Mardirossian, Aleksandr V. Marenich, Simon A. Maurer, Nicholas J. Mayhall, Eric Neuscamman, C. Melania Oana, Roberto Olivares-Amaya, Darragh P. O'Neill, John A. Parkhill, Trilisa M.

Perrine, Roberto Peverati, Alexander Prociuk, Dirk R. Rehn, Edina Rosta, Nicholas J. Russ, Shaama M. Sharada, Sandeep Sharma, David W. Small, Alexander Sodt, Tamar Stein, David Stck, Yu-Chuan Su, Alex J. W. Thom, Takashi Tsuchimochi, Vitalii Vanovschi, Leslie Vogt, Oleg Vydrov, Tao Wang, Mark A Watson, Jan Wenzel, Alec White, Christopher F. Williams, Jun Yang, Sina Yeganeh, Shane R. Yost, Zhi-Qiang You, Igor Ying Zhang, Xing Zhang, Yan Zhao, Bernard R. Brooks, Garnet K. L. Chan, Daniel M. Chipman, Christopher J. Cramer, William A. Goddard III, Mark S. Gordon, Warren J. Hehre, Andreas Klamt, Henry F. Schaefer III, Michael W. Schmidt, C. David Sherrill, Donald G. Truhlar, Arieh Warshel, Xin Xu, Aln Aspuru-Guzik, Roi Baer, Alexis T. Bell, Nicholas A. Besley, Jeng-Da Chai, Andreas Dreuw, Barry D. Dunietz, Thomas R. Furlani, Steven R. Gwaltney, Chao-Ping Hsu, Yousung Jung, Jing Kong, Daniel S. Lambrecht, WanZhen Liang, Christian Ochsenfeld, Vitaly A. Rassolov, Lyudmila V. Slipchenko, Joseph E. Subotnik, Troy Van Voorhis, John M. Herbert, Anna I. Krylov, Peter M. W. Gill, and Martin Head-Gordon
Molecular Physics, 113 (2015), pages 184-215

- **Calculating X-ray absorption spectra of open-shell molecules with the unrestricted algebraic-diagrammatic construction scheme for the polarization propagator**
  Jan Wenzel, Michael Wormit, and Andreas Dreuw
  Journal of Chemical Theory and Computation, 10 (2014), pages 4583-4598

- **Calculating core-level excitations and x-ray absorption spectra of medium-sized closed-shell molecules with the algebraic-diagrammatic construction scheme for the polarization propagator**
  Jan Wenzel, Michael Wormit, and Andreas Dreuw
  Journal of Computational Chemistry, 35 (2014), pages 1900-1915

- **Investigating excited electronic states using the algebraic diagrammatic construction (ADC) approach of the polarisation propagator**
  Michael Wormit, Dirk R. Rehn, Philipp H. P. Harbach, Jan Wenzel, Caroline M. Krauter, Evgeny Epifanovsky, and Andreas Dreuw
  Molecular Physics, 112 (2014), pages 774-784

- **Charge and energy transfer in a bithiophene perylenediimide based donor-acceptor-donor system for use in organic photovoltaics**
  Jan Wenzel, Andreas Dreuw, and Irene Burghardt
  Physical Chemistry Chemical Physics, 15 (2013), pages 11704-11716

Danksagung

Mein ganz besonderer Dank geht an Prof. Dr. Andreas Dreuw für die Bereitstellung des spannenden und vielseitigen Themas dieser Arbeit und für die sehr motivierenden Diskussionen, aus denen viele neue Ideen entstanden sind. Andreas war und ist zu jeder Zeit ein großartiger Mentor und Betreuer, der mich schon von Beginn meines Studiums unterstützt hat und mich auch an Tiefpunkten motivieren konnte, weiterzumachen. Danke für die wunderbare Betreuung und Freundschaft.

Ein weiterer großer Dank geht an meine Eltern, Tobi und die ganze Familie, die mich immer in jeder Hinsicht bedingungslos unterstützt haben. Ohne Euch wäre mein Chemiestudium und die anschließende Promotion nicht möglich gewesen.

Ein ganz besonders großer Dank geht an Dr. Michael Wormit. Ohne ihn wäre diese Arbeit nicht möglich gewesen. Man konnte ihn zu jeder Zeit um Rat fragen, den er mit großer Hilfsbereitschaft und seiner wunderbaren Art zu erklären gerne gegeben hat. Leider kann ich ihm dieses nicht mehr persönlich sagen, aber ich bin sehr dankbar dafür mit ihm zusammen gearbeitet zu haben.

Im möchte mich auch bei meinen Mentoren PD Dr. Markus Pernpointner, Dr. Shirin Faraji, Prof. Dr. Dres. h.c. Lorenz S. Cederbaum und Prof. Dr. Jochen Schirmer für die anregenden Gespräche und Diskussionen bedanken. Bei der *Heidelberg Graduate School of Mathematical and Computational Methods for the Sciences* bedanke ich mich recht herzlich für die Unterstützung. Meinen Bürokollegen Dirk Rehn, Matthias Schneider, Tim Stauch und Jie Han danke ich für die tolle Atmosphäre im Büro und für alle lustigen Momente, die wir hatten. Sehr bedanken möchte ich mich im Speziellen bei Tim Stauch, Dirk Rehn, Michael Herbst, Katharyn Fletcher und Maria Rupprecht für das sprachliche Korrekturlesen von Teilen dieser Arbeit und die nützlichen Anmerkungen. Bei Jan Mewes bedanke ich mich für das LaTeX Layout.

Beim gesamten AK Dreuw (Stefan, Mercedes, Max, Daniel, Tim, Chong, Jie, Katie, Tobi, Daria, Michi, Manu, Jan, Steffi, Georg, Jörg, Ben) möchte ich mich für die tolle Arbeitsatmosphäre und nützlichen Diskussionen bedanken. Das gilt natürlich auch für alle ehemaligen Mitglieder, insbesondere Shirin, Dirk, Matze und Philipp. Es hat mir sehr viel Spaß gemacht hier zu arbeiten und all die unzähligen außerfachlichen Aktivitäten zu genießen.

Zuletzt möchte ich mich bei all meinen Freunden bedanken, die mich ebenfalls zu jeder Gelegenheit unterstüzt haben.

Eidesstattliche Versicherung gemäß §8 der Promotionsordnung der Naturwissenschaftlich-Mathematischen Gesamtfakultät der Universität Heidelberg

1. Bei der eingereichten Dissertation zu dem Thema
   "Development and Implementation of Theoretical Methods for the Description of Electronically Core-Excited States"
   handelt es sich um meine eigenständig erbrachte Leistung.

2. Ich habe nur die angegebenen Quellen und Hilfsmittel benutzt und mich keiner unzulässigen Hilfe Dritter bedient. Insbesondere habe ich wörtlich oder sinngemäß aus anderen Werken übernommene Inhalte als solche kenntlich gemacht.

3. Die Arbeit oder Teile davon habe ich bislang nicht an einer Hochschule des In- oder Auslands als Bestandteil einer Prüfungs- oder Qualifikationsleistung vorgelegt.

4. Die Richtigkeit der vorstehenden Erklärungen bestätige ich.

5. Die Bedeutung der eidesstattlichen Versicherung und die strafrechtlichen Folgen einer unrichtigen oder unvollständigen eidesstattlichen Versicherung sind mir bekannt.

Ich versichere an Eides statt, dass ich nach bestem Wissen die reine Wahrheit erklärt und nichts verschwiegen habe.

Ort/Datum Unterschrift